Diss. ETH No. 17708

Numerical simulation of fluid flow in mid-ocean ridge hydrothermal systems

A dissertation submitted to

ETH Zurich

for the degree of

Doctor of Sciences

presented by

Dingeman Coumou

Drs. Geophysics., Utrecht University, Netherlands

born April 5, 1977

citizen of The Netherlands

accepted on the recommendation of

PD Dr. Thomas Driesner, examiner

Prof. Dr. Christoph A. Heinrich, co-examiner

Dr. Steve Ingebritsen, co-examiner

Dr. Sebastian Geiger-Boschung, co-examiner

2008

To Bas

CONTENTS

[1] Published as: D. Coumou, T. Driesner, S. Geiger, C.A. Heinrich and S.K. Matthai, 2006, The dynamics of mid-ocean ridge hydrothermal systems: Splitting plumes and fluctuating vent temperatures, *Earth Planet. Sci. Lett.* **245**, 218–231

[2] Published as: D. Coumou, S.K. Matthai, S. Geiger, T. Driesner, 2008, A Parallel FE-FV Scheme to Solve Fluid Flow in complex Geologic Media., *Comp. Geoscience* **in print**

ABSTRACT

Located in the deep oceans, the 60,000km chain of mid-ocean ridge spreading centers hosts the world's largest magmatic-hydrothermal systems. These so-called black smoker systems transport a major part of the total Earth's heat flux, affect the chemistry of crust and overlying ocean significantly and provide nutrients for chemosynthetic life on and beneath the seafloor. In addition, they are active ore-forming systems and the modern day analogue of massive sulfide deposits which have successfully been developed into world-class mines onshore.

To understand the physics of these sub-seafloor convection systems numerical modeling techniques are essential. However, the physics of these systems are complex especially because seawater can phase-separate, either by boiling or condensation, into a low-salinity vapor and high-salinity brine. To capture this process accurately in numerical models is challenging but key to understanding the true nature and dynamics of black smoker systems. Previous numerical studies avoided these complexities by taking severe assumptions on the thermodynamic properties of the fluid. In addition, high heat-flux thermal convection has only been studied in two dimensions so far.

The object of this thesis is to contribute to our understanding of black smoker hydrothermal systems in two fundamental ways: The first goal is to study thermal convection in three dimensions using high-resolution models. The second goal is to accurately simulate multi-phase thermohaline convection including the phase-separation of a seawater-like fluid into a low-salinity vapor and high-salinity brine.

To do so, two novel computational tools were developed during this thesis work. The first is the addition of parallel computing techniques to CSMP++, a simulation platform developed by research groups at ETH Zurich and Imperial College London, allowing the use of supercomputers to calculate simulations. The second consists of a new pressure-enthalpy-salinity simulation scheme, using finite element and finite volume numerical techniques, to solve mass and energy transport of multi-phase NaCl-H_2O fluids in geologic media.

In this thesis results from more than 50 simulations, including high-resolution 3D and multi-phase models, are presented, providing new insights into the nature and dynamics of sub-seafloor convection. The most important general conclusion from these simulations is that the non-linear dependence of the fluid properties on temperature, pressure and salinity can explain many of the key-observations at black smoker systems. Though all models are generic in nature, omitting geologic complexity of real systems, they accurately reproduce salient features as temperature and salinity variations measured in vent-fluids. Moreover, convection in three-dimensions naturally forms individual black smoker fields at regular spacing without any restrictions on the sub-seafloor permeability distribution.

High-resolution 3D simulations demonstrate that recharge of black smoker systems dominantly happens in narrow concentric zones surrounding pipe-like upflow zones. Recharge fluids are relatively warm, which enhances mass fluxes and therefore the energy output of

the system is optimized. The location and extend of recharge zones is usually inferred from indirect methods and hence poorly understood. However, apart from thermal and chemical implications, the location of recharge zones is of direct importance for successful hydrologic tracer injection experiments at active black smoker systems as currently debated within the scientific community. The 3D simulations presented in this thesis provide the first well-constrained quantitative predictions for the ideal location and time evolution for such challenging experiments.

Simulations including the full complexity of the NaCl-H_2O phase diagram system show that water depth is a major control on sub-seafloor phase-separation and associated convective flow patterns. Typically, in systems that discharge at ∼1500 m water depth, boiling zones develop which can transport both low-salinity vapor and high-salinity brines upwards. In contrast, in systems that discharge at ∼3500 m water depth, phase-separation is restricted to regions near the base of the hydrothermal system. Therefore, at these systems a seawater-like fluid diluted with a low-salinity vapor vents stably at sub-seawater salinity. The predicted salinities and their relative stability or instability as a function of water depth are in excellent agreement with long-term observations of natural black smoker systems.

ABSTRACT

ZUSAMMENFASSUNG

Im tiefen Ozean erstrecken sich auf insgesamt 60.000 Kilometern Länge mittelozeanische Sprei-zungsrücken und führen die grössten magmatisch-hydrthemalen Systeme der Welt. Diese so-genann-ten Black Smoker (Schwarze Raucher) Systeme transportieren einen Grossteil des gesamten Wärme flusses der Erde, beeinflussen massgeblich die Chemie der Erdkruste und des darüberliegenden Ozeans und versorgen das chemosynthetische Leben auf und unter dem Meeresboden mit Nährstoffen. Darüber hinaus sind sie aktive lagerstättenbildende Systeme und können als rezente Analogien schwefelreicher Ablagerungen(massive sulfide deposits) angesehen werden, welche, mittlerweile an Land aufgeschlossen, als profitable Bergwerke erschlossen wurden.

Um die physikalischen Prozesse dieser Konvektionssysteme unter dem Meeresboden erfassen zu können, sind numerische Modelliermethoden unerlässlich. Es handelt sich jedoch um ein hochkomplexes System, insbesondere da sich das Meerwasser durch Koch- oder Kondensationsvorgänge in zwei Phasen aufspalten kann - einen salzarmen Dampf (vapor) und eine salzreiche Flüssigkeit (brine). Diesen Prozess in numerischen Modellen adäquat erfassen zu können, ist anspruchsvoll aber entscheidend, um Black Smoker Systeme mitsamt der zu Grunde liegenden Antriebsprozesse im Kern zu verstehen. Bisherige numerische Studien umgingen diese Komplexität durch einschneidende, vereinfachende Annahmen bezüglich der thermodynamischen Eigenschaften des Fluids. Ausserdem wurden thermale Konvektionen mit hohen Wärmeflüssen bislang nur in zwei-dimensionalen Simulationen dargestellt.

Ziel der vorliegenden Arbeit ist es, zum Verständnis hydrothermaler Black Smoker Systeme mittels zweier grundlegender Ansätze beizutragen. Zum einen soll die thermale Konvektion drei-dimensional unter Verwendung eines hoch-auflösenden Modellgitter erfasst werden. Zum anderen soll die mehrphasige thermohaline Konvektion möglichst genau abgebildet werden und auch die Aufspaltung eines Meerwasser ähnlichen Fluids in einen salzarmen Dampf und eine salzreiche Flüssigkeit erfassen.

Dafür waren im Verlauf dieser Dissertation zwei entscheidende Neuentwicklungen nötig. Die erste bestand in der Ergänzung paralleler Rechentechniken in CSMP++, einer von Forschungsgruppen der ETH Zürich und dem Imperial College London entwickelten Simulationsplattform, um die Nutzung und Auslastung von Hochleistungsrechnern zu ermöglichen. Die zweite bestand aus einer neuen Druck, Enthalpie und Salinität basierten Simulationsmethode, die mithilfe numerischer Finite-Element- und Finite-Volumen-Verfahren Massen- und Energietransporte mehrphasiger NaCl-H_2O Fluide in geologischen Zusammenhängen abbildet.

Diese Arbeit stellt insgesamt mehr als 50 Simulationen vor, darunter 3D- und Mehrphasen-Modelle, die neue Erkenntnisse zur Natur und Dynamik von Konvektionen unter dem Meeresboden liefern. Die wohl wichtigste allgemeine Schlussfolgerung aus diesen Simulationen

ist, dass die nicht-linearen Abhängigkeiten der Fluideigenschaften von Temperatur, Druck und Salinität eine Vielzahl von Schlüsselbeobachtungen an Black Smoker Systemen erklären können. Obwohl alle Modelle generischer Art sind, die auf keine in der Natur vorhandenen geologische Strukturen eingehen, sind sie in der Lage, bedeutende Charakteristika wie Temperatur- und Salinitätsschwankungen in Messungen des aus den Schloten austretenden Fluids widerzuspiegeln. Ferner ergaben die drei-dimensionalen Simulationen, dass die Konvektion naturgemäss individuelle Black Smoker Felder ausbildet, die in regelmässigen Abständen zueinander stehen, und dass es hierfür keinerlei heterogener Permeabilitätsverteilungen bedarf.

Die hoch-auflösende 3D-Simulationen zeigen, dass der so-genannte Recharge (Erneuerungsfluss) in Black Smoker Systemen hauptsächlich in einem schmalen konzentrischen Ring um das rohr-förmigen Aufstromgebiet (pipe-like upflow zone) statt findet. Recharge-Fluide sind relativ warm und erhöhen dadurch Massenfluss und Energieumsatz des gesamten Systems. Lage und Ausdehnung der Recharge-Gebiete werden normalerweise durch indirekte Methoden bestimmt und sind daher noch kaum verstanden. Die Lokalisierung von Recharge-Gebieten ist jedoch neben den thermalen und chemischen Auswirkungen auch direkt für erfolgsversprechende hydrologische Tracer-Injection-Experimente an aktiven Black Smoker Systemen, welche derzeit innerhalb der wissenschaftlichen Gemeinschaft diskutiert werden, von grosser Bedeutung. Die in der vorliegenden Arbeit diskutierten 3D-Simulationen liefern die ersten, klar begrenzten, quantitativen Vorhersagen für die ideale Lage und die zeitliche Entwicklung solch anspruchsvoller Experimente.

Simulationen, welche die gesamte Komplexität des NaCl-H_2O-Phasendiagramms berücksichtigen, belegen, dass die Wassertiefe massgeblichen Einfluss auf die Phasenaufspaltung und das dadurch beeinflusste Fliessverhalten unter dem Meeresboden hat. In Systemen, die in einer Tiefe von ungefähr 1500 Metern austreten, bilden sich in der Regel Kochzonen, welche sowohl salzarmen Dampf, als auch salzreiche Flüssigkeiten nach oben transportieren können. In Systemen, die in einer Tiefe von ungefähr 3500 Metern austreten, hingegen beschränkt sich die Phasenseparation auf eine Region am Fuss des hydrothermalen Systems. Daher tritt in diesen Systemen beständig ein durch salzarmen Dampf verdünntes Meerwasser ähnliches Fluid aus. Die numerisch prognostizierten Salinitäten und ihre jeweilige Stabilität oder Instabilität als Funktion der Wassertiefe sind in ausgezeichneter Übereinstimmung mit langfristigen Beobachtungen natürlicher Black Smoker Systeme.

ACKNOWLEDGEMENTS

I like to thank my two supervisors Thomas Driesner and Christoph Heinrich. Thomas has spend an enormous amount of time and effort to make this thesis a success, which I really highly appreciate. Even during holidays we often kept in close contact and he just could not stop supporting me. Stoeff's drive, optimisme and confidence in me and the project kept me going during tougher periods of this thesis work. Also his approach to keep the important scientific goals in mind and place the results in a broader context were really crucial. All in all, I feel really lucky with my two supervisors not only scientifically but also on a personal level.

Further, I would like to thank all the people from the CSMP++ developers community. I have used much of Sebastian Geigers code during this work, something I am very thankful for, and also his continuous support and feedback is highly appreciated. I like to thank Stephan Matthai for working together on the parallel code, the pleasant stays in London, his general support and for organising the CSMP workshops which proved to be very useful. Special thanks go to Philipp Weis for many useful discussions, for doing an enormous ammount of proof reading and for quite often making a funny joke. I like to thank Adrianna Paluszny for using some of her code and helping me out with all kinds of coding problems. Arnold von Krechel has been extremely helpfull during the development of the parallel code.

Also I like to thank all other colleagues of the fluid and ore deposit group at the ETH, especially Svetoslav Georgiev, Wim Malfait, Caroline Harris, Claudia Pudack, Zoltan Zajacz, Gillian Gruen, Britt Meyer, Albrecht von Quadt, Werner Halter, Marcel Guillong, Jacob Hanley, Valentina Herzog, Ingo Steinberger, Ramon Aubert, Dieter Gebauer, Anthi Liati, Jung Hun Seo, Nicole Hurtig, Dimitri Meier, Melanie Moll and Elitsa Stefanova

Finally I like to thank Catherine for creating a super nice and spacy front for this thesis and for being the best sister I could imagine. Fabulous Fab is deeply thanked for the mental supervision during the years which proved to be crucial for the completion of this work: Ik hou van je, mops!

1. INTRODUCTION

1.1 Black-smoker fields

The discovery of seafloor hydrothermal systems in the 1970s (Corliss et al., 1979) has led to a major reassessment of the Earth's thermal and geochemical budgets and has revolutionized our understanding of biological processes (Lowell et al., 1995; Kelley et al., 2002). These hydrothermal systems are found in the deep ocean along mid-ocean ridge spreading centers where new oceanic crust is continuously created. Hydrothermal circulation of seawater is driven by magmatic heat which is ultimately coming from radiogenic decay within the Earth's deep interior. Seawater percolates into the crust, slowly heats up on its way down and reacts with the basaltic rock. Near the base of the system, at the magmatic-hydrothermal interface, fluids are expected to reach their hottest temperature, after which they rise vigorously and vent as hydrothermal fluids at so-called black-smokers. When the hot fluids discharge and contact cold seawater, minerals precipitate to form the black "smoke" and build large chimney structures (Hannington et al., 1995).

Energy fluxes associated with black-smoker hydrothermal systems are large, accounting for approximately 25% of Earth's total heat flux (Stein and Stein, 1994; Fisher, 2001). To dissipate this heat, it is estimates that the total mass of the oceans is circulated through the crust in less than one million years (Wolery and Sleep, 1976). These large mass fluxes indicate that chemical fluxes between ocean and crust, due to the reaction of fluid with the rock, are also substantial. Therefore, black-smoker systems play a fundamental role in regulating the chemistry of the oceans through geologic time.

Black-smoker systems are active ore forming systems and the modern-day, currently-forming equivalent to volcanogenic massive sulfide (VMS) deposits that have been successfully developed into world-class mines onshore (Kesler, 1994). VMS deposits are high-grade ore deposits rich in copper, zinc and lead, some with high gold and silver contents. Extensive marine exploration has been limited to less than 5% of the worlds oceans but has indicated that potential seafloor resources could be large (Rona, 2003). The high metal prices in recent years have ignited the first commercial activities towards harvesting these resources (Broad, 1997). With metal prices expected to rise further in the near future, this emerging market has the potential to grow substantially.

Possibly the most amazing of all, the discovery of entire biological communities of bizarre creatures, thriving in the so-called 'desert of the deep sea', has revolutionized our understanding of biological processes (Kelley et al., 2002). Rather than photosynthetic energy, these ecosystems are based on chemosynthetic energy which is provided by the hydrothermal fluids. The chemosynthetic bacteria attract organisms such as tube worms, soft corals and other larger organisms by acting as nutrient source. This way, isolated oases of life form around active venting black-smoker fields. Since the first scientific exploration dives in the 1970s, more than 500 new species have been identified (Von Damm, 2001), including ther-

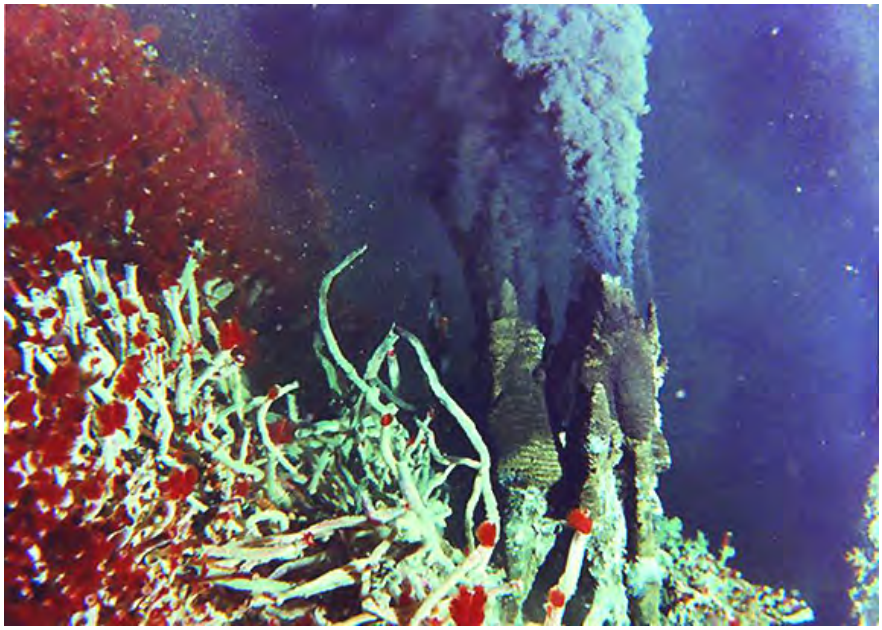

Fig. 1.1: Tubeworms in front of active black smoker chimneys (source: www.morning-earth.org).

mophiles which can resist temperatures up to 130°C. Bacterial life is known to continue in the sub-seafloor (Wirsen, 2004) and it has been suggested that cavities along ridge faults could even harbor large ocean-floor life forms down to several hundred meters depth (Holland et al., 2006). The archea and other micro-biological components are attracting increasing interest for both biotechnological applications and "origin of life" questions on Earth and other planets (Zierenberg et al., 2000).

1.2 Direct observational constraints

During the last decades direct observational data from both manned and unmanned submersibles has become available (Massoth et al., 1989; Charlou et al., 1996; Chiba et al., 2001; Von Damm et al., 2003), giving constraints on the size of sub-seafloor convection cells and the magnitude of energy- and mass transport. By now, active black-smoker fields have been identified along all spreading margins, irrespective of the spreading rate, at depths ranging from 800m to 3600m below sea level (Von Damm, 2001). Generally a distinction is made between black-smoker systems along fast spreading and slow spreading ridges. The latter have a substantially lower heat supply and seem controlled by tectonic rather than magmatic processes. In contrast to fast spreading systems, slow spreading ridges are located at much deeper ocean depths, often lack clear magmatic melt lenses (Fisher, 2001), and normally host fewer vent fields per kilometer of ridge axis. Nonetheless, black-smoker fields at both types of ridges share many of the same characteristics. Vent field size is typically on the order of 10^3 to 10^5 m^2 (i.e. one to tens of football fields) hosting few to several tens of individual black-smoker chimneys (Lowell et al., 1995).

The temperature of vents is often close to but never higher than 400°C, which is surprising since magmatic temperatures in this setting are expected to be much higher (i.e. ∼1200°C).

Adjacent to the highly focused, high-temperature venting at black-smoker chimneys, diffuse venting of lower temperature fluids (less than 100°C) has been observed at essentially all vent fields (Hannington et al., 1995). These lower temperature, diffuse vents are typically located at the edges of a hydrothermal field. Studies from individual vent fields suggest that a large part (up to 90%) of the advective heat loss may be due to diffuse, low-temperature discharge (Lowell et al., 1995). A third, intermediate style of venting at temperatures of 100°C to 300°C is often referred to as "white smokers" because of the precipitation of white particles of silica, anhydrite and barite (Hannington et al., 1995).

The salinity of most, if not all hydrothermal fluids sampled differs from seawater (Massoth et al., 1989; Butterfield et al., 1990; Von Damm et al., 2003). These anomalously high or low salinities can often only be explained by the mixing of normal seawater with either a high-salinity brine or a low-salinity vapor, implicating that seawater phase-separates at depth. Remarkable by itself, phase-separation can occur at the high pressures encountered in the deep ocean because seawater is not a pure water but rather a salty fluid. This process is expected to be a key process affecting the physics and chemistry of black-smoker hydrothermal systems. It is of special importance to the formation of ore-deposits since phase-separation has a great impact on solubility of metals and on their transport since metals preferentially fractionate either in the liquid or the vapor phase (Heinrich, 2007).

1.3 Geophysical constraints

In addition to the direct observational data, geophysical observations provide important constraints on the characteristics of sub-seafloor hydrothermal systems and associated heat fluxes (Fisher, 2001).

Seismic surveys have given insight into the structure of the upper oceanic crust. A feature common to many fast spreading ridges is an axial reflector at a depth of 1 to 2 km, generally thought to represent the top of a melt lens (Dunn et al., 2000). Below this melt lens, with a cross-ridge extent often no more than 2km, a larger mush zone has been identified, which, together with the melt lens, supplies the magma that forms the crust (Dunn et al., 2000; Fisher, 2001). The restricted width of this mush zone suggests that fluid flow and associated advective heat loss may occur through the full thickness of oceanic crust. Seismic studies of slow-spreading ridges have rarely revealed shallow axial reflectors indicative of melt lenses.

A first global estimate on the energy transported by ridge crest hydrothermal systems comes from the difference between predicted heat-fluxes from lithospheric cooling models and measured conductive heat flow through young oceanic crust (Stein and Stein, 1994; Hofmeister and Criss, 2005). In fact, the discrepancy between the two lead to initial speculations about the existence of thermal vent sites on the ocean floor (Le Pichon and Langseth, 1969). An upper estimate of the steady state heat output can be calculated from the energy added by the crustal accretion process. Such an estimate gives values ranging from 10 to 120 MW per kilometer of ridge axis depending on the spreading rate (Fisher, 2001). However, direct measurements from vent fields and ridge segments indicate a much higher heat output, implying that magma supply is episodic and local (Baker and Massoth, 1987; Ginster et al., 1994; Baker and Urabe, 1996; Ramondenc et al., 2006).

Constraining the structure of the sub-seafloor hydrothermal convection cell by means of geophysical methods is not straightforward, but a few methods have given some very valuable insights. Magnetic anomaly data can illuminate upflow zones since here the rock

has been leached of magnetic material, resulting in magnetic lows measured near the seafloor. Such data showed that, at least for the Main Endeavour vent field, upflow zones are narrow, near-vertical pipe-like features (Tivey and Johnson, 2002). In some areas possible downflow regions have been imaged with microseismicity, which is interpreted to be associated with penetration of cool water into hot rock. The depth extent of microseismic activity is thought to indicate the depth of circulation and typically reaches 2 to 4 km below the seafloor. Recent microseismic data suggest that recharge of fluids can occur very close to the axis, directly above the magmatic melt lens (Tolstoy et al., 2008). Additional evidence on hydrothermal cell structure comes from ophiolites, i.e. the fossilized remains of mid-ocean ridge spreading centers, which confirm that upflow regions are likely pipe-like structures (Saccocia and Gillis, 1995).

1.4 Transient observations

Long term observations of black-smoker vent fluids show that some remain chemically and thermally constant over periods of decades while others show variations on the timescale of weeks (Massoth et al., 1989; Von Damm, 1990; Von Damm et al., 1997, 2003). Several temperature variations were recorded directly following earthquakes in the region (Fornari et al., 1998; Johnson et al., 2000). Proposed mechanisms to explain the thermal oscillations included propagating cracking fronts and the replenishment of magma (Wilcock, 2004; Von Damm, 2005).

Variations in the salinity of vent fluids are attributed to changes in sub-seafloor phase-separation processes. There is mounting evidence for transient phase separation of seawater, potentially occurring anywhere between the seafloor and the deep magmatic-hydrothermal interface, in the form of major salinity variations at the time scale of days (Von Damm et al., 2003) to years (Butterfield et al., 1994b; Von Damm et al., 1997; Von Damm, 2005). Many observations support the hypothesis that vapor-phase fluids vent in the early period following a volcanic eruption or diking event, and that the liquid phase brines are stored within the oceanic crust and vent at a later time. This is supported by fluid inclusion studies providing evidence that brine forms near the base of the hydrothermal system and possibly in upflow zones (Nehlig, 1991; Kelley et al., 1993; Saccocia and Gillis, 1995).

1.5 Numerical modeling

To understand the physics of sub-seafloor convection, including phase-separation processes, numerical modeling techniques are essential. The physics are too complex to be addressed with analytical formulations, and lab experiments are hampered by the high pressure-temperature conditions. Knowledge of the physics and dynamics of circulation is important since all phenomena discussed in previous sections ultimately depend on them. For example, ecosystems are controlled by the temperature and composition of the fluid, which are in turn determined by the circulation structure and its dynamics. In general, numerical modeling can explain the observational data and elucidate physical processes. In the particular case of black-smoker hydrothermal systems it has an even more profound meaning, as direct observations are costly and scarce, and 3D observations are virtually absent.

However, accurately capturing the physics of sub-seafloor convection in numerical models

is challenging and therefore assumptions need to be made, limiting the physical realism of the simulations. The governing equations are non-linear and strongly coupled and properties of liquid and vapor can vary over orders of magnitude as a function of pressure, temperature and salinity. Therefore, most studies have been carried out with simplified fluid properties. Several earlier studies took a so-called Boussinesq approximation in which density terms are only considered in the buoyancy term and neglected elsewhere (Wilcock, 1998; Schoofs and Hansen, 2000), also commonly assuming constant values for fluid properties such as viscosity, heat capacity and thermal expansivity (Cherkaoui and Wilcock, 1999). These approximations can drastically reduce the tendency of a system to convect (Straus and Schubert, 1977) and, in the case of black-smoker systems, can in fact suppress the dominant physical processes (Jupp and Schultz, 2000, 2004). Recent numerical studies used realistic, non-linear, fluid properties, but treated convection as a single-phase system. One way to do this was to take pure water as a proxy for seawater, which at pressures above the critical point will always be single phase (Jupp and Schultz, 2000). Others used properties of seawater (i.e. H2O with 3.2wt% NaCl fluid) but treated fluids in the two phase regions as a single-phase fluid by taking a weighted average of the two phases (Fontaine and Wilcock, 2007).

These recent numerical studies, which used accurate thermodynamic properties of water, have provided a number of key insights into the physics of black-smoker systems but were limited in two important ways. First, they were restricted to two-dimensional geometries. Second, they assumed single-phase fluids and thereby excluded the effect of phase-separation of a salty fluid into a low-salinity vapor and high-salinity brine.

1.6 This study

In this study we present novel simulations of single-phase thermal convection in three dimensions and simulations of two-phase and three-phase convection in two dimensions. In order to do so, two major code development projects were undertaken and completed during this thesis work. The first consisted of the addition of parallel computing techniques into CSMP++ (Matthai et al., 2007) to reduce computation time to acceptable periods of typically a few weeks. The second consisted of a pressure-enthalpy-salinity (PHX) transport scheme that includes the full complex physics of phase-separation of a salty fluid into a low-salinity vapor and high-salinity brine. This scheme replaces the earlier pressure-temperature-salinity (PTX) scheme as implemented by Sebastian Geiger (Geiger, 2004).

With these new computational tools, we investigate sub-seafloor convection at mid-ocean ridge spreading centers taking two distinct approaches. First, we study large-scale fluid flow patterns in two and three dimensions using supercritical pure water as a proxy for seawater. This single-phase approach allows the use of the computationally efficient PTX scheme. Nevertheless, the enormous size of three-dimensional meshes requires the use of parallel computing techniques to reduce run time. Second, we study on smaller scales, restricted to two dimensions, phase-separation phenomena and the effect they have on heat transport, brine formation and salinity variation in black-smoker systems. Here the use of the PHX scheme is required, which is computationally less efficient but accurately accounts for all physical effects during phase-separation of an H_2O-NaCl fluid.

In both approaches we focus on understanding the complex physics of these systems and therefore geologic and geometric complexity is intentionally omitted.

1.7 Outline

This thesis is organized as follows. Chapter 2 presents two-dimensional models of convection of supercritical pure water, which emphasize the importance of using realistic fluid properties as well as high-resolution meshes. Chapter 3 documents the implementation and validation of the parallel code. Chapter 4 and 5 are applications of the parallel code, presenting the first high-resolution three-dimensional simulations of convection of compressible, supercritical pure water. The newly developed PHX scheme is described in detail in chapter 6, including a range of tests in which the code is validated. In a first application of the PHX scheme (chapter 7) the effects of two-phase flow on heat transport by convection in near-critically boiling pure water is studied. A second application (chapter 8), which includes salt transport, investigates the nature of phase-separation, brine formation and vent-salinity variations of black-smoker systems.

2. THE DYNAMICS OF MID-OCEAN RIDGE HYDROTHERMAL SYSTEMS: SPLITTING PLUMES AND FLUCTUATING VENT TEMPERATURES[1]

2.1 Abstract

We present new, accurate numerical simulations of 2D models resembling hydrothermal systems active in the high-permeability axial plane of mid-ocean ridges and show that fluid flow patterns are much more irregular and convection much more unstable than reported in previous simulation studies. First, we observe the splitting of hot, rising plumes. This phenomenon is caused by the viscous instability at the interface between hot, low-viscosity fluid and cold, high-viscosity fluid. This process, known as Taylor-Saffman fingering, could potentially explain the sudden extinguishing of black-smokers. Second, our simulations show that, for relatively moderate permeabilities, convection is unsteady resulting in transiently varying vent temperatures. The amplitude of these fluctuations typically is 40°C with a period of decades or less, depending on the permeability. Although externally imposed events such as dike injections are possible mechanisms, they are not required to explain temperature variations observed in natural systems. Our results also offer a simple explanation of how seismic events cause fluctuating temperatures: Earthquake-induced permeability-increase shifts the hydrothermal system to the unsteady regime with accompanying fluctuating vent temperatures. We demonstrate that realistic modeling of these high-Rayleigh number convection systems does not only require the use of real fluid properties, but also the use of higher-order numerical methods capable of handling high-resolution meshes. Less-accurate numerical solutions smear out sharp advection fronts and thereby artificially stabilize the system.

2.2 Introduction

Since the discovery of sub-seafloor hydrothermal systems in the 1970s, numerous manned and unmanned dives (Massoth et al., 1989; Haymon et al., 1993; Von Damm et al., 1997, 2003; Seyfried et al., 2003) have given insight into the underlying physical and chemical processes. Continued observation over the last decades revealed highly transient and complex flow systems. The sub-seafloor physics include the vigorous convection of chemically complex fluids, super-critical phase separation of saline fluids, and high-temperature fluid-rock interaction, including dissolution and precipitation of minerals (Lowell et al., 1995; Kelley et al., 2002).

[1] Published as: D. Coumou, T. Driesner, S. Geiger, C.A. Heinrich and S.K. Matthai, 2006, The dynamics of mid-ocean ridge hydrothermal systems: Splitting plumes and fluctuating vent temperatures, *Earth Planet. Sci. Lett.* **245**, 218–231

The observational data posed a number of key scientific questions, one of them concerns the temperature of black-smoker effluents (Jupp and Schultz, 2000): Even though magma-chambers have temperatures of $\sim 1200°C$, maximum temperatures of vent fluids are never greater than $\sim 400°C$. In addition, transient and spatial variations in black-smoker temperatures remain a key question of active current debate (German and Lin, 2005). Some black-smokers have effluent temperatures, which remain constant over decades (Campbell et al., 1988; Von Damm, 1990), while others show strong variation or extinguish without obvious reason (Johnson et al., 2000; Haymon et al., 1993; Fornari et al., 1998; Von Damm, 2005). Spatially, effluent temperatures from black-smokers can vary on the scale of tens of meters.

Numerical modelling can help to elucidate the sub-seafloor physics and explain observational data. For two reasons, the general approach has been to model convection in a two-dimensional open-top porous medium. First, at many locations deep circulation is believed to be primarily two-dimensional, in the plane of the spreading axis where fracture permeability is greatest (Haymon, 1996; Kelley et al., 2002). Second, the absence of a sediment layer above the axis allows for free flow of fluids in and out of the oceanic crust. Due to the extreme physical and chemical complexity, however, all numerical studies have to make simplifications, even in the two-dimensional case.

Most studies took a Boussinesq approximation in which fluid density variations are considered only in the buoyancy term (Rosenberg et al., 1993; Wilcock, 1998; Cherkaoui and Wilcock, 1999; Schoofs and Hansen, 2000). In addition to the Boussinesq assumption, Rosenberg et al. (1993) linearized density variations as a function of temperature and assumed viscosity to be constant. Despite these simplifications, they correctly showed that discharge areas are much smaller than recharge areas and suggested that hydrothermal convection at the ridge axis might never reach a steady state. Wilcock (1998) took a steady-state approach, adding non-linear terms for density, viscosity, and heat capacity of the fluid as well as including non-Boussinesq terms. He showed that doing so results in maximum venting temperatures up to 50% higher than those obtained with uniform fluid properties and the flow pattern includes much more recirculation. Further, Wilcock (1998) argued that the exit temperature in open-top hydrothermal systems reaches a limit of 0.65 times the bottom temperature. Rabinowicz et al. (1999), taking a steady-state approach as well, showed that this factor is independent of the Rayleigh number. By taking an inclined base of the porous medium, Rabinowicz et al. (1999) were able to increase exit temperatures to a maximum of 0.85 times the bottom temperature. The steady state approach of Rabinowicz et al. (1999) and Wilcock (1998) is limited, however, to low Rayleigh number calculations.

Employing a second-order-accurate finite-volume scheme, a Boussinesq approximation and a constant viscosity, Cherkaoui and Wilcock (1999) modeled time-dependent, high-Rayleigh number, open-top convection systems. They described the character of convection for Rayleigh numbers up to 1100. They showed that at such high Rayleigh numbers unsteady flow and heat transport display a sequence of bifurcations from periodic to quasi-periodic to chaotic patterns. Decades ago, Straus and Schubert (1977) showed that, compared with a Boussinesq approach with linearized properties, including the non-Boussinesq terms and using non-linear water properties greatly enhances the instability of convection. Recently, Jupp and Schultz (2000) included the non-Boussinesq terms as well as realistic fluid properties in open-top convective system. Based on simulations using the HYDROTHERM pure H_2O software package (Hayba and Ingebritsen, 1994a), they argued that maximum black-smoker

effluent temperatures of $\sim 400°C$ can be explained solely by the non-linear, temperature- and pressure-dependent properties of H_2O.

All these numerical studies have greatly contributed to our understanding of fluid flow patterns in open-top thermal convection systems. They were, however, not able to explain the observed spatial and transient variations in black-smoker temperatures. A steady-state approach (Wilcock, 1998; Rabinowicz et al., 1999) is limited to low-Rayleigh number systems. Frequently, the thermal expansivity, compressibility, viscosity and heat capacity were assumed to have constant values (Cherkaoui and Wilcock, 1999; Schoofs and Hansen, 2000; Cherkaoui et al., 1997, 2003), although for the temperature and pressure range encountered in mid-ocean ridge hydrothermal systems they vary highly non-linearly over several orders of magnitude and peak near the critical temperature. This greatly enhances the instability of convection in a water-saturated porous medium (Ingebritsen and Hayba, 1994).

Jupp and Schultz (2000) did include all non-linearities but nevertheless found steady-state temperature solutions. A first-order-accurate finite-difference method (Hayba and Ingebritsen, 1994a) and relatively coarse meshes were used in their study. This numerical approach smears out sharp advection fronts, which numerically stabilizes the convective system and might result in artificial steady-state solutions.

In this study we account for the full non-linearity of the properties of H_2O, including the effects of thermal expansion and compression on flow transients. In addition, we perform the calculations on a high-resolution mesh employing a numerical method that is second order accurate in space (Geiger et al., 2004). This allows us to detect new dynamic features that potentially explain a range of salient observations on MOR hydrothermal systems.

We will show that for reasonable permeability values, convection is much more vigorous than previously reported. The unsteady behavior of sub-seafloor convection can by itself explain temperature variations measured on the seafloor. The permeability structure does not necessitate any geometric complexity, nor transient events such as cracking or magma addition are required to produce temperature variations in the range of the observations. We will argue that the non-linearity of fluid properties not only explains the temperature of vent fluids (Jupp and Schultz, 2000), but also its transient variability. However, events such as earthquakes may have a profound influence on the permeability structure (Elkhoury et al., 2005) and by increasing permeability shift the systems from steady to unsteady convection.

Second, we will demonstrate that due to the large viscosity variations, the front of uprising thermal plumes may become unstable and can split into two plumes. This phenomena, known as Taylor-Saffman fingering, has to our knowledge never been reported within the context of thermal convection in hydrothermal systems. We show under which conditions this phenomenon occurs and discuss the numerical requirements.

This article is structured as follows. In sections 2.3, 2.4 and 2.5 the governing equations, numerical method and model setup are described. Section 2.6 summarizes the numerical results. A detailed discussion on the observed plume splitting phenomena is given in section 2.7. It also discusses possible implications for natural MOR hydrothermal systems and section 2.8 presents the final conclusions.

2.3 Governing Equations

Volumetric flow through porous media is usually described by Darcy's law (Bear, 1972):

$$\mathbf{v} = -\frac{k}{\mu_f}\left(\nabla p - \rho_f \mathbf{g}\right) \tag{2.1}$$

Where $\mathbf{v}$ is the Darcy velocity, k the permeability, μ_f the fluid's dynamic viscosity, p the pressure, ρ_f the fluid's density and $\mathbf{g}$ the gravitational acceleration vector. A mass balance for a single-phase fluid in a porous medium can be expressed in terms of the continuity equation:

$$\phi \frac{\partial \rho_f}{\partial t} = -\nabla \cdot (\mathbf{v}\rho_f) \tag{2.2}$$

Here we assume that the compressibility of the rock is orders of magnitude lower than that of the fluid. ρ_f is a function of temperature (T) and pressure (p). Writing the partial derivative of equation 2.2 in terms of p and T, and inserting equation 2.1 into equation 2.2 gives the following expression for the pressure field:

$$\phi\rho_f\left(\beta_f \frac{\partial p}{\partial t} - \alpha_f \frac{\partial T}{\partial t}\right) = \nabla \cdot \rho_f \left(\frac{k}{\mu_f}\left(\nabla p - \rho_f \mathbf{g}\right)\right) \tag{2.3}$$

where α_f is the fluid's thermal expansivity and β_f its compressibility. Assuming local thermal equilibrium between rock and fluid, the advection-diffusion equation for the temperature field at single phase condition can be written as:

$$\left(\phi\rho_f c_{pf} + (1-\phi)\rho_r c_{pr}\right)\frac{\partial T}{\partial t} = \nabla \kappa \nabla T - \nabla \cdot (\rho_f c_{pf} \mathbf{v} T) \tag{2.4}$$

With c_{pf} being the specific heat and κ the thermal conductivity. This formulation neglects the adiabatic term and this scheme thus assumes that c_{pf} is constant over a single timestep. For single phase fluids, however, this error is small (Geiger, 2004). Table 2.1 summarizes all symbols used in this paper.

2.4 Numerical Method

We employ the IAPS-84 equation of state of pure water (Haar et al., 1984) to determine μ_f, α_f, β_f, c_{pf}, ρ_f and enthalpy. Equations 2.3 and 2.4 are strongly non-linear, as all fluid properties are non-linear functions of p and T. They have mixed hyperbolic (advective) and parabolic (diffusive) character. We solve the system of equations within the framework of the object-oriented C++ code Complex System Platform, CSP (Matthai et al., 2001), using a mixed finite-element finite-volume (FE-FV) approach (Geiger et al., 2006a,b). FV methods are robust in solving advection-type problems, whereas FE methods perform better on diffusion-type problems. In the FE-FV method, the pressure equation 2.3 is solved decoupled from the energy conservation equation 2.4. An explicit FV method is used to solve the advective part of equation 2.4, while an implicit FE method, employing the SAMG multigrid solver (Stuben, 2002), is used to solve the parabolic equations of heat- and pressure-diffusion. Hence, the coupled equations 2.3 and 2.4 are solved sequentially but the best suited numerical method is applied on the respective sub-equations. Temperature diffusion is calculated first. Thereafter, advection of heat is solved using the velocities from the previous timestep. At this point the fluid properties are updated and the pressure field is calculated. From the pressure field new Darcy velocities (equation 2.1) are determined.

Geiger et al. (2006a,b) subjected this FE-FV-scheme within CSP to numerous analytical and numerical benchmark tests to verify its accuracy and computational efficiency.

2.5 Model Setup

Tab. 2.1: List of symbols used

	Physical parameter	Value	Unit
α_f	Fluid expansivity	$-\frac{1}{\rho_f}\frac{\partial \rho_f}{\partial T}$	$^\circ C^{-1}$
β_f	Fluid compressibility	$\frac{1}{\rho_f}\frac{\partial \rho_f}{\partial p}(*)$	Pa^{-1}
ϵ	Exponential term	3.0	-
κ	Thermal diffusivity	1×10^{-6}	$m^2 s^{-1}$
λ	Width of instabilities	Eq. 2.7	m
λ_c	Cut-off λ	Eq. 2.7	m
λ_m	λ of maximum growth	Eq. 2.8	m
μ_f	Fluid viscosity	EOS (*)	Pa s
ρ_f	Fluid density	EOS (*)	kg m^{-3}
ρ_r	Rock density	2700	kg m^{-3}
ϕ	Porosity	0.1	-
A	Aspect ratio of convection cell	$D/(2H)$	-
c_{pf}	Fluid isobaric heat capacity	EOS	J $(kg^\circ C)^{-1}$
c_{pr}	Rock isobaric heat capacity	880	J $(kg^\circ C)^{-1}$
D	Distance between adjacent upflow zones	-	m
$\mathbf{g}$	Gravitational accelation	$\|\mathbf{g}\| = 9.8$	m s^{-2}
H	Vertical extent model	$1000^{(*)}$	m
k	Permeability	$10^{-14(*)}$	m^2
κ	Thermal conductivity	2.0	W $(m^\circ C)^{-1}$
p	Pressure	Eq. 2.3	Pa
T	Temperature	Eq. 2.4	$^\circ C$
$\mathbf{v}$	Darcy velocity	Eq. 2.1	m s^{-1}
t^*	Dimensionless time	-	-
U	1-D vertical velocity	-	m s^{-1}
$\mathbf{v}_c$	Critical velocity	Eq. 2.5	m s^{-1}

EOS = equation of state according to (Haar et al., 1984).

(*) Unless stated differently.

Unless stated otherwise, we integrate equations 2.3 and 2.4 on a 3600 m by 1000 m rectangular geometry with a mesh of 50,000 uniform, triangular elements. Permeability k as well as porosity ϕ are kept constant during the simulations. The top boundary represents the seafloor at roughly 2.5 km water depth resulting in a constant pressure $p = 25$ MPa. To allow hot fluids to vent freely through the top boundary, we use a mixed thermal boundary condition (Wilcock, 1998; Jupp and Schultz, 2000; Schoofs and Hansen, 2000; Kawada et al., 2004). In finite elements along the top boundary experiencing upflow, the vertical temperature gradient is set to zero, allowing uninhibited outflow of hydrothermal fluid of any temperature. Boundary elements experiencing downflow take in water of a fixed temperature of 10°C. Fluids can leave or enter the model only through its top boundary. All other boundaries are no-flow boundaries. The bottom boundary is kept at a fixed temperature of 1000°C. Initially, the porous medium is saturated with 10°C water at hydrostatic pressures.

Though highly simplified, this geometry approximates a vertical plane of high permeability along the ridge axis with a continuous magma-chamber underneath. 2-D models have been used as a matter of numerical convenience. However, as permeability is expected to be higher along the axis compared to off-axis (Fisher, 1998), convection is likely primarily two-dimensional (Bachler et al., 2003; Haymon, 1996). Seismic studies have identified magma lenses stretching continuously for several kilometers at fast spreading ridges (Babcock et al., 1998). On the other hand, precipitation of anhydrite in narrow, along axis, recharge zones might limit along-axis convection (Lowell et al., 2003).

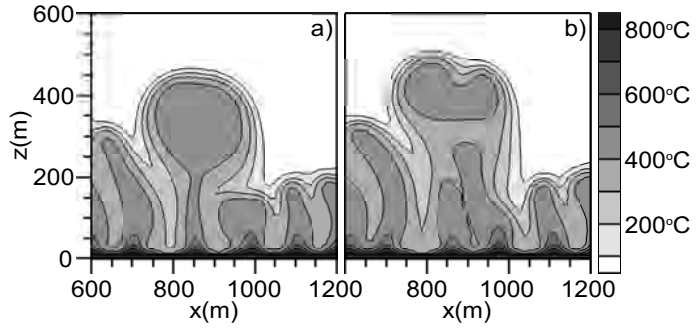

Fig. 2.1: Temperature field of a segment of simulation 2 (table 2.2) after (a) $t = 125$ years and (b) $t = 130$ years. The straight vertical line in (a) represents the position of the thermal profile plotted in Figure 2.7.

2.6 Results

2.6.1 Convection patterns at early times: Splitting plumes

Splitting of hot, rising plumes has been observed in all simulations with sufficiently large permeability. Here we discuss simulation results for $k = 10^{-14}$ m^2 (Figures 2.1 and 2.3). Plumes start to form after a relatively short period (~ 40 years) of vertical thermal diffusion. Initially these plumes have similar widths but due to merging, a variation in plume widths arises. Since the upward velocity of a plume is a function of its width (Tan and Homsy, 1986), some plumes grow faster than others. Plumes travelling faster than their direct neighbors typically spread in the transverse direction, thereby shielding their neighbors. Shielded small plumes eventually merge with larger ones. The cross-flow accompanying the spreading of the larger plumes, causes the thermal gradient at their tops to become steeper (Tan and Homsy, 1988). A steeper gradient is hydrodynamically less stable, since viscosity and density change over a shorter distance. Thus simultaneously the plume itself becomes broader and its front less stable. This can, when the front is steep enough and the width of the plume is broad enough, cause the plume to split. Figure 2.1 shows a typical case of plume splitting.

We have performed a series of simulations to investigate the plume-splitting phenomenon. Some selected simulations covering a range of physical parameters are summarized in table 2.2. They indicate that plume splitting occurs when two conditions are satisfied. First, convection needs to be vigorous, i.e. $k \geq 10^{-14}$ m^2. Second, a large viscosity contrast between cold and hot fluids is essential. The initial condition of a completely cold layer underlain by a 1000°C hot layer gives a very large initial viscosity contrast. To determine the influence of these initial conditions, a simulation was run which started with a 1000°C/km linear geotherm (simulation 4, table 2.2). This gave similar results in terms of convective behavior, including plume splitting. Table 2.3 summarizes the most important results for different numerical schemes. Based on these results, we will show in section 2.7 that the observed phenomena are caused by Taylor-Saffman instabilities (Saffman and Taylor, 1958) rather than a numerical artifact.

2.6.2 Convection patterns at late time: Temperature variations

In this section we discuss the characteristics of convection for the standard geometry (3600 m $\times$ 1000 m) and $k = 10^{-14}$ m^2 (simulation 2 in table 2.2). Plume splitting only occurs

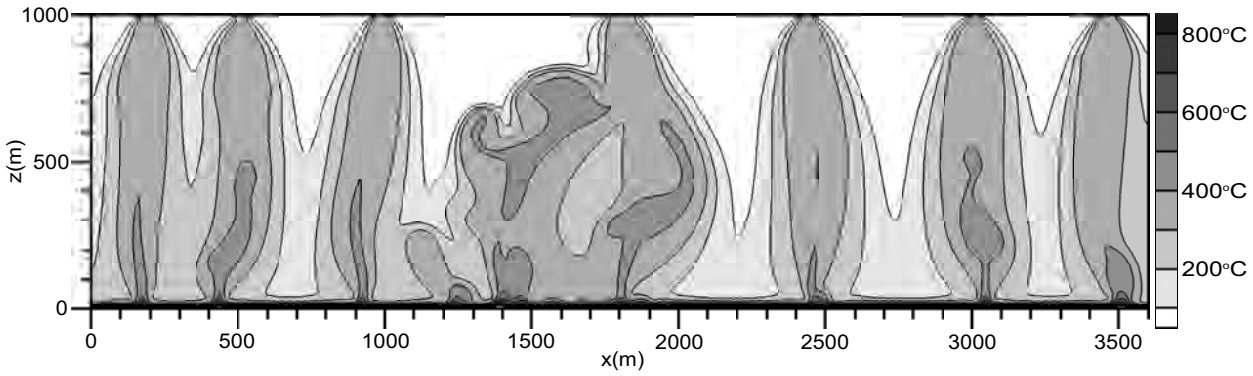

Fig. 2.2: Temperature T of simulation 2 (table 2.2) after $t = 3000$ years. Part of the system has become unstable and plume splitting can be observed.

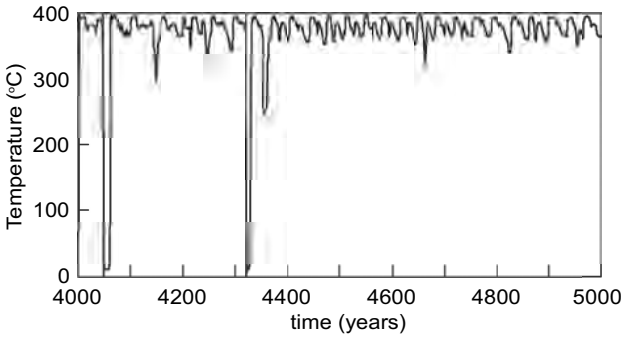

Fig. 2.3: Temperature T (simulation 2, table 2.2) at a location where hot fluids exit the top boundary measured over a time period of 1000 years, calculated by taking the mean temperature of a number of FE nodes along a 50 m length at the top boundary.

Tab. 2.2: Simulations (1)

#	Dimension $x \times z$[km]	k [m^2]	Fluid Prop. EOS, simpl.	Convection Mode	Convection A	Venting T [^{o}C]	Venting Area[m]	Plume Splitting
1	3.6×1.0	10^{-13}	(Haar et al., 1984)	Unsteady	-	374 ± 20	~ 60	yes
2	3.6×1.0	10^{-14}	(Haar et al., 1984)	Unsteady	0.22	377 ± 20	~ 60	yes
3	3.6×1.0	10^{-15}	(Haar et al., 1984)	Steady	0.26	387	~ 150	
4	3.6×1.0	10^{-14}	(Haar et al., 1984)	Unsteady	0.22	377 ± 25	~ 60	yes
5	3.6×1.5	10^{-14}	(Haar et al., 1984)	Unsteady	0.20	375 ± 25	~ 60	yes
6	7.2×2.0	10^{-14}	(Haar et al., 1984)	Unsteady	0.18	375 ± 25	~ 100	yes
7	3.6×1.0	10^{-14}	(Haar et al., 1984), $\beta_f = 0$	Unsteady	(?)	(?)	(?)	yes
8	3.6×1.0	10^{-14}	(Haar et al., 1984), $\alpha_f = 0$(eq. 2.3)	Unsteady	(?)	(?)	(?)	yes
9	3.6×1.0	10^{-14}	(Haar et al., 1984), $\mu_f = 3 \times 10^{-4}$	Unsteady	0.2/0.3	$50 - 400$	~ 200	
10	3.6×1.0	10^{-14}	(Haar et al., 1984), $\mu_f = 3 \times 10^{-5}$	Unsteady	0.14	$50 - 400$	~ 100	
11	3.6×1.0	10^{-14}	Boussinesq$^{(*)}$	Unsteady	0.3	$50 - 500$	~ 250	
12	7.2×2.0	10^{-14}	Boussinesq$^{(*)}$	Unsteady	0.23	$50 - 450$	~ 400	

CSP simulation results for different model geometries, permeability and used fluid properties. All results were obtained employing the same numerical method: 70 m^2 elements with linear interpolation functions, second order FV transport scheme and first order time-stepping. For parameters not listed here, values have been used as given in table 2.1. Except for simulation 4, which has an initial linear geotherm, all simulations started with cold water everywhere within the 2D-domain. $^{(*)}$ The Boussinesq approximation is used as well as constant μ_f and α_f. (?) Simulations not run long enough for accurate determination.

when hot fluid displaces cold fluid. Up to times of $\sim$ 2000 years, convection is highly unstable with plumes collapsing and new plumes forming continuously. Within this time frame, plume splitting has a profound effect on the overall convection pattern, making it much more irregular. At later times ($t \geq 2000$ years), the system becomes more stable with regularly spaced plumes. Their positions remain relatively constant over time. Still, parts of the system episodically become unstable, leading to the occasional collapse of plumes and rise of new ones. Figure 2.2 shows such a situation, where part of the system has becomes unstable. Clearly, plume splitting can be observed again. This "semi-steady" convection pattern is typically sustained for thousands of years. We define the aspect ratio of convection cells as $A = D/(2H)$, where D is the average horizontal distance between neighboring plumes and H the vertical extent of the model. Typical values for A are ~ 0.22. Close to the top, upward travelling, pipe-like plumes show necking. Though plumes have average widths of $\sim$ 200 m, at the top their width typically is only $\sim$ 60 m.

While the position of plumes is relatively stationary, the temperature of fluids leaving the top boundary varies with time. Their mean temperature is 377°C but oscillations with an amplitude of $\sim$ 40°C occur (Figure 2.3). The period of oscillation is on the order of decades. Temperatures reach maxima of $\sim$ 395°C and, although typically minimum fluid temperatures are $\sim$ 365°C, they can drop as low as $\sim$ 250°C. This is a direct consequence of the unstable convection patterns. Each of the high-temperature upflow zones behaves in a pulsating manner. In regular intervals, relatively hot volumes of water are mobilized at the bottom boundary and travel upward quickly.

Apart from this relatively regular oscillation, two sharp drops in temperature, for periods of $\sim$ 10 years, can be observed in Figure 2.3. They are caused by a locally increased inflow of cold seawater pushing down the thermal plume. The plume retains its horizontal position but does not reach the top boundary for a relatively short time. The process is caused by the counter balance of recharge and discharge. The discharge region temporarily becomes an inflow region while neighboring plumes vent at an increased rate.

Tab. 2.3: Simulations (2)

#	FV Scheme	FE Spatial Discretization		Temporal Discretization		Plume
	1st/2nd Order	Size[m^2]	Interpolation	Time stepping	1st/2nd Order	Splitting
13	1	12	Linear	CFL	1	yes
14	1	70	Linear	CFL	1	yes
15	2	70	Linear	CFL	1	yes
16	2	70	Quadratic	CFL	1	yes
17	2	70	Linear	0.1×CFL	1	yes
18	2	70	Linear	Iterative	-	yes
19	2	70	Quadratic	Iterative	-	yes
20	2	70	Linear	CFL	2(Pred-corr)	yes
21	2	70	Quadratic	CFL	2(Pred-corr)	yes
22	1	600	Linear	CFL	1	
23	1	600	Quadratic	CFL	1	

CSP simulation results for different numerical methods. We use several temporal discretization schemes as well as different FE interpolation functions to test for which numerical scheme plume splitting is observed. All simulations used a 3600 m × 1000 m geometry, $k = 10^{-14}$ m^2 and included all non-linearities in H_2O (Haar et al., 1984). Properties as given in table 2.1 have been used.

2.6.3 Influence of permeability

For $k = 10^{-13}$ m^2 (simulation 1, table 2.2), flow is extremely irregular and plume splitting occurs continuously. After 2000 years of simulation, no 'semi-steady state' has evolved. Only for relatively short periods ($\sim$ decades) fluids vent at the same location on the seafloor. Afterwards the plume becomes unstable and vanishes in the convection system. Within such a period the exit temperature of the plume still fluctuates between ~ 365°C and ~ 395°C, very similar to the $k = 10^{-14}$ m^2-case. The period of oscillation is much shorter, however. For $k = 10^{-13}$ m^2 it is of the order of years, compared to decades when $k = 10^{-14}$ m^2. The upflow zones are narrow and generally of the order of ~ 100 meters wide. This is considerably smaller than the 200 m wide plumes at $k = 10^{-14}$ m^2. Flow focussing near the top boundary, however, is less pronounced, such that the outflow areas are of a similar size (~ 60 m).

At $k = 10^{-15}$ m^2 (simulation 3, table 2.2), plume splitting does not occur at all. The evolution of the convection pattern is completely different. After 1500 years of vertical thermal diffusion, convection starts and a steady-state convection system is established at $t = 8600$ years. The convection cells have an aspect ratio of $A = 0.26$. The temperature of fluid exiting the top boundary is 387°C and remains constant through time. The convection systems become the hottest at $k = 10^{-15}$ m^2, which is in good agreement with simulation results by Hayba and Ingebritsen (Hayba and Ingebritsen, 1994b) for continental magmatic-hydrothermal systems.

2.6.4 Influence of magma-chamber depth

We have also conducted a number of simulations to test the effect of larger horizontal and vertical model dimensions (simulations 5-6, table 2.2). Increasing the vertical dimensions of the model decreases the aspect ratio A of convection cells. In other words, plumes become more elongated. The temperature of fluids exiting the top boundary for models with larger vertical dimensions (simulations 5-6, table 2.2) is very similar to those with $z = 1000$ m. One might expect that due to increased loss of heat by diffusion and expansion as the fluids have to travel over a larger distance, temperatures would be lower. However, the larger pressure at the bottom causes the upwelling temperatures to be higher. As argued by Jupp and Schultz (2004), upwelling temperatures will be such that the total power output of the convection cell is maximized. They showed that the upwelling temperature at which power output is maximized, increases with increasing pressure. Hence, the higher bottom pressures in simulations 5-6 (table 2.2) will cause upwelling temperatures to be hotter, which appears to compensate the heat loss due to diffusion and expansion along the extended upwelling path.

2.6.5 Influence of viscosity

A number of simulations have been run to determine the influence of simplified assumptions for μ_f (simulations 9-12, table 2.2). Making μ_f constant suppresses plume splitting. There is still a sensitivity to the absolute value of μ_f: When $\mu_f = 3 \times 10^{-5}$ (simulations 10, table 2.2) relatively narrow plumes form. For larger μ_f the width of plumes becomes larger. In all cases (simulations 9-12, table 2.2), no necking of plumes near the top boundary is observed. This results in larger areas where fluids exit the system, with temperatures ranging spatially from 50°C to 500°C. Although convection is unstable, the pulsating behavior in the upflow

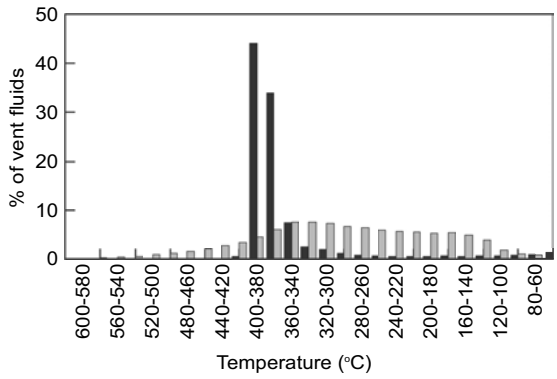

Fig. 2.4: The temperature distribution of fluid exiting through the top boundary. The vertical axis denotes the percentage of the fluid that traveled upward through the top boundary with a temperature given by the horizontal axis, measured over a period of 3000 years. Black bars show results from simulation 2 (table 2.2) which takes account of all non-linearities in fluid properties, grey bars show results from a simulation 11 (table 2.2) which employes a Boussinesq fluid.

zones, as observed in simulations using all non-linear fluid properties, is far less pronounced. Figure 2.4 compares exit temperatures of simulation 2 with those of simulation 11, which uses a Boussinesq approximation, a linear dependency of the density on temperature and a constant viscosity. In simulation 2 all fluids exit the top boundary at temperatures between 350°C and 400°C, reflecting the transient variability. For simulation 11, fluids exit the top boundary at temperatures ranging from 50°C to 500°C, reflecting spatial rather than transient variability.

2.7 Discussion

2.7.1 Theory of splitting plumes

Plume splitting, or viscous fingering, can occur when a less viscous fluid displaces a more viscous one. It is a well studied process in flow through porous media especially for the case of two immiscible fluids (Chouke et al., 1959; Kessler and Levine, 1986). In general when one fluid displaces another, a combination of density and viscosity ratios as well as the direction and magnitude of flow can conspire to trigger fingering (Homsy, 1987). In the one-dimensional case of two immiscible fluids, a critical velocity $\mathbf{v}_c$ can be found above which a moving plume head becomes unstable (Homsy, 1987). For the special case of buoyancy driven flow caused by temperature differences, we can find $\mathbf{v}_c$ when we assume that thermal diffusion is negligible. The critical velocity $\mathbf{v}_c$ for an upward migrating hot plume, displacing cold water (inset of Figure 2.5) is then given by

$$\mathbf{v}_c = \frac{k\mathbf{g}(\rho_c - \rho_h)}{\mu_c - \mu_h} \tag{2.5}$$

In this context, $\mathbf{v}_c$ can be regarded as the critical interface velocity above which instabilities will get amplified and plumes might split. The subscripts h and c respectively refer to hot fluids, with low viscosity and density, and cold fluids with high viscosity and density. If the difference in density between the fluids increases, the critical velocity increases. This, however, is of minor importance in the case of buoyancy driven convection systems, as velocities themselves are proportional to density differences. Viscosity variations have a much more profound effect. Equation 2.5 shows that when viscosity differences go to zero

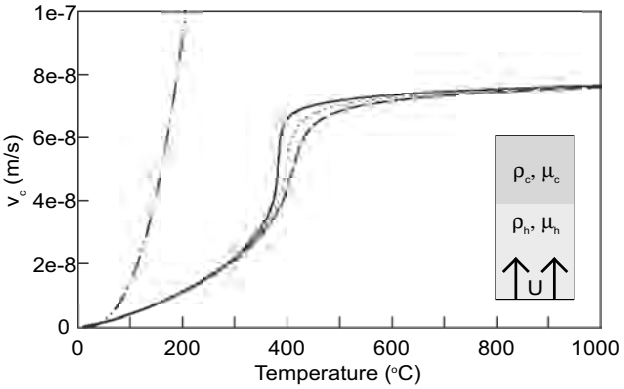

Fig. 2.5: The critical velocity above which an advection front becomes unstable plotted against T for $P = 25$ MPa (solid), $P = 30$ MPa (dotted) and $P = 35$ MPa (dashed). The dashed-dotted line represents the Darcy velocity for the 1D geometry as depicted in the inset.

the critical velocity goes to infinity. Simulations employing the non-linear fluid properties of H_2O but taking μ constant, showed, in agreement with equation 2.5, that plume splitting does not occur (table 2.2).

In Figure 2.5, $\mathbf{v}_c$ is plotted against relevant temperatures at pressures of 25 MPa, 30 MPa and 35 MPa. Also plotted is the approximate Darcy velocity at the interface between hot and cold fluid for the 1D case (inset of Figure 2.5). The vertical Darcy velocity $\mathbf{v}$ (equation 2.1) of the hot fluid at the interface can be approximated by $\mathbf{v} = k\mathbf{g}(\rho_c - \rho_h)/\mu_h$. Comparing this formulation with equation 2.5 shows that $\mathbf{v} > \mathbf{v}_c$ if $\mu_c > 2\mu_h$. This condition is fulfilled for an upward flowing fluid of 40°C when the cold fluid is 10°C. Temperature differences are much larger in the systems discussed here, hence $\mathbf{v}$ is typically an order of magnitude larger than $\mathbf{v}_c$.

As both $\mathbf{v}$ and $\mathbf{v}_c$ scale with k, one could conclude that viscous fingering should occur at all permeabilities, in disagreement with the numerical results. However, this is incorrect, as the relative influence of diffusion compared to advection plays a crucial role. If diffusion is included, equation 2.5 only holds for $t = 0$. For later times diffusion smears out the thermal front. The steepness of the front determines at which minimum width instabilities can form. The steeper the front, the smaller the minimum width of an instability will be. Tan and Homsy (1986) considered the one-dimensional horizontal flow of fluid with a solute-dependent viscosity. They found analytical solutions for $t = 0$ and numerical solutions for $t > 0$. In an analogous way, we can find first-order approximations for 1D vertical flow of hot water displacing cold water (inset of Figure 2.5). We assume that the decay of μ_f with increasing T can be written as an exponential function:

$$\mu_f \approx e^{-\epsilon T} \tag{2.6}$$

For $\epsilon = 3$ a reasonable fit of actual H_2O viscosities is achieved. Next, we take the so-called quasi-steady-state approximation. This assumes that the growth rate of disturbances is much faster than the rate of change in the base state. (For a detailed discussion and complete derivation of the formulae, see Tan and Homsy (1986)). We can now derive the following equations:

$$\lambda_c^0 = \frac{8\pi\kappa}{\epsilon U} \tag{2.7}$$

$$\lambda_m^0 = \frac{8\pi\kappa}{(2\sqrt{5} - 4)\epsilon U} \tag{2.8}$$

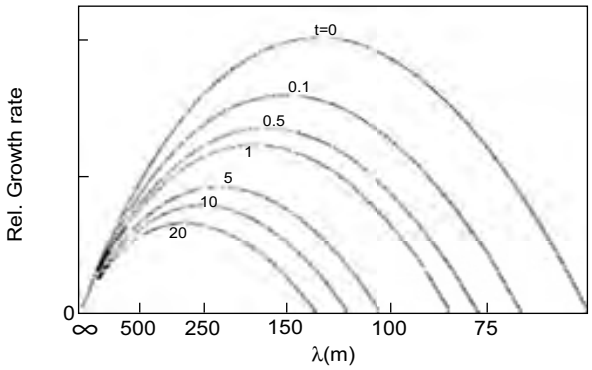

Fig. 2.6: Relative growth rate of instabilities plotted against the width of an instability (λ) for different dimensionless times t^*. The point where the curves cross the x-axis coincides with λ_c. The maximum of the curves resemble λ_m. The width of maximum growth rate increases with time due to smearing out of the front by diffusion. Note the inverted and non-linear x-axis scale. Modified from Tan et al.(Tan and Homsy, 1986).

Where λ is the width of an instability in meters. The subscripts c and m refer to the cut-off, or minimum width and the width of maximum growth of an instability, respectively. In other words, λ_c is the smallest plume that can form and λ_m is the width of a plume that is most likely to form. The superscript 0 indicates a non-dimensional time $t^* = 0$, with

$$t = t^* \frac{\kappa}{U^2} \tag{2.9}$$

In equations 2.7, 2.8 and 2.9, U is the upward velocity of the plume and κ is the thermal diffusivity.

Equations 2.7 and 2.8 show that, if $\epsilon = 3$, only for small κ/U ratios ($\kappa/U < 10^1$m) do λ_c and λ_m have values smaller than the model scale. The Peclet number Pe, defined as the ratio between advective transport and diffusive transport, consequently has to be large ($Pe \geq 10^3$). For a realistic thermal diffusivity of 10^{-6} m^2, this requires relatively large permeabilities ($k \geq 10^{-14}$).

For times larger than $t^* = 0$, analytical solutions cannot be found. Numerical solutions were obtained by Tan and Homsy (1986) and are shown in figure 2.6 for $\epsilon = 3$, $U = 1.0 \times 10^{-7}$m/s and $\kappa = 1 \times 10^{-6}$ m^2/s. Figure 2.6 shows the relative growth rate of instabilities for several values of t^*. The maximum of each curve corresponds to λ_m. The point where the curves cross with the x-axis, i.e. where instabilities have a zero growth rate, corresponds to λ_c. Figure 2.6 shows that for larger times the width of instabilities will increase, due to the diffusion of the initially steep thermal front.

2.7.2 Quantification of splitting plumes

Figure 2.6 shows that when t increases, λ_c and λ_m increase due to diffusion of the thermal front. In advection-dominated fluid flow systems, the steepness of thermal fronts is not only determined by the time they have had to diffuse, but also by the overall fluid flow pattern. As described in the previous section, plumes traveling faster than neighboring plumes spread in the lateral direction. The cross flow accompanied with this spreading process steepens the top of a thermal front (Tan and Homsy, 1988), making it less stable. Simultaneously

the plume itself becomes wider and the minimum width of instabilities becomes smaller. At the moment the width of the plume allows more than two instabilities to grow, its tip becomes unstable and splits. The width of a rising plume should therefore be at least be $2\lambda_c$ before it can split. This process occurs when convection is fully evolved, hence no direct semi-analytical comparison is possible.

In a first approximation, however, we can compare the temperature profile perpendicular to a front, just before plume splitting occurs, to an analytical pure-diffusion solution:

$$T(z) = \frac{T_{max} - T_{min}}{2} \mathrm{erfc}\left(\frac{z}{2\sqrt{\kappa t}}\right) \tag{2.10}$$

By fitting equation 2.10 to the observed thermal front, we can determine a dimensionless diffusion time t^*. Figure 2.1 shows the temperature field of a typical plume just before and after plume splitting. The solid curve in Figure 2.7 shows the thermal front just before the plume splits. An optimal fit of this thermal front with the analytical solution is produced for $t^* = 2.8$. From Figure 2.6 we estimate λ_c and λ_m for $t^* = 2.8$.

$$\lambda_c^{2.8} \sim 85 \pm 10 \text{ m} \tag{2.11}$$

$$\lambda_m^{2.8} \sim 170 \pm 10 \text{ m} \tag{2.12}$$

This is in good agreement with numerical observations. The plume, depicted in Figure 2.1 splits into two plumes having widths of ~ 150 m and ~ 100 m. Both plumes are larger than λ_c. The wider, 150 m plume travels upward faster, as is expected because its width is close to λ_m.

Since the upward velocities typically exceed $\mathbf{v}_c$ and the widths of the splitting plumes are in good agreement with our first order approximations, we conclude that these are Taylor-Saffman fingers (Saffman and Taylor, 1958) rather than numerical artifacts. Their absence in numerical models assuming constant viscosity further confirms this conclusion.

2.7.3 Numerical aspects of splitting plumes

The preceding discussion raises the question why previous numerical studies have not observed plume splitting. With their steady-state approach, Wilcock (1998) and Travis et al. (1991) could not resolve these transient processes, which occur at high Rayleigh numbers. Low-Rayleigh number simulations imply low Peclet numbers, resulting in very large values for λ_c. Most studies treated the fluids as incompressible and held thermal expansion coefficient (α_f) and viscosity (μ_f) constant. Jupp and Schultz (2000) modeled the full non-linear properties of H_2O, but still did not observe plume splitting. As discussed in the previous section, plume splitting occurs only if the thermal front is sufficiently steep. Transport schemes that are only first order accurate in space smear out thermal gradients and hence stabilize it artificially. Therefore, only higher order accurate transport schemes that preserve sharp gradational thermal fronts can model plume splitting. Table 2.3 summarizes different numerical schemes that have been tested for the standard geometry (3600 m $\times$ 1000 m) and $k = 10^{-14}$ m^2. Figure 2.8 compares first and second order transport schemes and two levels of mesh refinement. It shows that by employing first instead of second order accuracy, or by decreasing the spatial resolution, plume fronts become more diffuse. Figure 2.8a shows the results of a second order accurate transport scheme combined with a high-resolution mesh

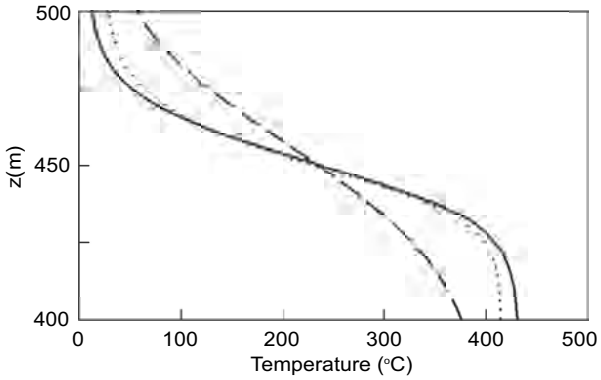

Fig. 2.7: Temperature cross-profile of a plume at $x = 800$ m after 125 years for different numerical schemes. The solid line shows results from a second order accurate transport scheme using a high-resolution (50k element) mesh (simulation 15, table 2.3). The dotted curve plots results of a simulation using the same high-resolution mesh but with a first order accurate scheme (simulation 14, table 2.3). The dashed line gives results using a first order accurate scheme in combination with a low-resolution (6k element) mesh (simulation 22, table 2.3). All curves have been fitted with analytical solutions, giving dimensionless times of $t^* = 2.8$, $t^* = 3.3$ and $t^* = 13.5$ respectively.

($\sim$70 m^2 elements with linear FE interpolation functions, simulation 15, table 2.3). The same mesh has been used in Figure 2.8b but now employing a first order accurate transport scheme (simulation 14, table 2.3). In this simulation plume splitting occurs only very rarely. In Figure 2.8c the spatial accuracy has further been reduced by employing a low-resolution mesh ($\sim$ 600 m^2 elements with linear FE interpolation functions, simulation 22, table 2.3). This leads to even more diffused fronts and the complete absence of plume splitting. Figure 2.7 illustrates how much less accurate schemes smear out thermal fronts. Taking the approach described previously, this leads to larger dimensionless diffusion times and results in larger values for λ_c and λ_m. Thus, a first order accurate scheme (Figures 2.8b and dotted line in Figure 2.7) strongly reduces plume splitting compared to a second order accurate scheme. Using a low-resolution mesh in combination with a first order accurate scheme (Figures 2.8c and dashed line in Figure 2.7) eradicates the phenomenon.

We conclude that accurately modelling the full dynamics of advection-dominated near-critical convection systems, requires (a) including the full non-linearity of the physical properties of water and (b) the use of high-resolution meshes, as well as (c) higher order numerical schemes. Previous studies either used first order accurate schemes, rather coarse spatial resolutions compared to this study or constant viscosities. As shown by Geiger et al. (2004) the decoupled pressure-temperature algorithm solved on a dual FE-FV mesh, as used in this study, is not only second order accurate in space, but, due to its high computational efficiency, allows the use of high-resolution meshes.

2.7.4 Black-smoker vent temperatures

Although our generic model setup does not reflect the complexity of real MOR hydrothermal system in any detail, the features emerging in the simulations strongly resemble many observations made on natural systems. To us, this implies that the non-linear dependence

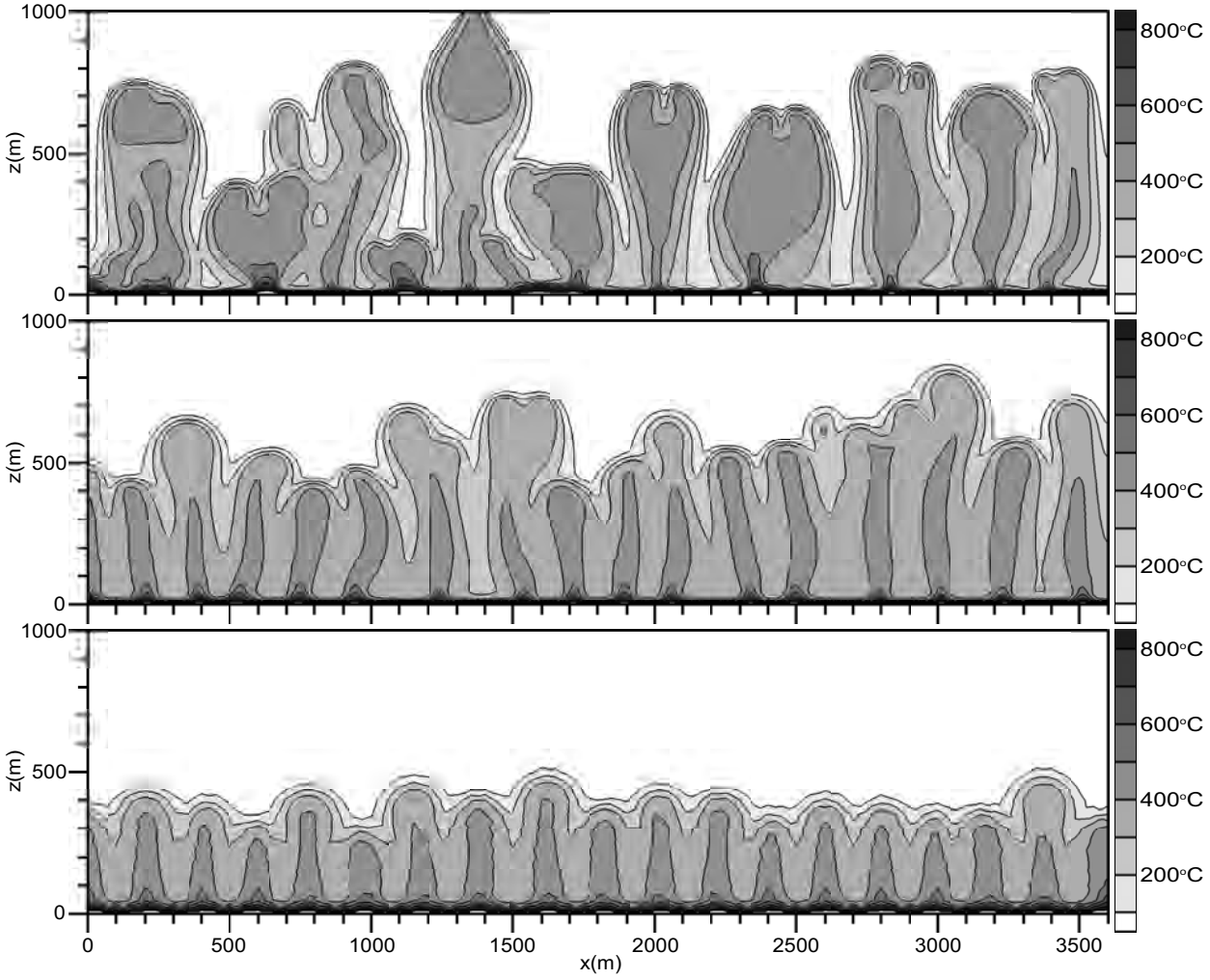

Fig. 2.8: Temperature field after 200 years for three different numerical schemes: (a) second order accurate transport with high-resolution (50k element) mesh, (b) first order accurate transport with high-resolution mesh and (c) first order accurate transport with low-resolution (6k element) mesh.

of water properties on pressure and temperature not only determines the maximum venting temperatures (Jupp and Schultz, 2000) but can also explain much of the variability in venting temperature. Our simulations show that already for relatively moderate permeability values (Fisher, 1998) convection is unsteady and black-smokers will vent at transiently varying temperatures. Though less pronounced, Cherkaoui and Wilcock (1999) observed similar periodic behavior in their high-Rayleigh number Boussinesq simulations.

We propose a simple physical explanation for temperature variations which have been observed after seismic events at black-smoker fields (Johnson et al., 2000; Fornari et al., 1998; Sohn et al., 1998; Von Damm, 2005): the earthquake induced permeability-increase (Elkhoury et al., 2005) shifts the convection system to unsteady, pulsating venting with accompanying temperature fluctuations. Over time, the system might reorganize itself, with clogging of fractures decreasing the bulk permeability, and vent temperatures becoming stable again. This provides a very simple explanation why some black-smokers have been observed to vent with a constant temperature on a decade timescale (Von Damm, 1990), while others, especially after earthquakes, show variability on timescales of weeks (Von Damm et al., 1995). Observed temperatures oscillations are typically on a smaller temporal timescale as described here (Johnson et al., 2000; Haymon et al., 1993; Fornari et al., 1998). Though part of the problem might be a lack of sufficient time series, this probably reflects the fact that actual permeability values are higher (up to 10^{-11} m^2 (Lowell and Germanovich, 2005)) than used in this study. Other proposed mechanisms to explain temperature variations, such as periodically propagating cracking fronts (Johnson et al., 2000) or magma replenishment (Von Damm, 2005), are physically much more complex. Currently, the only available dataset of vent-temperature over a period of many years is the one of the EPR 9°50′N (Von Damm, 2005), which has been monitored from 1991 till 2002. Over this period, effluent temperatures varied from 350°C to 395°C. Clearly those vents have been undergoing phase separation, which is outside the scope of this study, still the range of observed temperatures matches well with our simulations.

2.7.5 Spatial dynamics

The structure of the simulated hydrothermal system, with regularly spaced, narrow, pipe-like upflow zones, correlates well with observations. One of the few datasets available on subseafloor hydrothermal structures is given by Tivey and Johnson (2002), who inferred such narrow pipe-like upflow zones at the Main Endeavour Field. In contrast to the temperature of vent fluids, our models predict that vent locations will stay relatively constant in time. For $k = 10^{-14}$ m^2, vent fields remain essentially constant. For $k = 10^{-13}$ m^2, changes in the location of vent fields are on the order of a decade. Plume splitting can cause a single plume to surface at two different locations for a relatively short period, after which one of the plumes collapses. In another mechanism, a plume can retreat from the seafloor due to locally increased recharge. Those two mechanisms could either temporarily or permanently extinguish black-smokers. The first resembles the extinguishing of a single vent within a vent field, the second resembles the extinguishing of a whole vent area. Wether these processes actually occur is speculative. Few vents have been observed to cease venting, but this could reflect a lack of sufficient data. A possible candidate is Tube Worm Pillar at the EPR 9°50′N, which stopped venting while other nearby vents maintained or even increased in temperature (Von Damm et al., 2004). Von Damm et al. (2004) also reports two other vents at the EPR

going extinct without an apparent cause (Von Damm, personal communication, 2005).

2.7.6 Model limitations

Our isotropic, homogeneous permeability distribution is a highly idealized representation of actual ridge crest systems. Actual permeability measurements at ridge axis are not available and estimates point to values in the range 10^{-11} m^2 to 10^{-13} m^2 (Lowell and Germanovich, 2005), which is much higher than permeabilities used in this study. However, these estimates are based on a simple pipe model assuming a Boussinesq fluid. As pointed out earlier, real water tends to convect with the critical Rayleigh number up to 31 times lower (Straus and Schubert, 1977). If this effect can be directly translated into the pipe models, the estimates would indicate permeabilities for typical mid-ocean ridge fields that exactly match the range studied here. Further, permeability in reality is layered and anisotropic, especially within the dike segment where highly permeable fractures are superimposed, and appears to be temperature dependent. Basalt may become impermeable at the brittle-ductile transition at temperatures between 700°C and 800°C (Kelley et al., 2002), though some authors have argued that hydrothermal fluid flow starts at much higher temperatures of 900°C to 1000°C (Koepke et al., 2005). The clogging of fractures by mineral precipitation is an other important process affecting permeability (Lowell et al., 1993, 2003). The constant temperature boundary condition at the bottom assumes an infinite heat supply. Though an overestimation, this best approximates fast spreading ridges which have kilometer-long continuous magma chambers (Babcock et al., 1998). Downward propagating cracking fronts (Lister, 1974) could keep fluids in contact with fresh, hot rocks. This study demonstrates, however, that - provided that realistic fluid properties and accurate numerical schemes are used - geometrically simple, isotropic permeability models naturally predict dynamic features that closely resemble some observations at mid-ocean ridges.

Using a pure water equation of state instead of one for seawater simplifies the calculations considerably. Pure water above the critical point is a single supercritical fluid. A NaCl-H_2O fluid can boil at temperatures and pressures far above the critical point of pure water and separate into a high-salinity brine and low-salinity vapor. This will probably have a significant effect on the results presented above (Geiger et al., 2004). Extending similar model simulations to saline fluid systems will be a subject of future research.

2.8 Conclusion

Higher order numerical simulations of hydrothermal circulation in the highly permeable axial plane of mid ocean ridges, using realistic water properties, demonstrate that fluid flow patterns are much more irregular and convection less stable than previously inferred. The splitting of rising thermal plumes can be explained by the viscous, Taylor-Saffman instability at the interface between hot, low-viscosity fluids and cold, high-viscosity fluids. Analytical estimates of the width of splitted plumes are in good agreement with the numerical results. While plumes can vent at the same spatial position for thousands of years, vent temperatures can oscillate on the timescale of years and venting can stop temporarily. Unsteady convection (at $k \geq 10^{-14}$ m^2) alone can account for temperature variations of typically 40°C on the timescale of decades or less. Higher permeabilities shorten the period of oscillation, whereas an increase in pressure to values far above critical reduces its amplitude.

Our sensitivity analysis shows that, in order to realistically model high-Rayleigh number convection of aqueous fluids above the critical temperature and pressure, one not only needs to include the non-linearities in the fluid properties, but also to use higher-order transport schemes and high-resolution meshes. The use of less accurate numerical schemes smears out sharp gradients in fluid properties by numerical diffusion. This artificially stabilizes the system and can hide emergent properties like Taylor-Saffman fingering.

2.9 Acknowledgements

We thank Bob Lowell for reviewing two earlier manuscripts and giving useful comments during discussions at AGU 2005 and 2006. Also we like to thank William Wilcock for helping to improve this manuscript. This work was supported by the Swiss National Science Foundation.

3. A PARALLEL FE-FV SCHEME TO SOLVE FLUID FLOW IN COMPLEX GEOLOGIC MEDIA[2]

3.1 Abstract

Field data-based simulations of geologic systems require much computational time because of their mathematical complexity and the often desired large scales in space and time. To conduct accurate simulations in an acceptable time period, methods to reduce runtime are required. A parallelization approach is attractive because fast multi-processor clusters are nowadays readily available. Here we report on our recent efforts to parallelize our multi-physics code CSPMP++ (Complex System Modelling Platform). In particular, we describe a parallel finite-element finite-volume method for multi-phase fluid flow in heterogeneous porous media. We take a domain partitioning approach where the finite-element mesh is partitioned into sub-domains, assigning each of them to a single processor. For each sub-domain a local finite-volume mesh is constructed. We can now solve advection-dispersion type equations taking an operator splitting approach: Pressure diffusion is calculated with an implicit finite-element method and advection with an implicit or explicit finite-volume scheme. We have tested the accuracy, robustness and computational speedup of our new parallel scheme on a Linux cluster by means of three geologic applications. All tests give excellent computational speedup with increasing number of up to 32 processors. These results broaden the range of possible simulations in terms of spatial and temporal scale and resolution, as well as numerical accuracy, up to two orders of magnitude.

3.2 Introduction

Numerical analysis has greatly contributed to our understanding of fluid flow in the Earth's crust. It has been applied to a wide range of geologic systems, including oil-reservoirs (Aziz and Settari, 1979; Matthai et al., 2004), groundwater aquifers (Istok, 1989; Forsyth, 1991), geothermal reservoirs (Mercer and Faust, 1979; Pruess, 2002), ore-forming hydrothermal systems (Hayba and Ingebritsen, 1994b; Matthai et al., 2005) and fluid flow in the oceanic crust (Stein and Fisher, 2003; Fontaine and Wilcock, 2006).

Historically, the most widely applied numerical methods have been (1) finite-difference (FD) (Laumbach, 1975; Faust and Mercer, 1979), (2) integrated finite-difference (Narasimhan and Witherspoon, 1976; Pruess, 1987) and (3) finite-element (FE) (Istok, 1989; Huyakorn and Pinder, 1983) methods. More recently, the use of a combination of finite-element and finite volume (FEFV) methods (Baliga and Patankar, 1980) has become more wide-spread (Huber and Helmig, 1999; Durlofsky, 1993; Geiger et al., 2004; Paluszny et al., 2007). In this

[2] Published as: D. Coumou, S.K. Matthai, S. Geiger, T. Driesner, 2008, A Parallel FE-FV Scheme to Solve Fluid Flow in complex Geologic Media., *Comp. Geoscience* **in print**

approach, a node-centered finite-volume mesh is superimposed on the finite-element mesh. For convenience, this method is often used in combination with an implicit pressure, explicit saturation formulation (IMPES)(Aziz and Settari, 1979; Huber and Helmig, 1999; Geiger et al., 2004) where the pressure and saturation equations are solved sequentially. Pressure and solute diffusion are solved with the finite-element method and transport of the conserved quantity with the finite volume method. This approach has two major advantages: (1) the most suitable numerical method is used for each sub-calculation and (2) the resulting solution matrices are symmetric and diagonally dominant, allowing the use of fast solvers (Stuben, 2002). By taking sufficiently small timesteps, iterations between pressure and transport equations are not required. In many applications this specific scheme has proved to be computationally efficient (Geiger et al., 2004).

Despite the high computational efficiency of FEFV methods, calculation time remains a key obstacle to a high degree of physical realism of the simulation. For crustal convection systems, the spatial dimensions of numerical models need to be in the range of several to tens of kilometers while the time spans of interest range from days to tens of thousands of years. In such large systems, the resolution of small scale features is often crucial for the overall behavior. If so, a fine spatial and temporal discretization is required. Indeed, high-resolution meshes and higher-order accurate solution schemes are often necessary to discover essential system dynamics (see chapter 2). In many cases, the use of a realistic equation of state is also required (Geiger et al., 2004; Coumou et al., 2006; Straus and Schubert, 1977; Jupp and Schultz, 2000) (see chapter 2). Calculating the fluid's state using these complex equations (Haar et al., 1984; Palliser and McKibbin, 1998a; Driesner and Heinrich, 2003) can easily dominate the computational effort, especially when multiple fluid phases are present.

Apart from algorithmic or hardware improvements, a significant speedup can only be obtained by parallelization. This approach is especially attractive because of the wide spread availability of fast multiprocessor PCs or workstation clusters. The first parallel codes dealing with sub-surface fluid flow modeling were developed in the petroleum industry in the early 1980's (Calahan, 1982; Killough and Levesque, 1982; Scott et al., 1982). Through the mid 1990's progress was continuous but typically restricted to oil-reservoir modeling (Young and Hemanth-Kumar, 1991; Bhogeswara and Killough, 1982; Kaarstad et al., 1995). Only in the late 1990's did the emergence of PC and workstation clusters boost parallel computation techniques in sub-surface fluid flow modeling (Killough and Commander, 1999; Wang et al., 1999). Their usage spread to groundwater flow and contamination transport modeling (Pini and Putti, 1997; Tsai et al., 1999; Ashby et al., 1999), geothermal engineering (Zhang et al., 2001), multi-phase flow modeling (Peszynska and Yotov, 2001; Wu et al., 2002), CO_2 sequestration (Zhang et al., 2007) and nuclear waste storage (Elmroth et al., 2001; Wu et al., 2002). In these recent studies, the typical approach has been to decompose the FE (Pini and Putti, 1997), FV (Ashby et al., 1999) or FD (Ma and Chen, 2004) grid into multiple sub-domains with a sufficient overlap. Interprocessor communication is normally provided by one of the several available implementations of the Message Passage Interface (MPI) (Snir et al., 1996; Gropp et al., 1996a).

Here we report on our recent efforts to parallelize our C++ based multi-physics code CSMP++ (Complex System Modelling Platform) (Matthai et al., 2004). Similar to most other parallel porous media flow simulation codes, we take a domain partitioning approach, using the MPICH (Gropp et al., 1996b) implementation of MPI for inter-processor communication. The parallelization is implemented by means of numerous C++ classes combined

into a new CSMP++ library, which has been added to the existing set of CSMP++ libraries (Matthai et al., 2004; Paluszny et al., 2007). This way, the flexibility of CSMP++ to solve geologic problems using FE and/or FV spatial discretization methods (Paluszny et al., 2007) and implicit or explicit time-discretization methods is retained. Several routines have been implemented to manage communication between processors for both the FE and the FV method. To demonstrate that it gives correct results and to test its performance, we applied our parallel simulator to a number of geologic field-scale problems. First, the parallel FE method is tested by solving hydrostatic pressure on a complex multi-fracture high-resolution mesh. Second, the parallel FV method is tested by solving advection of a conservative tracer in fractured limestone. Third, we incorporate the full parallel FEFV method to solve transient sub-seafloor convection at mid-ocean ridge spreading centers. With these geologic applications, we show that the new parallel FEFV simulator gives correct results and that it gives, already for relatively small problems, very good speed-up with increasing number of processors.

3.3 Methodology and Implementation

The aim of a parallel code is to minimize runtime or make simulations requiring a large amount of memory possible. This is normally achieved by distributing the computational effort equally over several processors. To achieve a sufficiently good speedup, one has to find proper solutions to three issues: (1) equal partitioning of the problem domain, (2) efficient inter-processor communication and (3) effective input and output of data. These three objectives, and how we achieved them, are discussed over the next three subsections.

3.3.1 Domain partitioning

The quality of the partitioning of the computational domain impacts the performance of the parallel code to a great extent. Ideally, a partitioning algorithm should account for: (1) an even computational load balance, (2) a minimal total communication volume, (3) an even load balance in communication volume, (4) a minimum total number of neighboring processors and (5) an even load balance in the number of neighboring processors (Wu et al., 2002). As this is obviously a complex problem, especially in the case of large irregular meshes, one normally tries to optimimize the first two goals only.

In a first partitioning step, we employ the METIS (Karypsis and Kumar, 1998) multilevel graph partitioner. This tool performs a multilevel partitioning by computing a partitioning on a coarse mesh and successively refining this solution. It is widely used (e.g. Wu et al., 2002) and typically produces better solutions than other partitioning algorithms (Barnard and Simon, 1993; Schamberger and Wierum, 2005). We employ METIS to obtain a first, disjointly distributed partitioning of the nodes of a finite element mesh. The global domain Ω of n FE nodes is divided into P sub-domains, such that $\sum_{p=1}^{P} n_p = n$, where P is the number of processors available, or:

$$\Omega = \bigcup_{p=1}^{P} \Omega_p, \quad \Omega_p \cap \Omega_q = \varnothing (p \neq q) \tag{3.1}$$

Where Ω_p denotes the computational sub-domain, or *base* partition, assigned to processor p. Each processor is responsible for its local *base* partition. In a next step, all elements with

one or more nodes in a specific *base* partition are attributed to that partition. Since the nodes are disjointly distributed, this implies that partitions overlap by one layer of elements with their neighbors (see Fig. 3.1). This step brings the total number of nodes of partition p to $n_p + nhalo_p$, with $nhalo_p$ the number of nodes lying outside its *base* partition. For these outerhalo nodes, the *base* processor is not responsible. Instead, before each computational step, this processor receives current values of variables for the outerhalo nodes from its neighbor(s). Next to outerhalo nodes, we define inner-halo nodes as those for which values of the unknowns have to be sent to neighboring partitions. Naturally, the innerhalo nodes of one partition are the outerhalo nodes of its neighbors. Figure 3.1 shows a triangular mesh partitioned into four sub-domains, indicating innerhalo and outerhalo nodes of one of these. For larger meshes, the number of nodes duplicated in the regions of overlap represents only a small percentage of the total number of nodes as shown in figure 3.2.

Next, partitions are locally renumbered, with the outerhalo nodes and elements outside the local computational domain receiving the highest indices. Outerhalo nodes are flagged as internal boundary nodes for later recognition. The final step in the partitioning procedure involves the copying of all variable data from the global domain to the sub-domains. In CSMP++ scalar, vector or tensor variables are defined either on the element, node, constraint point or element face as a value plus a data-style flag (Matthai et al., 2004). For every physical variable, this information is copied to the sub-domains.

To keep memory usage limited, the partitioning is performed in a pre-processing step on a single (large memory) machine. This preprocessing step writes for each processor its subdomain plus variable data to a binary file and information it needs for communication to a text file. At the start of a parallel run, each processor loads its two files.

3.3.2 Inter-processor communication

We use the Message Passage Interface (MPI) (Snir et al., 1996; Gropp et al., 1996a) for inter-processor communication. So far, we have tested both the MPICH2 (version 1.0.4) (Gropp et al., 1996b) and the cluster-hardware optimized Quadrics MPI implementation. Outerhalo-to-innerhalo mapping is performed directly after partitioning of the sub-domains. From this mapping a send- and receive-list are created. The send-list contains the indices of nodes for which data is to be sent to the neighboring processors. This list corresponds to the processor's innerhalo nodes and will have entries $\leq n_p$. It can contain multiple entries with the same index when, as shown in figure 3.1, for a triple junction, data needs to be sent to several processors. The receive-list contains node indices for which data is to be received from neighboring processors. This list contains entries $n_p + 1$ to $n_p + nhalo_p$ and cannot contain multiple entries with the same index. The order of indices in the send-list and corresponding receive-list of the neighboring processor have to be consistent. Additional vectors for book keeping define the range of indices which need to be sent to, or received from, which neighboring processor, identified by its MPI rank.

Once these communication variables are initialized, updating of the variables stored on the outerhalo nodes is straightforward. This is done using MPI send-receive operations, in which two processors exchange data by a single MPI call. A processor sends data stored on its innerhalo to one of its neighboring processor and at the same time receives from the same processor data to be stored on its own outerhalo. Such communication can either be done using a blocking (MPI::Comm::Send() and MPI::Comm::Recv()) or non-blocking

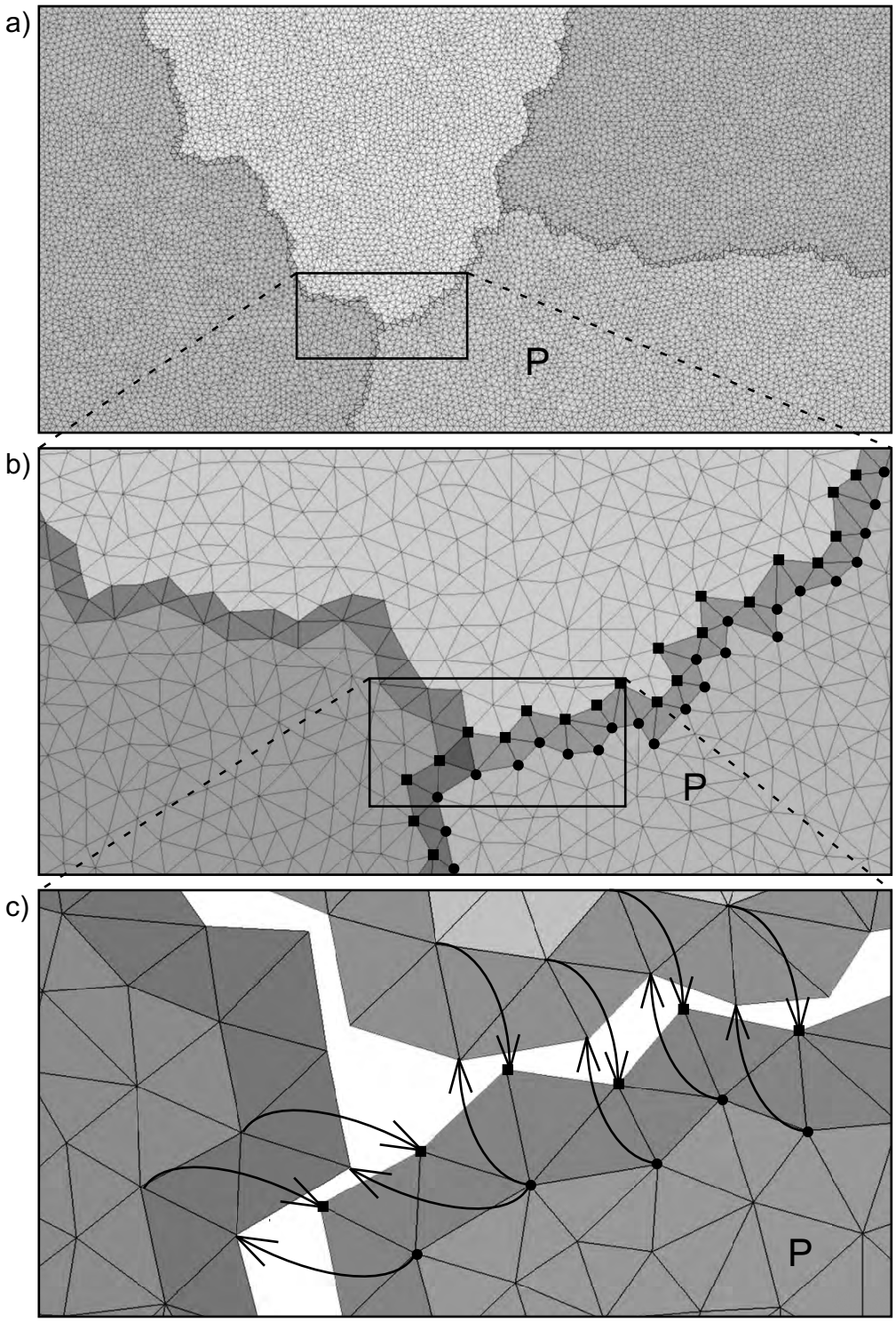

Fig. 3.1: Example of a fourfold partition of a 2D triangular mesh. a) Different shades of grey distinguish individual partitions and overlapping elements. b) Black squares and dots indicate outer- and innerhalo nodes of partition P respectively. c) Arrows indicate the direction of MPI messages.

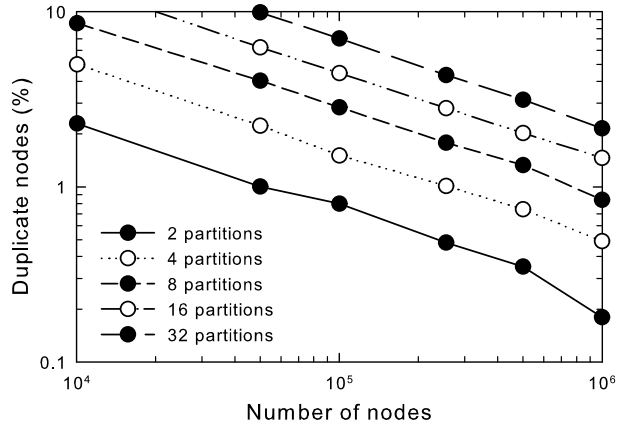

Fig. 3.2: Log-log plot of the percentage of duplicate nodes in variably partitioned models of increasing size.

(MPI::Comm::Isend() and MPI::Comm::Irecv()) MPI routines (Snir et al., 1996). In a blocking procedure, a processor which needs to receive data is blocked until the receive buffer actually contains the new message (Snir et al., 1996). In contrast, in a nonblocking procedure the receiving processor is allowed to continue computations until it encounters a separate complete-receive statement to verify that the data have been received. Since this makes the computation more tolerant of fluctuations in the speed of processors, nonblocking communication often gives better performance (Snir et al., 1996). We extensively tested and compared the performance of the blocking versus the nonblocking communication routines in our code. Both methods essentially gave the same performance, though this finding applies solely to the Linux system on which we tested our code.

Finally, a routine has been implemented to update multiple variables in a single send-receive step. This considerably improves performance, since sending multiple small MPI messages takes longer than one large message.

3.3.3 Input and output

Initial and boundary conditions can be defined both before as well as after partitioning. The easiest way is to define all initial and boundary conditions on the global domain before partitioning. In this case all variable values and flags as well as boundary flags are copied from the global domain to the sub-domains during partitioning. The partitioned sub-domains still have the same flexibility to change status flags as the global domain. Hence parameter values, flags and initial conditions can also be set and changed during a parallel run. This is possible because we store wether a subdomain boundary is only an internal boundary or also a global domain boundary. Finally, we have implemented a feature which allows for the storage of a parallel simulation in binary files for a potential restart. This is especially useful since the usage of continuous CPU time on super-computers is often restricted.

For speed considerations, we have decided to keep output of data completely parallel. That is, each processor directly writes its variable data to files. These files can later, in a automated post-processing step, be recombined into the global domain. An alternative would be to implement a master-slave structure for the output of data. In such a structure, all processors send their data to a central master processor which writes it to file. Though

perhaps more user-friendly, this is time consuming and memory intensive, since the master processor needs to keep the entire global domain in its memory.

3.4 Application

Transport of a conserved quantity $\psi(\mathbf{x}, t)$ in a porous medium is described by the general advection-dispersion equation:

$$\phi \frac{\partial \psi(\mathbf{x}, t)}{\partial t} = \nabla \cdot (D \nabla \psi) - \nabla \cdot (\mathbf{v} \psi) + q \tag{3.2}$$

where $\mathbf{x}$ is the coordinate vector, ϕ is a storage multiplier, D is the diffusivity parameter and q captures sources or sinks of ψ. The vector quantity $\mathbf{v}$ is the transport velocity. Operator splitting is done assuming that the total time derivative in equation 3.2 is the summation of a diffusive $\left(\frac{\partial \psi}{\partial t}\right)_{dif}$ and an advective time derivative $\left(\frac{\partial \psi}{\partial t}\right)_{adv}$. The diffusive derivative of equation 3.2 is given by:

$$\phi \left(\frac{\partial \psi}{\partial t} \right)_{dif} = \nabla \cdot (D \nabla \psi) + q \tag{3.3}$$

which we solve using the finite-element method. The advective derivative is given by:

$$\phi \left(\frac{\partial \psi}{\partial t} \right)_{adv} = -\nabla \cdot (\mathbf{v} \psi) \tag{3.4}$$

which we solve using the finite-volume method.

3.4.1 Finite element discretization

Equation 3.3 is solved using the standard Galerkin finite-element approximation (Huyakorn and Pinder, 1983; Istok, 1989). Linear or non-linear basis functions, N_i, are defined in a piecewise fashion inside each finite-element for each node. They are defined such that $N_i = 1$ on node i and $N_i = 0$ on all other corner nodes. The local variable, $\psi(\mathbf{x}, t)$, is approximated as $\widetilde{\psi}(\mathbf{x}, t) \simeq \Sigma_{i=0}^{m} N_i(\mathbf{x}) \widehat{\psi}_i(t)$ or in vector notation $\widetilde{\psi} \simeq \mathbf{N} \widehat{\psi}$, where $\widehat{\psi}$ is the nodal value. Substituting this in equation 3.3, multiplying with weighting functions (identical to $\mathbf{N}$ in the standard Galerkin approach) and integrating over each element, yields:

$$\int_{(e)} \phi \mathbf{N}^{\mathbf{T}} \mathbf{N} \frac{\partial \widehat{\psi}}{\partial t} \partial \mathbf{x} = \int_{(e)} \mathbf{N}^{\mathbf{T}} \nabla \cdot (D \nabla \mathbf{N}) \widehat{\psi} \partial \mathbf{x} + \int_{(e)} \mathbf{N}^{\mathbf{T}} q \partial \mathbf{x} \tag{3.5}$$

The first term on the righthand side is expanded by partial integration, after which Green's theorem is applied to obtain:

$$\int_{(e)} \phi \mathbf{N}^{\mathbf{T}} \mathbf{N} \frac{\partial \widehat{\psi}}{\partial t} \partial \mathbf{x} = -\int_{(e)} \nabla \mathbf{N}^{\mathbf{T}} D \nabla \mathbf{N} \widehat{\psi} \partial \mathbf{x} + \oint_{\partial \Omega} \mathbf{N}^{\mathbf{T}} (D \nabla \mathbf{N} \widehat{\psi}) \cdot \mathbf{n} dA + \int_{(e)} \mathbf{N}^{\mathbf{T}} q \partial \mathbf{x} \tag{3.6}$$

The surface integral on the righthand side is the natural boundary term and is omitted such that the equation can be written as:

$$\mathbf{MM}\frac{\partial}{dt}\widehat{\psi}(t) = \mathbf{KM}\widehat{\psi}(t) + \mathbf{Q} \tag{3.7}$$

With the element matrices given by:

$$\mathbf{MM} = \int_{(e)} \phi \mathbf{N}^{\mathbf{T}}\mathbf{N}\partial\mathbf{x}, \quad \mathbf{KM} = -\int_{(e)} \nabla\mathbf{N}^{\mathbf{T}} D \nabla\mathbf{N}\partial\mathbf{x}, \quad \mathbf{Q} = \int_{(e)} \mathbf{N}^{\mathbf{T}} q \partial\mathbf{x} \tag{3.8}$$

Using a backward Euler discretization of the time derivative gives, after further rearranging:

$$\left(\frac{\mathbf{MM}}{\triangle t} + \mathbf{KM}\right)\widehat{\psi}^{t+\Delta t} = \frac{\mathbf{MM}}{\triangle t}\widehat{\psi}^{t} + \mathbf{Q} \tag{3.9}$$

Finally the global matrices are assembled by the sequential accumulation of the element matrices. If ψ is a scalar variable, this results, for a serial computation, in a $n \times n$ system of linear equations of the from $\mathbf{Ax} = \mathbf{b}$. In a parallel computation, however, the element matrices associated with the outerhalo nodes are not assembled into the global matrix. This results, for each sub-domain, in a $n_p \times (n_p + nhalo_p)$ matrix equation of the form:

$$\begin{bmatrix} A_{1,1} & \cdots & A_{1,n_p+nhalo_p} \\ \vdots & \ddots & \vdots \\ A_{n_p,1} & \cdots & A_{n_p,n_p+nhalo_p} \end{bmatrix} \begin{bmatrix} x_1 \\ \vdots \\ \\ \vdots \\ x_{n_p+nhalo_p} \end{bmatrix} = \begin{bmatrix} b_1 \\ \vdots \\ b_{n_p} \end{bmatrix} \tag{3.10}$$

The system of equations 3.10 is solved using the parallel SAMGp matrix solver (Krechel and Stuben, 2005).

3.4.2 Finite volume discretization

The transport velocity $\mathbf{v}$ is calculated at the finite element centers since $\nabla\mathbf{N}$ is discontinuous at the element boundaries and therefore the derivative of the fluid pressure is undefined (Paluszny et al., 2007). By constructing a node-centered finite-volume mesh (Geiger et al., 2004), the element centers coincide with the boundary of the finite-volumes (see figure 3.3). Mass-conservative flux calculations can now be performed by integrating over the surface area of the finite-volume V_i. Equation 3.4 becomes, after applying Green's theorem:

$$\int_{V_i} \phi \frac{\partial\widehat{\psi}(t)}{\partial t} dV = -\int_{A_i} \mathbf{n_j} \cdot \mathbf{v}\widehat{\psi}(t) dA \tag{3.11}$$

Here, A_i is the boundary area of finite-volume V_i and $\mathbf{n_j}$ is the outward pointing normal vector of facet j of this boundary. The integral on the right-hand side can be written as a summation over all segments. Further discretizing equation 3.11 in time using a forward Euler approximation gives:

$$\widehat{\psi}_i^{t+\Delta t} = \widehat{\psi}_i^t - \frac{\Delta t_{CFL}}{\phi V_i} \sum_j \left[\mathbf{n}_j \mathbf{v}_j\right] \widehat{\psi}_i^t \tag{3.12}$$

In this explicit scheme, the timestep, Δt_{CFL}, is restricted by the CFL criterion given by:

$$\Delta t_{CFL} = \mathrm{MIN}_\Omega \left(\frac{r_i}{\mathbf{v}}\right) \tag{3.13}$$

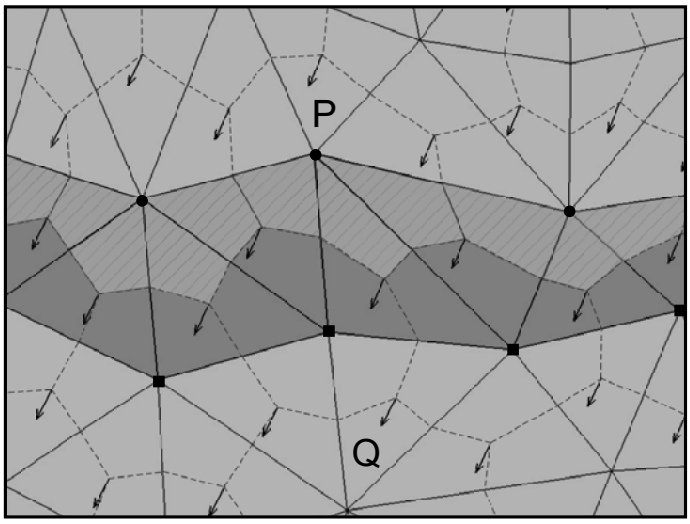

Fig. 3.3: Close-up of the boundary between partitions P and Q, showing the finite-elements (solid lines) and finite-volumes (dotted lines) as well as the velocity field (arrows). Black dots and squares indicate the outer- and innerhalo nodes respectively of processor Q. The idle finite-volumes of processor Q are hatched.

where r_i is the approximate radius of control volume i and the 'MIN$_\Omega$' refers to the minimum encountered value in computational domain Ω. Since the finite-volumes are node-centered, each partition contains $n_p + nhalo_p$ of them. However, only n_p volumes are involved in flux calculations, while the $nhalo_p$ finite-volumes centered on the outerhalo are idle. Flux calculations of those volumes are performed by the neighboring processor (see figure 3.3). Before each advection step, however, the conserved nodal quantity $\widehat{\phi}$ needs to be updated.

3.5 Results

We test the new parallel simulator for accuracy and computational efficiency using three geologic test cases. In a first application, we calculate static fluid pressure in a heterogeneous permeability field caused by the presence of fractures, cross-cutting the computational subdomains. Second, we test the quality of the parallel FV scheme by solving for the propagation of a conservative tracer in the same geometry. In the third test, we investigate thermal convection in a sub-seafloor mid-ocean ridge setting. With this last application we test the performance of the combined parallel FEFV scheme. All geologic test applications were performed on the "Gonzales" high-performance Linux cluster at the ETH Zurich (CH). This cluster consists of 288 dual-processor nodes with AMD Opteron 250 cpus, connected via a Quadrics QsNet II interconnect switch.

3.5.1 Static pressure

We test the performance of the parallel FE method by solving for fluid pressure on a multi-fracture, 8×5.5m domain consisting of $\sim 340,000$ elements (figure 3.4) (Matthai et al., 2004; Belayneh et al., 2006). The case study area is located at the British Channel coast and represents an oil reservoir analogue (Matthai et al., 2004; Belayneh et al., 2006). Fracture patterns were carefully mapped and discretized resulting in the mesh depicted in figure 3.4 (Belayneh, 2003; Belayneh et al., 2006). The static pressure equation is given by the simple differential equation:

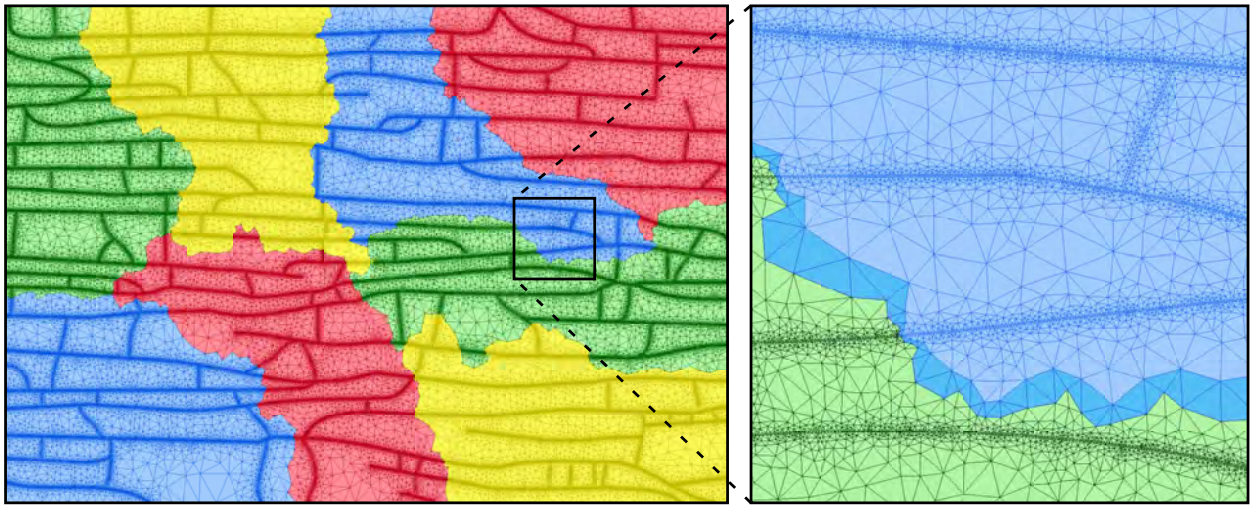

Fig. 3.4: Multi fracture finite-element mesh. Fractures are visible as thick black lines due to the mesh refinement towards them (see inset on right) An eight-fold domain partition is shown using contrasting colors. Fracture permeability is $10^{-14}\mathrm{m}^2$ and rock matrix permeability is $10^{-15}\mathrm{m}^2$ (From Belayneh et al. (2006) figure 4)

$$\frac{\mathbf{k}}{\mu}\nabla^2 p = 0 \tag{3.14}$$

where $\mathbf{k}$ is the permeability tensor and μ the pressure dependent fluid viscosity. Using a FE discretization, we solve equation 3.14 on 1,2,4,8,16 and 32 processors. We define parallel speedup and efficiency as:

$$\text{speedup} = \frac{\text{calculation time single processor}}{\text{calculation time } P \text{ processors}} \tag{3.15}$$

$$\text{efficiency} = \frac{\text{speedup}}{P} \times 100\% \tag{3.16}$$

Figure 3.6 shows that excellent speedup improvement is achieved by the parallel FE scheme. The parallel FE method achieves an efficiency of 93% for this specific application and hardware settings. Runs using different number of processors gave slightly different pressure solutions. Runs using the same number of processors always gave exactly the same results. The difference when using a different number of processors is of the order of the specified tolerance of the parallel matrix solver SAMGp (Ruge and Stuben, 1987; Stuben, 2002), and can therefore be set to arbitrary small. The difference is caused by the solution technique employed in multigrid solvers such as SAMGp. Multigrid methods build on the principle that relaxation methods, such as Gauss-Seidel, efficiently damp high frequency errors, but make little progress towards reducing low-frequency errors (Yang, 2004). If one moves the problem to a coarser grid, previously low frequency errors turn now into high frequency errors which can be reduced efficiently (Yang, 2004). Thus successively, the grid complexity is reduced, a coarse solver applied and the solution rebuilt back to a fine grid. Since SAMG's coarsening strategy is inherently sequential, finding a reasonable parallel analogue is a challenge (Krechel and Stuben, 2001). In SAMGp this has been achieved with a minimum subdomain blocking method (Krechel and Stuben, 2001). In this method a minimum number of

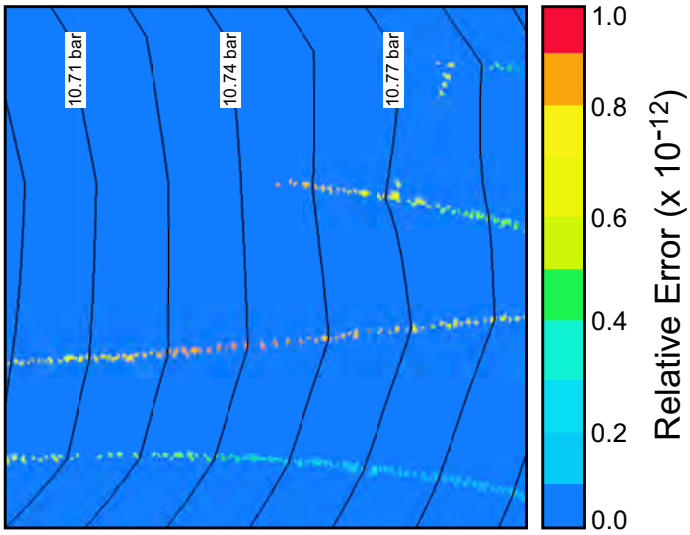

Fig. 3.5: Isobars and relative difference between a single and 8 processor pressure solution of the excerpted region of figure 3.4. The difference is larger near the high-permeability fractures but not towards the domain boundary.

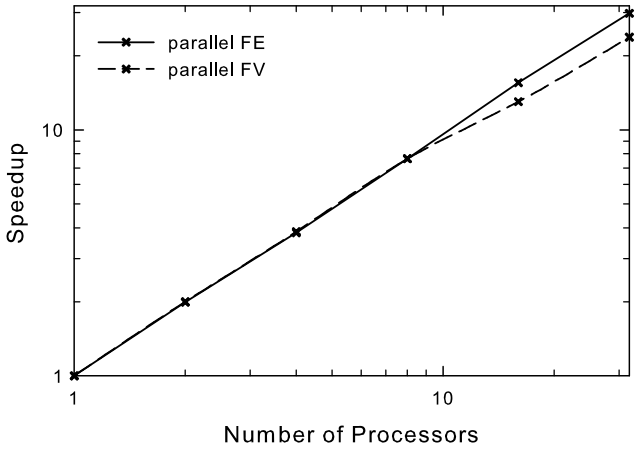

Fig. 3.6: Log-log plot of speedup versus the number of processors for the FE pressure problem (solid) and FV tracer advection problem (dashed)

required grid points at the boundary between processors go to the next level coarser grid. This implies that the exact solution procedure of SAMGp is affected by the location and number of partitions. This difference is illustrated in figure 3.5 for the multi-fracture mesh of figure 3.4. Figure 3.5 compares a single and 32 processor solution for static pressure. The figure shows that, though very small and below convergence tolerance, the difference is larger near the high-permeability fractures. More importantly, it shows that the difference does not increase near subdomain boundaries.

3.5.2 Fluid flow in fractured limestone

The performance of the parallel FV scheme is tested by solving fluid transport through the naturally fractured limestone beds discussed in the previous test case. In a first step, a static pressure field is calculated for the whole domain by solving equation 3.14 on a single processor, with the pressure drop between left and right boundary fixed at 1×10^5Pa. From

the pressure field the velocity field is determined using Darcy's law in the absence of gravity:

$$\mathbf{v} = -\frac{\mathbf{k}}{\mu}\nabla p \tag{3.17}$$

In a second step, the model is partitioned into either 2,4,8,16 or 32 sub-regions. Now the parallel run starts, with each processor calculating passive tracer transport in its local domain by solving:

$$\phi\frac{\partial C(\mathbf{x},t)}{\partial t} = -\nabla\cdot(\mathbf{v}C) \tag{3.18}$$

Here, C is the concentration of the tracer and ϕ indicates the porosity. Before each new advection step the CFL-calculated timestep is broadcast to all processors and C is updated on the outerhalo of each processor domain. Since the pressure field has been calculated before partitioning, all tests start with exactly the same pressure field. By doing so, we can solely test the behavior of the parallel FV scheme, independently of the FE method. FV flux calculations are local operations and therefore should not depend on the chosen partitioning. This proved to be the case, with all runs giving exactly the same results. Figure 3.6 shows that excellent speedup is achieved by the parallel FV scheme. With increasing number of processors, the communication volume increases, reducing the overall efficiency. This decrease in efficiency is evident in figure 3.6 as a shallowing of the gradient of the curve. For the parallel FV scheme using 32 processors and the mesh described above, efficiency still is $\sim 75\%$ for this specific application and hardware setup.

3.5.3 Thermal convection

In a third and final benchmark, we test the performance of the fully parallel FEFV scheme. We do this by solving transient thermal convection within the axial plane of a mid-ocean ridge spreading center at supercritical water pressures. We employ a pure water equation of state (Haar et al., 1984), including the non-linear pressure-temperature dependence of fluid viscosity, density, heat capacity, thermal expansivity and compressibility. A computational flow diagram, which lists the successive computations, is given in figure 3.7. Timesteps are sufficiently small such that iterations to account for the non-linearities are not required. Pressure at the top boundary is kept at 25MPa and temperature at the bottom boundary at 1000°C. Between successive FE and FV calculation steps, each processor updates all primary variables on its outerhalo nodes. Figure 3.8 shows the speedup versus the number of processors for three different-sized meshes. Computational efficiency drops faster for smaller meshes than larger ones because the communication volume is comparatively larger. The larger meshes give excellent near-linear speedup with increasing number of processors for this specific application and hardware setup.

Separate runs using the same number of processors will always produce exactly the same results. Runs using different number of processors show small differences in the location of the first thermal perturbations. This is an artifact of the slightly different solutions of the pressure equation by the SAMGp solver for different numbers of partitions as discussed in section 3.5.1. These small differences in pressure cause small differences in fluid properties and can trigger convection at slightly different locations. Since thermal plume formation is a self-enhancing process, this will cause plumes to form and evolve differently. This effect is shown in figure 3.9, comparing the temperature field after 500 years of a single-

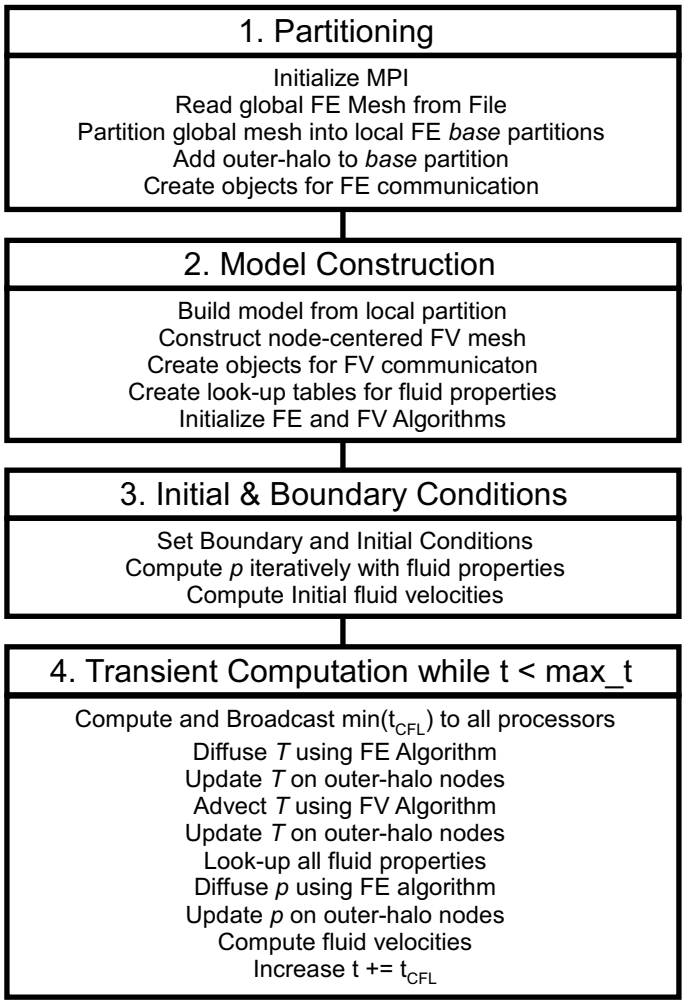

Fig. 3.7: Flow chart for the solution procedure of the parallel FEFV scheme for transient thermal convection

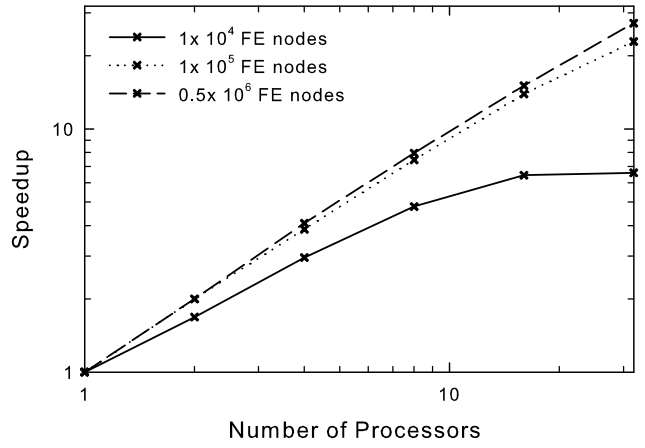

Fig. 3.8: Log-log plot of the speedup of the parallel FEFV scheme for various mesh sizes up to 32 processors.

and a 4-processor solution. Clearly, isotherms cannot be mapped one-on-one between the two solutions, however, the number of plumes, as well as rise-height, are the same. When convection is fully developed, the global behavior of convection, in terms of how many plumes form, how fast they rise, aspect ratio of convection cells, etc, is the same when one or more processors are applied.

Our new parallel code for FEFV computations achieves an efficiency of 85% for a 500,000 node mesh ($\sim$ 1 million elements) and 32 processors on a Linux cluster. One explanation for the high efficiency of our parallel simulator is that much of the calculation can be performed locally. Local computations, such as calculating fluid properties or explicit finite-volume operations, require very limited inter-processor communication. This is illustrated in figure 3.10 which shows, for the 32-processor case, the computational efficiencies of each sub-calculation of the scheme. It shows that the local FV and equation of state (EOS) computations have efficiencies >90%. The efficiency of the calculation of temperature diffusion is even higher at 98%.

3.6 Discussion

The parallel FEFV code provides a powerful tool for tackling larger and more complex geologic problems. The serial FEFV method has been applied successfully to a number of case studies of great geologic interest. These studies include multi-phase flow in geologically realistic representations of fractured rocks (Belayneh et al., 2006), the transient evolution of world-class copper deposits using detailed geological models (Matthai et al., 2004) and liquid-vapor convection in magmatic-hydrothermal systems (Geiger et al., 2005; Coumou et al., 2006). One of the crucial next steps is to study these processes in 3D. Recently, it has been shown how finite-elements and finite-volumes can be combined efficiently to represent geometrically complex three-dimensional structures (Paluszny et al., 2007). However, the runtime necessary to simulate transient and non-linear flow and transport processes in models containing millions of elements on a single processor often renders their use impracticable. With the parallel simulator, run time is effectively reduced from weeks or even months

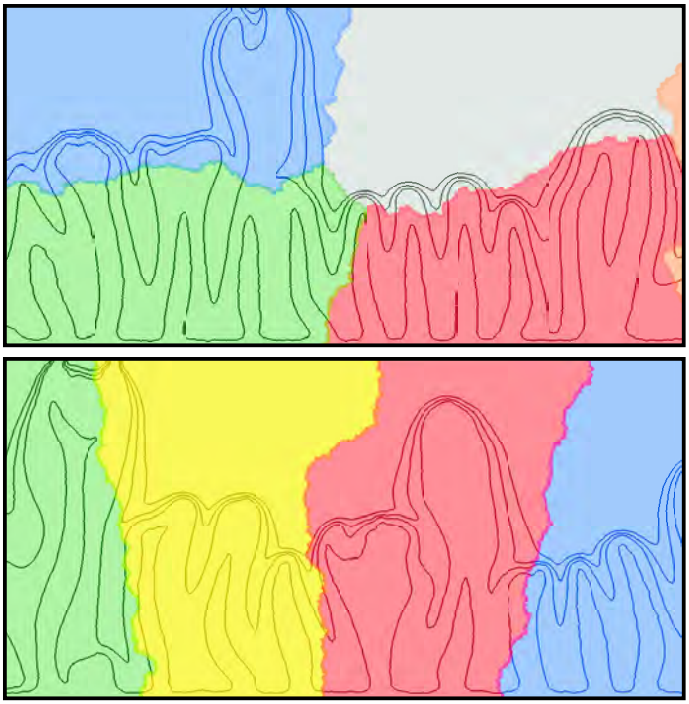

Fig. 3.9: Comparison of isotherm positions after 200 years of convection between two differently partitioned parallel runs. Isotherms are plotted every 100°C, colors indicate the different computational domains and only a small part (2000 × 1000 m) of the complete domain is shown.

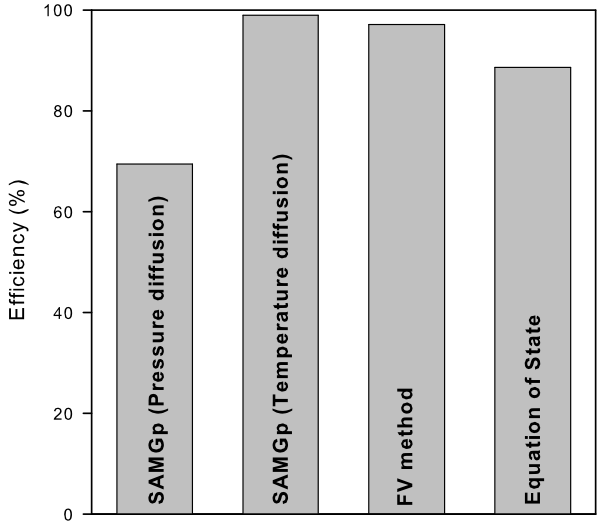

Fig. 3.10: Computational efficiencies of all sub-calculations of the parallel FEFV scheme for 32 processors and a mesh of 0.5×10^6 nodes (10^6 elements).

to days. Therefore different parameters and scenarios can be investigated efficiently and improve our fundamental understanding of complex geologic systems. Currently, we apply the parallel simulator to investigate thermal convection at mid-ocean ridges using 3D meshes consisting of several million elements. In the near future, we will perform 3D simulations of continental ore-forming hydrothermal systems with discrete fracture networks.

3.7 Conclusions

An efficient parallel version of CSMP++ has been developed for simulating porous medium flow type problems. The flexibility of CSMP++ to solve geologic problems in 2D or 3D, using FE and/or FV spatial discretization methods (Paluszny et al., 2007) and implicit or explicit time-discretization methods, is retained. Other CSMP++ modeling capabilities such as a specific equation of states, are preserved within the parallel simulator.

We tested the quality and efficiency of our new parallel code on a Linux cluster by means of three geologic applications. All tests gave excellent speedup improvements with increasing number of processors. Based upon these initial, hardware-dependent results, it is expected that the parallel simulator can enhance modeling capabilities in terms of memory and cpu usage by up to 2 orders of magnitude. High-resolution, higher-order accurate simulations, in 3D over geologic time scales, are now feasible.

3.8 Acknowledgements

The authors would like to thank the SAMG team, and in particular Arnold von Krechel, for their very helpful cooperation during this project. Also, we thank Mandefro Belayneh for providing the mesh depicted in figure 3.4 and two anonymous reviewers for giving very helpful comments to improve the first manuscript.

4. THE STRUCTURE AND DYNAMICS OF MID-OCEAN RIDGE HYDROTHERMAL SYSTEMS

4.1 Abstract

Sub-seafloor hydrothermal convection at mid-ocean ridges transfers 25% of the Earth's heat flux and can form massive sulfide ore deposits. Yet, the three-dimensional structure and transient dynamics are largely unknown. Using novel, realistic numerical simulations we demonstrate that convection cells self-organize into pipe-like upflow zones surrounded by narrow zones of focused, relatively warm, downflow. This configuration ensures optimal heat transfer and allows more efficient metal leaching for ore deposit formation. The results also predict the ideal location for hydrologic tracer tests, which seem feasible since simulated fluid-residence times are as short as 3 years. The unexpected concentric flow geometry results from previously neglected non-linearities in fluid properties, and this may have broader implications for the behavior of other fluid flow systems in the Earth's crust.

4.2 Introduction

Hydrothermal convection at mid-ocean ridge spreading centers transports a major part of the Earth's total heat flux, significantly affects the chemistry of crust and overlying ocean, and provides nutrients for chemosynthetic life on and beneath the seafloor. Mass, heat and associated chemical fluxes from the crust to the ocean at mid-ocean ridge spreading centers are large (Stein and Stein, 1994; Fisher, 2001) and have therefore been studied widely since the discovery of black smoker fields 30 years ago (Corliss et al., 1979). In spite of these efforts, fundamental features such as the location of seawater recharge, notably the relative importance of off- versus along-axis convection, are still poorly understood. Knowledge of the thermal and flow structure of mid-ocean ridge hydrothermal convection is key to understanding (1) their concrete role in modifying heat flow near spreading ridges, (2) the amount and distribution of rock alteration and associated chemical fluxes to the ocean and (3) the efficiency of massive sulfide ore formation (Herrington et al., 2005). Recent studies of active (Tivey and Johnson, 2002) and ancient (Coogan et al., 2006) systems show that discharge can be highly focussed in pipe-like regions, possibly continuing to the base of the hydrothermal system (Tivey and Johnson, 2002). Recharge is commonly thought to occur over extensive areas (Johnson et al., 1993; Kelley et al., 2002), with off-axis faults guiding fluid pathways towards the base of the hydrothermal system. Lately, however, this view has been challenged by micro-earthquake data indicating that recharge could be focussed close to the spreading center (Tolstoy et al., 2008).

Recent numerical studies which included accurate thermodynamic properties of water have given a number of key-insights into the physics of these systems but were restricted

to 2D geometries (Ingebritsen and Hayba, 1994; Jupp and Schultz, 2000; Coumou et al., 2006), and hence could not address the relative importance of along-axis versus across-axis circulation. These studies proved, however, that the non-linear dependence of fluid properties on pressure and temperature is a first-order control, determining the self-organization of convection cells. Quantitative, 3D numerical models have been applied to low-permeability (Travis et al., 1991) or sedimented systems (Rabinowicz et al., 1998), but not to the more highly permeable basaltic systems, which represent the greater and most active part of mid-ocean ridge spreading centers.

Recent developments of numerical simulation schemes for hydrothermal fluid flow with accurate fluid properties have prepared the ground for realistic models of these systems in 3D (Paluszny et al., 2007; Coumou et al., 2008). As a first study, we have set up a model that we consider the simplest possible representation, without geological complexity, in order to identify the first-order physical factors controlling the behavior of mid-ocean ridge convection cells. In spite of its geometric simplicity, the model predicts effects that closely match observations from natural systems, and makes a number of testable, quantitative predictions for currently debated questions in mid-ocean ridge research.

4.3 Model Setup

The governing equations are an appropriate version of Darcy's law (Ingebritsen et al., 2006), conservation of mass and energy in an incompressible porous medium (Coumou et al., 2006) and an accurate equation of state for water (Haar et al., 1984). Taking pure water as a proxy for seawater substantially reduces the computational complexity since pure water above the critical pressure (21.1MPa) is always a single phase fluid. Used water properties, however, adequately represent those of single-phase seawater for all results presented here. The equations are solved within the 3-dimensional box shown in figure 4.1, which has been discretized by a total of $\sim$ 2.5 million tetrahedral elements. The total amount of energy added to the system can be estimated from the spreading rate of the oceanic plates. At the spreading axis magma crystallizes and cools to ambient temperatures, thereby releasing energy. This way heat fluxes of up to $\sim$ 120MW per kilometer of spreading axis are found (Fisher, 2001). Direct measurements from individual vent fields or ridge segments have given substantially larger values, indicating that magma supply is episodic and local (Ginster et al., 1994; Baker and Urabe, 1996; Ramondenc et al., 2006). In the model, we therefore set the heat flux at an intermediate value of 350MW/km, which is distributed to the bottom of the model assuming a Gaussian profile that mimics an elongated magma chamber with an across axial width of roughly 1 km (see figure 4.1). We set a bulk permeability of $k = 5.0 \times 10^{-14}\mathrm{m}^2$. At these specific values of permeability and heat flux, the temperature near the bottom of the model establishes itself to be close to expected magmatic temperatures of $\sim 1200°\mathrm{C}$ (Sinton and Detrick, 1992). At lower permeability, the system cannot remove heat fast enough and the system would heat up to unrealistically high values. In natural systems, this would imply an upward migration of the magma chamber, which we do not consider in our models. At higher permeabilities, heat is mined faster, suppressing bottom boundary temperatures to values much smaller than magmatic temperatures. The top boundary represents the seafloor and is kept at a pressure of 25MPa. To allow hot fluids to vent through the top we use a mixed thermal boundary condition (Jupp and Schultz, 2000; Coumou et al., 2006): in elements experiencing upflow the thermal gradient is set to zero to represent unobstructed

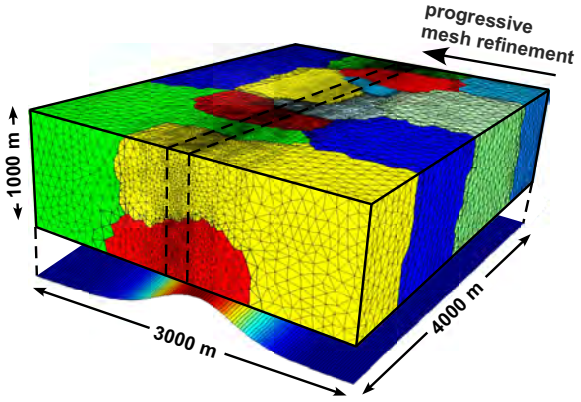

Fig. 4.1: 3D mesh consisting of 2.5 M tetrahedron elements. Resolution is refined towards the axial center and colours indicate computational domains assigned to separate processors (see "Methods" section for details). At the bottom boundary the bellshaped form of the heat flux profile is plotted.

outflow to the ocean, whereas elements experiencing downflow take in 10°C water.

4.4 Numerical Results

After a short initialization period, convection develops into pipe-like upflow regions, spaced at regular distances of roughly 500m (see figure 4.2a). Although thermal instabilities form and rise periodically close to the axial center, the locations of the main upflow regions remain relatively fixed. Within these pipes, fluids of $\sim$ 400°C move upward vigorously and vent at the seafloor, forming near-circular discharge areas. The surface area of these fields is $\sim 2\times10^4\mathrm{m}^2$, which is in good agreement with the range observed for natural black smoker fields of $3\times10^3\mathrm{m}^2$ to $1\times10^5\mathrm{m}^2$ (Lowell et al., 1995). The great surprise from our calculations is that downflow is maximized in concentric, tube-shaped regions directly surrounding the upflow plumes (figure 4.2a-c). Fluids in these regions of enhanced downflow have temperatures ranging from of 100°C to as high as 300°C. At a radius of less than twice that of the upflow zone, the downward mass flux reaches values 5 times larger than the average downward mass flux and becomes about half the value of the maximum upward mass flux. At 500m depth, the integrated upward mass flux through the whole model is approximately 800 kg/s, which implies $\sim$200kg/s per kilometer of ridge segment and $\sim$100kg/s per vent field. Roughly 2/3 of this mass is provided by downflow in the warm, near-axial, regions and only 1/3 comes from further off-axial regions. The fact that downflowing fluids are relatively warm (up to 300°C) implies that substantial recirculation of heat occurs. In fact, roughly one quarter of the heat traveling upwards is lost conductively to the adjacent downflow zones, in which it is recirculated back to the bottom. This recirculation process therefore controls the thermal structure of the downflow zone, heating it to average temperatures of $\sim$ 200°C. Darcy fluxes in the system are $\sim 5.0\times10^{-6}$m/s in the upflow zone and $\sim 0.75\times10^{-6}$m/s in the surrounding, near-axial downflow zone. By converting these values to actual pore velocities, the residence time of a fluid particle which enters the system close to a discharge area and travels to the base of the hydrothermal convection cell and up again, can be estimated to be as low as three years. This estimate is in good agreement with recent estimates from studies using natural radionuclide tracers (Kadko and Butterfield, 1998; Kadko et al., 2007).

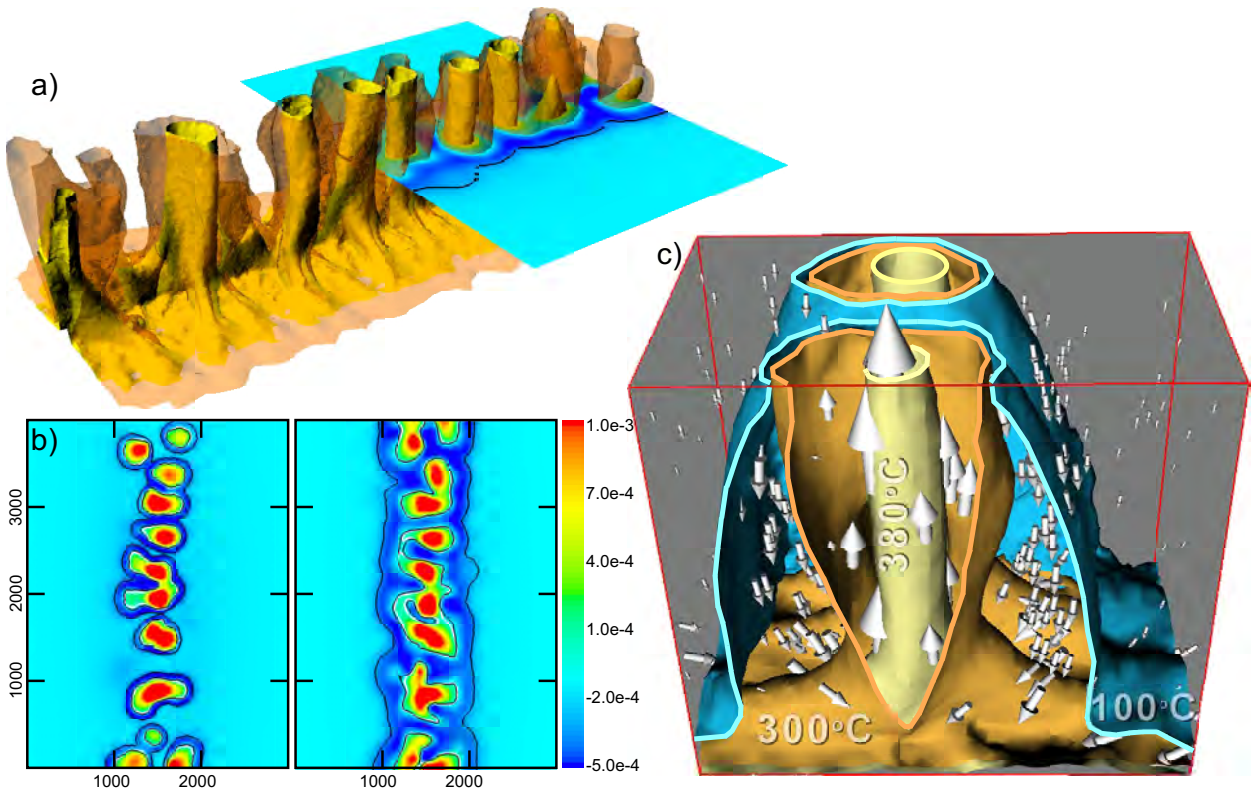

Fig. 4.2: Thermal and fluid flow structure of simulation after ∼100 years. Figure a) shows the 3D contours of the 300°C (transparent) and 380°C (yellow) isotherms. The horizontal cross-section plots vertical mass fluxes. b) Mass fluxes [kg $m^{-2}s^{-1}$] through horizontal cross-sections at 100 and 500 meter depth. Thin black lines plot the 100°C and 300°C isotherms and the white line separates up-flow from down-flowing regions. c) Cross-section through thermal plume, plotting 100°C (blue), 300°C (brown) and 380°C (yellow) isotherms as well as mass fluxes (arrows). High-hydraulic downflow zones between the 100°C and 300°C isotherms are clearly visualized.

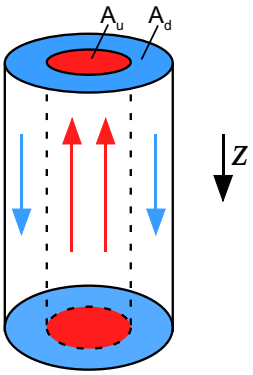

Fig. 4.3: Simplified pipe-model used for analytical conceptualization of numerical results.

4.5 Mathematical Analysis

The simulation showed that recharge is concentrated in a narrow concentric zone surrounding a pipe-like upflow zone. This characteristic structure has not been reported before and poses the question why systems evolve this way. Some insight can be gained by analyzing how the pressure (p) gradient settles in a simplified geometry, controlled by the non-linearity of the fluid properties. In the near-axial region, the vertical pressure gradient will have a value between cold and hot hydrostatic, such that cold fluids can be brought downwards and hot fluids can be brought upwards. In a first approximation, we assume that recharge is limited to a region directly surrounding a pipe-shaped upflow zone (figure 4.3). We can now write the mass balance between up- and down-flowing water:

$$A_u \rho_u \frac{k_u}{\mu_u} \left[\frac{\partial p}{\partial z} - \rho_u \mathbf{g} \right] = A_d \rho_d \frac{k_d}{\mu_d} \left[\rho_d \mathbf{g} - \frac{\partial p}{\partial z} \right] \tag{4.1}$$

Here, A_u is the cross-sectional area of the upflow zone and A_d the cross-sectional area of the downflow zone. Subscripts u and d indicate properties of the upwelling and the downwelling fluid respectively and $\mathbf{g}$ is the acceleration due to gravity in the direction of z (see figure 4.3). Equation 4.1 assumes that horizontal pressure gradients between up- and downflow areas can be neglected. This assumption can be made since in the axial region, fluid flow is dominantly vertical (up or down), which implies that horizontal pressure gradients are negligible compared to the vertical component. By re-ordering equation 4.1, we find the following expression for the vertical pressure-gradient:

$$\frac{\partial p}{\partial z} = \left[\rho_u + (\rho_d - \rho_u) \frac{1}{\gamma \frac{\mu_d \rho_u}{\mu_u \rho_d} + 1} \right] \mathbf{g} \tag{4.2}$$

Here γ is the ratio $A_u k_u / A_d k_d$ and, physically, the product $\gamma \frac{\mu_d \rho_u}{\mu_u \rho_d}$ can be seen as the ratio of the resistance against flow of the downflow region versus the upflow region and, depending on pressure and temperature, can have values from $0.1 \times \gamma$ to $10 \times \gamma$. We can express the net upward energy transported through the pipe model as:

$$Q = A_u \left[h_u - h_d \right] \rho_u \frac{k}{\mu_u} \left[\frac{\partial p}{\partial z} - \rho_u \mathbf{g} \right] \tag{4.3}$$

where h is the specific enthalpy of the fluid. In a first approximation, γ can be taken as 1 since k is homogeneous ($k_d = k_u$) and the area of upflow is roughly the same as the area of

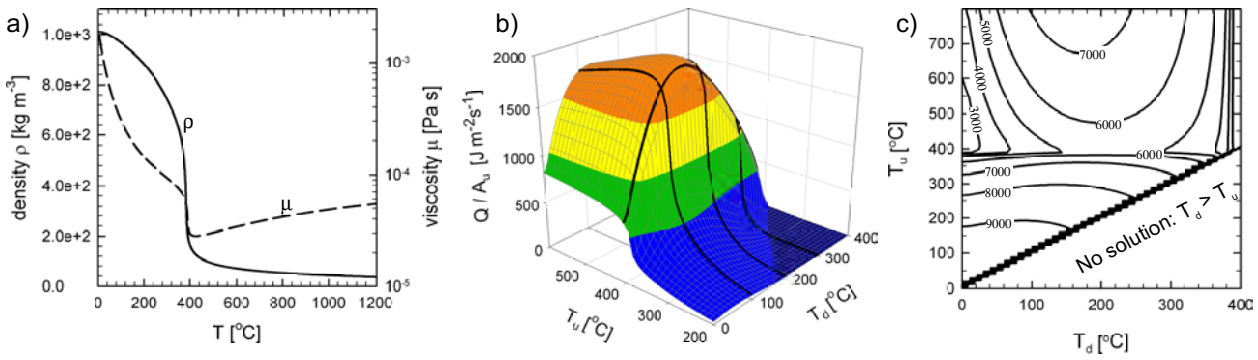

Fig. 4.4: (a) Density (solid) and viscosity (dashed) as function of temperature at 30MPa. (b) Upward energy (Q) normalized to the upflow width A_u plotted against upwelling and downwelling temperatures (equation 4.3). Solid black lines follow contours at $T_d = 100°C$, $T_d = 200°C$, $T_d = 300°C$ and $T_u = 400°C$. (c) Vertical pressure gradient plotted against upwelling and downwelling temperatures (equation 4.2)

.

increased downflow (see figure 4.2b).

4.6 Conceptualization

Figure 4.4a shows that heating water from 10°C to 200°C decreases its viscosity (μ) by approximately one order of magnitude whereas the density (ρ) changes by only about 10%. As a consequence, 200°C fluids can be brought downward highly efficiently: The greatly reduced viscosity makes them very mobile, while their only weakly decreased density maintains a substantial downward buoyancy force compared to the upflow zone. Heating the fluid to even higher temperatures would cause the density to decrease substantially and hence lower the downward buoyancy force. This indicates that at temperatures of around 200°C the downward mass flux can be optimized.

Figure 4.4b plots Q normalized to the surface area of the upflow zone, against temperatures of the up-flowing and down-flowing fluid using $\gamma = 1$ and $k = 5.0 \times 10^{-14}\text{m}^2$. It shows that energy transport is maximized when upflowing water reaches temperatures of $\sim$ 400°C and downflowing water is $\sim$ 200°C, exactly like the thermal structure observed in the numerical simulations. The thermal structure of the numerical simulations featured enhanced downflow for fluids in the temperature range $100 - 300$°C, which neatly fits with the peak of maximum heat transport in figure 4.4b. At these conditions, the vertical pressure gradient given by equation 4.2 is $\sim$ 6000Pa/m (figure 4.4c), which is in good agreement with simulation results. If the upflow temperature is either higher or lower than $\sim$ 400°C, then the pressure gradient goes to larger values (figure 4.4c), because the resistance of the upflowing fluid is increased. Similarly, the resistance of the downflow zone increases if its temperature is either larger or smaller than $\sim$ 200°C. Cooling a $\sim$ 200°C fluid will increase its viscosity more rapidly than its density, whereas heating a $\sim$ 200°C fluid will decrease its density faster than its viscosity (see figure 4.4a). Both effects result in a larger hydraulic resistance of the fluid. This analysis shows that the convection cells operate in a state of least hydraulic resistance.

Convection cells evolve towards, and remain in, this state of least resistance by counter-

acting feedback mechanisms which self-regulate the flow in convection cells. For instance, increasing resistance by cooling the downflow zone to temperatures lower than $\sim$ 200°C slows down the fluid flow through the system. This reduced flow increases conductive heat losses from the upflow area, heating up the downflow area again to temperatures of $\sim$ 200°C. Furthermore, the upflow temperature cannot become hotter than $\sim$ 400°C (Jupp and Schultz, 2000). Therefore if, due to external forces, convection stagnates, the boundary layer between magma chamber and hydrothermal cell will broaden but upflow temperatures will stay at $\sim$ 400°C.

4.7 Discussion

In summary, our 3D simulations indicate that convection cells operate in a state of least resistance, which maximizes mass and therefore energy transport through the system. Narrow pipe-like upflow regions can efficiently heat surrounding areas, creating downflow corridors of high hydraulic conductivity. The upflow zone loses substantial amounts of heat to the downflow zone, but by doing so the mass flux is increased over-proportionally such that overall energy transport is raised.

Previous studies indicated that black smoker systems could well be operating in a state of maximum energy transport (Busse and Joseph, 1972; Wilcock, 1998). For instance, the observation that black smoker vent fields are often close to but never higher than $\sim$ 400°C can be explained with convection cells operating at maximum energy transport (Jupp and Schultz, 2000). Indeed, many complex systems, as different as the Earth's climate and the growth of crystals, tend to organize themselves in such a state if permitted by their circumstances (Dewar, 2003; Lorenz, 2003). Our study supports the theory that black smokers operate in a state of maximum energy transport and clarifies its consequences for three-dimensional thermal and flow structure of convection cells.

Another distinct feature of natural mid-ocean ridge systems is the regular spacing between black smoker fields. This observation has often been explained with a slot-convection model in which convection dominantly takes place in a high-permeability axial plane and therefore could be considered a 2 dimensional system (Coumou et al., 2006). Our simulations prove that this restriction is not required and that, at high heat flux conditions, convection naturally forms individual black smoker fields at regular spacing. This shows that the non-linear temperature-pressure dependence of the fluid's properties is a first-order control on the thermal and flow structure of convection cells in these systems.

The Main Endeavour field on the Juan de Fuca ridge, with an estimated heat production of 364 ± 73MW (Ginster et al., 1994) over a few kilometers ridge length (the full ridge segment of 10km has an estimated heat output of 1700 ± 1100MW (Baker and Massoth, 1987)), appears to be a natural example closely matching our simulation results. Here, regularly spaced vent fields, with black smokers venting fluids close to 400°C, have been active for several years (Van Ark et al., 2007; Glickson et al., 2007). Moreover, magnetic anomaly data show that upflow zones are narrow pipe-like structures which reach at least to a few hundreds of meters depth and possibly to the base of the hydrothermal system (Tivey and Johnson, 2002). This finding, and the size and distance between magnetic anomalies expressed at the seafloor, closely resemble our simulation results.

4.7.1 Hydrologic tracer tests

Drilling an active seafloor-spreading center has been a long-standing goal of scientific ocean drilling (Fisher, 2005) and would, apart from in situ observations, permit pressure tests and hole-to-hole or hole-to-smoker tracer tests. Successful tracer tests, however, require some pre-drilling knowledge of the subseafloor flow regime. In sedimented systems, local outcrops of basaltic crust form likely recharge and discharge sites (Fisher et al., 2003a,b) and are therefore logical drilling targets. Unsedimented systems lack such structurally defined intake points and hence recharge could potentially occur anywhere along, or many kilometers away from the ridge. Our simulations provide the first quantitative prediction that recharge is likely to occur close to the vent fields. Fluids entering the oceanic crust here flow all the way down to the base of the hydrothermal cell and have an expected residence time of as little as a few years, making tracer tests seem possible in an acceptable time frame. The optimal location for tracer injection therefore seems to be at a small radial distance outward from the edge of the much easier-to-map outflow zone, though this prediction should be further refined for a specific site. Such tests could provide unique and critical data on permeability, porosity and flow paths which could be used again to fine-tune more detailed and sophisticated numerical models. In our opinion, the Main Endeavour field would be the prime candidate for such an experiment, owing to its regular geometry and relatively simple tectonics.

4.7.2 Sulfide deposits

One major implication of this work relates to the chemical alteration of the oceanic crust and associated massive sulfide ore formation. These mineral deposits form by leaching of new basaltic crust by convecting seawater and re-precipitation of metals as sulfide minerals when the fluid is quenched at the outflow points in fields of active black smokers. The solubility of ore metals such as iron, zinc and copper increases almost exponentially with temperature (Hemley et al., 1992). Our simulations indicate that the average temperature of fluid-rock interaction is much higher than would be expected from dispersed seawater infiltration across the spreading axis (Franklin et al., 2005). As a result of the higher temperature, solubility-limited leaching is expected to be significantly more effective. Conversely, a smaller volume of rock immediately surrounding the smoker field is leached at any one time. However, using average copper content in mid-ocean ridge basalt of 25ppm, a typical seafloor sulfide deposit of 0.2 million tonnes with 3% Cu (Hannington et al., 1995) can be formed by leaching the upflow zone and its immediate surrounding only. The large Cu solubility due to the high temperature in these regions (i.e. $\sim 10^{-7}$mol/kg at 200° and $\sim 4 \times 10^{-4}$mol/kg at 350°) ensures that the rock is quickly leached and deposits can form within a period of 100-1,000 years.

In summary, our mathematical analysis shows that unexpectedly focussed hydrothermal fluid flow at mid-oceanic ridges results from the non-linear dependence of the fluid properties on pressure and temperature. In particular, we demonstrate that zones of high hydraulic conductivity can form even in rock media of constant and homogenous permeability, as a direct consequence of such non-linearities. These results are generic, and thus have broader implications for other fluid flow environments where non-linear fluid properties are commonly neglected in hydraulic studies. These include continental ore-forming systems, active volcanoes, geothermal reservoirs, and possibly CO_2 sequestration and enhanced oil recovery

from sedimentary basins.

[0] **Methods** In this study we boosted computational power by applying parallel computing techniques as described in chapter 3 which were recently implemented in the multi-physics code CSMP++ (Matthai et al., 2007). These techniques allow the usage of many processors calculating simultaneously on one simulation. Figure 4.1 shows how the global domain is divided in a number of sub-domains, each being assigned to a single processor. The calculation time still took several weeks using 16 processors.

The numerical method combines finite element and finite volume techniques which achieve accurate results in advection dominated problems (Paluszny et al., 2007) and is computationally efficient (Geiger et al., 2006a). The diffusive and advective terms of the conservation equations are solved sequentially. The finite element method is employed for the diffusive parts and the finite volume method for the advective parts (Geiger et al., 2006a).

5. HIGH-RESOLUTION 3D SIMULATIONS OF MID-OCEAN RIDGE HYDROTHERMAL SYSTEMS

5.1 Abstract

High-resolution numerical simulations give clear insights into the 3D structure of thermal convection associated with black-smoker hydrothermal systems. We present a series of simulations that show that, at heat fluxes expected at mid-ocean ridge spreading axes, upflow is focussed in circular, pipe-like regions, with the bulk of the recharge taking place in the near-axial region. Recharging fluids have relatively warm temperatures. In this configuration, the system maximizes its heat output, which can be shown to be linked to the non-linearity in the fluid properties. Further, we present a series of simulation with different permeability scenarios. These show that when the permeability contrasts are moderate, convection maintains this pipe-like fluid flow structure. For sharp permeability-contrasts upflow is focussed in high permeability regions and downflow in low permeability regions. Another feature of our simulations is that at early stages of convection, diffusive vent styles can emerge, which look remarkably similar to diffuse vent fields in natural systems. Finally, simulations in which permeability is defined as a function of temperature indicate that the brittle-ductile condition is likely to occur at temperatures not lower than 650°C. At lower brittle-ductile transition temperatures, the system cannot remove the heat delivered from the magma chamber and vent temperatures are substantially lower than 400°C. We discuss a number of implications for black-smoker systems based on these results.

5.2 Introduction

Mid ocean ridge hydrothermal systems transport a significant part of the energy released by crystallization and cooling of the oceanic crust (Fisher, 2001). Magmatic heat sources at depths of less than one to a few kilometers below the seafloor drive convection of seawater, with venting occurring at black-smoker fields located near the axial spreading center. Two key observations constrain the sub-seafloor thermal cell structure: (1) Measured venting temperatures are never substantially higher than ∼400°C (Jupp and Schultz, 2000) and (2) venting occurs in focused regions (active black-smoker fields) separated by regions of inactivity (Lowell et al., 1995; Lowell and Germanovich, 2005). The first observation is remarkable since inferred magmatic temperatures are around 1200°C. The second observation has led to the suggestion that convection is mainly 2-dimensional in the axial plane, so-called slot-convection. In this paper, we argue that both observations can be explained by sub-seafloor 3D convection-cell structures operating at maximum energy transport.

Early numerical studies of black-smoker systems used simplified fluid properties, with viscosity assumed constant and density varying linearly with temperature (Rosenberg et al.,

1993; Cherkaoui and Wilcock, 1999; Schoofs and Hansen, 2000). In addition to these simplified fluid properties, the fluid was often assumed to be incompressible, with density variations only accounted for in the buoyancy term (Boussinesq approximation). Although these studies contributed considerably to our understanding of fluid flow in the oceanic crust, other numerical studies showed that this approach is deficient when dealing with high-temperature convection systems (Straus and Schubert, 1977; Jupp and Schultz, 2000, 2004; Coumou et al., 2006).

Some recent numerical studies included real fluid properties in their simulations which resulted in a number of important insights into the physics of black-smoker convection systems (Ingebritsen and Hayba, 1994; Jupp and Schultz, 2000, 2004; Coumou et al., 2006; Fontaine and Wilcock, 2007). Ingebritsen and Hayba (1994) showed that convection cells operating near the critical point of water (21 MPa, 374°C) can transport energy much more rapidly than pure water convection cells operating at any other pressure-temperature conditions. Seawater, in contrast to pure water, can undergo phase separation at higher than critical pressures which complicates the thermodynamics of black-smoker systems. It is clear, however, that most of them operate near the critical point of seawater of 29.8 MPa and 407°C, (Von Damm et al., 2003) and are therefore likely to be able to transport energy efficiently. Following up on these results, Jupp and Schultz (2000, 2004) argued that the non-linear thermodynamics of water can explain why vent temperatures are close to 400°C. In a recent paper, we showed that, in addition to realistic fluid properties, the usage of high-resolution meshes and second-order accurate advection schemes is key to capturing the dynamical features of convection (Coumou et al. (2006), chapter 2). At permeabilities exceeding $10^{-15}\mathrm{m}^2$, convection is unstable, thermal plumes can split on their way to the seafloor and venting temperatures can oscillate on timescales ranging from years to centuries. Fontaine and Wilcock (2007) confirmed these dynamic features and pointed out that downflow areas can become relatively warm, commonly exceeding 150°C.

Realistic numerical studies in 3D have been hampered by a lack of available computational power. Previous studies investigating 3D hydrothermal convection at mid ocean ridges assumed incompressible fluids and low permeability values ($< 10^{-15}\mathrm{m}^2$, i.e. Travis et al. (1991); Rabinowicz et al. (1998, 1999)), greatly reducing computational requirements. Rabinowicz et al. (1998) studied single phase fluid circulation, including non-linearities in the fluid properties, at sediment hosted ridges where permeability is expected to be much lower than at more common un-sedimented ridges. Higher permeabilities and the usage of compressible fluids can substantially increase computational requirements since, depending on the numerical method, computational timesteps can become very small. More problematic is the necessity to use high-resolution meshes when modeling high-permeability systems (i.e. Coumou et al. (2006), chapter 2). To achieve the same resolution in 3D, the size of a mesh increases by 1 to 2 orders of magnitude compared to a 2D mesh. This massive increase makes 3D simulation of these systems, using standard single-processor numerical techniques, practically impossible.

In this study, we use parallel computing techniques (see Coumou et al. (2008), chapter 3) to boost computational power to simulate hydrothermal convection in 3D, using high-resolution meshes and real properties of compressible fluids. We present simulations of 3D box-shaped models, consisting of several million elements, solved using 16 processors. We constrain the permeability to best fit observations at mid-ocean ridges. We next run a series of simulations investigating hydrothermal convection in 3D with different permeability

scenarios.

5.3 Model Setup

5.3.1 Equation of state and governing equations

By assuming that the fluid is pure water and by taking pressures larger than the critical-point of water (22.1MPa), we ensure that the fluid is in the single phase regime. This assumption substantially reduces the complexity of the problem, allowing the energy equation to be written into a temperature (T) formulation (Geiger, 2004; Lowell and Germanovich, 2005; Coumou et al., 2006):

$$(\phi\rho_f c_{pf} + (1-\phi)\rho_r c_{pr})\frac{\partial T}{\partial t} = \nabla \mathrm{K} \nabla T - \nabla \cdot (\rho_f c_{pf} \mathbf{v} T) \tag{5.1}$$

Here, ϕ is the porosity, $\mathbf{v}$ the Darcy velocity (Bear, 1972) and ρ and c_p stand for density and heat capacity respectively, with the subscripts f and r referring to fluid and rock. The pressure equation is solved decoupled from the energy equation, with the thermal expansion term entering as a source term into the pressure (p) equation:

$$\phi\rho_f\beta_f\frac{\partial p}{\partial t} = \nabla \cdot \left(\frac{k}{\mu_f}(\nabla p - \rho_f \mathbf{g})\rho_f\right) + \phi\rho_f\alpha_f\frac{\partial T}{\partial t} \tag{5.2}$$

Here, α_f is the fluid expansivity, β_f its compressibility, μ_f its viscosity and $\mathbf{g}$ the gravitational acceleration. Properties of pure water at supercritical conditions vary non-linearly and over several orders of magnitude with changing pressure and temperature. The fluid properties, ρ_f, μ_f, α_f, β_f and c_{pf} are obtained using lookup tables based upon the pure water equation of state by Haar et al. (1984). Equations 5.1 and 5.2 are solved using a finite-element finite-volume method (FE-FV), in which advective parts of the equations are solved using the finite-volume method and diffusive parts using the finite-element method. The exact details of this scheme have been described in previous publications (Geiger et al., 2004, 2006a; Coumou et al., 2006).

5.3.2 Model dimensions

We solve equations (1) and (2) within a 3 dimensional, box-shaped domain extending 4km in the along-axis direction and 3km in the across-axis direction with a height of 1km (Figure 5.1). We tested the validity of the 4km along-axis dimension with a number of 2D along-axis simulations. These showed that if $\mathrm{k} > 10^{-15}\mathrm{m}^2$, the aspect ratio, i.e. the horizontal dimension divided by the vertical dimension of a single convection cell, becomes sufficiently small such that the vertical boundaries do not influence the solution. The axial plane is located in the center of the model, resulting in an off-axis extent of 1500m in both directions. This should be sufficient since observed axial magma chambers typically have an across-axis dimension of 500m on either side.

5.3.3 Discretization

The model domain is discretized using irregularly sized tetrahedron elements (Paluszny et al., 2007), with the resolution of the mesh increasing towards the axial center (Figure 5.1). To

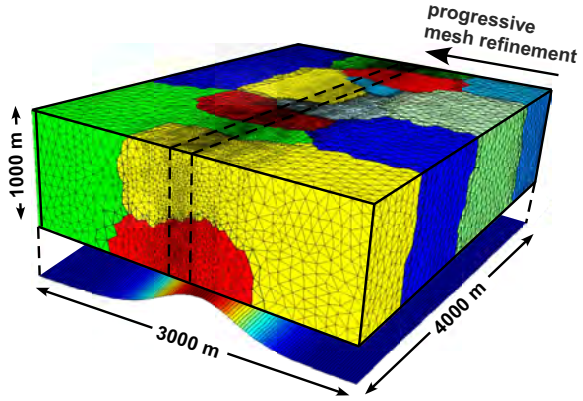

Fig. 5.1: 3D mesh consisting of 2.5 M tetrahedron elements. Resolution is refined towards the axial center and colors indicate computational domains assigned to separate processors. At the bottom boundary the bellshaped form of the heat flux profile is plotted.

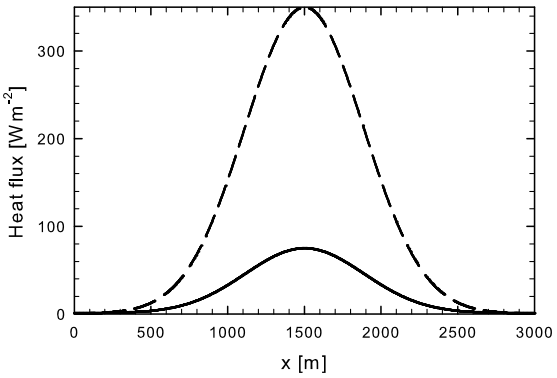

Fig. 5.2: 350MW km^{-1} (dashed) and 75MW km^{-1} (solid) heat flux curves versus off-axis distance.

capture the true dynamics of transient thermal convection systems, high-resolution meshes and second-order accurate transport schemes are required (Coumou et al., 2006; Fontaine and Wilcock, 2007). Therefore, we ensure that in the central region of our 3D models, the resolution of the mesh is similar to the resolution found to be sufficiently fine in 2D models described in chapter 2. This implies node-to-node distances of roughly 20 m. In the across-axis direction, the mesh-resolution is gradually relaxed, resulting in a mesh consisting of 2.5 M tetrahedron elements (Figure 5.1). Figure 5.1 shows the partitioning of the global domain into 16 sub-domains, each one assigned to a single processor. We employ parallel computing techniques as described in detail in chapter 3 (Coumou et al., 2008). The use of this high-performance processing power was absolutely essential for calculating these simulations within an acceptable time frame. Typically, with 16 processors it took two weeks to calculate $\sim$ 150 years of convection, whereas on a single processor, expected computation time would have been at least half a year.

5.3.4 Boundary conditions

The top boundary represents the seafloor at roughly 2.5 km water depth resulting in a constant pressure of $p = 25$MPa. Fluids are free to enter and leave the model via the top boundary, all other edges are no-flow boundaries. To allow hot fluids to vent, we use a mixed thermal boundary condition at the top. In elements along the top boundary experiencing upflow, the vertical temperature gradient is set to zero, elements experiencing downflow take in 10°C water. At the bottom boundary, the system is heated by a fixed heat flux. This

is physically more realistic than a constant-temperature boundary condition since the latter essentially assumes that an infinite amount of heat can be transport into the system. The total bottom heat flux is constrained by the amount of basalt that crystallizes and cools, which is directly dependent on the spreading rate. Such an estimate gives values ranging from 10 to ∼120 MW per kilometer of ridge axis (Fisher, 2001). However, direct measurement from vent fields and ridge segments indicate a much higher heat output, implying that magma supply is episodic and local (Baker and Massoth, 1987; Ginster et al., 1994; Baker and Urabe, 1996; Ramondenc et al., 2006). We therefore decided to work with two heat fluxes: a moderate value of 75MW/km and a high heat flux value of 350MW/km. The 350MW/km heat flux is probably a better estimate for heat fluxes at systems on medium to fast spreading ridges like the Endeavour segment and 9°50'N and 13°-18°S areas on the East Pacific Rise. The heat flux is delivered in a bellshaped profile to the bottom of our model-domain with the peak at the axial center. The half-width of this function is taken as half the across-axial width of a typical magma-chamber (i.e. Sinton and Detrick (1992); Lowell and Germanovich (2005)) and the background heat flux is set to 1 W/m2 (figure 5.2).

5.4 Simulation Results

5.4.1 Permeability

In a first series of simulations we constrained the permeability (k) to such values that near-bottom temperature conditions fit expected temperature distributions of magmatic melt lenses. Several seismic studies have identified low-velocity zones at 1-2 km below spreading centers, interpreted to be (partly) molten magmatic lenses, stretching over several kilometers along-axis (Singh et al., 1998; Kent et al., 2000; Dunn et al., 2000). The occurrence of molten basaltic rock indicates temperatures close to 1200°C (Sinton and Detrick, 1992). This observation can be used to constrain the permeability since heat flux and bottom temperatures of ∼1200°C can only be combined within a small permeability range (Cathles, 2007: personal communication). At higher permeabilities the hydrothermal system will cool the bottom layer more efficiently, resulting in lower bottom temperatures. On the other hand, if permeability is too low, the systems cannot remove heat efficiently and bottom temperatures will rise to unrealistically high values. Figure 5.3 explains this principle in more detail, plotting the temperature at the bottom of the model for slightly different permeabilities with heat fluxes of 75MW/km and 350MW/km. Figures 5.3c shows that, for a 350MW/km heat flux and a permeability of $5\times10^{-14}\mathrm{m}^2$, only a very few bottom nodes reach 1200°C. When permeability is decreased by only a small factor, i.e. to $3\times10^{-14}\mathrm{m}^2$, large areas appear where the temperature is 1200°C or higher (Figure 5.3d). Likewise, for the 75MW/km models, a similar permeability range is observed, but permeabilities are smaller due to the lower heat flux applied (Figure 5.3a and b).

5.4.2 Low heat flux

First, we investigate 3D thermal convection at a relatively low heat flux value of 75MW per km of ridge axis. For a homogeneous permeability, $k = 1.0e-14\mathrm{m}^2$, a near-steady-state upflow region develops along the full length of the ridge (see Figure 5.4a and b). Here, upwelling fluids have a moderate temperature of $\sim$ 300°C. Fluid flow is dominantly across-axis, with recharge occurring away from the axis and discharge occurring along the

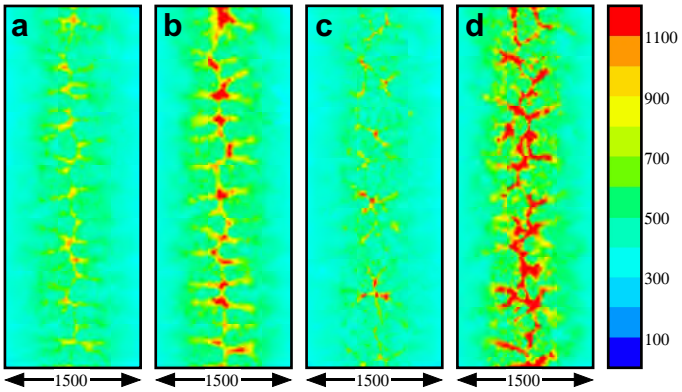

Fig. 5.3: Bottom temperatures in the axial region for models with different (homogeneous) permeability-heat flux combinations: (a) q = 75MW km^{-1} and k = 1×10^{-14}m^2 after 660 years (b) q = 75MW km^{-1} and k = 0.75×10^{-14}m^2 after 660 years (c) q = 350MW km^{-1} and k = 5×10^{-14}m^2 after 150 years and (d) q = 350MW km^{-1} and k = 3×10^{-14}m^2 after 150 years

full length of the axial center. Only if we increase k in the near-axial region do separate vent areas develop (see Figure 5.4c and d). In this example, k is increased by an order of magnitude within a 100m wide corridor along the axis. At the bottom boundary, the highest temperatures are now reached at the edges of the high-permeability layer instead of at the axial center (see Figure 5.4c). Rapid fluid flow within the permeable layer cools the bottom boundary much more efficiently, limiting the bottom-boundary temperatures in the near axial region. As a result, thermal plumes develop not at the axial center but slightly off-axis (see Figure 5.4c and d). Plumes merge close to the top boundary, resulting in regularly spaced discharge areas along the axial center with a spacing of $\sim$ 500m.

5.4.3 High heat flux

Homogeneous permeability

Figure 5.5 shows the thermal structure of simulations with a high heat flux (350MW/km) with homogeneous permeabilities of respectively 3.0e-14 and 5.0e-14 m2. Both simulations show that at these high heat flux conditions, upflow naturally forms into circular, near-vertical, pipelike regions. Thermal instabilities form away from the axis near the bottom boundary (Figure 5.5a and c) and travel towards the main upflow regions at the axis. This results in sub-horizontal tube-like structures in which hot fluids flow along the bottom boundary towards the axis (5.5b and d). Adjacent to these features, cold fluid flows downward which is expressed in the rhythmic depressions of the isotherm in Figures 5.5b and d. At the axis, the fluids reach temperatures of $\sim$400°C and move upwards in circular, pipe-like discharge regions. At the top boundary, fluids discharge in regions with an average diameter of $\sim$250m. Directly outside these upflow regions, fluids of moderate temperature flow downward at an increasing rate. This is explained in more detail in Figure 5.6, shows the vertical mass flux through horizontal cross-sections at different depths. Directly adjacent to the discharge areas, downflow through the top surface is maximized, as expressed by the dark blue regions in the left-hand plots of Figure 5.6. Further away from the axis, the mag-

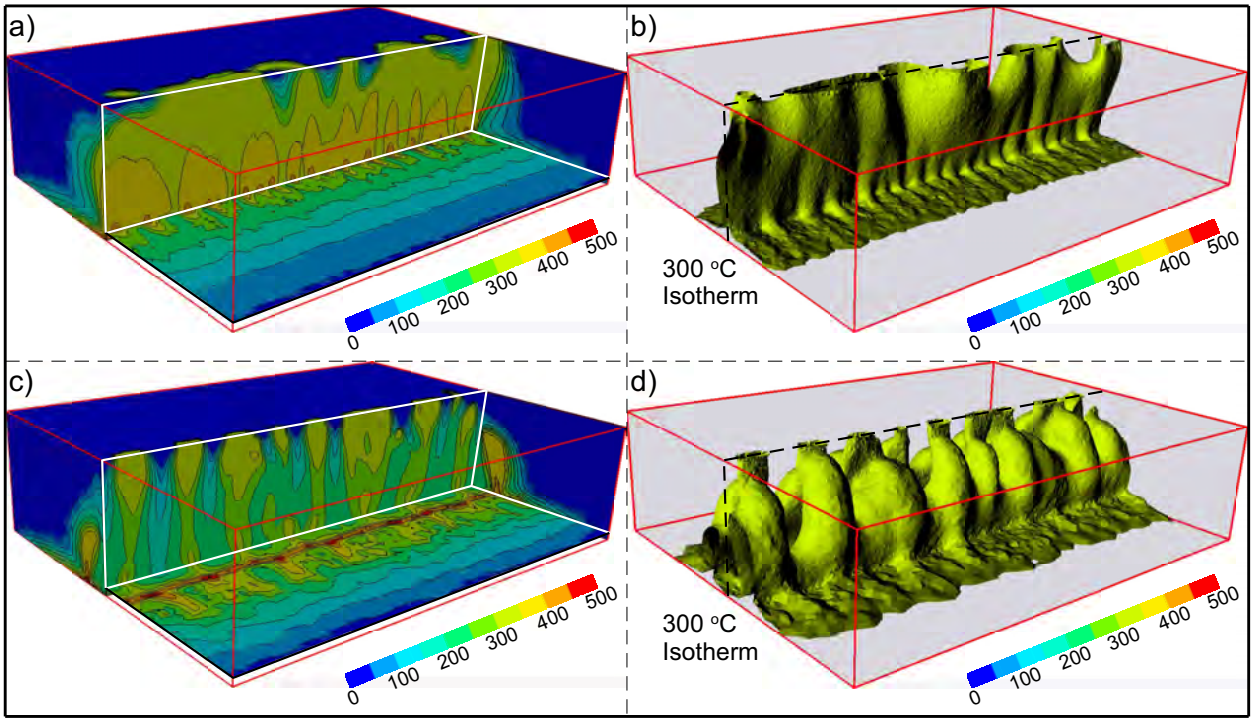

Fig. 5.4: Thermal structure of homogeneous permeability simulations with a 75MW/km heat flux. Figure a) shows cross-sections plotting isotherms every 50°C, figure b) shows the 300°C isotherm, both from a simulation with $k = 1.0 \times 10^{-14}\mathrm{m}^2$ after 660 years. Figures c) and d) plot the same results for a simulation with a 100m thick axial plain having a permeability of $k = 1.0 \times 10^{-13}\mathrm{m}^2$ in the center after 330 years.

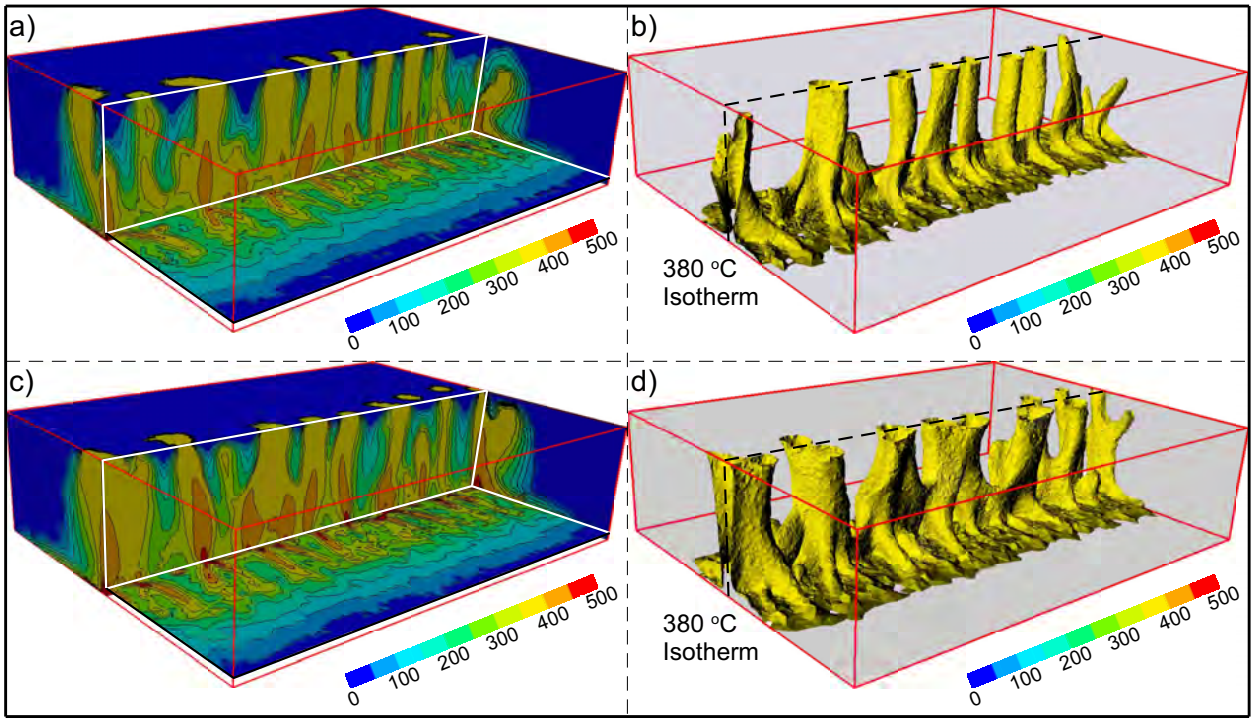

Fig. 5.5: Thermal structure of homogeneous permeability simulations with a 350MW/km heat flux after ∼120 years. Figure a) shows cross-sections plotting isotherms every 50°C, Figure b) shows the 380°C isotherm, both from a simulation with $k = 5.0 \times 10^{-14}\text{m}^2$. Figures c) and d) plot the same results for a simulation with $k = 3.0 \times 10^{-14}\text{m}^2$.

nitude of downflow decreases. The same pattern of increased downflow directly surrounding the upflowing regions, is observed in the horizontal cross-sections at 100m, 500m and 900m depth. Fluids in these regions have temperatures between 100°C and 300°C, as shown by the isotherms plotted in Figure 5.6. The 300°C isotherm also more or less overlaps the white line separating up and down flowing regions, indicating that fluids of 300°C are close to neutral buoyancy. Figure 5.7 plots the average recharge through the top boundary of the two homogeneous permeability models as a function of off-axial distance, reflecting the increased recharge close to the axis.

Heterogeneous permeability

Next to homogeneous permeability models, a series of simulations was done with different heterogeneous permeability structures. The permeability structure of these simulations as a function of off-axial distance is plotted in Figure 5.8. Figure 5.9 plots the thermal structures of these simulations when convection is fully evolved. With increasing average permeability values in the model, near bottom temperatures become smaller, reflecting the more efficient removal of heat from the bottom. Upflow zones in the simulation using permeability model 1, which has the largest average permeability, therefore become less hot and hardly reach 380°C (Figure 5.9b). In Figure 5.9 the permeability contrast increases from top to bottom, which results in the upflow zones becoming more and more aligned in the high-permeability region. In the simulation with the sharpest permeability contrast (curve 4 in Figure 5.8 and Figure 5.9g and h), upflow dominates in the axial plane and discharge occurs over nearly

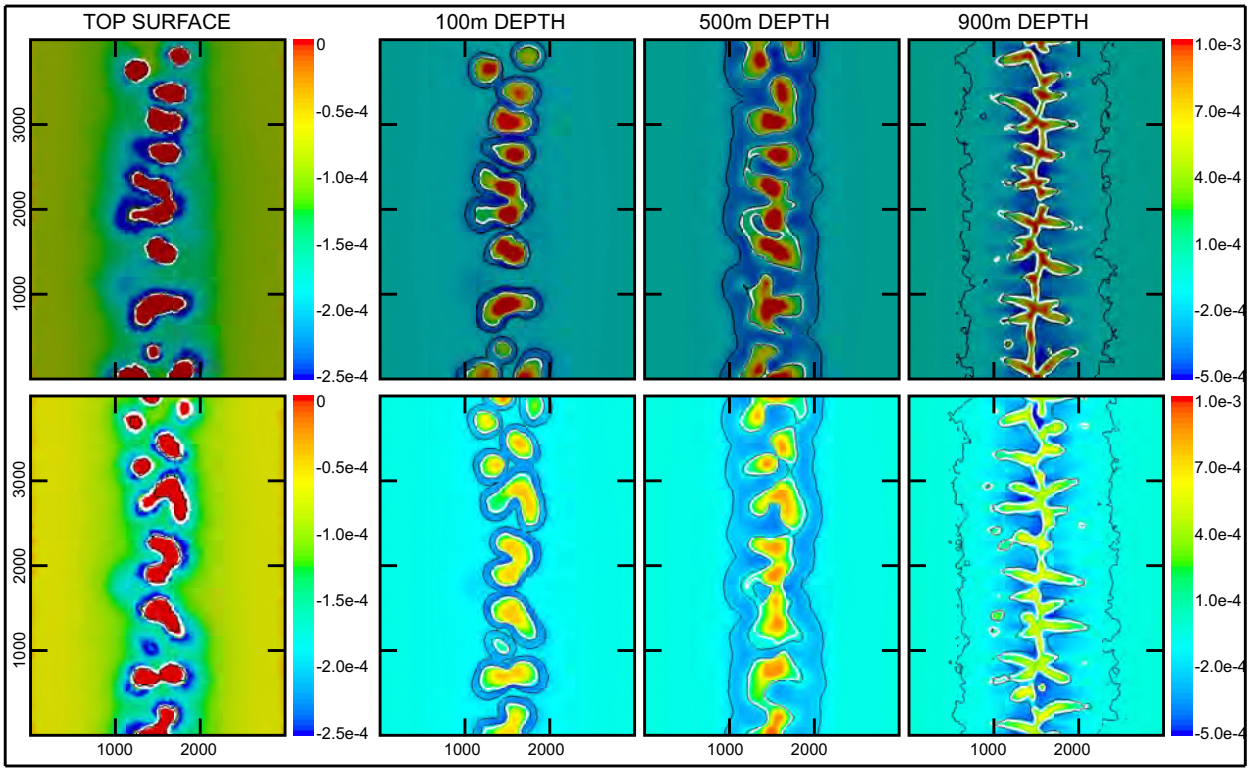

Fig. 5.6: Recharge through the top and vertical mass fluxes [kg $m^{-2}s^{-1}$] through horizontal sections at 100, 500 and 900m depth, for homogeneous permeability models with a heat flux of 350MW/km after ∼120 years. The two black lines represent the 100°C and 300°C isotherms. The top pictures were generated using a permeability of $k = 5.0 \times 10^{-14}m^2$. The bottom pictures were generated using a permeability of $k = 3.0 \times 10^{-14}m^2$. Note the difference in scale between pictures on the left and the rest.

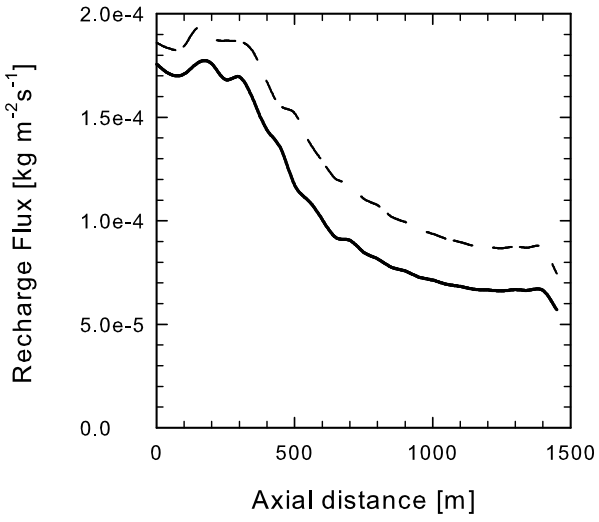

Fig. 5.7: Average recharge [kg $m^{-2}s^{-1}$] versus distance from the axis for homogeneous permeability models of $k = 3.0 \times 10^{-14}m^2$ (solid) and $k = 5.0 \times 10^{-14}m^2$ (dashed)

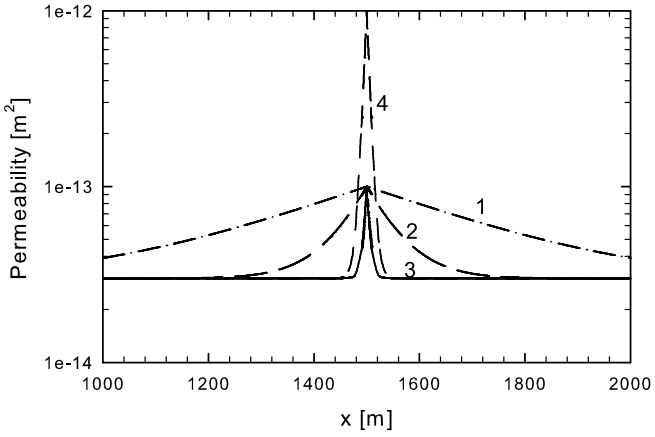

Fig. 5.8: Investigated permeability models with an increased permeability towards the axis.

the full length of the axial center with discharge temperatures close to 300°C (Figure 5.9g). When the permeability contrast is made progressively less sharp, the typical pipe-like upflow geometry appears again (Figure 5.9a and b). However, convection of the simulation with the sharpest permeability contrast (curve 4 in Figure 5.8) is not yet fully developed. The snapshot in Figure 5.9g and h depicts an intermediate stage through which all simulations pass: upflow zones have developed but downflow zones still have a low temperature. Further evolution of the system results in heating of the downflow zone and convective structures which are more similar to the pipe-like geometries observed in homogeneous systems.

Figure 5.10 shows the mass flux through horizontal cross-sections of models with an increased axial permeability. It shows that for moderate permeability contrasts, downward mass fluxes are maximized close to the axial plane, where the downward flowing fluids are heated to temperatures of 100°C to 300°C, just as in the homogeneous permeability cases. For progressively sharper permeability-contrasts, the fluid flow becomes more and more localized in the high-permeability plane, resulting in elongated discharge areas. In the simulation with the sharpest permeability contrast (curve 4 in Figure 5.8), downflow is maximized in the high-permeability region and downflow areas with temperatures between 100°C to 300°C are small. Further evolution of this system will likely lead to diffusive heat loss from upflow to downflow resulting in larger warm downflow areas.

Figure 5.11 plots the average recharge through the top of each of the heterogeneous permeability models. All models with a moderate permeability contrast (curves 1-3 in Figure 5.8) show increased recharge by heating of downflowing fluids to temperatures in the range 100°C to 300°C. Heating of downflowing fluids in the simulation with the sharpest permeability contrast (curve 4 in Figure 5.8) is very limited and therefore recharge depends on the permeability structure alone. This causes recharge through the top to be moderate everywhere away from the axis and peak sharply in the high-permeability zone at the axis itself.

In summary, we observe in our simulations a switch from a convective structure characterized by pipe-like upflow, with relatively warm downflow, at moderate permeability contrast to a convective structure where elongated upflow zones form in the high-permeability region, with downflow being relatively cold, at high permeability contrasts.

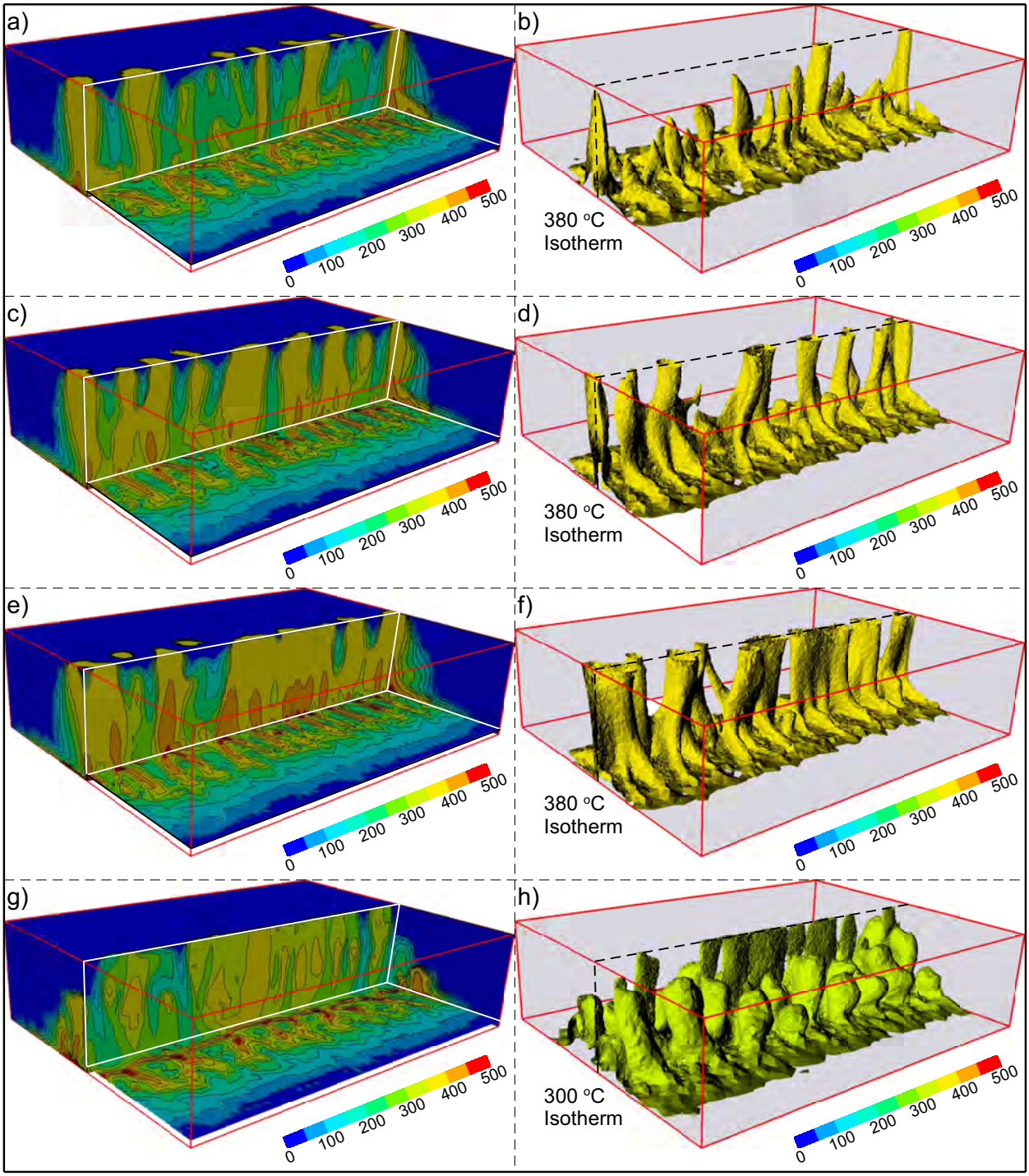

Fig. 5.9: Thermal structure of heterogeneous permeability simulations. Figure a) shows cross-sections plotting isotherms every 50°C, b) shows the 380°C isotherm using permeability profile 1 (see Figure 5.8) after ∼120 years. Figures (c)-(f) plot the same results for, respectively permeability profile 2 (c and d) and profile 3 (e and f). Figures g) and h) show simulation results using permeability profile 4 after 70 years. Note that in h) the 300°C isotherm is plotted.

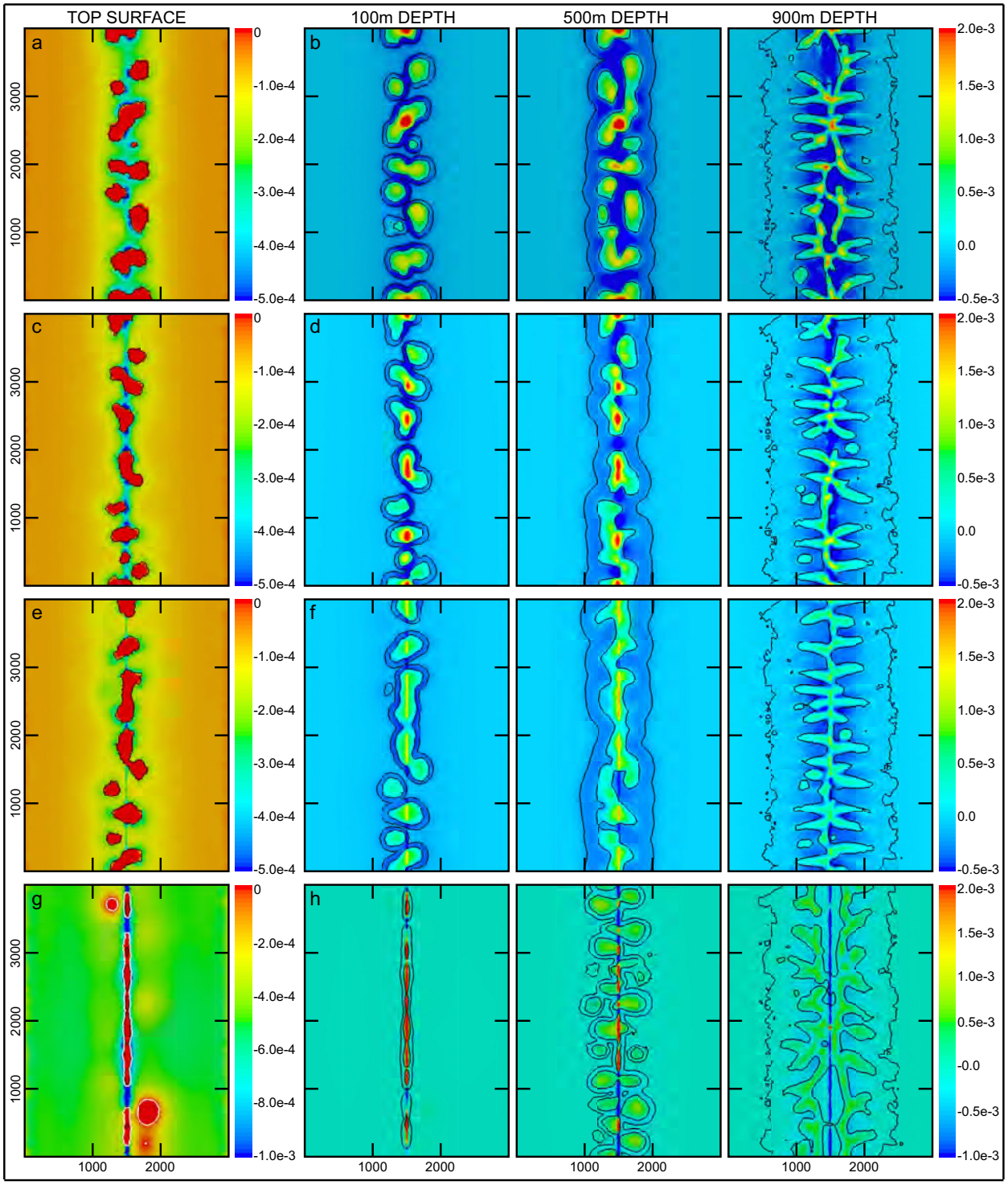

Fig. 5.10: Recharge through the top and vertical mass fluxes [kg $m^{-2}s^{-1}$] through horizontal sections at 100, 500 and 900m depth, for heterogeneous permeability models: Using permeability profile 1 (top row), permeability profile 2 (2^{nd} row), permeability profile 3 (3^{rd} row) and permeability profile 4 (4^{th} row). Figures a) to f) were generated after simulation time of ∼120 years. Figures g) and h) after a simulation time of 70 years. Note the difference in scale between pictures on the left-hand panels and the others.

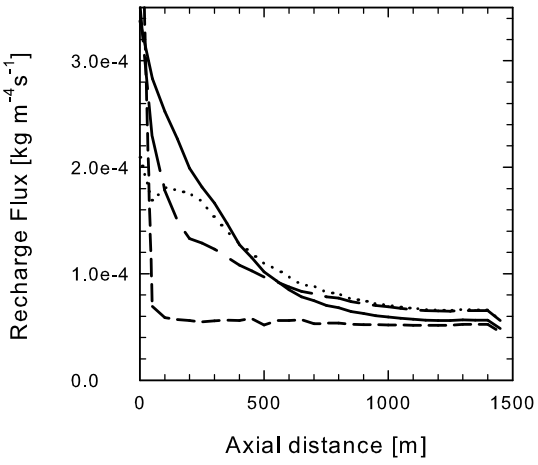

Fig. 5.11: Average recharge [kg $m^{-2}s^{-1}$] versus distance from the axis for heterogeneous permeability models. Using permeability profile 1 (solid line), permeability profile 2 (dashed line), permeability profile 3 (dotted line) and permeability profile 4 (short-dashed line).

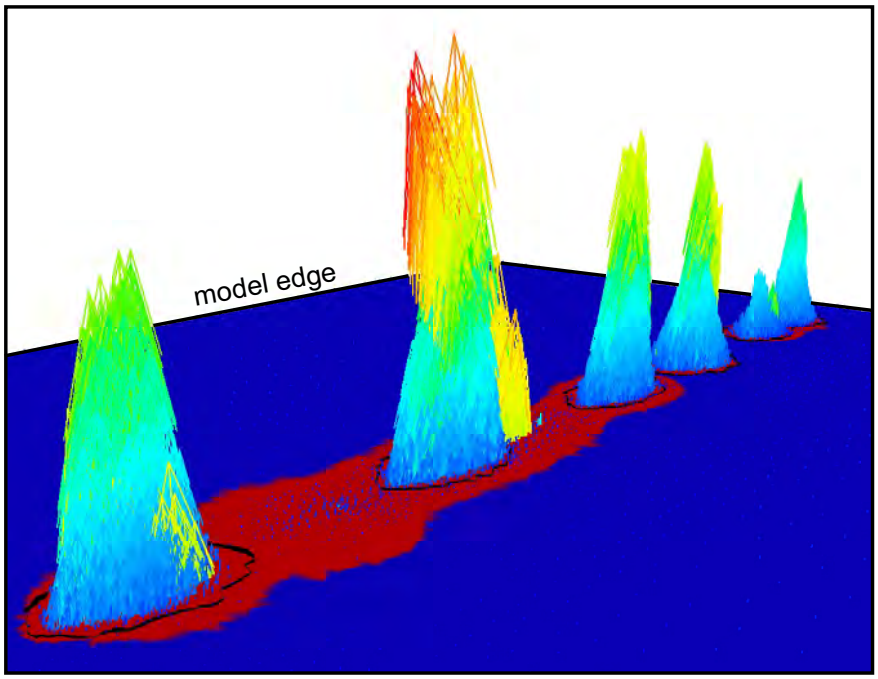

Fig. 5.12: Bird-eye's view of the top surface of the simulation using permeability profile 3 (Figure 5.8) during initialization of convection (50 years), showing diffusive discharge of low-temperature fluids. Blue areas are recharge areas, red areas are discharge areas. Large colored structures indicate areas of vigorous discharge, where the height of the structures is a measure for the volume flux through the top surface. The black line is the 100°C isotherm.

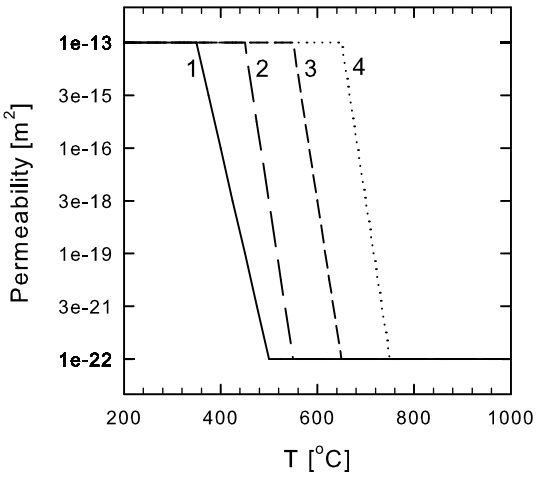

Fig. 5.13: Investigated temperature dependent permeability models $k(T)$.

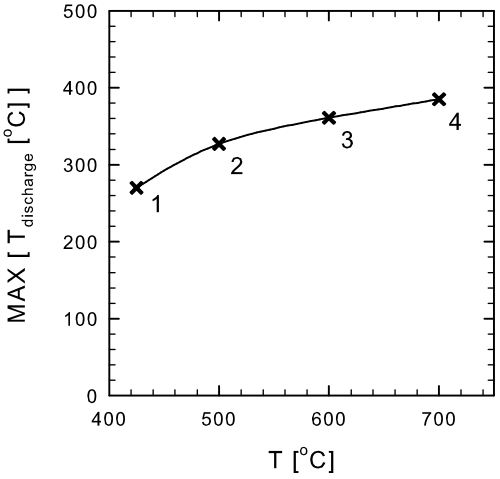

Fig. 5.14: Maximum discharge temperature as a function of temperature-dependent permeability profile. Numbers refer to permeability profiles as defined in figure 5.13

Intermediate convective stage

So far, we have mainly described convection when it is fully evolved. Before this state is reached, a different convection style can be discerned. This style is characterized by large surface areas of low-temperature, low-volume-flux venting surrounding and connecting smaller, circular areas of high-temperature, high-volume-flux venting. This behavior is plotted in Figure 5.12 with low-temperature, diffusive style venting appearing in red. This snapshot in time occurs shortly after the first thermal plumes reach the top boundary of the model. This intermediate stage of convection was observed in several simulations, but was most prevalent in simulations with a high-permeable axial plane. However, over time the red regions in Figure 5.12 become downflow zones and the typical convection style, as described in the previous sections, emerges. Still, the diffuse-venting state can remain active for several years. In section 5.6.3, we explain the physical reason for the occurrence of this state and show that it can explain some observations at natural systems.

Temperature-dependent k

Permeability in the oceanic crust is expected to be a function of temperature. The temperature range over which brittle rock becomes ductile is however poorly known. To investigate this, we perform a number of simulations with a temperature-dependent permeability and set the brittle-ductile transition progressively to higher temperatures. The associated log-linear permeability-temperature functions are plotted in Figure 5.13 and the heat flux is set to a value of 350MW/km of ridge axis. The results show that only when the brittle-ductile transition is set at the temperature interval from 650°C to 750°C, discharge temperature

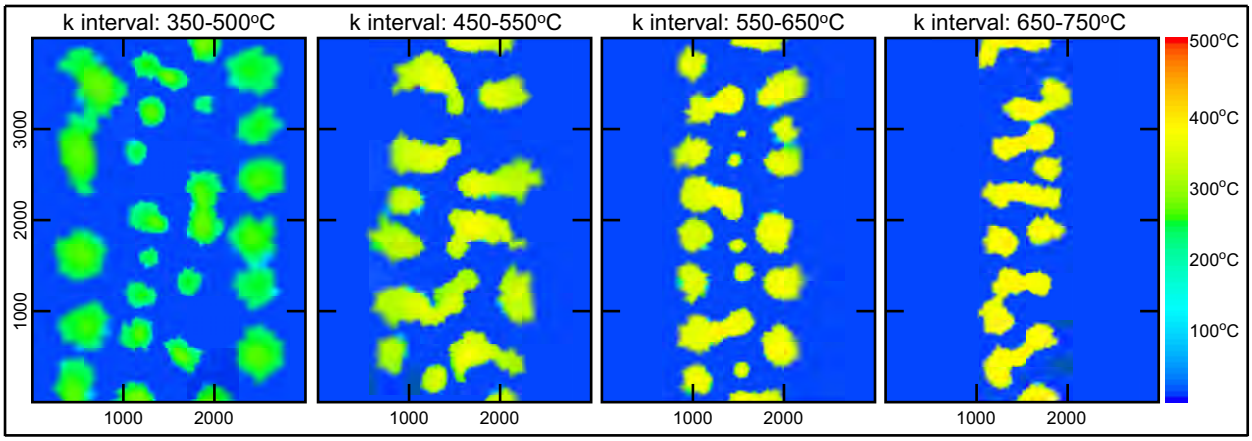

Fig. 5.15: Temperature at the top surface of temperature-dependent-permeability simulations, using $k(T)$-function 1 (a), $k(T)$-function 2 (b), $k(T)$-function 3 (c) and $k(T)$-function 4 (d) (see Figure 5.13)

become larger than 375°C (Figure 5.14). If the brittle-ductile transition is set to a lower temperature interval, then the system cannot remove the heat supplied to the bottom. This results in the formation of a broad hot zone near the bottom, and plumes can rise at considerable distance away from the axial center. Discharge therefore occurs at many locations on- and off-axis, but temperatures are relatively low. With the brittle-ductile transition set at 650°C to 750°C, the system can remove the supplied heat, resulting in near-axial discharge areas with temperatures close to 400°C (Figure 5.14).

5.5 Mathematical Analysis

5.5.1 Pipe-like upflow

The typical convection style of concentric recharge zones around pipe-like upflow zones, which occurs at high heat flux and permeability, can be understood by analyzing non-linearity of the fluid properties. Figure 5.16a shows that heating a fluid from 0°C to $\sim$ 200°C will decrease its viscosity by an order of magnitude but will decrease its density by a much smaller fraction (i.e. from 1000kg m^{-3} to $\sim$900kg m^{-3}). As a consequence, 200°C fluids can be brought downwards very efficiently: the reduced viscosity makes them very mobile and the large density ensures a substantial downward buoyancy force. This behavior can be quantified by writing a simple formula for the vertical mass flux in the axial region:

$$M_z = \rho(T)\mathbf{v}_z = \rho(T)\frac{k}{\mu(T)}\left(\frac{\partial p}{\partial z} - \rho(T)\mathbf{g}\right) \tag{5.3}$$

Where $\partial p/\partial z$ is the vertical pressure gradient in the near-axial region. The vertical pressure gradient takes a value somewhere between hot- and cold hydrostatic such that hot fluids can be transported upwards and cold fluids transported downwards. Several studies assumed that the pressure gradient is very close to cold hydrostatic (Wilcock and McNabb, 1995; Jupp and Schultz, 2004), based on the idea that discharge zones are much smaller than recharge zones and therefore their resistance would be much higher. The much lower viscosity of the fluid in discharge zones, however, has a counteracting effect, greatly reducing upflow

resistance. In our simulations, fluids with temperatures of ∼350°C are at neutral buoyancy in the near-axial region, implying that $\partial p/\partial z$ has a value of ∼6000 Pa/m, roughly half-way in between cold (∼10.000 Pa/m) and hot (∼3000 Pa/m) hydrostatic. Figure 5.16d plots M_z, taking $\partial p/\partial z = 6000$Pa/m, showing that downward mass flux is optimized at ∼200°C and upward mass flux is optimized at ∼400°C. In chapter 4, we derived a simple formula for $\partial p/\partial z$ assuming a pipe-model in which recharge occurs in a halo surrounding a pipe-shaped upflow zone:

$$\frac{\partial p}{\partial z} = \left[\rho_u + (\rho_d - \rho_u)\,\frac{1}{\gamma\frac{\mu_d\rho_u}{\mu_u\rho_d} + 1}\right]\mathbf{g} \tag{5.4}$$

Here γ is the ratio $A_u k_u / A_d k_d$, with A_u the cross-sectional area of the upflow zone and A_d the cross-sectional area of the downflow zone. Subscripts u and d indicate properties of the upwelling and downwelling fluid respectively. Physically, the product $\gamma\frac{\mu_d\rho_u}{\mu_u\rho_d}$ can be seen as the ratio of the hydraulic resistance of the downflow region versus the upflow region. Whenever the resistance in the downflow region increases, compared to the upflow region, this term becomes larger and pushes $\partial p/\partial z$ towards hot hydrostatic (i.e. $\rho_u\mathbf{g}$). Vice versa, if the resistance in the upflow region increases the pressure gradient is pushed towards cold hydrostatic (i.e. $\rho_d\mathbf{g}$). Equation 5.4 assumes that the pressure gradient in the upflow zone is the same as in the near-axial downflow zone. This assumption can be made since in this region fluid flow is dominantly vertical and horizontal pressure gradients are therefore negligible. We can express the total heat flux through the system as (chapter 4):

$$Q = [h_u - h_d]\,\rho_u \frac{k_u}{\rho_u}\left[\frac{\partial p}{\partial z} - \rho_u\mathbf{g}\right] \tag{5.5}$$

where h is the enthalpy of the fluid. Figure 5.16 plots the pressure gradient (b and e) and the heat flux Q (c and f) as functions of the upwelling temperature T_u and downwelling temperature T_d, for γ taken as 1 and 3 respectively, and $k = 5.0e-14\text{m}^2$. In both cases, the point of maximum energy transport, i.e. the peak of the curve plotted in Figures 5.16c and f, coincides with upwelling temperatures of ∼400°C and downwelling temperatures of ∼200°C. The vertical pressure gradient at these locations, however, is substantially different for different γ values. If $\gamma = 1$ the calculated pressure-gradient is ∼6000Pa/m (Figure 5.16b), whereas for larger γ, it drops to smaller values of ∼4000Pa/m (Figure 5.16e). These results have a number of implications which are outlined in the next sections of the discussion.

5.6 Discussion

5.6.1 Maximum energy transport

Since discharge areas and areas of increased recharge have roughly the same surface area in the homogeneous permeability case (see Figure 5.6), in a first approximation γ can be taken as ~ 1. At these conditions, heat flux through the system maximizes at $T_u \approx 400$°C and $T_d \approx 200$°C (Figure 5.16c) accompanied with a pressure gradient of $\partial p/\partial z \approx 6000$Pa/m. These values are very similar to what we observe in our homogenous permeability simulations. This suggests that fluid flow patterns evolve to a state in which the transport of energy is maximized. Upflow in circular, pipe-like zones efficiently heats the surrounding downflowing

water, and thereby maximizes mass and energy transport through the system. Previous studies showed that vent temperatures of ~ 400°C indicate that black-smoker hydrothermal systems could be in a state of maximum energy transport (Jupp and Schultz, 2000, 2004). Here, we demonstrate that, in a state of maximum energy transport, upflow will be in narrow, circular pipes with concentric downflow of relatively warm water providing the bulk of the recharge.

5.6.2 Permeability heterogeneity

For the heterogenous permeability case, the use of formulas 5.4 and 5.5 is less straightforward, but can still give some useful insights. The simulation results showed that the assumption $A_u/A_d \sim 1$ still holds, so γ scales with k_u/k_d. Increasing the permeability in the upflow region, therefore, pushes the vertical pressure gradient towards hot hydrostatic, since $\gamma > 1$. For $\gamma = 3$, the peak in heat flux is still at the same upwelling and downwelling temperatures, but the pressure gradient is much smaller, i.e. ~ 4000Pa/m. This value, however, should be treated with care since the assumption that horizontal pressure gradients in the near axial region are close to zero could be violated at such low vertical pressure gradients. Nevertheless, heterogeneous permeability systems still operate at upwelling temperatures of ~ 400°C and the bulk of the downflow has temperature of ~ 200°C, as confirmed by the simulations, and pressure gradients in the near-axial region decrease due to the low hydraulic resistance of the upflow zone.

5.6.3 Diffuse venting

In the previous sections we showed that optimal energy transport is achieved in a pipe-like upflow region with concentric zones of relatively warm downflowing fluids. This state, however, is only achieved when convection is fully developed, which can take many years. Before that, in the initialization phase, we observed a diffusive venting style in our simulations, with relatively low temperature fluids venting in regions connecting high-temperature "black-smoker" style vent fields. Again, formula 5.4 can provide some understanding in what is causing this phenomenon. During initial plume formation, downflow zones are still essentially at ambient seawater temperatures, since regions surrounding upflow zones have not heated up yet. At this point, the hydraulic resistance of downflow is large due to the large viscosity at ambient temperatures. Therefore, the pressure gradient will settle at a value close to hot-hydrostatic (see also Figure 5.16e) to drive the required downflow to the base of the hydrothermal system. Such a low pressure gradient implies that relatively warm fluids can become neutrally buoyant. Indeed, fluids at the periphery of upflow regions, which lose heat by diffusion and mixing, can easily become neutrally buoyant. Graphically, this is expressed in the steep gradient of the curve in Figure 5.16d in the range from 350°C-400°C: Only a small temperature drop can decrease the upwards buoyancy force substantially. Consequently, fluids in the periphery of upflow zones can lose their upward buoyancy force, which is expressed as low-velocity, diffusive-style, venting at the seafloor. This phenomenon was in particular observed in simulations with an increased axial permeability. In these simulations, rising thermal plumes preferentially take flow paths in the high-permeable zone, whereas downflow is mainly restricted to the lower permeable regions. This affects the relative resistance between up- and downflow zones, pushing the pressure gradient even more towards hot hydrostatic. Once convection is fully developed into high-temperature upflow

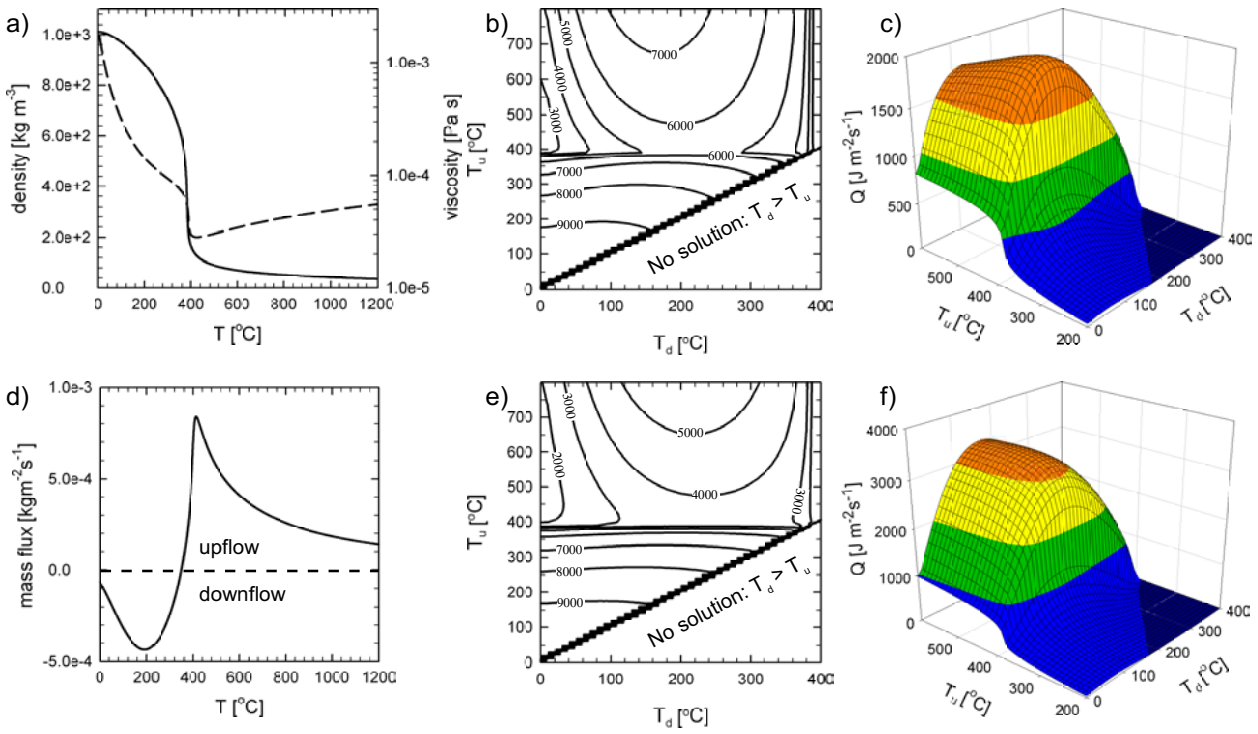

Fig. 5.16: (a) Density (solid line) and viscosity (dashed line) as function of temperature. (b) Vertical pressure gradient (equation 5.4) as function of upwelling and downwelling temperature, $\gamma = 1$. (c) Heat flux (equation 5.5) as function of upwelling and downwelling temperature, $\gamma = 1$ and $k = 5.0e - 14\text{m}^2$. (d) Vertical mass flux (equation 5.3) as function of temperature. Figures (e) and (f) plot the same as (b) and (c) respectively with $\gamma = 3$. For generation of all of these plots a pressure of 25MPa was used.

and surrounding, moderate temperature downflow, diffuse venting ceases and only focussed black-smoker style venting occurs.

We therefore propose that diffuse vent sites might be an indication for sub-seafloor convection being recharge dominated and not yet in its state of optimal energy transport. This hypothesis is supported by several observations of natural diffuse vent fields. First, diffuse vent fields are always at lower temperatures and typically found at the periphery of active black-smoker vent fields (Hannington et al., 1995). Second, diffusive style venting is often observed directly after a dike injection, *before* the emergence of high-temperature black-smokers (Hannington et al., 1995). A possible explanation is that the magmatic event process increases the permeability predominantly in the upflow region and therefore the system becomes recharge dominated. Over time, venting tends to become more and more focussed in black-smoker fields, reflecting the heating of near-axial recharge zones and an accompanying shift of the pressure gradient towards cold hydrostatic.

5.6.4 Permeability

We constrained the permeability by fitting bottom temperatures to expected temperatures of magmatic melt lenses. We find values for k ranging from $0.75\times10^{-14}\text{m}^2$-$5\times10^{-14}\text{m}^2$, using heat fluxes of respectively 75MW/km and 350MW/km, which are at the lower range of axial permeability estimates from previous studies (Lowell and Germanovich, 1994; Wilcock and

McNabb, 1995; Fisher, 1998; Lowell and Germanovich, 2005). The approach, however, has an important limitation. It assumes that the boundary layer between the magma lens and the hydrothermal system is in a thermal steady state: i.e. the amount of heat coming from the magma chamber is removed by the hydrothermal system but the magma lens itself is not cooled, remaining at temperatures around 1200°C. Though plausible, such a balance is by no means required in nature. In fact, measurements indicate that some hydrothermal systems remove heat at a faster rate than can be delivered by the oceanic crustal accretion process (Baker and Massoth, 1987; Ginster et al., 1994; Baker and Urabe, 1996; Ramondenc et al., 2006). This could mean that the magma lens cools and the hydrothermal cell pushes the magma lens down by means of thermal cracking fronts (Lister, 1974). If this is the case, our permeability estimates should be seen as a lower limit for the heat fluxes used.

The simulations with a temperature-dependent permeability show, for this specific model geometry and boundary conditions, that if the brittle-ductile transition is at relatively low temperatures then the systems cannot remove the supplied heat. If the brittle-ductile transition is set from 650°C to 750°C, then the seafloor expression, in terms of location of vent fields and venting temperature matches much better with observations.

5.6.5 Vent field distribution

One key observation at mid-ocean ridges is that venting is focussed in black-smoker fields separated from each other by stretches of unaffected seafloor. In our low-heat-flux simulations, an axial plane with increased permeability is required to produce such discrete vent fields. Though no strict slot-convection mode develops, fluid flow patterns are dominantly in the high-permeability axial plane. Without a high permeability plane, fluid flow in low-heat-flux systems is mainly across-axis and venting occurs everywhere along the axial center, in contradiction with observations. Further, at a heat flux of 75MW/km maximum vent temperatures are substantially lower is typically observed (only 300°C), which indicates that the heat fluxes at active systems are likely larger and that a heat flux of 75MW/km is probably more representative of a dying system.

The high heat flux models (350MW/km) give a better match with observations at natural systems, both in terms of vent temperature and in terms of vent field spacing. In particular, they do not require a high-permeable axial plain to produce separate vent fields. Instead, for a homogeneous permeability, convection organizes itself in circular, pipe-like upflow regions surrounded by regions of increased downflow. Increasing the permeability in a narrow zone at the axial center does not affect this convective behavior significantly. For moderate permeability contrasts, this pipe-like flow structure remains dominant. When the permeability contrast becomes sharp, then convection switches to a different mode in which upflow is dominantly in the high-permeability zone. This results in elongated vent fields which stretch over most of the axial center with only small localized recharge areas. However, this particular simulation (curve 4, Figure 5.13) might not have reached its final semi-steady convective structure yet[1]. Continued circulation could possibly heat up surrounding downflow zones more substantially, creating a more pipe-like flow structure. Nevertheless, elongated vent fields stretching over the bulk part of the axial center are rarely observed at mid-ocean ridge spreading centers. We therefore propose that the regular spacing of vent fields indicates that

[1] Large fluid velocities in the high permeability region, where element sizes are also smallest, cause timesteps to become very small, thereby limiting the simulation time.

subseafloor convection is characterized by pipe-like upflow and zones of increased downflow of relatively warm fluids surrounding these pipes. At early stages of convection permeability structure plays a dominant role. Once convection is fully evolved and downflow zones heated then the non-linearity of the fluid properties are a first-order control on convection.

5.6.6 Field evidence

Substantial evidence exists in nature for pipe-like convective systems, as observed in our simulations. Tivey and Johnson (2002) gathered magnetic anomaly data from the Endeavour segment of the Juan de Fuca Ridge to infer the sub-seafloor structure of upflow regions. They observe circular magnetic lows at active and inactive venting areas, which look remarkably similar to the thermal structure at the top of homogenous permeability models. Tivey and Johnson (2002) interpret the sub-seafloor structure as near-vertical pipe-like source regions, in agreement with our results. Further evidence for focussed, pipe-like upflow regions comes from ophiolites (Saccocia and Gillis, 1995; Juteau et al., 2002).

An additional feature of pipe-like upflow observed in our simulations is the existence of halos of increased downwelling surrounding the upflow zones. Recharge regions therefore might be less extensive than previously thought. In our homogeneous permeability simulations, $\sim$2/3 of the recharge occurs within $\sim$500m of the axis. Temperatures within these 'focused recharge' zones are substantially higher than often assumed for recharge regions, but are in agreement with results from recent 2D simulations (Fontaine and Wilcock, 2007). They are also compatible with temperature distributions inferred from the study of mineral-assemblages at different levels in oceanic crust (Alt, 1995). To draw these relatively warm fluids down, the pressure gradient needs to be sufficiently low (i.e. $\sim$ 6000Pa/m). No direct pressure data exists from black-smoker upflow zones, but boreholes from geothermal systems reveal pressure roughly mid-way hot- and cold-hydrostatic (Grant et al., 1984). Finally, recent seismic data from the East Pacific Rise 9°50'N indicate that recharge can indeed occur focussed and very close to the axis, directly above the magmatic melt lens (Tolstoy et al., 2008).

5.7 Conclusions

We report the first high-resolution 3D simulations of thermal convection at mid-ocean ridges, including the full non-linearity of the properties of super-critical H_2O. The simulations show that pipe-like upflow, observed in several natural systems, forms naturally at sufficiently high heat flux and permeability. This style of convection is accompanied by halos of increased downflow surrounding upflow regions. As a result of the non-linear dependence of the viscosity, density and heat capacity of the fluid on temperature and pressure, the systems' heat output is maximized for this configuration. Venting occurs in circular high-temperature regions separated from each other by recharge areas, even when the permeability is homogeneous. Therefore, slot-convection, in which convection is dominantly 2D within a high-permeable axial plane, is neither required, nor physically or geologically likely, to explain separately spaced vent fields in nature. Pressure gradients in the near-axial regions might be substantially smaller than cold hydrostatic, as often assumed. In fact, when the near-axial permeability is large, the pressure gradient can approach hot hydrostatic values during the early stages of convection, causing rather warm fluids to become near neutral

buoyancy. Based on this mechanism, we propose a new hypothesis to explain diffuse venting at the edges of black-smoker fields and after dike-injections.

6. A FEFV SCHEME BASED UPON A PRESSURE-ENTHALPY-SALINITY FORMULATION TO SOLVE MULTI-PHASE FLOW OF H_2O-NACL FLUIDS

6.1 Abstract

We present a novel finite-element finite-volume (FEFV) numerical simulator which can handle multi-phase fluid transport of mass, heat and dissolved salt in porous media. The code is based upon a pressure-enthalpy-salinity (PHX) scheme and includes an accurate description of the phase relations and properties of H_2O-NaCl fluids over pressure, temperature and salinity ranges encountered in the Earth's crust. This method accurately accounts for the non-linear variation in fluid properties and the separation of a saline fluid into a low-salinity vapor and high-salinity brine phase, including the possibility of solid-state halite formation. The governing equations are decoupled, resulting in a set of hyperbolic and parabolic equations, which are solved sequentially by the FV and FE method respectively. Temperature is determined with an iterative procedure equilibrating energy stored in the fluid and rock at constant pressure and bulk salinity. With the newly found temperature, the fluid's state and associated phase properties can be determined directly. The difference between fluid volume and pore volume caused by temperature and salinity changes enters as a source term into the pressure equation. By using the appropriate adiabatic compressibility for single, two-phase, and three-phase states (liquid, vapor, halite), the pressure solution can now be solved. With this approach, energy changes associated with phase- and pressure-changes are properly accounted for. We test the accurateness and robustness of this approach with a series of benchmark tests focussing on its reliability to model two-phase pure water boiling systems. Reference results for these tests were obtained with the USGS HYDROTHERM code that solves the governing equations fully coupled (Hayba and Ingebritsen, 1994a). Though in its current state the code has some limitations in its usage, which we discuss, it enables solid numerical simulations of high-temperature salty fluids in the Earth's crust.

6.2 Introduction

Flow of heat and dissolved salt in crustal fluids, known as thermohaline convection, is an important process driving many geologic systems in the Earth's crust. At oceanic spreading centers, newly accreted crust is cooled by salty, oceanic fluids, estimated to transport roughly 25% of the Earth's total heat flux (Stein and Stein, 1994). Phase-separation of seawater occurring below the seafloor is expected to be a key process affecting the physics and chemistry of convection at mid-ocean ridge hydrothermal systems (Von Damm, 1990; Lowell and Germanovich, 2005). On the continents, magmatic-hydrothermal systems associated with subduction volcanism are thought to be responsible for the creation of porphyry

ore-deposits, the most important Cu deposits in the world (Titley and Beane, 1981). In such systems, phase-separation has a great impact on solubility of metals and their transport, since they preferentially fractionate into either the liquid or the vapor phase (Heinrich, 2007). Geothermal energy reservoirs, in which deep heat is mined by circulating fluids, often harbor very salty fluids at multi-phase conditions (Anorsson et al., 2007). Crustal fluids in all these systems contain various dissolved elements, but due to the predominance of sodium-chloride, the thermodynamics of these fluids can in many cases reliably be approximated by the system H_2O-NaCl.

Thermohaline convection in the Earth's crust is found under a wide range of temperature, pressure and salinity conditions. Crustal fluid flow may occur down to depths of 15km on the continents (Nesbitt and Muehlenbachs, 1991) and possibly all the way to the Moho in parts of the oceanic crust (Nicolas and Mainprice, 2005). Magma chambers can reach temperatures around 1200°C, and fluids possibly penetrate to regions of such high temperatures (Nicolas and Mainprice, 2005). Fluid inclusion data from both continental and marine hydrothermal systems indicate that fluids can become hypersaline, regularly containing halite crystals (Nehlig, 1991; Kelley et al., 1993). Therefore, to accurately handle such extreme conditions, an equation of state should incorporate a very large range in temperature, pressure and salinity. A consistent description of the properties of the phases of H_2O-NaCl over the pressure-temperature-salinity ranges encountered in the Earth's crust was recently provided by Driesner and Heinrich (2007) and Driesner (2007).

In addition to a consistent equation of state, a robust numerical method to transport mass, energy and salt in multi-phase, highly-compressible fluids is required. Such a numerical scheme is challenging to develop since the system is highly non-linear for a number of reasons. Both fluid properties and phase boundaries depend non-linearly on temperature, pressure and composition and, at the critical point of water, most derivatives of thermodynamic properties with respect to temperature, pressure and composition diverge to $+/-\infty$. Additionally, the governing equations describing multi-phase fluid transport are non-linear and the pressure and energy equations are strongly coupled. The system is further complicated since, in contrast to pure water, a salty fluid can phase separate at pressures well above the critical point of pure water. When phases separate, a low-salinity, low-density vapor and a high-salinity, high-density brine are produced, often leading to spatial segregation of the two-phases due to the large buoyancy difference between the two. Finally, the simultaneous transport of heat and salt causes double-diffusive double-advective motion, producing complex, non-linear flow behavior even when the fluid is not boiling (Schoofs et al., 1999; Geiger et al., 2005). This phenomenon occurs because salt, since it is stored in the pore volume only, advects faster but diffuses slower than heat.

To cope with these complex issues, previous numerical studies were forced to make a range of simplifications investigating component problems of thermohaline convection.

Many studies employed the so-called Boussinesq approximation, in which density changes are neglected in all terms but the buoyancy term. This approach has been applied to both single-phase (Schoofs and Hansen, 2000) and two-phase systems (Kawada et al., 2004). However, this approach, often used in combination with linearized fluid properties, reduces the tendency of a system to convect (Straus and Schubert, 1977), and for near-critical systems almost completely suppresses the actual behavior of the system (Jupp and Schultz, 2000; Coumou et al., 2006). In other studies, the fluid was assumed to be pure water, neglecting double-diffusive double-advective motion and restricting phase separation to pressures and

temperatures below the critical point of water (Hayba and Ingebritsen, 1994b; Ingebritsen and Hayba, 1994). Often, two-phase conditions were avoided by either using pure water at super-critical conditions (Jupp and Schultz, 2000; Coumou et al., 2006) or assuming a single phase, mixed-density fluid for the two-phase region (Fontaine and Wilcock, 2007). Other studies included salt at multi-phase conditions, but limited the simulations to 1D domains, modeling liquid-vapor counter-flow in so-called two-phase heat pipes (Bai et al., 2003; Seyfried et al., 2003).

Recently, algorithmic improvements in two porous media codes enabled the first insights into the full complexity of thermohaline convective systems by numerical simulation. Kissling (2005b) developed a new simulation code for H_2O-NaCl fluids based upon the TOUGH2 porous-medium transport code and the equation of state by Palliser and McKibbin (1998a,b,c). This equation of state, however, contains some inconsistencies at near-critical conditions (Driesner and Heinrich, 2007), predicting non-physical effects like negative heat capacities in some pressure-temperature-salinity regions. Geiger et al. (2006a) developed a FEFV numerical method, implemented in the CSMP++ simulator, in combination with the equation of state by Driesner and Heinrich (2007) to model thermohaline convection. They formulated energy conservation in terms of temperature, in which, rather than explicit mass and energy conservation, the advancement of the thermal front is calculated. Though appropriate when the fluid is a single phase, this method neglects some derivative terms in the energy equation when the fluid is multi-phase, possibly leading to non-physical effects during boiling (Driesner and Geiger, 2007).

In this study, we present a novel simulation scheme, based upon the work by Geiger et al. (2006a), which accurately models boiling processes in NaCl-H_2O systems. Similar to Geiger et al. (2006a), we decouple the pressure and energy equations, solving them using a FEFV method. However, rather than using a temperature formulation for the energy equation, we explicitly conserve enthalpy, as well as fluid and salt mass. We subject the PHX scheme, implemented into the CSMP++ simulator, to a range of benchmark tests of pure and salt water at multi-phase conditions. These tests confirm that the scheme can accurately handle boiling at sub- and near-critical conditions.

6.3 Computational Method

6.3.1 Conservation equations

The most general form of the conservation equation is given by:

$$\frac{\partial A_k}{\partial t} = -\nabla \cdot (\overline{F}_k) + Q_k \tag{6.1}$$

where A_k is an accumulation term of the conserved quantity k, $\overline{F}_k$ a flux term and Q_k a source term. We assume that H_2O and NaCl are the only chemical species present which can exist in seven different phase states: single-phase liquid (L), vapor (V) or halite (H); two-phase vapor plus liquid (V+L), vapor plus halite (V+H), or liquid plus halite (L+H); or three-phase vapor plus liquid plus halite (V+L+H). Energy is stored in all fluid phases and the rock. The solid halite phase (H) is assumed to be immobile. With these assumptions we derive the following conservation equations for water, salt and energy respectively:

$$\frac{\partial(\phi m_t)}{\partial t} = -\nabla \cdot (\mathbf{v}_l \rho_l) - \nabla \cdot (\mathbf{v}_v \rho_v) + Q_{H_2O+NaCl} \tag{6.2}$$

$$\frac{\partial(\phi m_s)}{\partial t} = -\nabla \cdot (\mathbf{v}_l \rho_l X_l) - \nabla \cdot (\mathbf{v}_v \rho_v X_v) + \nabla \cdot (D_l \nabla \rho_l X_l) + \nabla \cdot (D_v \nabla \rho_v X_v) + Q_{NaCl} \tag{6.3}$$

$$\frac{\partial H_t}{\partial t} = \nabla \cdot (K \nabla T) - \nabla \cdot (\mathbf{v}_l \rho_l h_l) - \nabla \cdot (\mathbf{v}_v \rho_v h_v) + Q_{Energy} \tag{6.4}$$

where m_t is the total fluid's mass (H_2O+NaCl) per pore volume, m_s is the salt mass (NaCl) per pore volume and H_t the total energy stored in the rock and the fluid. Variables m_t and m_s have units of density (kg m^{-3}), but they are *not* thermodynamic densities but rather accumulation terms for mass and salt conservation. Further, in equations 6.2-6.4, ρ stands for density, S for volumetric saturation, X for the mass fraction of NaCl, h for specific enthalpy, T for temperature, K for the thermal conductivity and D for salt diffusivity. Subscripts l, v and r stand for liquid, vapor and rock respectively.

Conservation of momentum is described by the Darcy velocity ($\mathbf{v}$) for multi-phase fluid flow (Ingebritsen and Hayba, 1994):

$$\mathbf{v}_i = -\mathbf{k}\frac{k_{ri}}{\mu_i}\left[\nabla p - \rho_i \mathbf{g}\right] \qquad i = \{l, v\} \tag{6.5}$$

Here p is pressure, $\mathbf{k}$ permeability, k_r the relative permeability and $\mathbf{g}$ gravitational acceleration. In our simulations, we do not account for capillary pressure explicitly, the relative permeability approach however captures some of its effects by the reduction of fluid velocity when two-phases are present. Relative permeability values for the individual phases depend on their relative amounts in the pore volume, and both linear and non-linear (Brooks and Corey, 1964) relationships can be used. A fluid phase can become immobile when its saturation drops below the residual saturation, which in our simulations is normally set to 0.3 for the liquid phase and 0. for the vapor phase, i.e. the vapor is always mobile.

6.3.2 Pressure equation

From the conservation of fluid mass (equation 6.2), we can derive an expression for the fluid pressure p, by expanding the derivative of m_t into its p, T and X components. The left-hand side of equation 6.2 can now be written as:

$$\phi\frac{\partial m_t}{\partial t} = \phi\frac{\partial m_t}{\partial p}\Big|_{T,X}\frac{\partial p}{\partial t} + \phi\frac{\partial m_t}{\partial t}\Big|_{p} = \phi m_t \beta_f \frac{\partial p}{\partial t} + \phi\frac{\partial m_t}{\partial t}\Big|_{p} \tag{6.6}$$

Here, β_f is the fluid's compressibility. In the case of boiling, the compressibility of a fluid is dominated by the phase change and accompanying volume change. The change in specific volume during pressurization of each separate phase is much smaller. Therefore the appropriate adiabatic compressibilities need to be used, similar to the one derived by Grant and Sorey (1979) for the two-phase (V+L) case.

Neglecting porosity changes due to salt precipitation, we can express porosity changes by the volumetric compressibility of the rock itself (Geiger et al., 2006a):

$$\frac{\partial \phi}{\partial t} = (1-\phi)\beta_r \frac{\partial p}{\partial t} \tag{6.7}$$

By inserting equations 6.6 and 6.7 into the left hand side of equation 6.2 and the Darcy velocity (equation 6.5) into the right hand side, we derive the following transient pressure equation:

$$\begin{aligned} m_t \left[\phi\beta_f + (1-\phi)\beta_r\right] \frac{\partial p}{\partial t} = \nabla \cdot \left[\mathbf{k}\left(\frac{k_{rl}}{\mu_l}\rho_l + \frac{k_{rv}}{\mu_v}\rho_v\right)\nabla p\right] \\ + \mathbf{k}\left(\frac{k_{rl}}{\mu_l}\rho_l^2 + \frac{k_{rv}}{\mu_v}\rho_v^2\right) g \nabla z \\ - \phi \frac{\partial m_t}{\partial t}\Big|_p \end{aligned} \tag{6.8}$$

This equation is analogous to the one derived by Geiger et al. (2006a) but has a different expression for the source term. This term, $\phi \frac{\partial m_t}{\partial t}\Big|_p$, represents the change in the density of the fluid due to temperature and salinity changes with constant pressure and is directly computed from the volume change of the fluid (see section 6.3.7)

6.3.3 Fluid properties

All fluid properties are obtained from the H_2O-NaCl equation of state of which we will give a brief description here. For full details we refer the reader to Driesner and Heinrich (2007) and Driesner (2007). Figure 6.1 plots the phase diagram of H_2O-NaCl in temperature-pressure-salinity space, showing the phase boundaries dividing the system into a total of seven possible phase states. Above the vapor-liquid coexistence surface (black surface) the fluid is in the the single-phase domain, having either vapor-like properties (V) at low salinity and/or high temperature, or liquid-like properties (L) at high salinity and/or low temperature. At zero salinity, the H_2O boiling curve follows the vapor-liquid coexistence surface up to the critical point of H_2O, after which it continues as the critical curve, following the crest of the vapor-liquid surface. Below this surface, vapor and liquid coexist (VL), with the liquid phase having a much higher salinity than the vapor phase. The lower-pressure boundary of this domain is given by the three-phase surface, i.e. the vapor-liquid-halite surface (VLH, blue surface), which also forms the upper pressure boundary for vapor and halite (VH) coexistence. The halite liquidus (green surface) is the surface along which a liquid-like fluid is saturated with halite. At higher salinities liquid and halite (LH) will coexist. Phase separation of a single-phase fluid can occur either by boiling or condensation. If a liquid-like fluid hits the liquid-vapor surface, boiling will take place. If a vapor-like, single-phase fluid hits the liquid-vapor surface then liquid droplets condense out of the vapor.

6.3.4 Numerical methods

The governing equations 6.2-6.4 and equation 6.8 are solved using a finite element-finite-volume method implemented in the CSMP++ multi-physics simulation tool. In this method, a finite-volume mesh is superimposed on top of a finite-element mesh (Geiger et al., 2004,

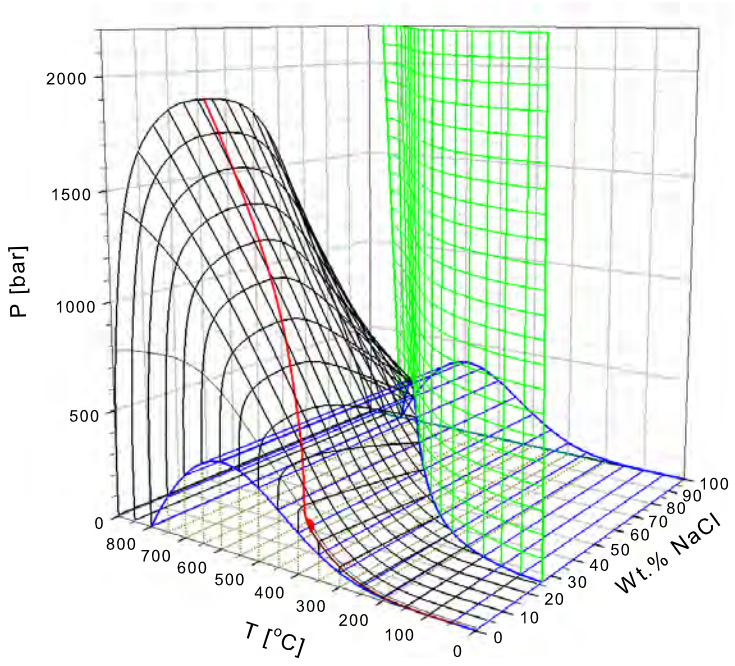

Fig. 6.1: Phase diagram of the system H_2O-NaCl in pressure-temperature-salinity space. Phase boundaries are indicated by the V+L surface (black), V+L+H surface (blue), halite liquidus (green), critical curve (red line) and critical point of H_2O (red point).

2006a), such that the corners of the finite-volumes coincide with the center of the finite-elements. The main advantage of this dual mesh approach is that the best suited numerical method can be used for each sub-problem. The FV method is robust and strictly mass-conserving in solving advection-type (hyperbolic) equations whereas the FE method performs better on diffusion-type (parabolic) equations. We therefore split the advection-dispersion type conservation equations of salt and energy (equations 6.3 and 6.4) into their advective and diffusive parts and solve them sequentially. Since $H_t = \phi H_f + (1-\phi)H_r$, with H_f being the energy stored in the fluid and H_r the energy stored in the rock, we can split equation 6.4 into a rock-diffusive and fluid-advective part:

$$(1-\phi)\frac{\partial H_r}{\partial t}\Big|_{dif} = (1-\phi)\rho_r c_{pr}\frac{\partial T}{\partial t} = \nabla\cdot(K\nabla T) + Q_{Energy} \tag{6.9}$$

$$\phi\frac{\partial H_f}{\partial t}\Big|_{adv} = -\nabla\cdot(\mathbf{v}_l\rho_l h_l) - \nabla\cdot(\mathbf{v}_v\rho_v h_v) \tag{6.10}$$

Similarly, the salt mass conservation equation 6.3 is split into a diffusive and advective equation:

$$\phi\frac{\partial(m_s)}{\partial t}\Big|_{dif} = \nabla\cdot(D_l\nabla\rho_l X_l) + \nabla\cdot(D_v\nabla\rho_v X_v) + Q_{NaCl} \tag{6.11}$$

$$\phi\frac{\partial(m_s)}{\partial t}\Big|_{adv} = -\nabla\cdot(\mathbf{v}_l\rho_l X_l) - \nabla\cdot(\mathbf{v}_v\rho_v X_v) \tag{6.12}$$

The full solution of the derivatives is found by summation of the partial solutions for advection and diffusion. In equation 6.9 the change in enthalpy is written as the change in temperature times the heat capacity of the rock, which is assumed to be constant. The conservation equation for fluid mass (equation 6.2) is not affected since it only contains advective terms. The set of governing equations (6.2, 6.9-6.12) is solved in a sequential process described in detail in section 6.3.9.

6.3.5 Spatial and temporal discretization

We discretize the two-dimensional domain with triangular elements (Delauney triangulation), which allows us to resolve complex structures in great detail (Matthai et al., 2007). So far, this specific scheme has only been tested using 2D triangular meshes, though CSMP++ has the capability to solve the equations in 3D using multiple element type meshes (Paluszny et al., 2007). All conserving variables (m_t,m_s,H_t) as well as pressure (p), temperature (T) and salinity (X) are defined on the nodes. Rock properties and phase velocities are defined on the the element center, which coincides with FV corners. The fluid pressure equation (6.8) and the energy and salt diffusion equations (6.9,6.11) are solved using the Bubnov-Galerkin formulation, taking an implicit Euler discretization in time. As the Galerkin method is well known, and excellent descriptions are available (Huyakorn and Pinder, 1983; Zienkiewicz and Taylor, 2000), we omit further details here. From the updated pressure field, fluid velocities are calculated at the element center by solving Darcy's law (equation 6.5). Although the fluid velocities are discontinuous between adjacent finite-elements, they are continuous across the face of a finite-volume (Geiger et al., 2006a). Mass conserving flux calculations can now

be performed by integrating over the finite-volumes. Using standard finite-volume methods, we discretize the advection equations 6.2, 6.10 and 6.12 in time respectively as follows:

$$m_t^{n+1} = m_t^n - \frac{\Delta t}{\phi V}\left[\sum_j^N [A_j(\mathbf{v}_l\rho_l)^{n+1/2}]\cdot\mathbf{n}_j - \sum_j^N [A_j(\mathbf{v}_v\rho_v)^{n+1/2}]\cdot\mathbf{n}_j\right] \tag{6.13}$$

$$m_s^{n+1} = m_s^n - \frac{\Delta t}{\phi V}\left[\sum_j^N [A_j(\mathbf{v}_l\rho_l X_l)^{n+1/2}]\cdot\mathbf{n}_j - \sum_j^N [A_j(\mathbf{v}_v\rho_v X_v)^{n+1/2}]\cdot\mathbf{n}_j\right] \tag{6.14}$$

$$H_f^{n+1} = H_f^n - \frac{\Delta t}{\phi V}\left[\sum_j^N [A_j(\mathbf{v}_l\rho_l h_h)^{n+1/2}]\cdot\mathbf{n}_j - \sum_j^N [A_j(\mathbf{v}_v\rho_v h_v)^{n+1/2}]\cdot\mathbf{n}_j\right] \tag{6.15}$$

These equations can be solved locally, for each finite-volume, by looping over all segments j of the finite-volume, with A_j the area of segment j and $\mathbf{n}_j$ the outward pointing normal vector to segment j. V is the volume of the finite-volume. The right-hand-side terms of equations 6.13-6.15 are determined at timestep $n + 1/2$, which we define as:

$$\psi^{n+1/2} = \frac{\psi^{n+1'} + \psi^n}{2} \tag{6.16}$$

Here, $\psi^{n+1'}$ is determined in a first pre-calculation step in which the full sequence of a single timestep is calculated up to the new velocities. Then, right-hand-side properties of equations 6.13-6.15 and velocities are averaged according to formula 6.16. This approach suppresses possible oscillations which are introduced when the fluid starts to boil, due to the decoupling of the pressure and energy equations.

6.3.6 Thermal equilibration[1]

In the decoupled scheme, once energy has been transported by advection in the fluid and by diffusion in the rock, rock and fluid are not in thermal equilibrium. Hence, taking into account that from equations 6.9 and 6.10 the total energy is $H_t = (1-\phi)H_r + \phi H_f$, the temperature T at which both rock and fluid are at thermal equilibrium for the given H_t, can be found by iteratively solving:

$$m_r h_r(T) + m_l(T)h_l(T) + m_v(T)h_v(T) + m_h(T)h_h(T)) - H_t = 0 \tag{6.17}$$

Notice that this iteration is done at constant pressure and bulk salinity. Before an actual iteration is invoked, the scheme checks whether a univariant equilibrium (i.e., pure water boiling, halite melting, or crossing the V+L+H coexistence surface) may be encountered in the iteration procedure. This needs to be done since at an univariant equilibrium $\frac{dH}{dT} = \infty$ and any iteration in T will fail (the best known example being boiling of pure water). If this is the case, the temperature $T_{univariant}$ at which the univariant curve is located at the current pressure is computed. Then, the specific enthalpies h_{high} and h_{low} of the high- and low-enthalpy phases, respectively, of the univariant equilibrium are computed and compared

[1] Section contributed by PD. Dr. Thomas Driesner

to the specific enthalpy $h_{univariant}$ of the fluid at $T_{univariant}$. If $h_{univariant} > h_{high}$, iteration can proceed in the stability field of the high-enthalpy phase (e.g., pure water vapor). If $h_{univariant} < h_{low}$, iteration will proceed in the stability field of the low-enthalpy phase (e.g., pure water liquid). If, otherwise $h_{low} \leq h_{univariant} \leq h_{high}$, the system has two fluid phases (or, in the case of the V+L+H equilibrium, three fluid phases), the mass fractions of which can be computed from the proper mass- and energy-balance constraints as well as their properties from the equation of state, and $T_{univariant}$ is then accepted as the new temperature.

If no univariant equilibrium is encountered, the following procedures apply. In the case of a single-phase fluid, iteration is a straightforward Newton scheme, as the temperature-dependence of the m_i term is zero and h_i is usually a well-behaved functions of T (except very close to the critical point of water). As a convergence criterion, we use:

$$\frac{m_r h_r(T) + m_l(T)h_l(T) + m_v(T)h_v(T) + m_h(T)h_h(T)) - H_t}{m_l(T)h_l(T) + m_v(T)h_v(T) + m_h(T)h_h(T))} \leq 10^{-4} \tag{6.18}$$

This criterion, i.e., convergence to a difference that is smaller than a fraction of the fluid's enthalpy, was chosen in order to be able to handle also cases with low porosities where the fluid's enthalpy may be smaller than an arbitrarily chosen fraction of H_t. Convergence is typically reached within one or two Newton steps. In the two-phase case (V+L, V+H, or L+H), saturation and densities (and, hence, masses $m_i = S_i\rho_i$) are functions of T. Again, a Newton iteration may be invoked in which the derivative $\frac{d}{dT}(S_i\rho_i h_i) \mid_{P,X_{bulk}}$ is obtained analytically from the equation of state and the appropriate mass balance constraints. In the single-phase case near the critical point of water, or in the two-phase case at phase boundaries where values of these derivatives may become very large, convergence of a Newton scheme to the criterion shown in equation 6.18 is not guaranteed. Therefore, once the Newton iteration does not converge within five cycles, iteration switches to a bisection scheme. This requires knowledge of an upper and a lower temperature limit (T_{max} and T_{min}, respectively), which are obtained in the following way. First, $H_{test} = m_r h_r(T_{previous}) + m_l(T_{previous})h_l(T_{previous}) + m_v(T_{previous})h_v(T_{previous}) + m_h(T_{previous})h_h(T_{previous}))$ is computed for the current pressure, at the temperature $T_{previous}$ of the previous step and the current (i.e., after transport) salinity and fluid mass. If $H_t = H_{test}$, the correct temperature is $T_{previous}$; if $H_t > H_{test}$, then $T_{previous} = T_{min}$; if $H_t < H_{test}$, then $T_{previous} = T_{max}$. The corresponding T_{min} or T_{max} can be found by computing $T_{previous} + \Delta T$, where $\Delta T = \frac{H_t - H_{test}}{c_{p,r}}$. This is guaranteed to find a correct bracket, as the usage of $c_{p,r}$ underestimates the total heat capacity and will, hence, provide too large a ΔT. Bisection then proceeds either in a standard way or is improved by introducing an enthalpy-weighing, in which the differences $H_t(T_{max}) - H_t$ and $H_t(T_{min}) - H_t$ are used to speed up convergence. This is essential near phase boundaries with very steep gradients in enthalpy.

6.3.7 Pressure source

As thermal equilibration was done at constant p and X, the fluid volume was allowed to vary freely along the isobaric equilibration path. It is a central part of our scheme that at this state the fluid's volume is *not* constrained to fit the pore volume. Rather the mismatch between the two is the information needed to compute the new pressure. Hence, the volume mismatch enters as a volumetric source term into the pressure equation. The volume mismatch ε is

given by the total mass of fluid per pore volume (i.e. m_t) divided by the thermodynamic density of the bulk fluid after equilibration:

$$\varepsilon = \frac{m_t}{S_l\rho_l + S_v\rho_v + S_h\rho_h} \tag{6.19}$$

The volumetric source term for the pressure equation 6.8 arising from a change in density due to temperature and salinity changes is now given by:

$$\phi\frac{\partial m_t}{\partial t}\Big|_p = \phi\frac{m_t - (S_l\rho_l + S_v\rho_v + S_h\rho_h)}{\Delta t} = \phi m_t\frac{(\varepsilon - 1.0)}{\varepsilon\Delta t} \tag{6.20}$$

This source term presses or expands the fluid back into the pore space. An ε smaller than one, i.e. the fluid volume is smaller than the pore volume, results in negative source terms (equation 6.20) lowering p in the pressure-step. Vice versa, if ε is larger than one pressure will increase, resulting in outward flux during the next transport step. In addition, if ε is not equal to one, than the amount of fluid is not equal to its density times the pore volume. To account for this in the transport step, the right-hand-side terms of the FV equations 6.13-6.15 are multiplied by ε. Note that this multiplication does *not* affect mass-conservation in any way.

6.3.8 Timestepping

In general, the timestep of an explicit Euler FV transport scheme is limited by the Courant-Friedrich-Levy (CFL) criterion (i.e. Geiger et al. (2006a)):

$$\Delta t_{CFL} = \mathrm{MIN}_\Omega\left(\frac{r_i}{\mathbf{v}}\right) \tag{6.21}$$

where r_i is the approximate radius of control volume i, $\mathbf{v} = \mathbf{v}_l + \mathbf{v}_v$ and 'MIN$_\Omega$' refers to the minimum encountered value in computational domain Ω. However, our decoupled sequential solution method introduces an error in the flux of conserved variables due to the mismatch of the volume of the fluid and the pore space (ε). This flux-error can be estimated by the difference in transporting a "thermodynamic" fluid and a "compressed" fluid:

$$error_\varepsilon = \frac{\Delta t}{\phi V_{FV}}\frac{(\varepsilon - 1)}{m_t}\left[\rho_l \mid \mathbf{v}_{FV,l} \mid_{max} + \rho_v \mid \mathbf{v}_{FV,v} \mid_{max}\right] = \sigma\Delta t \tag{6.22}$$

We can now set a specific tolerance to the transport step by defining a maximum allowed error due to volume mismatch. Since the error scales with the timestep, we can simply calculate the maximum allowed timestep to meet this tolerance (in %), giving:

$$\Delta t_\varepsilon = \frac{tolerance}{\sigma \times 100\%} \tag{6.23}$$

This tolerance can in principle be set rather relaxed ($\sim$10%) since this error only affects fluxes but not mass or energy conservation.

Since the size of the timestep directly affects the source term of the pressure equation 6.20, abrupt changes in its size can trigger oscillations in the pressure field. To suppress this and smooth timestepping, Δt is multiplied with a smoothing factor $\left[\frac{\varepsilon_{min}}{\varepsilon_{max}}\right]^N$, where ε_{min} and ε_{max} are the minimum and maximum value of ε encountered in the computational domain.

Larger powers (N) resuls in more substantial smoothing. The timestep is now calculated as follows:

$$\Delta t = \begin{cases} \Delta t_{CFL} \left[\frac{\varepsilon_{min}}{\varepsilon_{max}}\right]^N & \text{if } \Delta t_{CFL} \times \sigma \times 100\% < tolerance, \\ \frac{tolerance}{\sigma \times 100\%} & \text{if } \Delta t_{CFL} \times \sigma \times 100\% > tolerance. \end{cases} \tag{6.24}$$

6.3.9 Sequential approach

Figure 6.2 shows a computational flow diagram for the computation of a single timestep. In a first pre-calculation step, velocities and dependent variables are determined at timestep $n + 1'$ consisting of the following sub-calculations: (1) Starting from primary and dependent variables at timestep n, the advection and diffusion type equations are solved to obtain the conserving variables at timestep $n + 1'$. (2) These values are fed into the equilibration algorithm, which finds a new temperature at which fluid and rock are in thermal equilibrium ($T^{n+1'}$). (3) Using temperature and salinity at timestep $n + 1'$ and pressure at timestep n, new fluid properties are found by consulting the NaCl-H_2O equation of state. (4) The fluid's volume mismatch from the thermal equilibration step enters the pressure equation which is solved using the FE method. (5) From the newly calculated p, new phase velocities are calculated by solving the Darcy equation 6.5, concluding the pre-calculation step. The velocities and right-hand-side advection variables are now averaged, and the primary and conserving variables are reset to their values at timestep n. The new velocities are used to calculate a new timestep size. Now, the full timestep can be calculated from n to $n+1$, using the averaged velocities and fluid properties. This step consists of exactly the same sub-steps as discussed for the pre-calculation step.

6.4 Benchmark Tests

We verified the correctness of our numerical method with a large number of benchmark problems in which we focussed on pure water boiling at low and near-critical pressures. Geiger et al. (2006b) already verified the accuracy of the FE and FV methods implemented in CSMP++ with a number of benchmark tests. This way, component processes like incompressible, non-miscible 2-phase flow (Buckley-Leverett problem), single-phase salt convection (Elder problem) and single-phase, incompressible thermal convection were verified. Here, we focus on benchmark tests dealing with highly compressible boiling systems where the decoupling of pressure and temperature introduces the largest errors. For such problems no analytic solutions are available, and only for the pure water systems a well-tested and reliable comparison code is available. Therefore, the bulk of the tests consisted of comparisons with the pure water multi-phase code HYDROTHERM, a widely used finite difference code developed by the USGS (Hayba and Ingebritsen, 1994a). We tested the three-phase handling of our code, i.e. including salt, by comparison of results of a 1D problem versus published results which were generated with TOUGH-NaCl (Kissling, 2005b,a). All benchmarks are summarized in table 6.1.

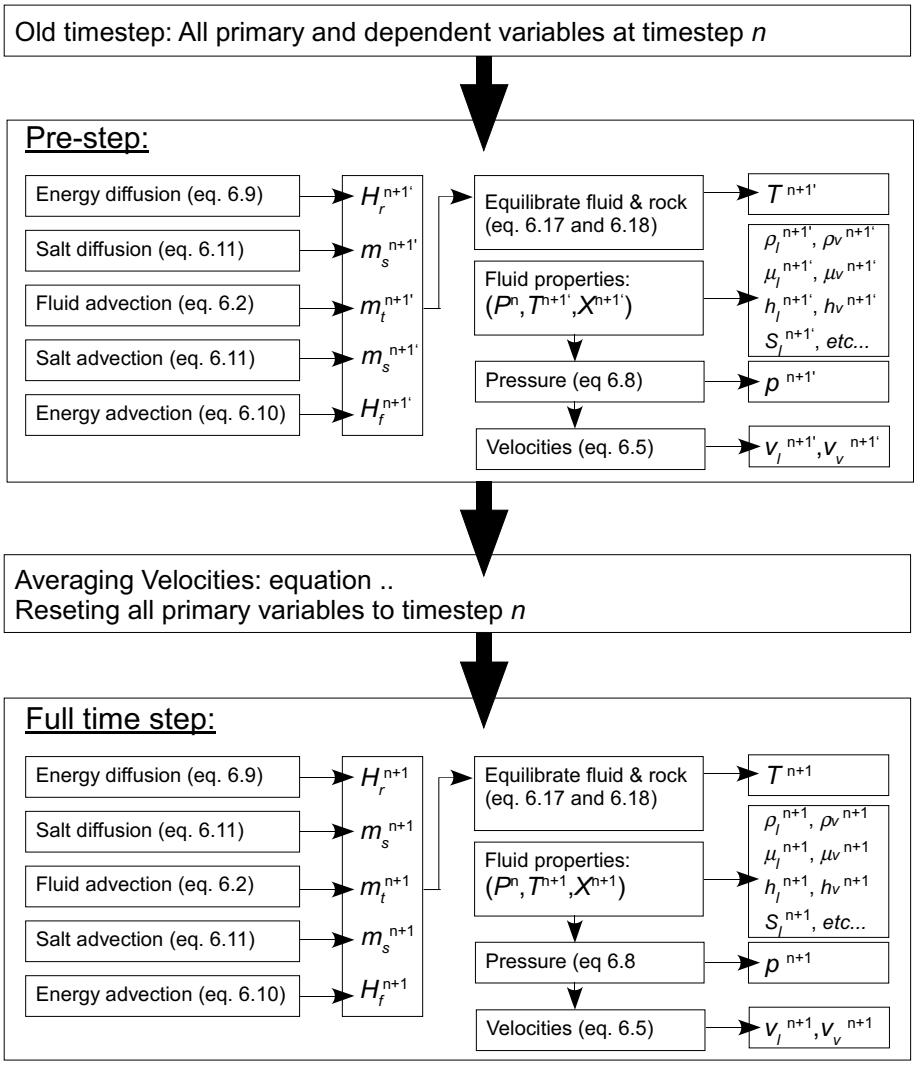

Fig. 6.2: Computational flow scheme for calculating a single timestep

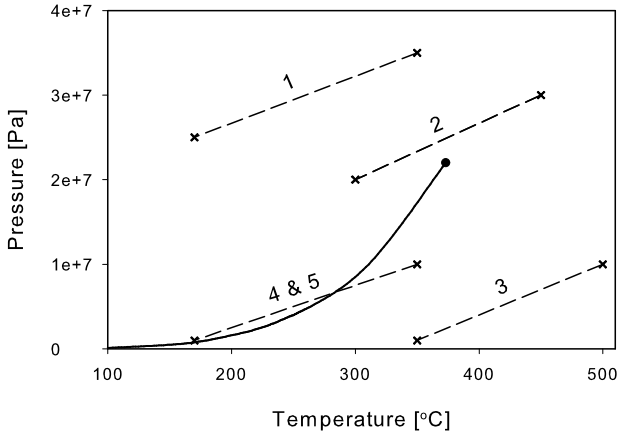

Fig. 6.3: Graphical representation of performed 1D benchmark tests between CSMP++ and HYDROTHERM. The solid thick line indicates the boiling curve of pure water. Numbers refer to benchmark tests as listed in table 6.1

Tab. 6.1:

1D pure water benchmarks with HYDROTHERM

#	Length	Boundary Conditions		State
	[m]	Left	Right	-
1*	2000	35MPa, 350°C	25MPa, 170°C	Single-phase liquid
2*	2000	30MPa, 450°C	20MPa, 300°C	Single-phase near-critical
3*	2000	10MPa, 500°C	1MPa, 350°C	Single-phase vapor
4*	100	10MPa, 350°C	1MPa, 170°C	Two-phase, sharp p-gradient
5*	2000	10MPa, 350°C	1MPa, 170°C	Two-phase

2D pure water benchmarks with HYDROTHERM

#	Length	Boundary Conditions		k	State
	x×z[km]	Top	Bottom	[m^2]	-
6*	3.0×1.0	0.2MPa, 10°C	3.0 Wm^{-2}	10^{-15}	Two-phase[1]
7	3.0×1.0	10MPa, 10°C	3.0 Wm^{-2}	10^{-15}	Two-phase[2]
8	3.0×1.0	15MPa, 10°C	3.0 Wm^{-2}	10^{-15}	Single-phase[2]
9	3.0×1.0	20MPa, 10°C	3.0 Wm^{-2}	10^{-15}	Single-phase[2]
10	3.0×1.0	25MPa, 10°C	3.0 Wm^{-2}	10^{-15}	Single-phase[2]
11	3.0×1.0	0.2MPa, 10°C	3.0 Wm^{-2}	10^{-14}	Boiling near bottom[2]
12*	3.0×1.0	10MPa, 10°C	600°C	10^{-15}	Boiling-zone[3]
13	1.5×1.0	0.2MPa, 10°C	3.0 Wm^{-2}	10^{-14}	Boiling near bottom
14*	1.5×1.0	0.2MPa, 10°C	6.0 Wm^{-2}	10^{-14}	Boiling neat bottom and top
15	1.5×1.0	0.2MPa, 10°C	3.0 Wm^{-2}	10^{-13}	Single-phase
16	1.5×1.0	0.2MPa, 10°C	6.0 Wm^{-2}	10^{-13}	Single-phase
17	1.5×1.0	14MPa, 10°C	3.0 Wm^{-2}	10^{-14}	Single-phase, near critical
18	1.5×1.0	14MPa, 10°C	6.0 Wm^{-2}	10^{-14}	Single-phase, near critical
19	1.5×1.0	14MPa, 10°C	10. Wm^{-2}	10^{-14}	Critical boiling[4]
20	1.5×1.0	14MPa, 10°C	6.0 Wm^{-2}	10^{-13}	Single-phase, near critical
21	1.5×1.0	17MPa, 10°C	20. Wm^{-2}	10^{-14}	Critical boiling
22	1.5×1.0	17MPa, 10°C	6.0 Wm^{-2}	10^{-16}	Single-phase diffusive
23	1.5×1.0	20MPa, 10°C	20. Wm^{-2}	10^{-14}	Single-phase

1D salt water benchmark with TOUGH-NaCl (Kissling, 2005a)

#	Length	Boundary Conditions		State
	[m]	Left	Right	-
24*	1000	200bar, 350°C, 30wt%	massflux: 0.05kg s^{-1}	Multi-phase

*: Result of simulations assigned an asterix are discussed in this article.

1: Heat flux applied along 400m of bottom boundary.

2: Heat flux applied along 900m of bottom boundary.

3: Temperature fixed along 400m of bottom boundary.

4: HYDROTHERM crashes near critical point.

6.4.1 1D pure water tests

In a first validation of our code, we compare one-dimensional energy transport in pure H_2O at liquid, vapor, two-phase and near-critical conditions with HYDROTHERM. All tests consisted of a hot fluid flowing down a pressure gradient, displacing cold liquid and heating up initially cold, fluid-saturated rock. Rock properties were uniform and set to $\lambda = 2.25$W m$^{-1\circ}$C^{-1}, $c_{pr} = 880$J kg$^{-1\circ}$C^{-1}, $\rho_r = 2750$kg m^{-3}, $\phi = 0.1$ and $k = 1.0 \times 10^{-14}$m^2. For the fluid, the relative permeability k_r was assumed linear, with a residual liquid saturation of 0.3 and a residual vapor saturation of 0. Tests were performed using 100m and 2000m horizontal domains, with spatial resolution of respectively 1m and 10m in both CSMP++ and HYDROTHERM. Figure 6.3 shows graphically the applied boundary conditions. In all 1D setups the left side of the domain was kept at high pressure-temperature conditions and the right-side at low pressure-temperature conditions.

Figure 6.4 compares CSMP++ and HYDROTHERM pressure (right vertical axis) and temperature (left vertical axis) profiles of 1D tests in the single-phase liquid, vapor and supercritical regions. The advancement and steepness of the thermal fronts match very well and the same holds for the pressure profile where the kink associated with a change in fluid properties is identical for both simulations. Interestingly, in the single-phase vapor simulation (figure 6.4c), both codes predict an undershoot in temperature towards the right boundary. The exact thermodynamic reasons for this to happen have not been determined but are likely related to the very small enthalpy difference between left and right boundary. At the inlet (10MPa, 500°C) the vapor enthalpy is roughly ~ 3400kJ kg^{-1} whereas at the outlet (1MPa, 350°C) it is roughly ~ 3200kJ kg^{-1}.

Figure 6.5 compares pressure, saturation and temperature profiles of 1D tests undergoing 2-phase conditions. Figures 6.5a-c plot results of benchmark test 4 (see table 6.1), which uses a sharp pressure drop and a residual saturation for the liquid phase of zero. For this large pressure drop, the thermal front in HYDROTHERM has propagated slightly further but the match between the two codes is still acceptable. Figure 6.5d-f plot results for the same initial and boundary conditions but by solving it on the 2000m instead of the 100m mesh the pressure gradient is greatly reduced. In addition, this test used a residual liquid saturation of 0.3. This test produces a very accurate match between HYDROTHERM and CSMP++ in terms of pressure, temperature and saturation.

6.4.2 2D pure water tests

A total of 18 2D pure water benchmarks with different pressure, temperature or heat-flux boundary conditions at different permeabilities have been performed. For all tests, the onset of convection, advancement of thermal front and boiling zones as well as the number of plumes accurately matched between HYDROTHERM and CSMP++. Here we will discuss some key tests in more detail. Tests were performed on domains of 3.0×1.0km and 1.5×1.0km, both consisting of roughly 1000 elements in CSMP++ and similar resolutions in HYDROTHERM. Rock properties were uniform and set to $\lambda = 2.25$W m$^{-1\circ}$C, $c_{pr} = 880$J kg$^{-1\circ}$C, $\rho_r = 2750$kg m^{-3}, $\phi = 0.1$ and permeability was varied as listed in table 6.1. This table also lists applied boundary conditions and the observed state of convection. Most simulations contained a bottom heat flux boundary condition since we encountered problems with fixed temperature boundary conditions in HYDROTHERM. Only when just part of the boundary was set to a fixed high temperature did we manage to get HYDROTHERM running (test 13, table 6.1).

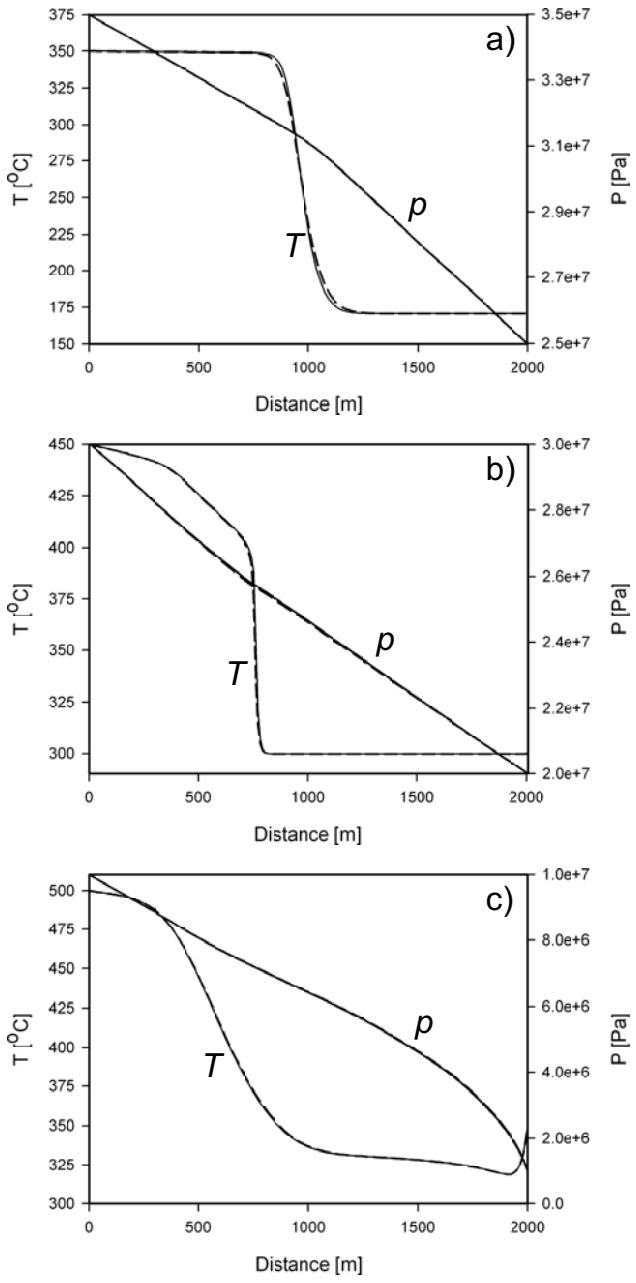

Fig. 6.4: Comparison between CSMP++ (solid lines) and HYDROTHERM (dashed lines) for selected 1D single-phase benchmark tests. Left axis plots temperature and right axis plots pressure. Figure a) shows results after 20,000 days for benchmark test 1, figure b) shows results after 6,000 days for benchmark test 2 and figure c) shows results after 160,000 days for benchmark test 3 (see table 6.1).

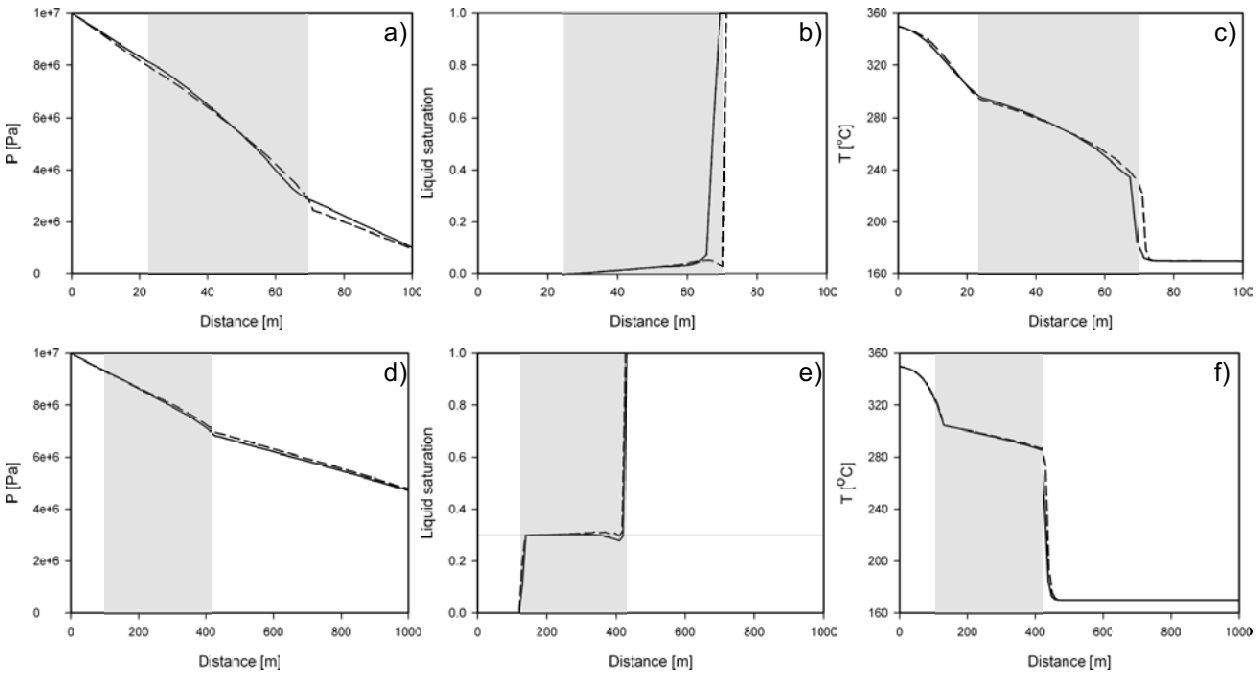

Fig. 6.5: Comparison between CSMP++ (solid lines) and HYDROTHERM (dashed lines) of 1D two-phase benchmark tests. Figures a), b) and c) show pressure, liquid saturation and temperature respectively of 1D benchmark test 4 after 45 days (see table 6.1). Figures d)-f) show the same variables for benchmark test 5 after 4,500 days.

Here we will discuss three of the 2D tests in detail, presenting comparisons between the two codes.

Figure 6.6 compares temperature and saturation contours of simulation 12, using a 600°C fixed temperature along a 400m distance at the left side of the bottom boundary and a fixed 10MPa pressure at the top. All other boundaries are no-flow, the permeability is set to $k = 1.0 \times 10^{-15}\mathrm{m}^2$, and linear relative permeability relations with a residual liquid saturation of 0.3 are used. After 1000 years, a boiling zone has developed (see figure 6.6a and b), with both codes predicting the same upward speed of the boiling front as well as saturations within the boiling zone. After 20,000 years, a steady state boiling zone has evolved, with isotherms and saturation profiles matching accurately between the two codes (figure 6.6c and d).

Figure 6.7 plots results from a similar simulation (6) though, instead of temperature, a fixed heat flux of $3.0\mathrm{Wm}^{-2}$ is imposed on the bottom boundary over a distance of 400m The top pressure is set to 2 bar. A boiling zone develops with very small vapor saturations, and a steady state boiling zone has evolved after 6000 years. Isotherms and saturation profiles generally match properly between the two codes showing an increased vapor saturation of 0.2 near the top of the system. HYDROTHERM results show some artifacts in the saturation near the bottom heat source for unexplained reason.

These two tests both produced single boiling zones which achieve a steady state, which allows one-to-one comparison by plotting results on top of each other. In a final test, we investigate unsteady, oscillatory convection at boiling conditions. In this simulation (14), the permeability is set an order of magnitude higher (i.e. $k = 1.0 \times 10^{-14}\mathrm{m}^2$), the heat flux is fixed along the full length of the bottom boundary at $6.0\mathrm{Wm}^{-2}$ and the top boundary is

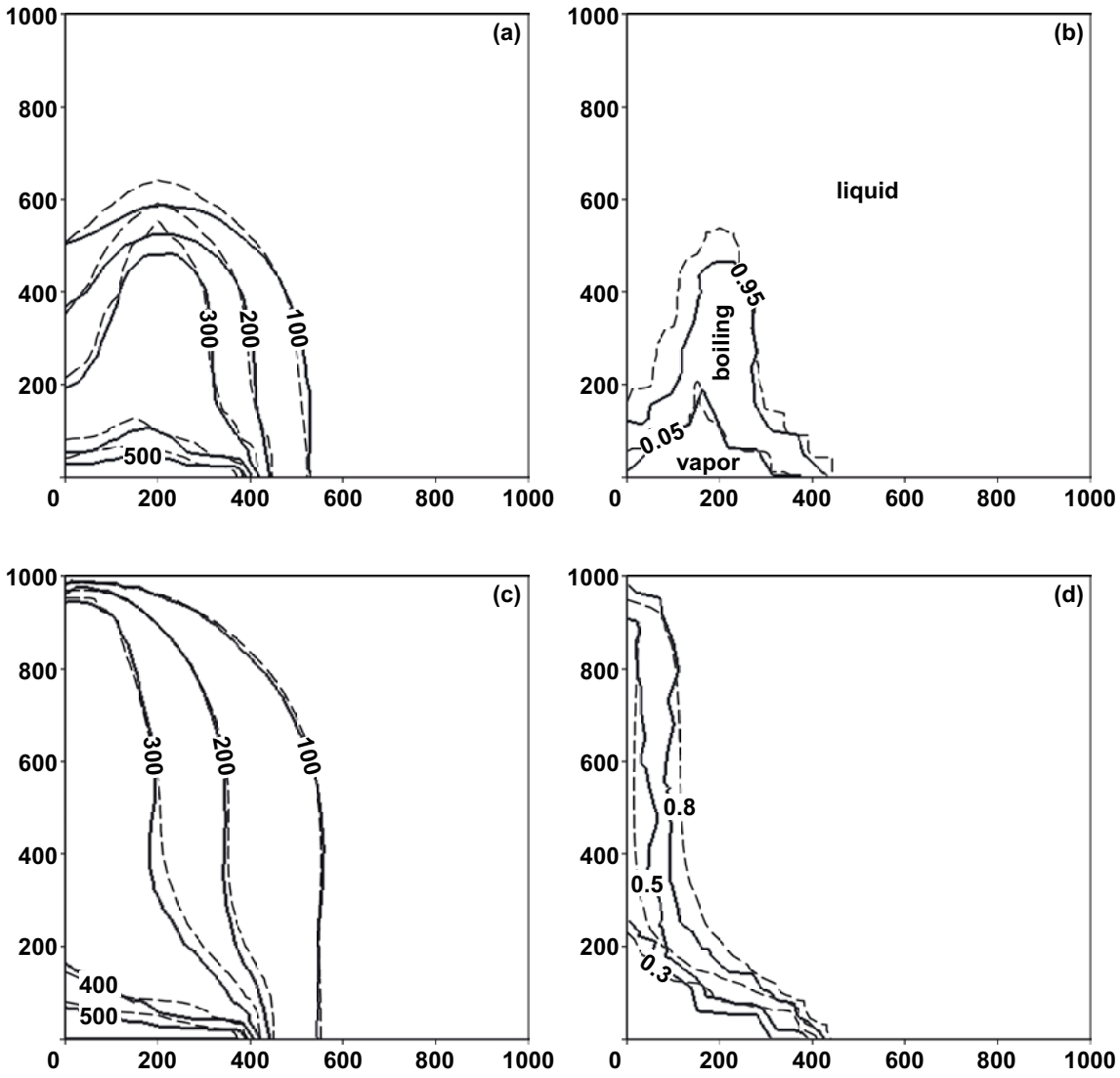

Fig. 6.6: Comparison between CSMP++ (solid lines) and HYDROTHERM (dashed lines) of the block-shaped temperature profile simulation 12 (table 6.1). Figures a and b plot isotherms (°C) and liquid saturation contour lines at 1,000 years. Figures c and d plot the same variables at 20,000 years.

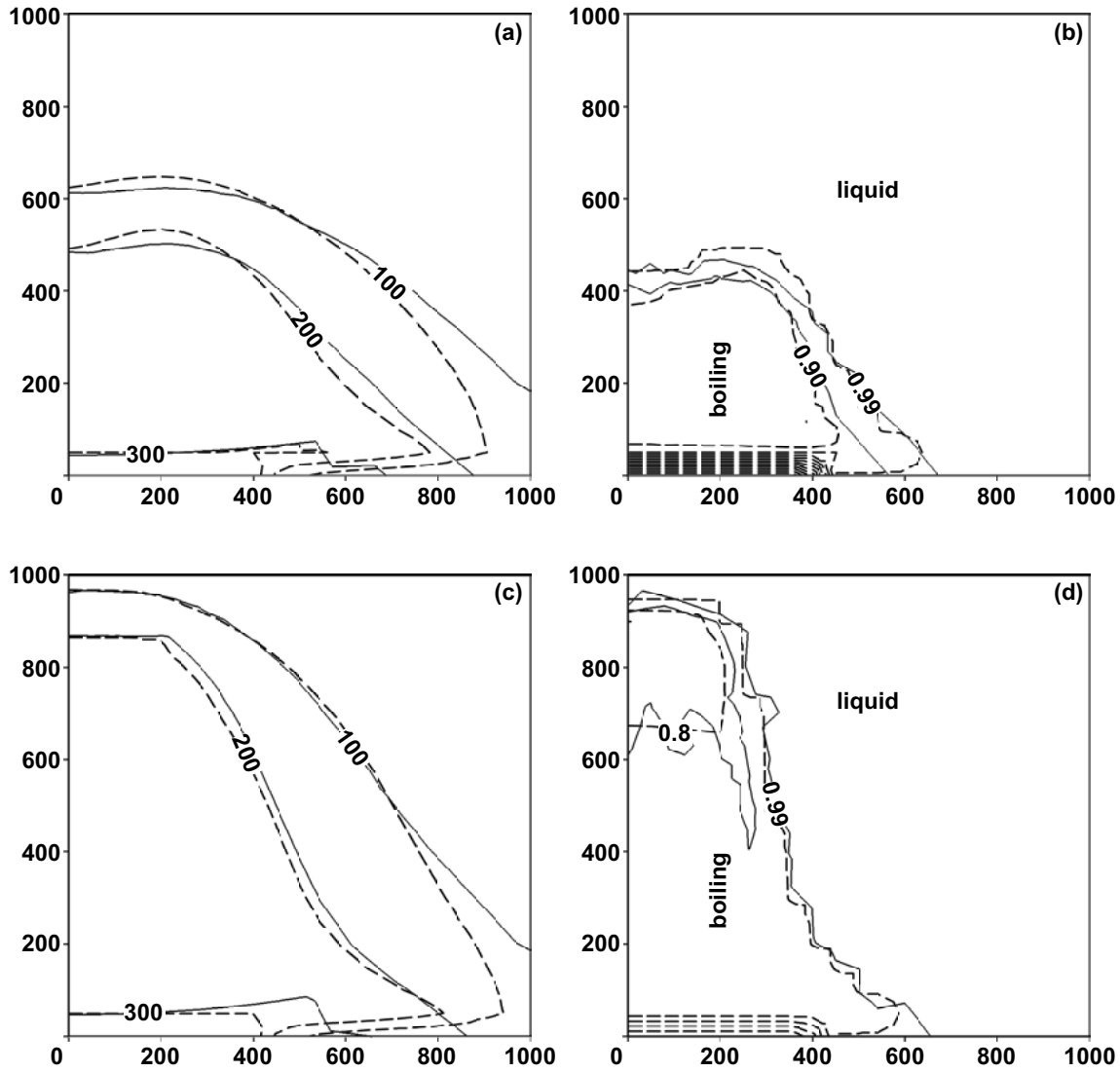

Fig. 6.7: Comparison between CSMP++ (solid lines) and HYDROTHERM (dashed lines) of the block-shaped heat-flux profile simulation with a top pressure of 2 bar. Figures a and b plot isotherms (°C) and liquid saturation contour lines at 4,000 years. Figures c and d plot the same variables at 6,000 years.

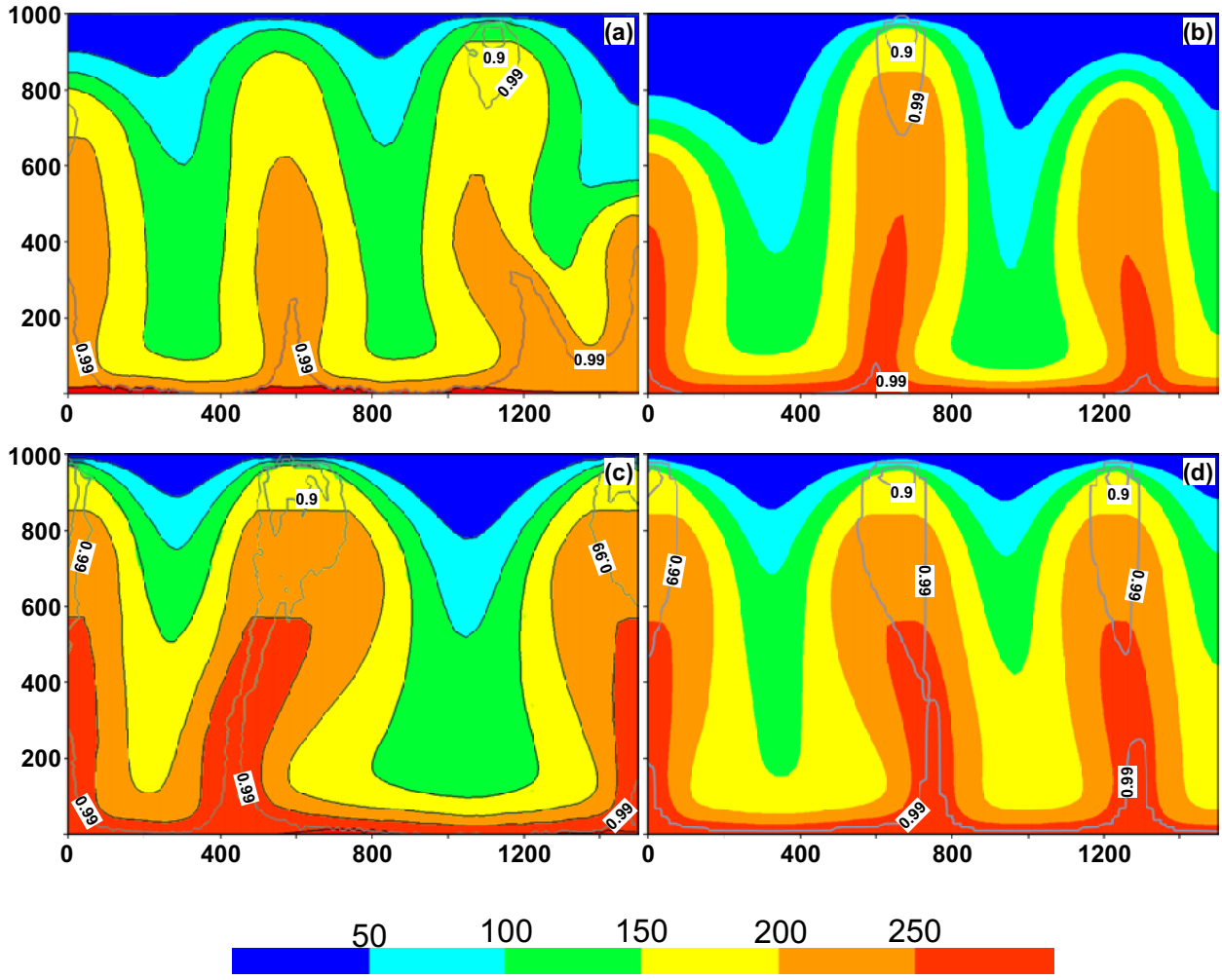

Fig. 6.8: Benchmark test 14 (table 6.1). a) CSMP++ temperature field (colors) and labeled saturation contours (grey lines) after 2000 years. b) HYDROTHERM temperature field (colors) and labeled saturation contours (grey lines) after 2000 years. Figures c and d plot the same variables after 4000 years.

set to 2bar. At these conditions, oscillatory convection develops, consisting of three thermal plumes as shown in figure 6.8. Boiling occurs in the upwelling regions near the bottom boundary where a very small amount of liquid boils off. The fluids then move upwards as a single-phase liquid, hitting the boiling curve again at low pressures, where again only a small amount of liquid boils off into vapor. HYDROTHERM and CSPMP++ both show this typical convective behavior, giving the same number of upflow zones, liquid saturations in the separate boiling regions and isotherm patterns. Full boiling zones stretching from bottom to top develop regularly, with a very small vapor content, something which is observed in both codes.

6.4.3 1D salt water test

In a final test, we reproduce the results from a 1D multiphase brine flow experiment as published by Kissling (2005a) using NaCl-TOUGH2. The simulation consists of a 1000m

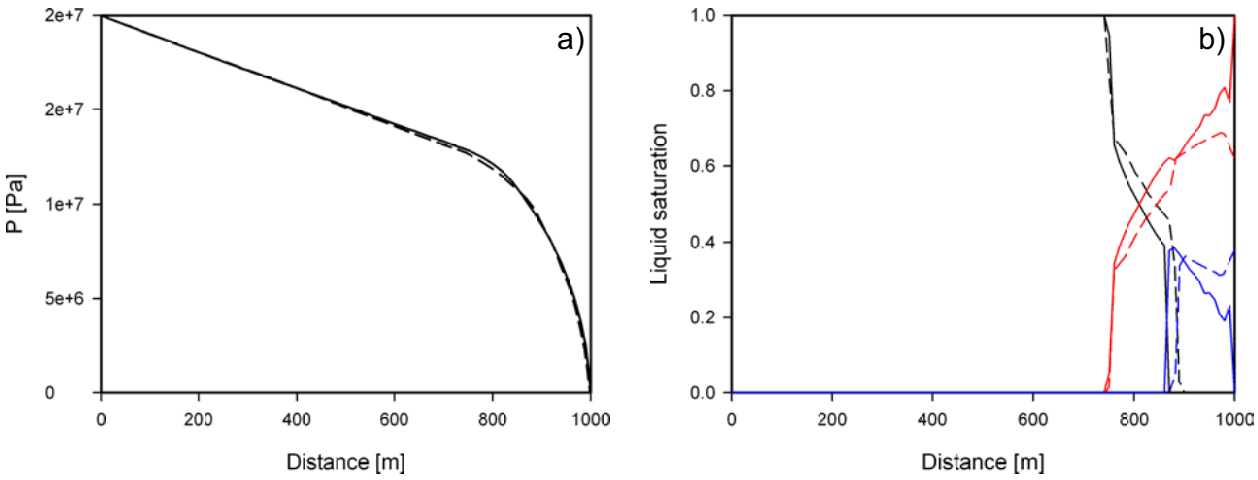

Fig. 6.9: Benchmark test 24. a) 1D pressure profile and b) liquid (black), vapor (red) and halite (blue) saturation of CSMP++ (solid lines) and NaCl-TOUGH2 (dashed lines). NaCl-TOUGH2 results were taken from Kissling (2005a)

horizontal column, with fluid production at one end and a fixed pressure, temperature and salt mass fraction at the other end. Initially the fluid in the column is in the liquid state at 200 bar, 350°C and 30wt% salt. The left end of the domain is kept fixed at these conditions, whereas at the right end fluid is withdrawn at a rate of 0.05kg/s. Properties of the rock are $k = 5.0\text{e}{-15}\text{m}^2$, $\phi = 0.01$, $c_{pr} = 1000\text{J kg}^{-1}\text{°C}^{-1}$ and $\lambda = 3.0\text{W m}^{-1}\text{°C}^{-1}$ and $\rho_r = 2650\text{kg m}^{-3}$. As described by Kissling (2005a), due to the fluid production, the pressure steadily drops in the domain, causing a number of phase changes. At the withdrawal end, the fluid state successively changes from liquid to vapor-liquid, to vapor-liquid-halite and finally to vapor-halite, as reported by Kissling (2005a). After some time, the pressure on the withdrawal end drops below zero and the fixed flux can no longer be maintained. At this point, the pressure and state distribution in the horizontal column are as plotted in figure 6.9. This figure shows in general a good agreement between our results and those produced with THOUGH-NaCl by Kissling (2005a). The pressure curves fit accurately and the state changes occur essentially at the same locations. Saturations are similar though small deviations are observed. Kissling (2005a) reports that this state is reached after ~ 55 days whereas in our simulations pressure drops below zero only after 108 days. We attribute this difference to the different equation of state used in the two different codes. Kissling (2005a) uses the equation of state from Palliser and McKibbin (1998a,b,c), which is known to contain some erroneous formulations (Driesner and Heinrich, 2007). For instance, this EOS produces un-physical negative heat capacities of fluids with a finite NaCl concentration just above the critical temperature of water. Also, the values for specific enthalpy can be substantially different between the two NaCl-H_2O formulations, which could well cause the observed differences between the two codes.

6.5 Outlook

We showed that the newly implemented PHX scheme, which is the first of its kind, accurately resolves multiphase flow of an H_2O-NaCl fluid at high-temperature conditions. During the course of this work, a number of intrinsic features of this scheme proved to be problematic,

some of which still need further attention in the near future. More precisely, the handling of large pressure source terms, associated with phase-separation, is currently treated in a numerically stable way but requires small timestepping. On the one hand, this is a consequence of using an explicit time-discretization method, whereas implicit methods would likely suffer convergence problems. Still, it is likely that the current scheme is too conservative, taking very small timesteps where this is not necessarily required. Smarter timestep calculation algorithms need to be developed to resolve this issue and are likely to reduce calculation time substantially. Next to that, the use of lookup tables, enabling fast access to all phase properties, and parallel computing techniques will certainly reduce calculation time.

Next to these algorithmic improvements, more elaborate benchmarking, especially including boiling salty fluids, is advisable. The current lack of other transport codes with consistent equation of state of the H_2O-NaCl system, hinders more thorough comparisons. The equation of state by Driesner and Heinrich (2007) is currently the best description of high-pressure and high-temperature H_2O-NaCl thermodynamic properties and may eventually be included in other codes, taking different numerical approaches. This would enable direct comparisons and useful benchmarking. Ideally, a number of generally accepted, relevant, standard tests would need to be defined, for all codes to reproduce the associated results. Clearly something like this will still take several years to accomplish, but ultimately would greatly enhance confidence in simulation codes that handle the complex physics of multi-phase, incompressible fluid flow.

6.6 Conclusions

We developed a novel method, based upon a FEFV numerical scheme, to simulate the transport of high-temperature multi-phase H_2O-NaCl fluids. We prove the correctness of our numerical approach with a range of comparison tests against the USGS code HYDROTHERM (Hayba and Ingebritsen, 1994a), as well as one against published results produced with NaCl-TOUGH2 (Kissling, 2005a). All tests give accurate results, but a limitation of the code remains that often small timesteps need to be taken. Nevertheless, solid numerical studies of high-temperature boiling salty fluids in the subsurface are now possible. Hence a broad range of Earth-scientific questions can now be addressed, including salinity variations at black-smoker systems and the formation of hydrothermal ore-deposits.

7. HEAT TRANSPORT AT BOILING, NEAR-CRITICAL CONDITIONS

7.1 Abstract

Near-critical phenomena and two-phase flow are of fundamental importance in submarine hydrothermal systems, and are likely to enhance energy transport considerably. We present a series of 2D simulation runs investigating two-phase fluid flow of pure water at near-critical conditions. The results show that two-phase convection can be even more efficient in transporting energy than single-phase convection can do at near-critical conditions. The highest heat fluxes are reached whenever two-phase heat-pipes form near the bottom boundary, recharging the root of the upflow zone and thereby enabling the formation of broad upflow regions. However, when the system becomes more vapor-dominated it loses this ability and the energy efficiency drops to more moderate values.

7.2 Introduction

The pressure-temperature conditions of many black-smoker vent fluids are close to both the critical points of water (22.1 MPa, 374°C) and seawater (29.8 MPa, 407°C) (Von Damm et al., 2003). Therefore, it is expected that near-critical behavior of fluids influences energy transport in the sub-seafloor convection cell. Near the critical point, the thermal expansivity of water peaks and coincides with a minimum in the kinematic viscosity such that buoyancy forces are maximized and viscous drag forces are minimized. Together with a peak in the heat capacity this leads to very efficient energy transport mechanisms. Another distinct feature of black-smoker vent fluids is the large range in measured vent salinities, from ~ 0.05 to ~ 2.5 times seawater salinity (Von Damm et al., 1995, 1997, 2003; Seyfried et al., 2003). This observation testifies that phase separation takes place in many black-smoker systems, indicating that two-phase liquid-vapor interactions are also important in sub-seafloor convection (Foustoukos and Seyfried, 2007).

Numerical modeling of convection at near-critical conditions is challenging, due to the aforementioned extrema in fluid properties, the singularity in the equation of state at the critical point of water and two-phase flow at sub-critical conditions. Most studies investigating black-smoker hydrothermal convection avoided the near-critical region by setting pressures sufficiently high, such that pure water is a single-phase, supercritical fluid (Jupp and Schultz, 2000, 2004; Coumou et al., 2006). Other studies used properties of salt water, which can boil at pressures above the critical point (Driesner and Heinrich, 2007), but treated fluids in the two-phase region as single-phase by taking a weighted mean of liquid and vapor (Wilcock, 1998; Fontaine and Wilcock, 2007). Although both approaches avoided critical conditions as well as two-phase flow, they showed that the non-linearity in fluid properties

is a first-order control on convection. Jupp and Schultz (2000) showed that at supercritical pressures, cells operating at $\sim$ 400°C can transport energy most efficiently, a value which is expected to shift towards critical temperatures ($\sim$374°C) when the pressure is lowered towards critical pressures. They argued that for any driving temperature larger than 500°C, upwelling temperatures will be around 400°C and therefore the associated energy transport will be similar.

Commonly, the efficiency of heat transport is described by the Nusselt number (Nu), which is the transported energy divided by the energy transport by conduction only. Fontaine and Wilcock (2007) studied the efficiency of energy transport in open-top systems, in which fluids are allowed to flow undisturbed through the top of the model, at super-critical conditions using non-linear fluid properties. For their specific model, they found Nu numbers ranging from $\sim$12 for low-permeability systems (2.25×10^{-15}m^2) to $\sim$ 50 for a higher permeability of 1.12×10^{-14}m^2. This shows that at supercritical conditions energy transport can be very efficient.

Other studies took a different approach by focussing on heat transport very close to the critical point of H_2O but using models with very small spatial scales, comparable to those of lab-experiments (Cox and Pruess, 1990; Ingebritsen and Hayba, 1994). Ingebritsen and Hayba (1994) showed that heat transfer by single-phase fluids close to the critical point can be highly efficient, reaching Nu numbers of up to $\sim$ 200. In order to create such large Nu numbers, relatively large permeabilities (10^{-12}-10^{-13}m^2) were required, leading to the conclusion that superconvection, i.e. convection with $Nu > 100$, is probably not very common in nature (Ingebritsen and Hayba, 1994). However, their only two-phase simulation produced a substantially higher efficiency ($Nu \sim 500$), suggesting that near-critical two-phase processes can enhance heat transfer substantially. Intuitively, this makes sense, since the low density of the vapor phase enhances buoyancy forces which could reinforce convection, and the vapor's specific enthalpy is larger at sub-critical pressures than at the critical point itself (Ingebritsen et al., 2006). In addition, under two-phase conditions the counter-current flow of liquid and vapor, so-called heat-pipes, is a likely mechanism to enhance energy transport.

Heat-pipes can form if the pressure gradient in two-phase upflow zones settles between vapor-static and liquid-static, such that liquid will flow downwards and vapor upwards. This way, energy is absorbed at the base of the heat-pipe and carried upward by the low-density vapor phase (Ingebritsen et al., 2006). Within the context of black-smoker systems, heat-pipe solutions have been studied by Bai et al. (2003) and Seyfried et al. (2003), though not in terms of Nu numbers.

In this study, building upon the work by Fontaine and Wilcock (2007) and Ingebritsen and Hayba (1994), we investigate the effects of two-phase flow at near-critical conditions in two dimensions. In contrast to Ingebritsen and Hayba (1994), we study convection over larger domains, using model sizes appropriate for black-smoker hydrothermal systems. In contrast to Fontaine and Wilcock (2007), we include two-phase flow of liquid and vapor in our simulations. We apply different top pressures, permeability and relative-permeability scenarios and present the simulation results in terms of the Nu number. The results show that very large Nu can be achieved, up to $\sim$ 1000, but only under restricted conditions.

7.3 Computational Method

We use the pressure-enthalpy (PH) based multi-phase fluid transport scheme of our numerical modeling code CSMP++, in which the following expressions for mass and energy conservation are solved (see chapter 6):

$$\phi \frac{\partial[(S_l\rho_l + S_v\rho_v)]}{\partial t} = -\nabla \cdot (\mathbf{v}_l\rho_l) - \nabla \cdot (\mathbf{v}_v\rho_v) \tag{7.1}$$

$$\frac{\partial[(1-\phi)\rho_r h_r + \phi(S_l\rho_l h_l + S_v\rho_v h_v)]}{\partial t} = -\nabla \cdot (\mathbf{v}_l\rho_l h_l) - \nabla \cdot (\mathbf{v}_v\rho_v h_v) - \nabla \cdot K\nabla T \tag{7.2}$$

Here, ϕ is the porosity, S volumetric saturation, ρ density, h specific enthalpy, K thermal conductivity and T temperature, and subscripts l, v and r stand for liquid, vapor and rock respectively. We assume that the volume flux $\mathbf{v}$ can be described by the two-phase form of the Darcy equation (Ingebritsen et al., 2006):

$$\mathbf{v}_i = -\mathbf{k}\frac{k_{ri}}{\mu_i}\left[\nabla p - \rho_i \mathbf{g}\right] \qquad\qquad i = \{l, v\} \tag{7.3}$$

Where $\mathbf{k}$ is the intrinsic permeability, k_r the relative permeability, μ viscosity, p pressure and $\mathbf{g}$ the acceleration due to gravity. In our approach we assume that fluid and rock are in thermal equilibrium, capillary-pressure effects are negligible, the rock matrix is incompressible and that the fluid can be described by pure H_2O (Haar et al., 1984).

We solve equations 7.1-7.3 on a rectangular 2-dimensional 1500x500 meter domain, discretized with a total of 21,000 triangular elements. The side boundaries were set to no flow and the bottom boundary to constant temperature and no flow. The top boundary represents the seafloor and was set to constant pressure. To allow hot fluids to vent, a mixed energy boundary condition was applied at the top. In elements where the total volume flux $(\mathbf{v}_l + \mathbf{v}_v)$ was upwards, the temperature gradient was set to zero to allow undisturbed venting of upwelling fluids. Elements with the total volume flux pointing downwards take in cold water. In successive simulation runs, we vary the temperature at the bottom boundary from 300°C up to 700°C, and analyze energy transport through the top of the domain. In most simulation runs, we set the pressure at the top to 15MPa, use linear relative permeability functions with residual saturations for liquid and vapor of 0.3 and 0 respectively, and take a homogeneous permeability of $5.0 \times 10^{-15}\text{m}^2$. In successive simulation runs we vary the top pressure (to 18MPa and 21MPa) and permeability (to $5.0 \times 10^{-14}\text{m}^2$) and test non-linear relative permeability relations.

7.4 Results

We present results in terms of the Nu number, which is the ratio of the simulated heat transfer over the heat transfer by conduction only: $Nu = Q/(K\triangle T/\triangle z)$, with Q being the horizontally averaged heat flux through the top boundary and $\triangle z = 500$m.

We can identify four basic convection types which we will refer to as: (1) single-phase, (2) two-phase heat-pipe, (3) two-phase vapor-dominated and (4) supercritical systems. Single-phase fluid flow occurs when bottom temperatures are set below the boiling temperature for

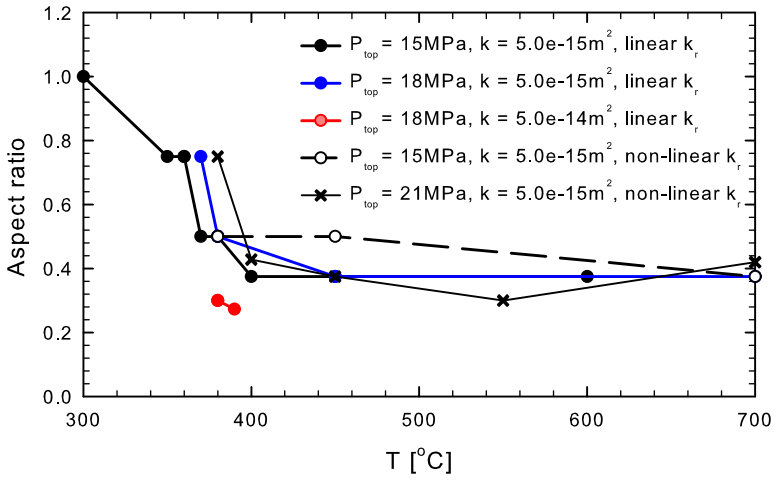

Fig. 7.1: Aspect ratio of convection cells as a function of temperature specified at the bottom boundary for different pressure, permeability and relative permeability settings.

near-bottom pressures. Single-phase convection is characterized by relatively large aspect ratios (0.75-1.0), defined as the horizontal width of one convection cell divided by its vertical length (figure 7.1). The efficiency in transporting energy is relatively low with $Nu < 5$. The temperature of upwelling fluids drops substantially on their way up, as shown in the pressure-temperature diagram (figure 7.2).

Two-phase heat-pipe systems develop when the bottom temperature is set close to but slightly higher than the boiling temperature for near-bottom pressures. For $k = 5.0 \times 10^{-15}\text{m}^2$, the aspect ratio ranges from 0.4 to 0.5 (fig. 7.1). This type of convection is characterized by broad two-phase upflow zones, which are recharged in the bottom regions through heat-pipes mechanisms (figure 7.3e). At the center of the upflow zone a perfect heat-pipe forms with liquid and vapor flowing near-vertical in opposite directions. At the edges, liquid flows downward but also has a substantial horizontal flow-component, so fluid flow is not truly counter-current. On its way down, the liquid phase steadily boils off, creating vapor that rises swiftly. This mechanism is very efficient in transferring energy and enables the formation of broad upflow zones (figure 7.3b) which can still be efficiently recharged. This convection style produces the largest Nu numbers observed at $k = 5.0 \times 10^{-15}\text{m}^2$ of up to 90.

For higher bottom temperatures ($\sim 450°\text{C}$ or higher), the system shifts towards two-phase vapor-dominated upflow zones which have substantially smaller heat-pipe zones (figure 7.3c and f). These systems are characterized by small aspect ratios (~ 0.33, fig. 7.1), narrow upflow zones, and large pure vapor regions directly above the bottom boundary (figure 7.3f). Nu numbers for two-phase vapor-dominated convection are moderate, from 10-20 for $k = 5.0 \times 10^{-15}\text{m}^2$, with a trend towards slightly higher Nu for larger bottom temperatures.

Thus, Nu numbers as a function of bottom temperature evolve from low values at single-phase conditions to a peak at two-phase heat-pipe conditions and towards moderate values at vapor dominated conditions. This is summarized in figure 7.4 which plots the Nu number

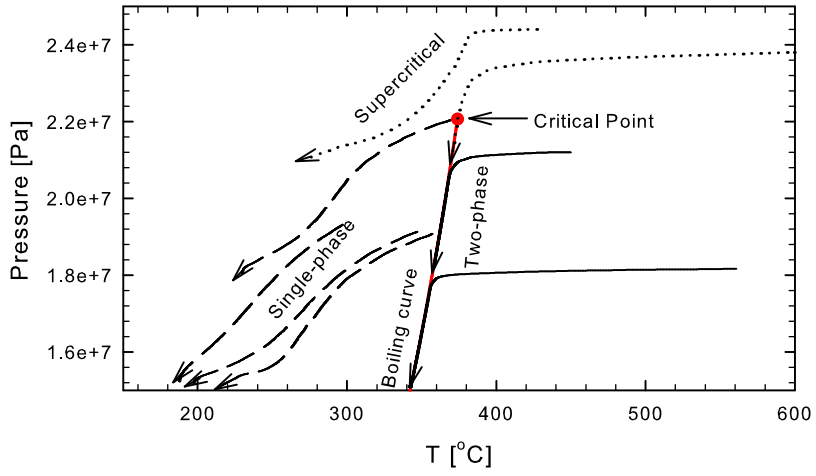

Fig. 7.2: Pressure-temperature paths of fluids in upflow zones of single-phase (dashed), two-phase (solid) or supercritical (dotted) simulation runs. Also plotted is the boiling-curve and critical point of pure water (solid red).

against the temperature specified at the bottom boundary for different pressure, permeability and relative permeability scenarios. It shows that high Nu numbers can be reached when permeability is sufficient with several simulations close to $Nu = 100$ and some even close to $Nu = 1000$. The peak of maximum Nu number shifts to higher temperatures when the top pressure is increased, reflecting the increased boiling temperature at higher pressures. Increasing the top pressure will increase the Nu number as long as bottom pressures do not exceed the critical pressure. This happens since two-phase fluids closer to the critical point will have a larger fluxibility F, which is a measure of the ability of a fluid to transport energy (Jupp and Schultz, 2004) and for a two-phase fluid is given by (Geiger et al., 2005):

$$F = \frac{k_{rl} S_l \rho_l}{\mu_l}(h_l - h_0)(\rho_0 - \rho_l) + \frac{k_{rv} S_v \rho_v}{\mu_v}(h_v - h_0)(\rho_0 - \rho_v) \tag{7.4}$$

Figure 7.5 plots the fluxibility of a two-phase fluid along the boiling curve for different saturations. It shows that, for all pressure-temperature conditions, the vapor phase has a larger fluxibility than the liquid phase and both increase towards the critical point. The maximum of the vapor-fluxibility actually lies at slightly lower pressure-temperature conditions than the critical point itself due to its larger specific enthalpy at slightly sub-critical conditions.

The drop in Nu number from the peak at moderate bottom temperatures (370°C-400°C) towards substantially lower values at high bottom temperatures (450°C-700°C) is surprising and requires further explanation. To this end, we analyze two typical simulations in more detail. The first has standard conditions ($p_{top} = 15$MPa and $k = 5.0e-15\text{m}^2$) with the bottom boundary set to 370°C. This simulation gave a Nu number of 35 and a snapshot is plotted in figure 7.3b. The second simulation has the same conditions except for a bottom temperature of 600°C (plotted in figure 7.3c). It has a Nu number of ~ 8 and lies within the vapor-dominated region in figure 7.4. The relatively low value of the Nu number results partly from the way the Nu number is calculated, since for a 600°C bottom temperature

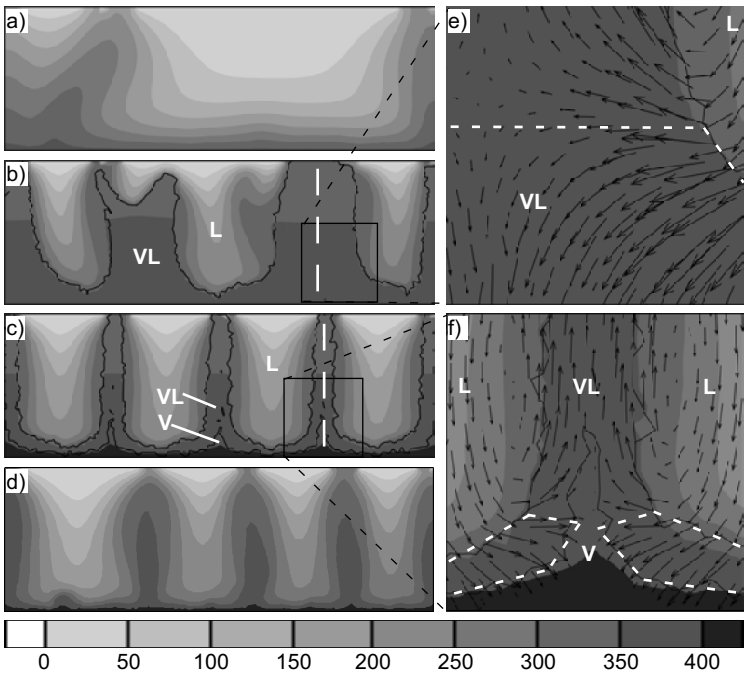

Fig. 7.3: Thermal structure (grey contours) and phase regions (black lines) of the four identified types of convection. a) single-phase fluid flow. b) Two-phase fluid flow with heat-pipe formation. c) Vapor-dominated two-phase fluid flow. d) Supercritical fluid flow. e) and f) show zoomed-in regions with the liquid velocity plotted, vapor velocities (not plotted) are always near-vertical, pointing upwards. Further indicated are phase-regions: two-phase (VL), liquid (L) and vapor (V). Long dashed white lines are vertical cross-sections as plotted in figure 7.6. Dashed white lines in figures e) and f) bound the region where counter-current flow takes place.

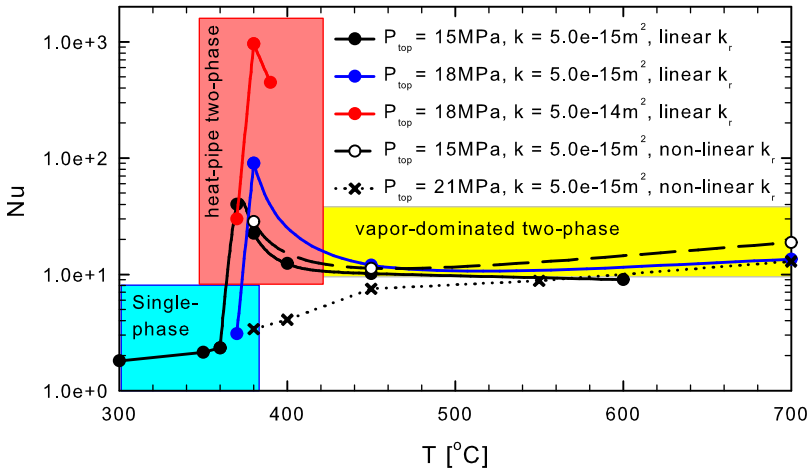

Fig. 7.4: *Nu* number as function of temperature specified at the bottom boundary for different pressure, permeability and relative permeability settings. Boxes indicate if convection was typified by single-phase, two-phase heat-pipe or two-phase vapor-dominated heat flow.

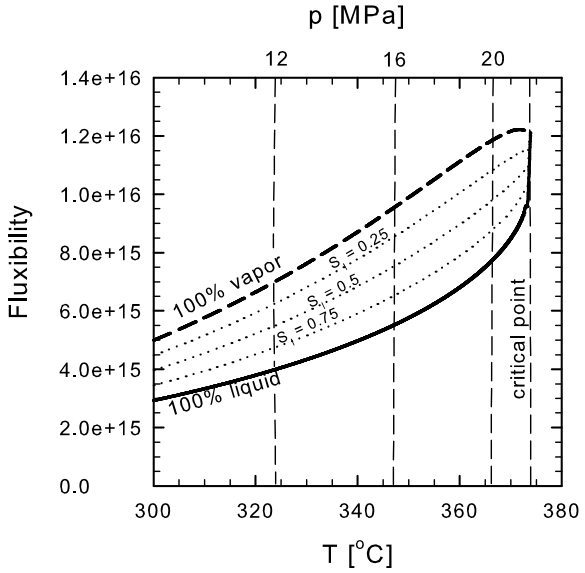

Fig. 7.5: Fluxibility (equation 7.4) along the boiling curve for different saturations plotted against temperature (bottom axis) and pressure (top axis).

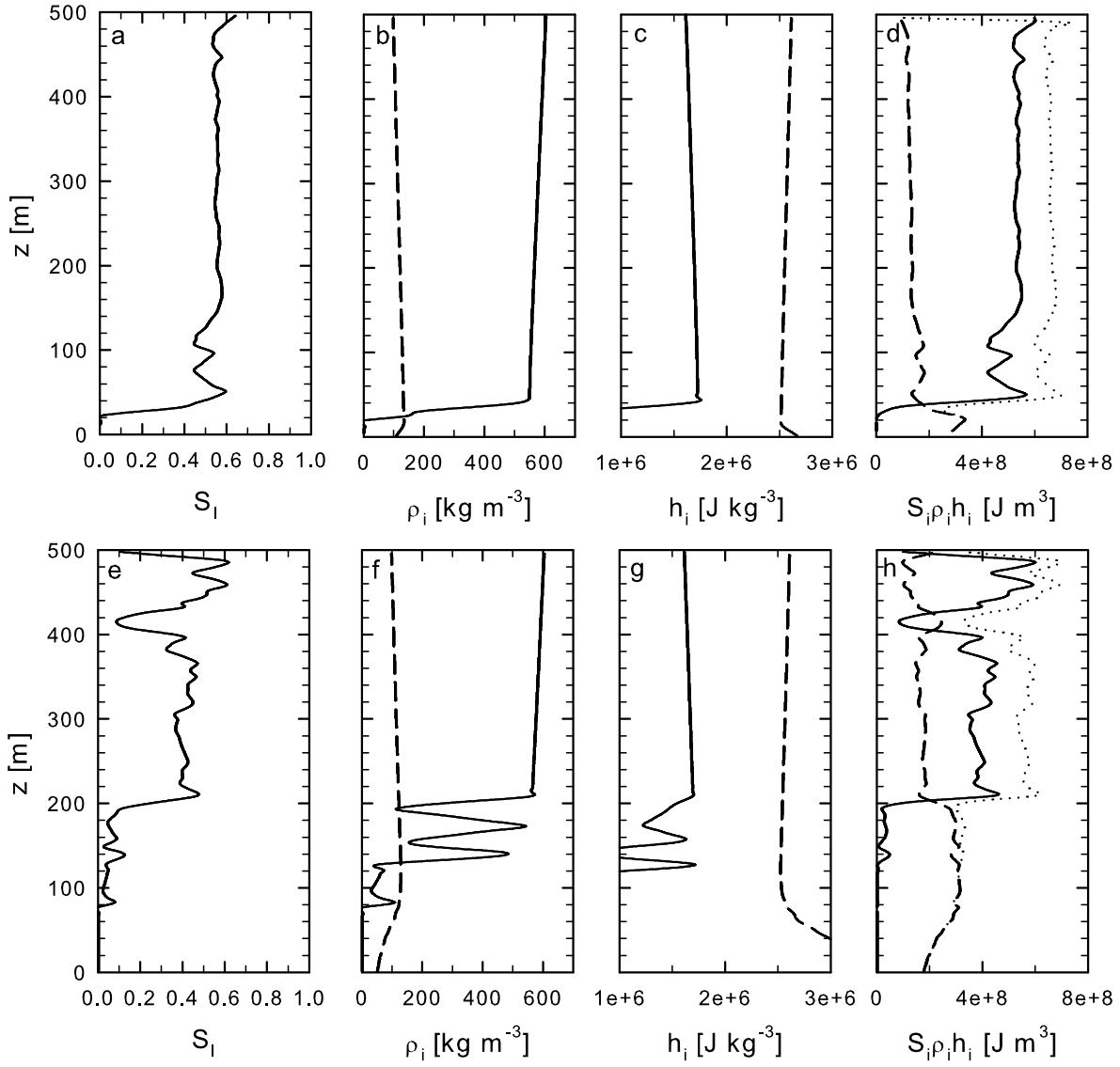

Fig. 7.6: Liquid (solid) and vapor (dashed) properties in the upflow zone of a two-phase heat-pipe simulation (fig. 7.3b). a) liquid saturation, b) density, c) specific enthalpy and d) volumetric enthalpy. The dotted curve in d) is the sum of liquid and vapor. Figures e)-h) plot the same variables for properties in upflow zone of two-phase vapor-dominated simulation (fig. 7.3c)

the heat flux by conduction only is larger. Still, its absolute energy transport is nearly 3 times smaller. Figure 7.6 plots the fluid properties in vertical cross-sections through the upflow zone in the two simulations. It shows that the volumetric enthalpy ($S_i\rho_i h_i$) for the liquid phase is larger (figure 7.6d and h) and, since liquid saturations in the vapor-dominated simulation are smaller (fig. 7.6a and e), the total volumetric enthalpy ($S_l\rho_l h_l + S_v\rho_v h_v$) is slightly smaller in the vapor-dominated case. In the top 300m, liquid saturations in both simulations are similar ($\sim$0.5 and $\sim$0.4 respectively), such that also the fluxibility of fluids in this part of the upflow zone is similar. Therefore, a difference in fluid properties cannot account for the different amount of energy transported by the two simulations. However, since liquid saturations are below residual (0.3) in the bottom 200m of the vapor dominated case (fig. 7.6e), counter-current flow paths cannot develop here. In fact only a very narrow zone at the edge of the two-phase area shows counter-current flow (fig. 7.3f). Also, the low density of the vapor phase precludes the formation of a stable horizontal vapor layer at the bottom. Instead, the vapor phase will rise quickly, resulting in many but narrow upflow zones. In contrast, in the lower bottom-temperature simulation, the region where vapor and liquid flow in opposite directions is much larger (fig. 7.3e). The heat-pipe mechanism efficiently recharges the root of the hydrothermal upflow zone and thereby allows the formation of a broad upflow zone. Therefore, upflow occurs in a horizontal surface area roughly 3 times larger in this simulation than in the vapor-dominated one (compare figure 7.3b and c). This results thus in larger total mass fluxes and therefore energy fluxes through the system.

If bottom pressures exceed the critical pressure, single-phase super-critical fluid flow develops, which can achieve similar Nu numbers as vapor-dominated systems (figure 7.4). Supercritical convection at $k = 5.0 \times 10^{-15}\text{m}^2$, with bottom temperatures set to 450-550°C, are characterized by aspect ratios ~ 0.35 and Nu numbers of $\sim 7.5 - 9.0$. Buoyancy forces in supercritical systems are smaller compared to boiling systems, and counter-current fluid flow cannot develop. Figure 7.7 plots the pressure in upflow and downflow regions, as well as hydrostatic pressures calculated from the fluid density distribution, for subcritical (18MPa at the top) and supercritical (21MPa at the top) systems, with bottom temperature set to 450°C. It shows that driving forces are much larger in the sub-critical case, due to the density-lowering effect of the vapor phase. In one particular simulation, in which k was set to $5.0 \times 10^{-15}\text{m}^2$, the top pressure to 21MPa and the bottom temperature to 700°C, rising supercritical fluids hit the critical point and follow the boiling-curve from there (figure 7.2). However, this simulation produced only moderate Nu numbers of ~ 13.

In three simulations, an order of magnitude higher permeability was used, $5.0 \times 10^{-14}\text{m}^2$, producing Nu numbers of up to 1000. In three other simulations, we tested the effect of non-linear instead of linear relative permeability functions, in two-phase fluid flow. The use of non-linear relative permeabilities did not affect the Nu-curve as function of temperature substantially (figure 7.4).

7.5 Discussion

Energy transport in near-critical boiling systems is affected by several factors which interact non-linearly, influencing the efficiency of convective systems to transport energy. Due to this interaction it is hard to establish the quantitative effect of each one individually and therefore we will rather qualitatively summarize them.

1) Two-phase fluids close to the critical point have a larger fluxibility than fluids at lower

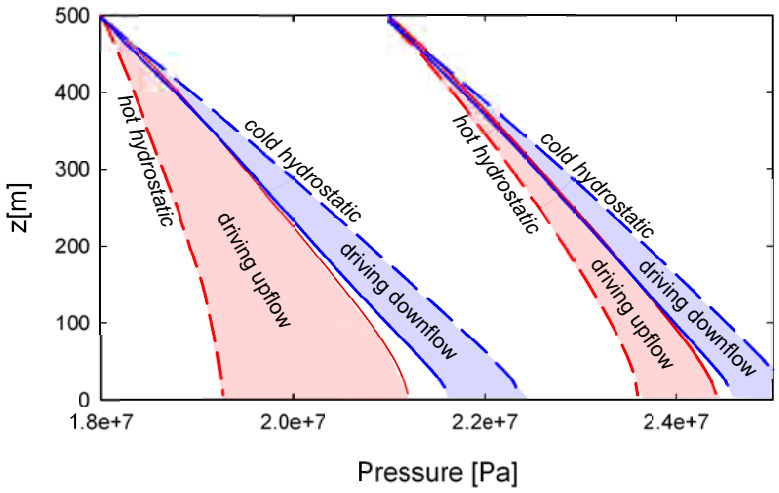

Fig. 7.7: Pressure-depth distribution in upflow zone (solid red) and downflow zone (solid blue) of a two-phase systems (18MPa at top) and supercritical system (21MPa at top). Also plotted are hydrostatic pressure values derived from the fluid density distribution in the upflow (dashed red) and downflow (dashed blue) zone.

pressure and temperature indicating their enhanced ability to transport energy.

2) The presence of vapor in two-phase systems reduces the fluid's densities and thereby increases buoyancy forces in comparison to single-phase systems, which can increase energy efficiency.

3) Two-phase heat-pipes are efficient energy transfer mechanisms and, specifically, enable the formation of broad upflow zones. Their impact decreases at pressures closer to the critical point, since here the density and enthalpy of the liquid approach the density and enthalpy of the vapor phase.

4) The formation of (near) 100% vapor zones below two-phase upflow zones immobilizes the liquid phase, hence zones of counter-current flows become small and broad upflow zones cannot form. This reduces the efficiency of energy transport.

These four mechanisms interact with each other, some having opposing effects, to form convection with associated energy fluxes which vary highly non-linearly with specified pressure-temperature boundary conditions. This leads to the counter-intuitive effect that applying higher temperatures at the bottom can decrease the efficiency of a system to transport energy.

The findings of this study have implications for the occurrence of 'super-convective' systems, i.e. systems with $Nu > 100$, in nature. On the one hand we were able to produce super-convection at relatively low permeability, indicating that super-convection might be more common than previously thought (Ingebritsen and Hayba, 1994). On the other hand, the conditions under which super-convection occurred were very restricted, i.e. overly hot bottom temperatures reduce energy transport. Therefore it remains to be seen if such conditions are widespread in nature. In fact, a possible run-away effect could play a role: If a super-convecting two-phase heat pipe would, by external forces, be heated to higher bottom

temperatures, then its efficiency would drop, increasing bottom temperatures even more. Also, the temperature at which the rock becomes permeable could potentially have an effect on the occurrence of two-phase super-convection. If this transition is at high temperatures, then two-phase super-convection at moderate permeability seems unlikely.

Nevertheless, this study proves that near-critical two-phase convection, facilitated by heat-pipe mechanisms, can transport energy very efficiently. The impact of heat-pipes could be even more significant in nature since the applied top-boundary condition in our models precluded the formation of heat-pipes at the top. Fluid flow at the top was allowed to be either up or down but not counter-current.

For computational reasons, we used relatively moderate permeabilities in this study. At mid-ocean spreading centers permeability is likely to be an order of magnitude or more higher (Fisher, 1998; Lowell and Germanovich, 2005) and highly heterogeneous, which could push the Nu number to larger values. In addition, the presence of salt in seawater allows phase-separation at pressures well above the critical region, possibly broadening the range of conditions where heat-pipes can form. However, its effect on our results is hard to anticipate, since double-diffusive double-advective convection will also occur when salt is present (Geiger et al., 2005). Also, the possible formation of static brine layers near the bottom could have an insulating effect, reducing the energy transport (Kawada et al., 2004). Further numerical studies are required to investigate the effects of these issues.

7.6 Conclusions

We have presented simulations of two-phase fluid flow at near-critical conditions of pure water. These simulations show that, under restricted conditions, two-phase fluid flow can greatly enhance energy transport by convection. The possibility of counter-current flow at two-phase conditions gives an additional degree of freedom for convection cells to find a state of optimum energy transport. This way broad upflow zones can be formed, with roots recharged by heat-pipe mechanisms which are highly efficient in transporting energy. Due to the restricted conditions under which they can form, it remains to be seen if such high-heat-flux systems exist in nature.

8. PHASE-SEPARATION, BRINE FORMATION AND SALINITY VARIATION AT BLACK SMOKER HYDROTHERMAL SYSTEMS

8.1 Abstract

We present the first 2D numerical simulations of black-smoker hydrothermal systems using realistic fluid properties, including the phase-separation of convecting seawater into a low-salinity vapor and high-salinity brine. We investigate convection, multi-phase flow and phase segregation at pressures below, near and above the critical point of seawater. Our simulations accurately predict the range in vent salinities, from 0.05 to 2.5 times seawater salinity measured at natural systems. In low-pressure systems at ∼1500m water-depth, phase-separation occurs in boiling zones stretching from the bottom of the hydrothermal cell to the seafloor. Low-salinity vapors and high-salinity brines can vent simultaneously, and transient variations in vent-fluid salinities can be rapid. In high-pressure systems at roughly ∼ 3500m water-depth, phase-separation is limited to the region close to the underlying magma chamber and vent fluids consist of a low-salinity vapor mixed with a seawater-like fluid. Therefore, vent salinities from these systems are much more uniform in time and always below seawater salinity as long as phase-separation occurs in the subseafloor. Only by shutting down the heat source can, in the high pressure case, the brine be mined, resulting in larger than seawater salinities. These numerical results are in good agreement with long-term observations from several natural black-smoker systems.

8.2 Introduction

The large variation in the measured salinity of black smoker vent fluids provides clear evidence for phase separation taking place in the sub-seafloor (Massoth et al., 1989; Von Damm et al., 1995, 2003). Seawater enters the crust at the seafloor, heats up while flowing down, and is expected to phase-separate near the base of the hydrothermal cell, after which it returns to the seafloor as a hydrothermal fluid. When undergoing phase-separation, a seawater-like fluid will separate into a low-salinity, low-density vapor and a high-salinity, high-density brine. The presence of salt allows this process to take place at pressure-temperature conditions both below and above the critical point of seawater (29.8MPa, 407°C, 3.2wt%). When phase separation takes place below the critical point seawater will boil, generating a very low-salinity vapor and high-salinity brine. In contrast, at pressure-temperature conditions above the critical point, small amounts of a dense brine will condense leaving the remaining

vapor with considerable salinity, depending on the pressure-temperature conditions. [1]

One of the key question is why some systems are chemically stable in space and time for periods of decades while others are not (Von Damm, 1995; Von Damm et al., 1997, 2004; Chiba et al., 2001). Low-salinity fluids (0.05-0.5× seawater salinity) have been observed at several relatively shallow systems, where phase-separation has been inferred to take place by boiling (Massoth et al., 1989; Butterfield et al., 1990; Von Damm et al., 1995; Oosting and Von Damm, 1996). In several of these fields, simultaneous venting of low-salinity and high-salinity fluids through black-smoker chimneys separated only tens of meters apart has been observed (Butterfield et al., 1990). The most extreme case of this type is the Brandon vent, where phase-separation may occur at the critical point of seawater in the chimney itself, resulting in simultaneous brine and vapor venting from different holes in the same chimney (Von Damm et al., 2003). In addition to these sharp spatial variations, rapid temporal variations in vent-salinity have been observed at such relatively shallow systems. (Von Damm et al., 1997). In contrast, such large variations have so far not been observed in systems where phase-separation is inferred to occur by condensation at high pressures (Butterfield et al., 1994b; James et al., 1995; Gallant and Von Damm, 2006). In several of those systems, all black-smoker chimneys have similar vent salinities, showing little spatial variation (James et al., 1995; Edmonds et al., 1996; Gallant and Von Damm, 2006). At the Main Endeavour field on the Juan de Fuca ridge, one of the few from which long-term time-series are available, all black-smoker chimneys have vented low-salinity fluids since their discovery more than 10 years ago, with only small variations (Seyfried et al., 2003). On the other hand, at the TAG field on the Mid-Atlantic ridge, for a period of 12 years only high-salinity fluids have been measured, with the low-salinity vapor phase absent (Edmonds et al., 1996; Chiba et al., 2001).

To understand the physics of sub-seafloor convection, including phase-separation processes, numerical modeling techniques are essential. The physics are too complex to be addressed with analytical formulations, and lab experiments are hampered by the high pressure-temperature conditions, requiring the use of a different binary fluid as an analogue for the NaCl-H_2O system, limiting their applicability (Cherkaoui and Wilcock, 2001; Emmanuel and Berkowitz, 2007). However, accurately capturing the physics of these systems in numerical models is challenging and therefore assumptions need to be taken, limiting the physical realism of the simulations. Many studies have taken a so-called Boussinesq approximation, in which density terms are only considered in the buoyancy term and neglected elsewhere (Travis et al., 1991; Rabinowicz et al., 1999; Schoofs and Hansen, 2000). Moreover, fluid properties such as density, viscosity and heat capacity were commonly taken as constant or linearized (Cherkaoui and Wilcock, 1999) whereas they vary non-linearly over orders of magnitude in the pressure-temperature range of black-smoker systems. These approaches can drastically reduce the tendency of a system to convect (Straus and Schubert, 1977) and, in the case of black-smoker systems, can in fact suppress the dominant physical processes (Jupp and Schultz, 2000, 2004; Coumou et al., 2006). Recent numerical studies used realistic, non-linear, fluid properties, but treated convection as a single-phase system. One way

[1] In the mid-ocean ridge literature these distinct types of phase-separation are often referred to as "sub-critical" and "supercritical" phase-separation. This terminology, however, strictly refers to a seawater fluid. The fact that phase-separation takes place implies that fluids of all kinds of salinity are present in the subseafloor. Therefore, this terminology is contradictory, and the usage of "boiling" and "condensation", referring to the actual physical processes, is preferred.

to do this is by taking pure water as a proxy for seawater, which at pressures above the critical point will always be single phase (Jupp and Schultz, 2000; Coumou et al., 2006). Other studies used properties of seawater (i.e. H_2O with 3.2wt% NaCl fluid) but treated fluids in the two-phase regions as a single-phase fluid by taking a weighted average of the two phases (Fontaine and Wilcock, 2007). None of these approaches include two-phase fluid-flow including phase-separation and segregation and therefore cannot address issues such as salinity variations of black-smoker fluids and the formation of brine layers.

Studies to date which included two-phase processes have been limited to one-dimensional heat-pipe solutions in which liquid flows downwards and vapor upwards, and the study by Kawada et al. (2004). Although heat-pipe solutions greatly simplify physics and ignore geometry, these models were the first to simulate the formation of brine layers at the bottom of seafloor hydrothermal systems (Bai et al., 2003; Seyfried et al., 2003). Kawada et al. (2004) studied two-phase convection of water and salt in 2D taking several assumptions, including the Boussinesq approximation, constant and equal viscosities and heat capacities for both phases, and neglecting latent heat. Despite of these assumptions, they showed that in principle low (2.5wt%) and high (4.4wt%) salinity fluids can vent simultaneously at the seafloor.

Two recent numerical developments have prepared the ground to study convection of black-smoker systems using realistic properties and including the phase separation of a salty fluid into a low-salinity vapor and high-salinity brine. First, a realistic model for the properties of the fluid phases of the NaCl-H_2O system, valid for the full pressure-temperature-salinity range encountered at black-smoker hydrothermal systems (Driesner and Heinrich, 2007; Driesner, 2007). Second, a pressure-enthalpy-salinity based multi-phase transport scheme which accurately conserves mass of water and salt as well as energy. The combination of these novel tools, incorporated in the CSMP++ finite-element finite-volume simulator (Matthai et al., 2007) enables accurate multi-phase simulations of both submarine and continental magmatic-hydrothermal systems as well as geothermal and basin reservoir simulations.

This study represents the first application of the novel transport scheme in which we investigated salinity variations observed in black-smoker vent fluids. In order to quantify the first order physical controls and the effects of phase-separation on convection, we use a geometrically simple 2D representation of mid-ocean ridge crust with a homogeneous permeability. A high resolution mesh is used to solve the simultaneous convection of heat and salt at multi-phase conditions. We explore convection at different permeabilities and water depths, with the distance from seafloor to magma chamber kept constant. We show that two distinct convection styles can develop, dependent on whether phase separation occurs by boiling or by brine condensation. The corresponding predicted vent-salinities and their variability in space and time neatly fit measurements from active natural systems.

8.3 Computational Method

8.3.1 Governing equations

We use the pressure-enthalpy-salinity (PHX) multi-phase transport scheme which was recently implemented into the CSMP++ porous medium simulator (see chapter 6). Conservation of total fluid mass, energy and salt mass is given by the following three expressions

(for simplicity we have omitted source terms):

$$\frac{\partial[\phi(S_l\rho_l + S_v\rho_v + S_h\rho_h)]}{\partial t} = -\nabla\cdot(\mathbf{v}_l\rho_l) - \nabla\cdot(\mathbf{v}_v\rho_v) \tag{8.1}$$

$$\frac{\partial[(1-\phi)\rho_r h_r + \phi(S_l\rho_l h_l + S_v\rho_v h_v + S_h\rho_h h_h)]}{\partial t} = -\nabla\cdot(\mathbf{v}_l\rho_l h_l) - \nabla\cdot(\mathbf{v}_v\rho_v h_v) - \nabla\cdot K\nabla T \tag{8.2}$$

$$\frac{\partial[\phi(S_l\rho_l X_l + S_v\rho_v X_v + S_h\rho_h X_h)]}{\partial t} = -\nabla\cdot(\mathbf{v}_l\rho_l X_l) - \nabla\cdot(\mathbf{v}_v\rho_v X_v) + \nabla\cdot(D\nabla\rho_l X_l) + \nabla\cdot(D\nabla\rho_v X_v) \tag{8.3}$$

Where subscripts l, v and h stand for the liquid, vapor and halite phase respectively and r for the rock matrix. ϕ is the porosity, S volumetric saturation, ρ density, h enthalpy, X the mass fraction of NaCl compared to H_2O, K thermal conductivity, D salt diffusivity and T temperature. Equations 8.1-8.3 assume that halite is immobile and therefore advective terms on the right-hand-side for halite are absent. The volume flux $\mathbf{v}$ is prescribed by conservation of momentum, for which we assume that the two-phase form of the Darcy equation is valid (Ingebritsen et al., 2006):

$$\mathbf{v}_i = -\mathbf{k}\frac{k_{ri}}{\mu_i}\left[\nabla p - \rho_i\mathbf{g}\right] \qquad i = \{l, v\} \tag{8.4}$$

where, $\mathbf{k}$ is the intrinsic permeability, k_r the relative permeability, μ viscosity, p pressure and $\mathbf{g}$ the acceleration due to gravity. In our approach we assume that fluid and rock are in thermal equilibrium, capillary-pressure effects are negligible and that the rock is incompressible.

8.3.2 Equation of state of H_2O-NaCl

All fluid properties are obtained from the H_2O-NaCl equation of state which we will only briefly describe here. For full details we refer the reader to Driesner and Heinrich (2007) and Driesner (2007). The phase diagram of H_2O-NaCl in temperature-pressure-salinity space (figure 8.1) has a number of phase boundaries dividing the system into a total of seven possible phase states. Above the vapor-liquid coexistence surface (black surface) the fluid is in the the single-phase domain having either vapor-like properties (V) at low salinity and/or high temperature or liquid-like properties (L) at high salinity and/or low temperature. At zero salinity, the H_2O boiling curve follows the vapor-liquid coexistence surface up to the critical point of H_2O, after which it continues as the critical curve, following the crest of the vapor-liquid surface. Below this surface, vapor and liquid coexist (V+L) with the liquid phase having a much higher salinity than the vapor phase. The lower pressure boundary of this domain is given by the three-phase surface, i.e. the vapor-liquid-halite surface (V+L+H, blue surface), which also forms the upper pressure boundary for vapor and halite (V+H) coexistence. The halite liquidus (green surface) is the surface along which a liquid-like fluid is saturated with halite. At higher salinities liquid and halite (L+H) will coexist. Phase separation of a single-phase fluid can either occur by boiling or condensation. If a liquid-like fluid intercepts the liquid-vapor surface, boiling takes place. If a vapor-like, single-phase fluid intercepts the liquid-vapor surface, liquid droplets condense out of the vapor.

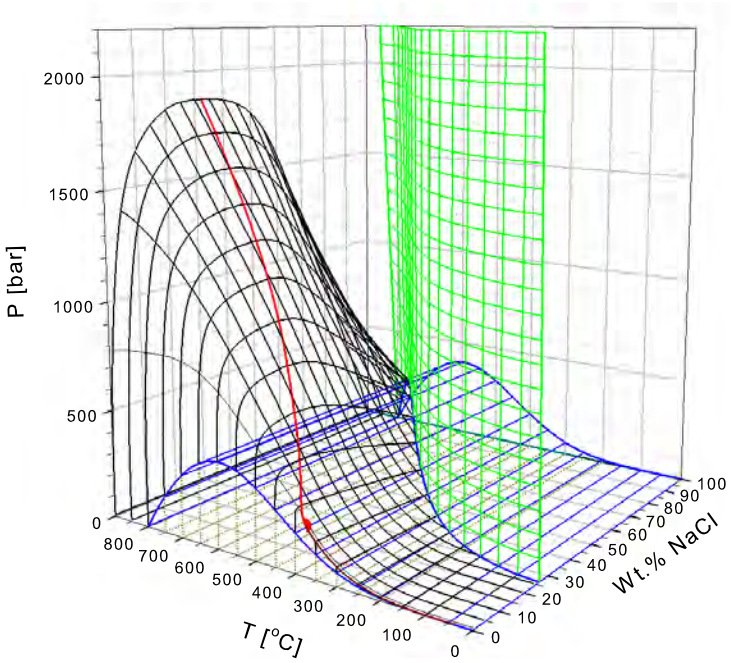

Fig. 8.1: Phase diagram of the system H_2O-NaCl in pressure-temperature-salinity space. Phase boundaries are indicated by the V+L surface (black), V+L+H surface (blue), halite liquidus (green), critical curve (red line) and critical point of H_2O (red point).

8.3.3 Model setup

We solve equations 8.1-8.4 on a rectangular 2-dimensional 3500x1000 meter domain, discretized with triangular elements with resolution refining towards the center where node-to-node distances are $\sim$ 15m. The side and bottom boundaries are no flow. The top boundary represents the seafloor and was set to constant pressure. To allow hot fluids to vent, a mixed energy boundary condition is applied at the top. In elements where the total volume flux $(\mathbf{v}_l + \mathbf{v}_v)$ is upwards, the temperature gradient is set to zero to allow undisturbed venting of upwelling fluids. Elements with the total volume flux pointing downwards take in cold seawater (10°C, 3.2wt% NaCl). At the bottom boundary, a bell-shaped heat-flux profile with a half-width of 500m is assigned. This is a geometrically simple, first-order representation of an across-axis section of a ridge with a 1km-wide magmatic lens at a depth of 1km below the seafloor. Geophysical evidence indicates that the length scales used are typical for intermediate- to fast-spreading ridges (Sinton and Detrick, 1992; Dunn et al., 2000). We intentionally do not add any geometric complexity, in order to identify the first-order physical controls of two-phase saline fluid convection at black-smoker systems. Linear relative permeability functions were used with a residual saturation of 0.3 for the liquid phase and 0.0 for the vapor phase. A total of six simulations were done with different top pressure (p_{top}) and permeability (k) versus heat-flux ($Q^{max}_{bot.}$) combinations as summarized in table 8.1, along with some key results. The higher permeability models were assigned a higher heat-flux than the lower permeable ones, such that near-bottom temperatures in both type of simulations reach similar values ($\sim$ 700°C). For computational reasons, both permeability and heat-flux are set to moderate values, which in natural systems could well be higher (Fisher, 1998, 2001; Lowell and Germanovich, 2005).

Tab. 8.1: Simulations

#	MODEL SETUP			VENTING		VARIATION	
	p_{top}[MPa]	$Q^{max}_{bot.}$ [W m^{-2}]	k[m^2]	T[°C]	X_{av}[wt%]	Period	Irregular outliers
1	15	60	10^{-14}	345.8 ± 3.0	1.4 ± 1.0	$\sim$ years	up to 12wt%
2	15	10	10^{-15}	345.0 ± 2.0	1.5 ± 1.0	$\sim$ decades	up to 12wt%
3	25	60	10^{-14}	380.0 ± 8.0	1.9 ± 0.5	$\sim$ decades	no
4	25	10	10^{-15}	383.7 ± 0.7	1.7 ± 0.1	$\sim$ centuries	no
5	35	60	10^{-14}	407.3 ± 7.0	2.1 ± 0.1	$\sim$ decades	no
6	35	10	10^{-15}	399.0 ± 2.0	1.8 ± 0.2	$\sim$ centuries	no

Values for used constants are: $\phi = 0.1$, $\rho_r = 2700$kg m^{-3}, $cp_r = 880$J kg^{-1}°C^{-1}, $K = 2.0$J m^{-1}°C^{-1}s^{-1}.

8.4 Results

8.4.1 Shallow water systems leading to seawater boiling

Two simulations with a top boundary pressure of 15MPa ($\sim$ 1.5km water depth) were performed (simulations 1 and 2), in which bottom boundary pressures do not exceed $\sim$25MPa. Therefore fluids in these simulations remain at pressures below the critical point of sea-water (29.8MPa).

Figure 8.2 shows the onset of convection in a simulation with the permeability set to 10^{-14}m^2 (simulation 1). Several small vapor-dominated V+L plumes develop with temperature ranging from 380°C at the bottom to 350°C at the tip of the plume. Salinities in these plumes are very low with 0.05wt% in the vapor and 0.9wt% in the liquid phase. Upon hitting the 22MPa isobar, the vapor salinities drop to extremely low values ($<10^{-3}$wt%, fig.

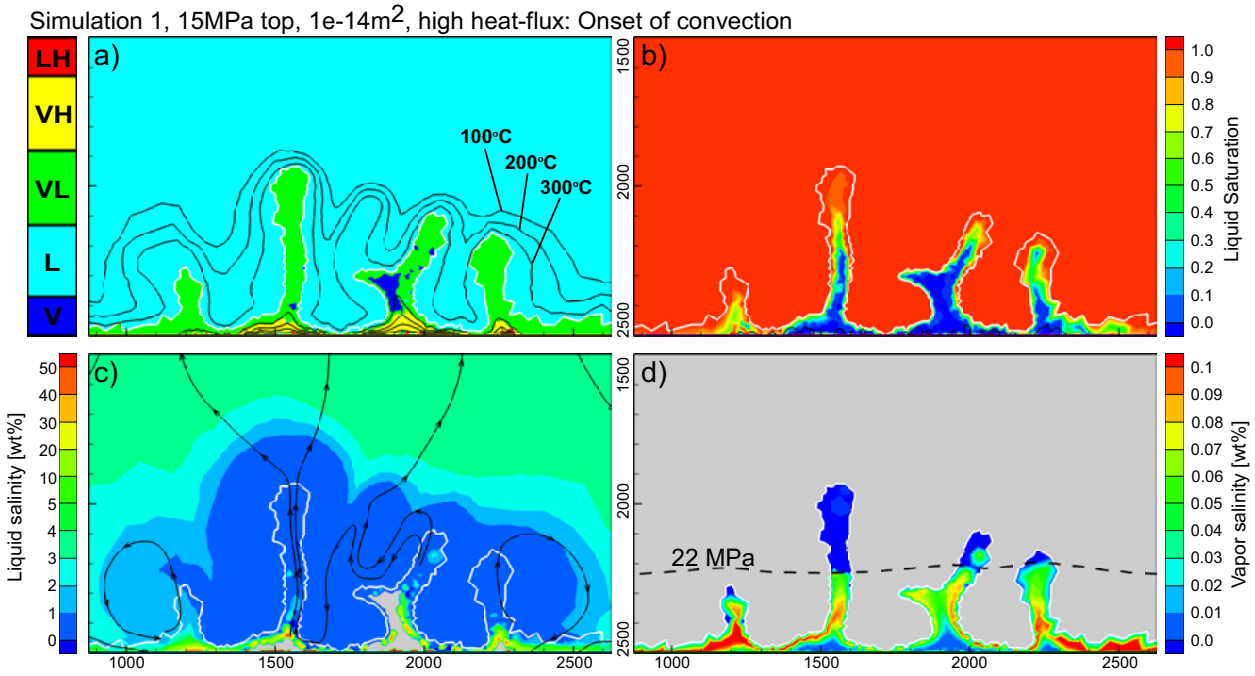

Fig. 8.2: Simulation results for a top pressure of 15MPa and $k = 10^{-14}\text{m}^2$ after 200 years. a) Phase state in color and isotherms (black lines) every 100°C. b) Liquid saturation in color and halite saturation of 0.1 (black line). c) Liquid salinity and liquid flow lines. d) Vapor salinity and vapor flow lines. The white line in all plots marks the boundary between single-phase (L) and other phase regions. Grey areas in figures c) and d) indicate that the phase does not exist there. Depth is given in meters below sealevel.

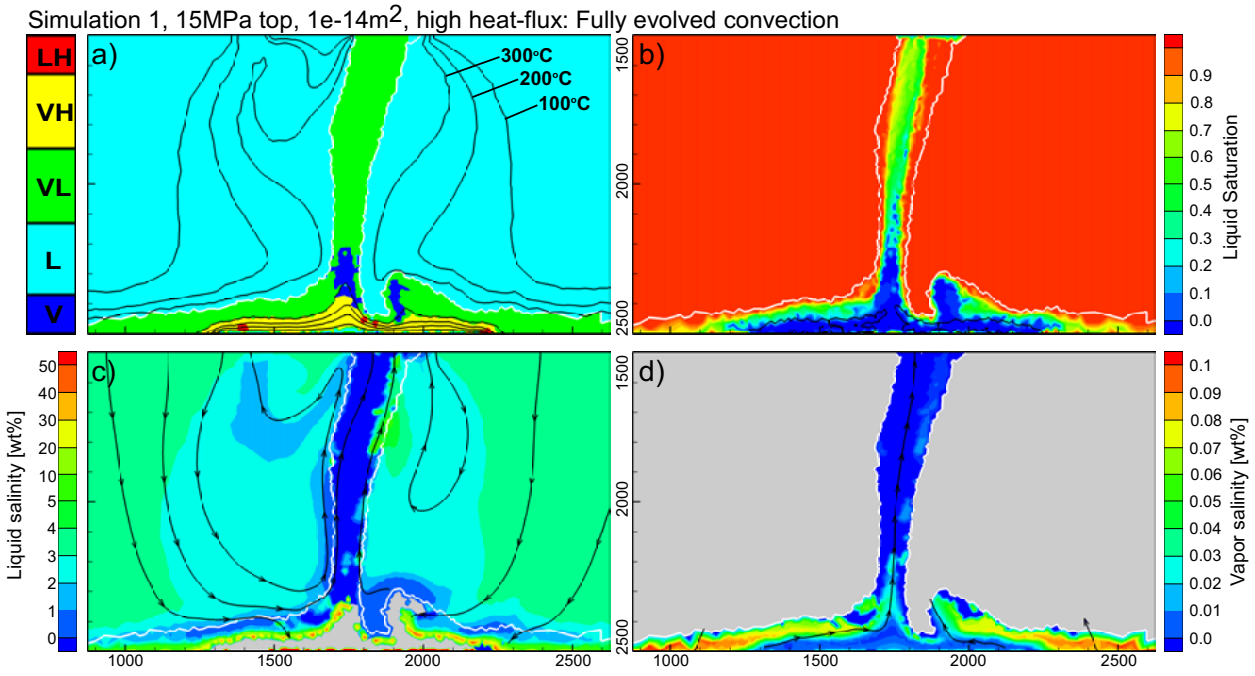

Fig. 8.3: Simulation results for a top pressure of 15MPa and $k = 10^{-14}\text{m}^2$ after 400 years, legend as described in figure 8.2

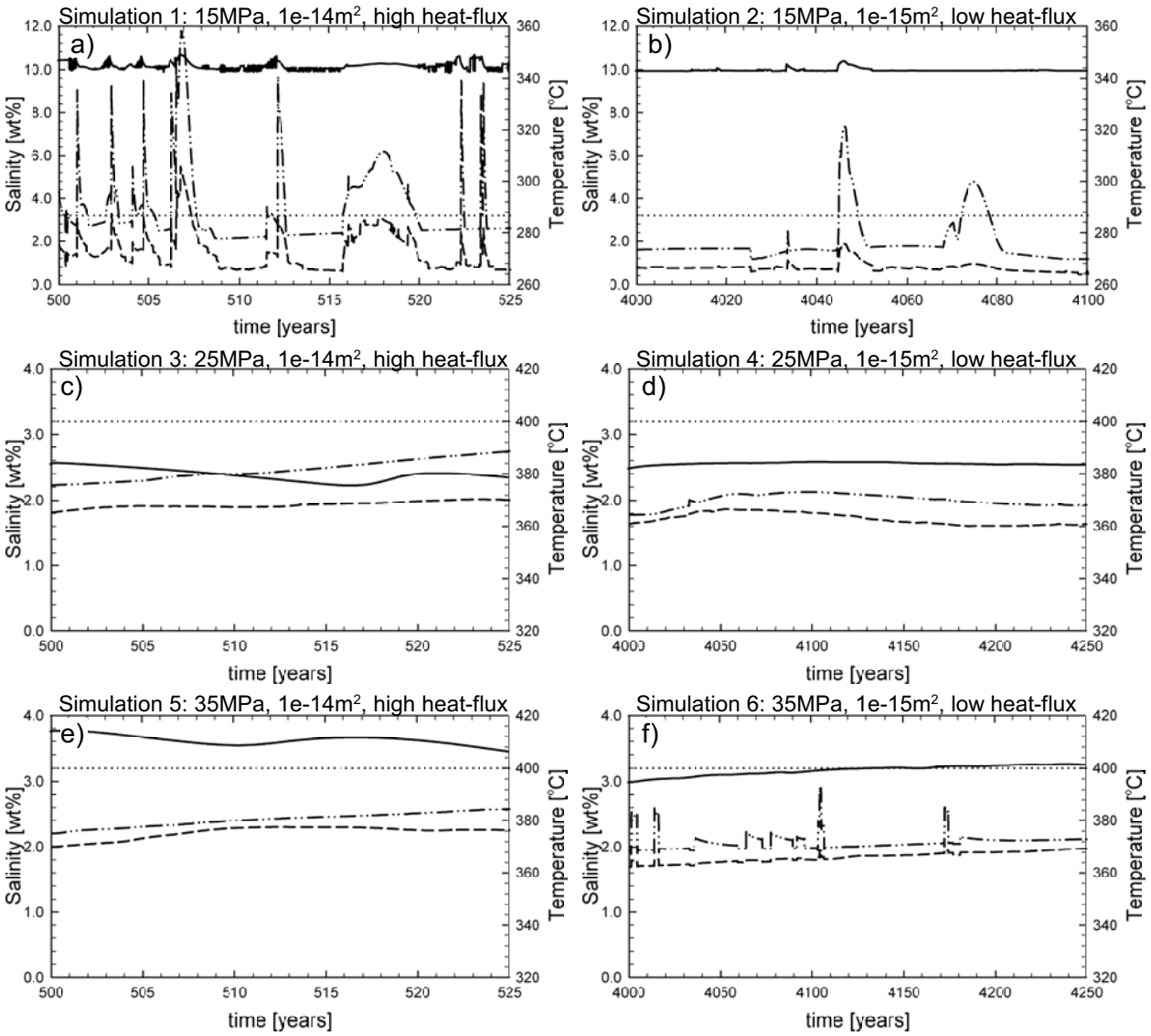

Fig. 8.4: Temperature (solid line), average (dashed line) and maximum (dashed-dotted line) bulk salinity of fluids venting through the top boundary for a) simulation 1, b) simulation 2, c) simulation 3 and d) simulation 4, e) simulation 5 and f) simulation 6 (see table 8.1). The dotted line represents seawater salinity.

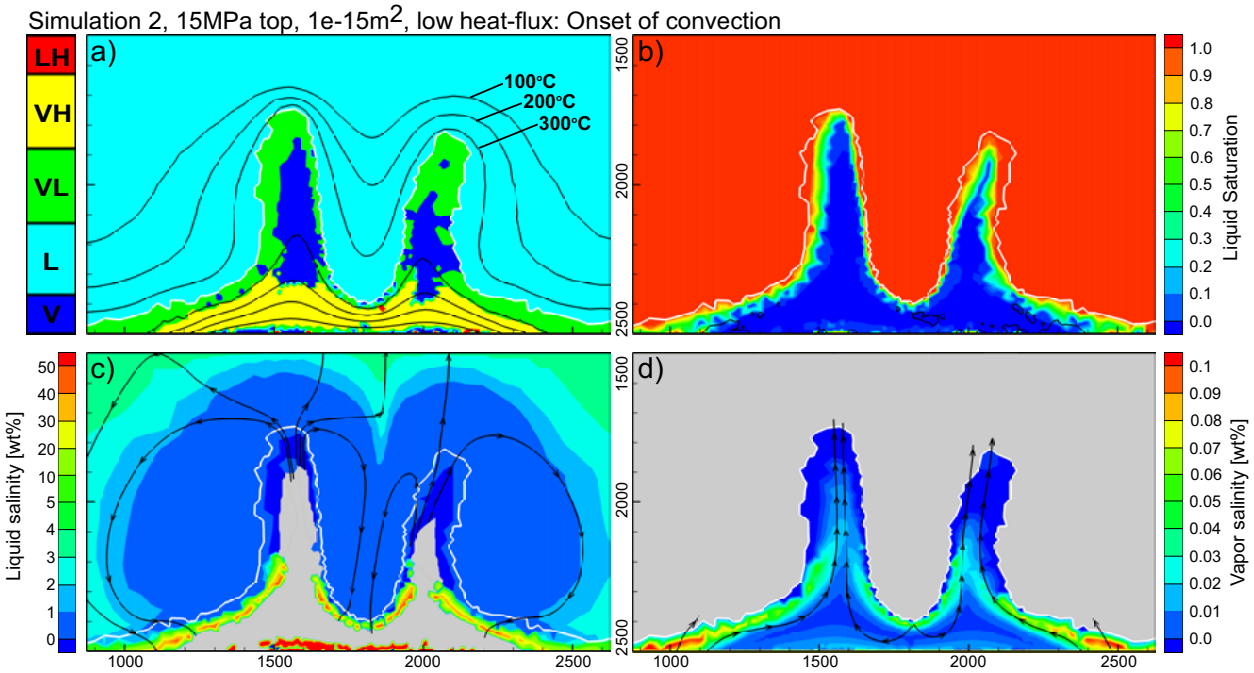

Fig. 8.5: Simulation results for a top pressure of 15MPa and $k = 10^{-15}\text{m}^2$ after 2000 years, legend as described in figure 8.2

8.2d). In the discussion section we explain the thermodynamic reasons for this to happen. Below the plumes, in the thermal boundary layer, a thin region of V+H coexistence forms with small pockets of very saline L+H regions. Over time, the plumes merge, forming a single V+L upflow zone rising all the way from the bottom thermal boundary layer to the top (fig. 8.3). In the central region of this upflow zone, liquid and vapor saturations are roughly equal (~ 0.5), both phases having low salinities ranging from 0.5-1.5wt% for the liquid and from essentially pure water to 0.02wt% for the vapor. At the edges of the upflow zones the liquid has a higher saturation (fig. 8.3b) and this area functions as a brine corridor: Seawater-like fluids hit the upflow zone and boil, generating a brine phase which gets diluted with low-salinity vapors from the upflow zone, becoming a moderate salinity fluid (up to 12wt%). These fluids generated at mid-depth have an upward buoyancy and hence rise at the edges of the upflow zone. This process has a pulsating nature and therefore the bulk salinity of fluids traveling through the top boundary is generally low (0.5-1.5wt%) but shows a strong variability, with intermittent bursts of high salinity fluids which can last as long as 5 years (fig. 8.4a). The temperature of these fluids is 345 ± 3.0°C, which is very close to the boiling temperature of seawater at this pressure (343°C). Brines created in the near-bottom thermal-boundary layer are trapped, forming a thin brine layer at the bottom of the V+L region (fig. 8.3c) with salinities up to $\sim$ 50wt%. This V+L brine layer overlies a V+H region which has temperatures from 400°C to 700°C, containing small pockets of L+H. The V+H region stores considerable amounts of salt with the halite saturation commonly larger than 0.1 (fig. 8.3b). The flow lines show that the bulk of the circulating fluids will phase separate at some stage, either in the thermal boundary layer or in the two-phase upflow zone (fig. 8.3c).

Figure 8.5 shows the onset of convection of simulation 2 which has the same boundary

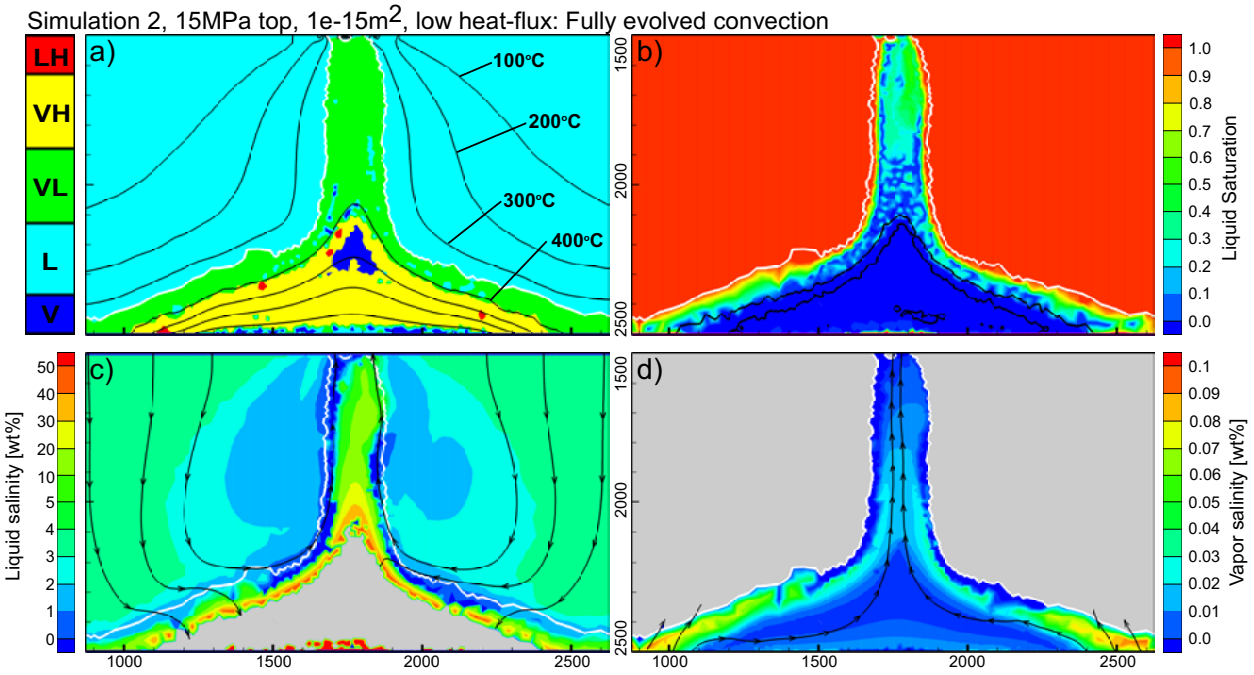

Fig. 8.6: Simulation results for a top pressure of 15MPa and $k = 10^{-15}\text{m}^2$ after 4000 years, legend as described in figure 8.2

conditions but an order of magnitude lower permeability (10^{-15}m^2) in combination with a lower heat-flux. Initially two plumes rise which have vapor zones in their centers but otherwise shows a broadly similar distribution of the same phase states observed in simulation 1. The low-salinity vapor (~ 0.05wt%) moves up rapidly in the plumes, cools, and condenses, creating similarly low salinity fluids in the cooler regions outside the V+L plumes. Brine is trapped at the flanks of the plumes near the thermal boundary layer (fig. 8.5c). Over time, similar to the high-permeability simulation, a single V+L upflow zone develops, but the liquid saturation is substantially lower and generally below residual (fig. 8.6a and b). Therefore, boiling of seawater-like fluids hitting the upflow zone results in a build up of salt, creating a vertical brine zone within the thermal plume, with bulk salinities ranging from 5wt% at 100m to nearly 40wt% at 500m depth below seafloor (fig. 8.6c). A continuous increase of salt shifts saturations in the upflow zone towards more liquid and less vapor. Once liquid saturations rise above the residual value, salty fluids temporarily mobilize, flushing the brine out of the central regions of the upflow zone. This is expressed in figure 8.4b, showing bursts of fluids with bulk salinities up to 8wt% (over the whole simulation period maximum values reached 12wt%) moving through the top boundary lasting roughly a decade. Generally fluids traveling through the top have bulk salinities of 1.5±1.0wt% and temperatures of 345°C. In the bottom region, the dominant fluid state is V+H (fig. 8.6a), with a layer of relatively large halite saturations at its top (fig. 8.6b). Above the V+H region, brine is trapped in a V+L layer generating salinities up to 50wt%.

8.4.2 Near-critical pressure: Brine condensation followed by boiling

Next, low- and high-permeability simulations were performed with a top pressure fixed to 25MPa ($\sim$ 2.5km water depth, simulations 3 and 4), creating maximum pressures in the

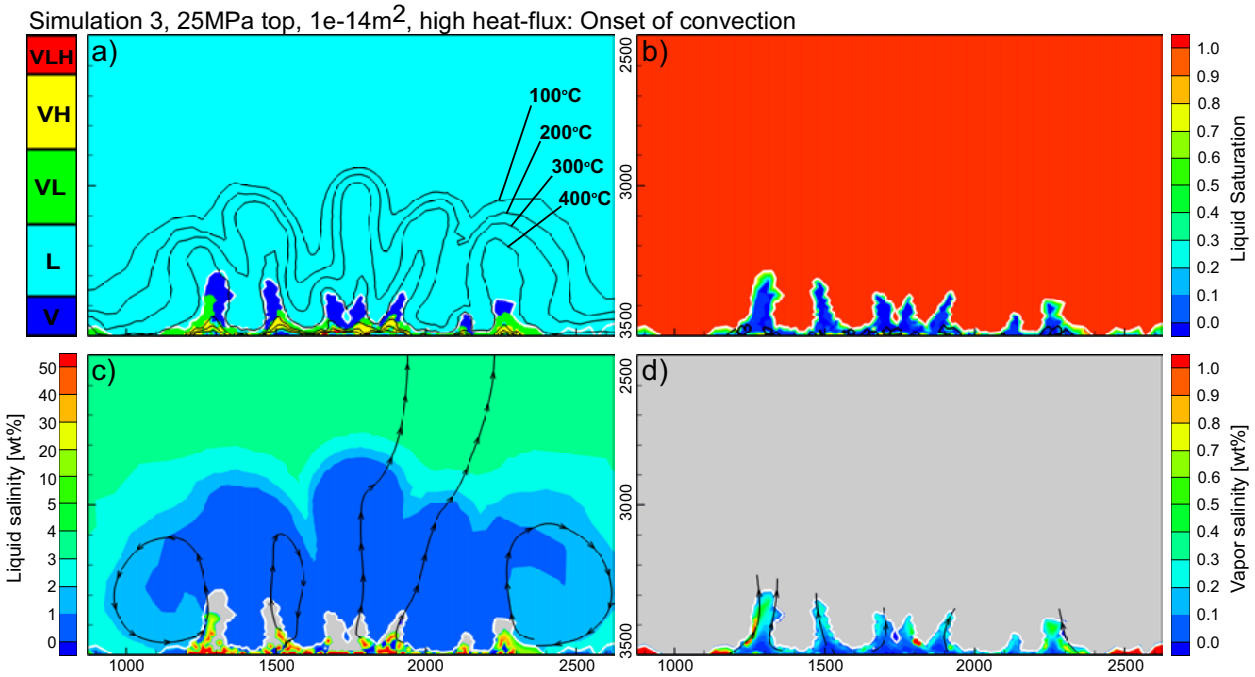

Fig. 8.7: Simulation results for a top pressure of 25MPa and $k = 10^{-14}\text{m}^2$ after 200 years, legend as described in figure 8.2

domain of ∼35MPa and thereby including the critical-pressure region of seawater.

The onset of convection in the high-permeability simulation (10^{-14}m^2) shows many small V and V+L plumes with vapor salinities of 0.5wt% which dilute the overlying water column (fig. 8.7). Once the plume is fully developed, two separate V+L regions develop. Near the bottom, low-salinity fluids form by condensing out brine, then mix with non-phase-separated fluids to form a ∼2wt% single-phase upflow zone. Roughly 200m below the top, this single-phase fluid hits the two-phase surface again, resulting in boiling and creation of a 0.25wt% vapor and ∼2.5wt% liquid phase (fig. 8.8c and d). The V+L region near the top, however, is not stable, and periodically emerges and retreats with time. Generally, fluid traveling through the top has a bulk salinity close to 2±0.5wt% and temperatures of 380±8°C. This temperature is close to but below the two-phase temperature of seawater at this pressure (387°C). At the very bottom, a V+L+H region develops with very high salinities of up to ∼80wt% (fig. 8.8a and c). Flow patterns show that far less fluid, compared to simulation 1, undergoes phase-separation. Brine forms in the near-bottom thermal boundary layer, remaining immobile, but not in the upflow zone.

The onset of convection in the low-permeability simulation (simulation 4) looks very similar to that of simulation 2, with the exception that at these higher pressures, vapor salinities in the upflow zone are considerably higher (∼0.25wt%, fig. 8.9d) as is its saturation. Due to the lower permeability, the system becomes hotter than to simulation 3, and a V+L upflow zone is formed. During the course of this simulation, the liquid saturation in this zone remains always below residual and hence a vertical immobile brine zone forms (fig. 8.10c). Fluids moving through the top therefore have rather constant and low vent salinities of 1.7±0.1wt% with temperatures of 383±0.7°C. Near the bottom, two separate brine layers develop: One dense liquid phase layer (up to 80wt%) below the V+H region and one thin

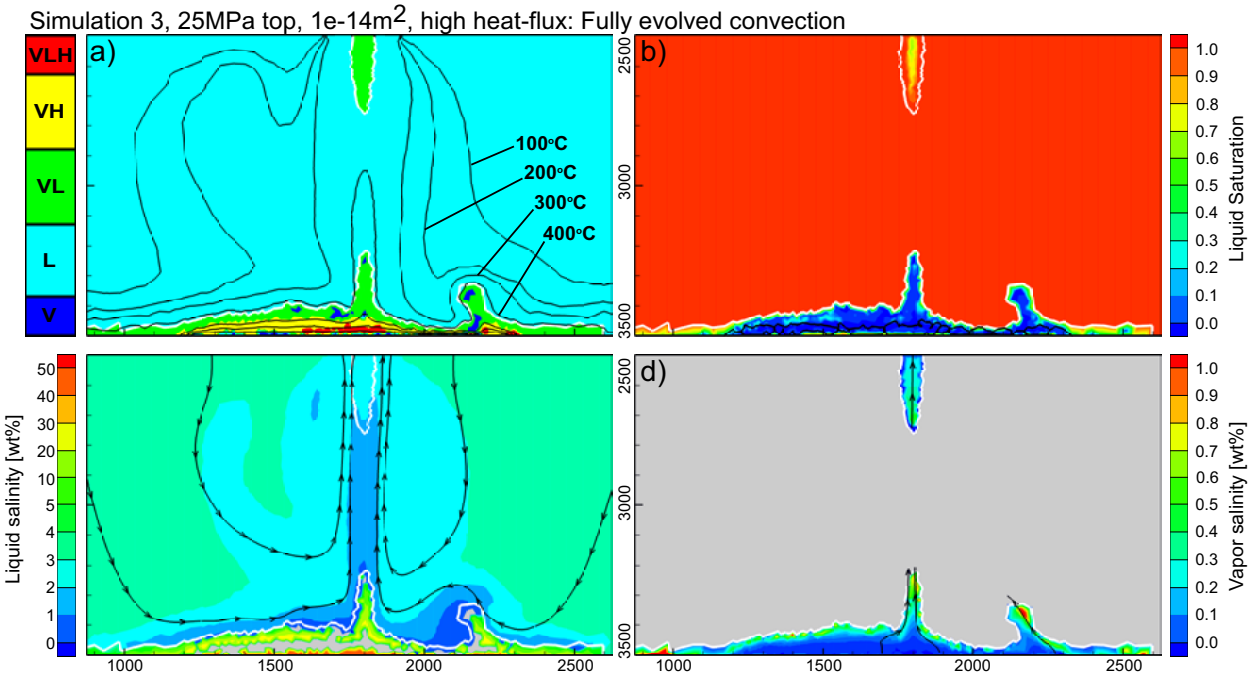

Fig. 8.8: Simulation results for a top pressure of 25MPa and $k = 10^{-14}\mathrm{m}^2$ after 400 years, legend as described in figure 8.2

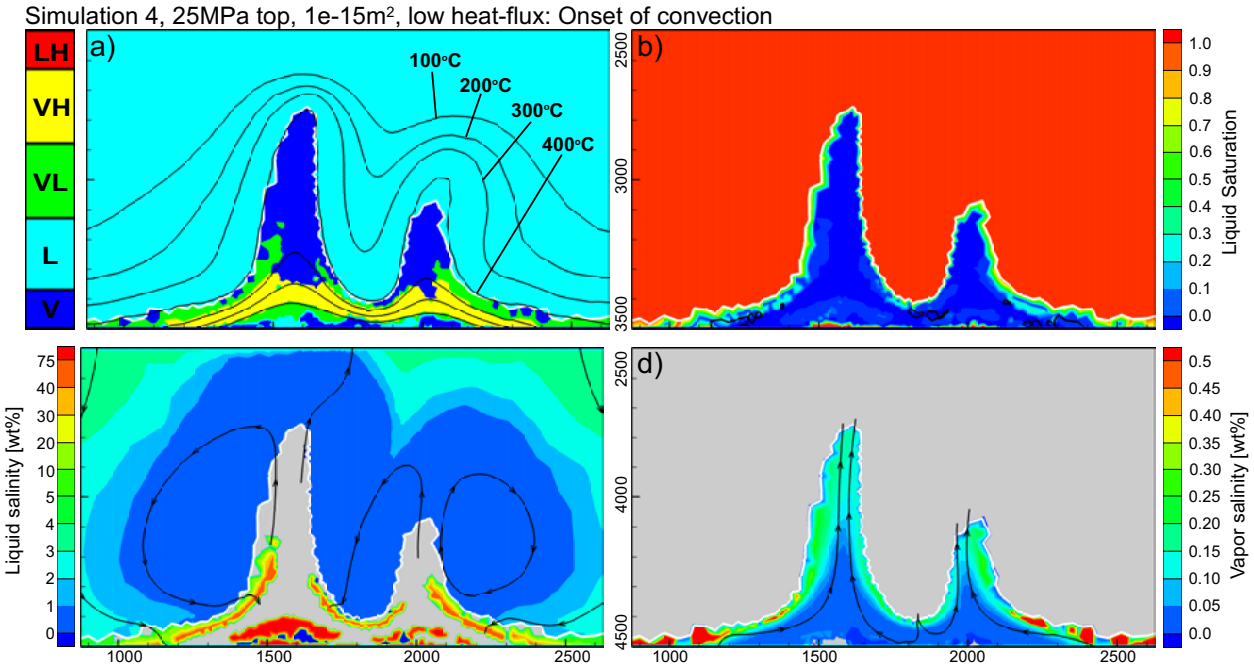

Fig. 8.9: Simulation results for a top pressure of 25MPa and $k = 10^{-15}\mathrm{m}^2$ after 2000 years, legend as described in figure 8.2

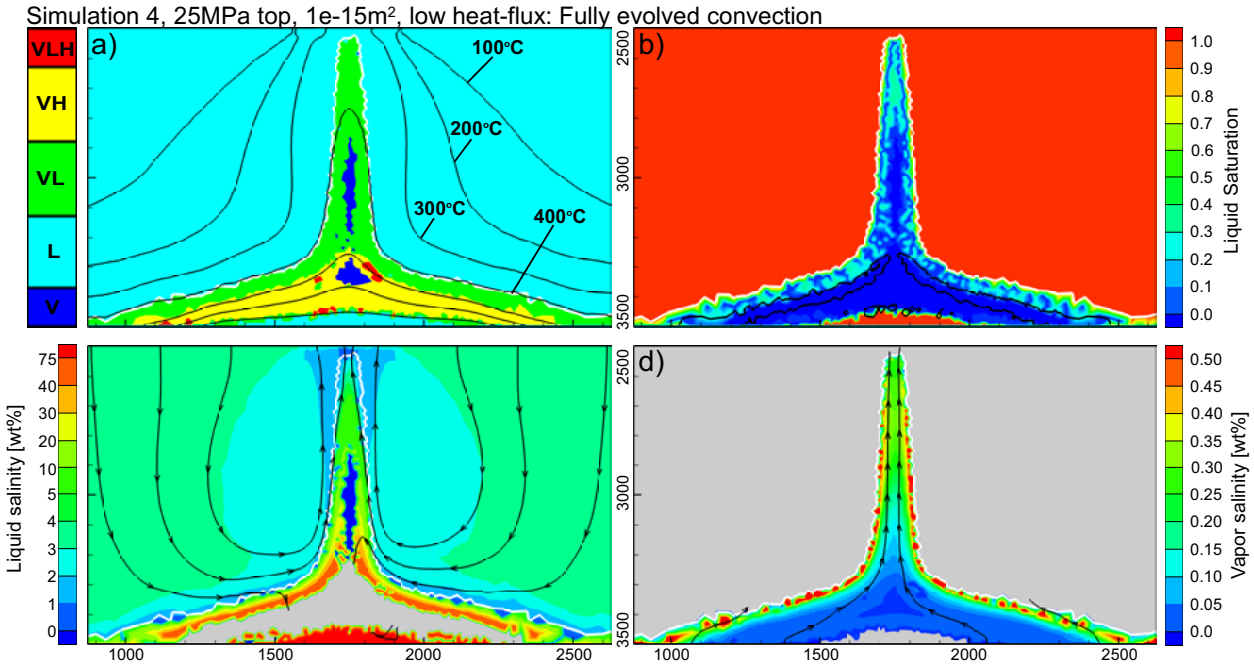

Fig. 8.10: Simulation results for a top pressure of 25MPa and $k = 10^{-15}\text{m}^2$ after 4000 years, legend as described in figure 8.2

V+L brine layer (up to 60wt%) above it (fig. 8.10a and c). In the V+H region itself, halite saturations increase again towards the top of the region, as indicated by 0.1 halite saturation contour (black line) in figure 8.10b.

8.4.3 Deep-water systems leading to brine condensation

Finally, high- and low-permeability simulations were performed using a top boundary pressure of 35MPa (∼3.5km water depth, simulations 5 and 6), ensuring higher than critical seawater pressures in the whole domain.

Figure 8.11 shows results at the onset of convection for the high-permeability simulation (simulation 5). Initially five thermal plumes of $\sim 425°\text{C}$ rise, of which one is a vapor plume with relatively large vapor salinity of ~ 1.0wt%. Vapor salinities in the thermal boundary layer can become as high as 2.0wt%. Over time a single-phase upflow zone develops, consisting of fluids resulting from dilution of seawater by a ~ 1.0wt% vapor-phase which condensed out a brine at depth. On its way to the top, this single-phase fluid is progressively mixed with more and more seawater, moving through the top as a 2.1 ± 0.1wt% fluid with a temperature of $407 \pm 7.0°\text{C}$ (8.4e). This temperature is considerably lower than the two-phase temperature of seawater at this pressure (423°C). Flow lines, as shown in figure 8.12c, rarely cross the multiphase regions, indicating that limited phase-separation takes place, and only in the near-bottom thermal boundary layer. Therefore only a thin brine layer develops in the V+L region (fig. 8.12a and c), with salinities as high as ∼80wt%.

In the last simulation (simulation 6), with $k = 10^{-15}\text{m}^2$, a single-phase upflow zone develops with salinities close to 2wt% (fig. 8.14a and b). In the bottom region brine is condensed out while the vapor phase moves upward. This low-salinity vapor gets progressively mixed with non-phase-separated seawater-like fluid, resulting in a 1.8 ± 0.2wt% fluid with a tem-

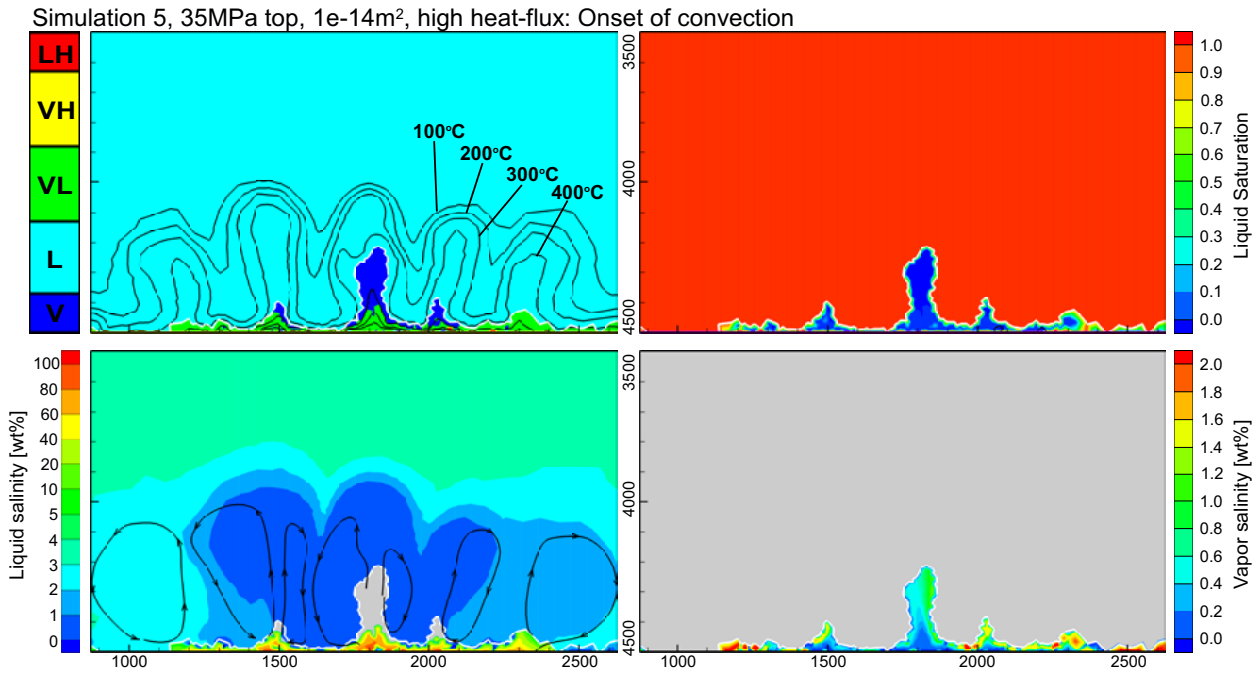

Fig. 8.11: Simulation results for a top pressure of 35MPa and $k = 10^{-14}\mathrm{m}^2$ after 200 years, legend as described in figure 8.2

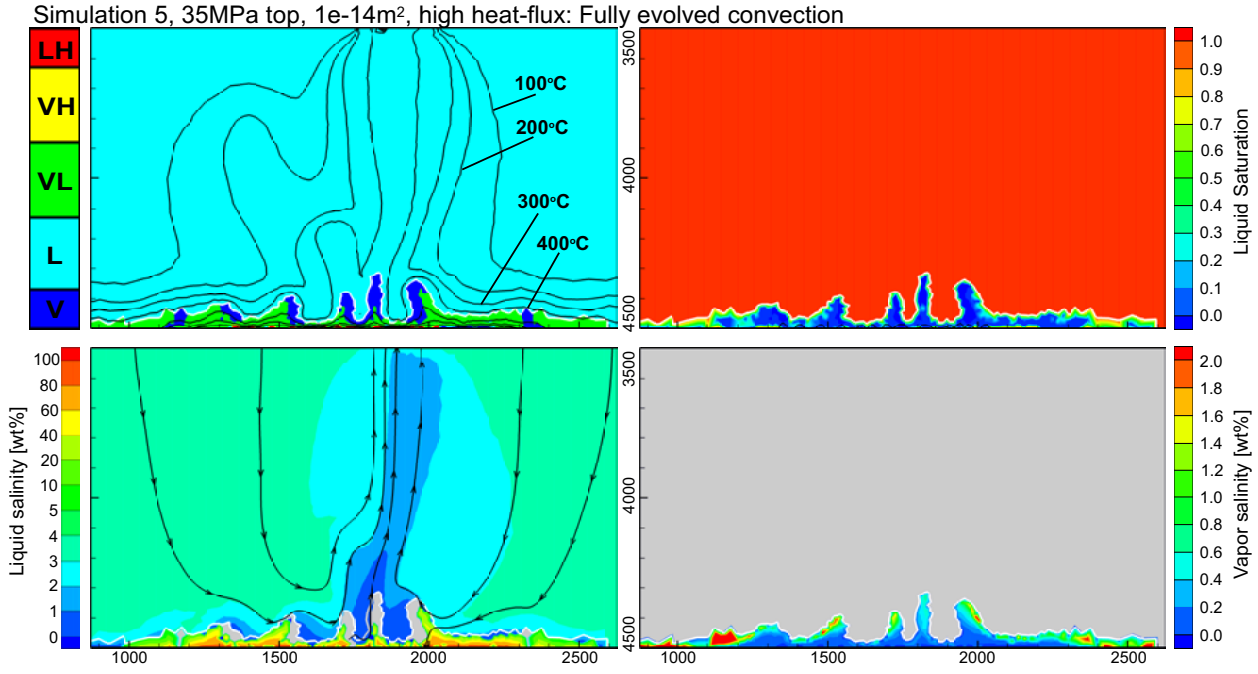

Fig. 8.12: Simulation results for a top pressure of 35MPa and $k = 10^{-14}\mathrm{m}^2$ after 400 years, legend as described in figure 8.2

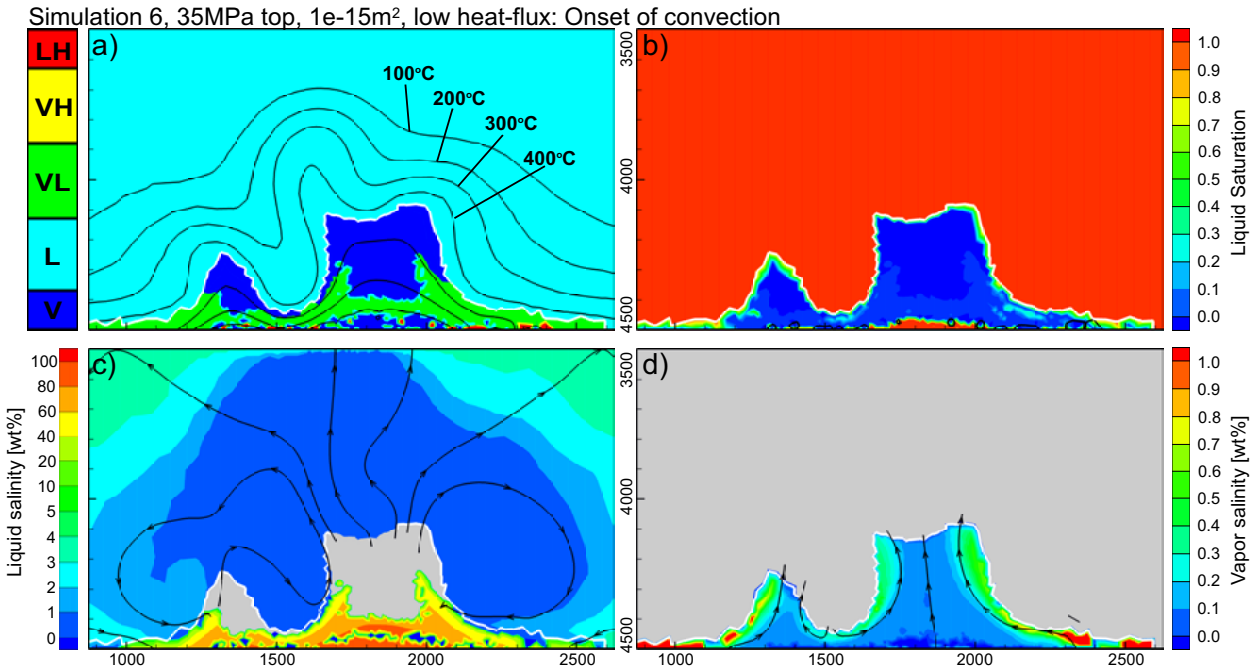

Fig. 8.13: Simulation results for a top pressure of 35MPa and $k = 10^{-15}\mathrm{m}^2$ after 2000 years, legend as described in figure 8.2

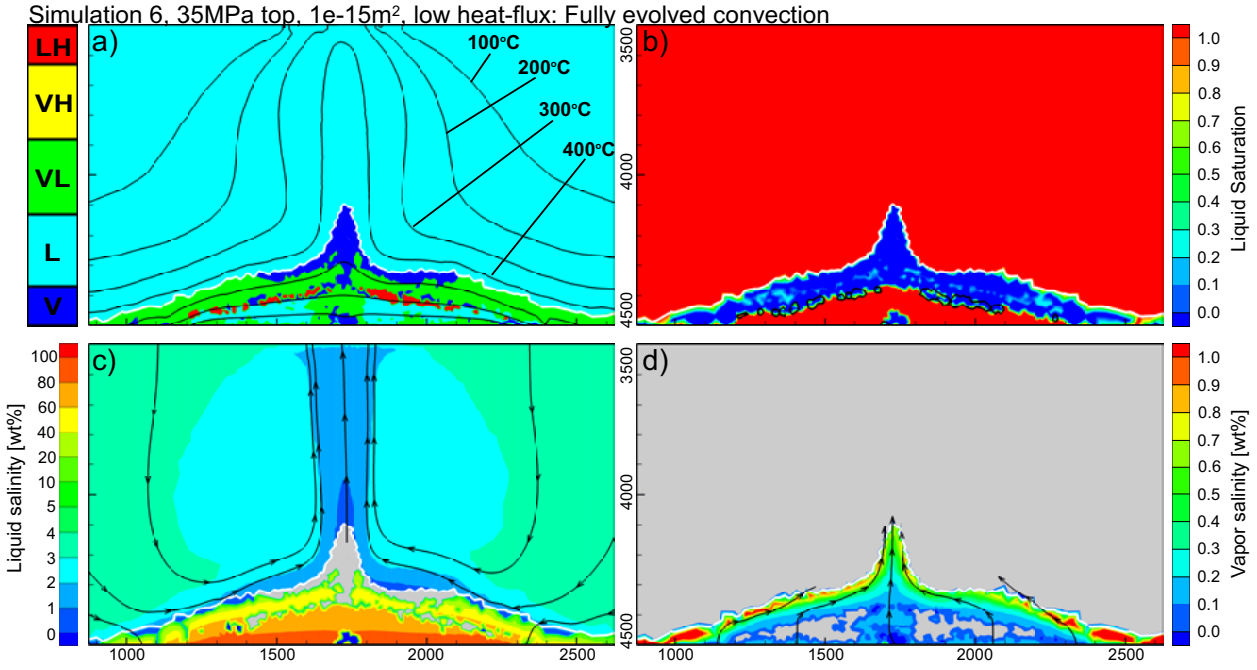

Fig. 8.14: Simulation results for a top pressure of 35MPa and $k = 10^{-15}\mathrm{m}^2$ after 4000 years, legend as described in figure 8.2

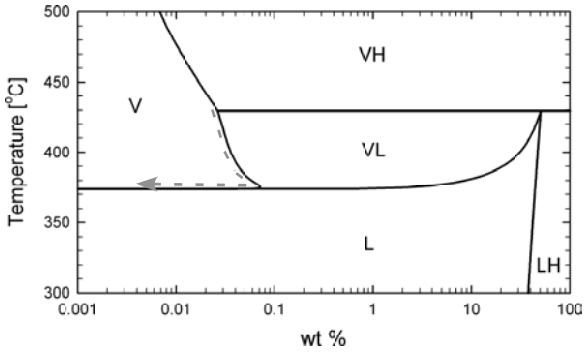

Fig. 8.15: 22MPa-isobaric section through H_2O-NaCl phase-diagram.

perature of 399 ± 2.0°C traveling through the top boundary (fig. 8.4f). Though the average salinity moving through the top boundary is rather constant, the maximum salinity shows some short-period small-amplitude peaks of higher salinities. At the bottom boundary a thick brine layer develops, with salinities of up to 90wt%, which partly resides in the L and partly in the V+L phase region, but vapor saturations are negligibly small (fig. 8.14b). Between the 500°C and 600°C isotherm, liquid becomes over-saturated with salt and halite precipitates (fig. 8.14a and b). Above this halite layer, the fluid is in the V+L field with liquid saturations close to zero.

8.5 Discussion

8.5.1 Low-pressure boiling

Figure 8.2d shows that rising vapors with a very low salinity of $\sim$ 0.05wt% (or 0.015× seawater salinity) suddenly lose essentially all their salt content when hitting the 22MPa isobar. This is a direct consequence of the shape of the phase-diagram at these near-critical conditions. The rising vapor cools and depressurizes along the vapor-side of the V+L surface, as indicated by the grey arrow in the phase-diagram in figure 8.15. Upon reaching a temperature of $\sim$ 374°C, vapor salinities drop to extremely low values, since here the V+L phase-region merges with the boiling curve of pure water. This way, the vapor-phase can essentially become a pure water. In nature, relatively shallow systems where phase-separation was inferred to be by boiling (i.e. "sub-critical") have been observed to vent low-salinity fluids (0.2-1.0wt%, Massoth et al. (1989); Butterfield et al. (1990); Von Damm et al. (1995)), though not as low as observed in this simulation. Still, pore-water analysis from a shallow system at the Bransfield Strait near Antarctica indicate that the creation of essentially pure water hydrothermal fluids seems possible (Dahlmann et al., 2001). The mechanism to do this is by the described feature of the phase-diagram of the H_2O-NaCl system and is accurately captured by our modeling code.

8.5.2 Brine trapping and flushing

In our simulations we observed two distinct brine-forming areas. All simulations showed the formation and trapping of brines in the thermal boundary layer. In the lower-pressure simulations (15-25MPa, simulations 1-4) brine is generated in a V+L region overlying a

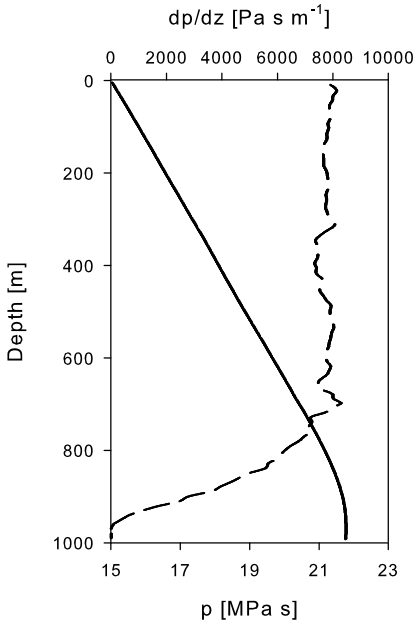

Fig. 8.16: Pressure (solid line) and vertical pressure gradient (dashed line) in a vertical cross-section through the upflow zone of simulation 1 (see table 8.1).

V+H region. The heavy brine phase sinks and is trapped at the boundary between V+L and V+H since here liquid saturations become near-zero. In the high-pressure simulation (35MPa, simulations 5 and 6), no V+H region develops and the heavy brine phase can sink undisturbed to the base of the hydrothermal system. This dense brine layer remains immobile since it is stably stratified and pressure-gradients in this region are much too small for dense fluids to rise. As shown in figure 8.16, in the thermal boundary layer the vertical pressure gradient rapidly drops, and hence only very low-density fluids can rise.

If a boiling zone develops, phase separation occurs at all depths in the upflow zone and hence brine also forms at all depths, as seen in the simulations with p_{top} set to 15MPa. At high pressure, i.e. $p_{top} = 35$MPa, phase separation occurs by brine condensation, and a two-phase upflow zone does not develop. At intermediate pressure, i.e. $p_{top} = 25$MPa, a fully-developed V+L upflow zone is only formed for the low-permeability system since here the temperature in the upflow zone are slightly hotter. For all simulations, the pressure gradient in the upflow zone is much larger than in the thermal boundary layer, $\sim$ 8000Pa m^{-1} (fig. 8.16). At such a pressure gradient, fluids with a density larger than 800kg m^{-3} will move down and fluids with a density less than 800kg m^{-3} will move up. Hence a relatively heavy liquid phase can potentially move upwards. For typical pressure-temperature conditions in the upflow zone, this implies that liquids with salinities of up to $\sim$ 12wt% have an upward buoyancy. Whether such fluids will rise depends on the saturation of the liquid phase in the upflow zone. Whenever it is below residual, brines are immobile, whenever it is above residual, fluids up to $\sim$ 12wt% can vent. In simulation 1, which has a high permeability, the liquid phase is always mobile, and hence generated and subsequently diluted brine will immediately rise. Simulation 2, with a lower permeability, shows that brine build up and flushing can occur in a pulsating way: At low saturations, brine accumulates in the upflow zone, which will increase the liquid saturation. Once the residual saturation is exceeded, the accumulated brine can be flushed out, reducing the liquid saturation again.

Both mechanisms of brine-trapping - above a V+H layer and in a boiling zone - depend

on the residual liquid saturation, a value which is poorly known. Nevertheless, it is generally accepted that at some finite saturation, the liquid phase becomes immobile.

8.5.3 Brines in nature

Substantial evidence exists from fluid-inclusion studies that brine forms near the base of the hydrothermal system and possibly in upflow zones. Several studies have measured very saline fluids in inclusions close to the magmatic-hydrothermal interface. Fluid-sinclusion studies from ophiolites (Nehlig, 1991) and oceanic crust (Kelley et al., 1993) have documented the existence of 60-70wt% brines near the hydrothermal base. Moreover, Saccocia and Gillis (1995) showed that upflow zones can become quite saline with salinities of 11-13wt%, in good agreement with our modeling results.

Near-bottom brines do not necessarily form thick insulating layers at the base of the hydrothermal system. Instead, brine can get trapped above a V+H region, considerably above the base, and vapors can still efficiently mine heat from the base of the hydrothermal system. Such a mechanism could potentially explain the continuous low-salinity and high-heat flux venting at the Main Endeavour Field (Seyfried et al., 2003). Based on estimates of the rate at which brines are accumulating, it has been suggested that the brine layer at the base of this system is likely at least 100m thick which could insulate the heat source (Fontaine and Wilcock, 2007). However, no decay in heat flux has been observed. To resolve this apparent paradox, Fontaine and Wilcock (2007) argued that the vapor phase will segregate into the main fractures whereas the brine moves into the smaller fissures and backwaters. This would allow the vapor to flow efficiently through the system and transport large amounts of heat while most of the porosity in the lower part of the system fills with brines. Here we suggest an analogous scenario in which brines are trapped away from the hydrothermal base, which would also allow the vapor to mine heat from the base of the system. The presence of halite in the subseafloor has been inferred for some vent sites from Cl-Br fractionation data in vent fluids (Oosting and Von Damm, 1996), but this has not yet been done for the Main Endeavour field. Further, systems like the Main Endeavour field are likely to have a larger permeability than the one used in this study, though, since permeability is probably a function of temperature, permeability at depth could be similar to the one used here. Nevertheless, more detailed numerical studies are required to investigate this hypothesis, using different permeability scenarios and preferably 3D simulations.

8.5.4 Waning of Magmatic Heat

In the high-pressure simulations (35MPa, simulations 5 and 6), brine formed only in the near-bottom thermal boundary layer and remained immobile. Hence these simulations only vented lower-than-seawater salinities. Under these conditions, the brine can never move upward, due to its high density, and requires dilution by excess seawater to be 'mined' and expelled. This is most likely to happen when the heat source wanes, such that phase separation stops and a single-phase convection cell can mine the brine layer (Schoofs and Hansen, 2000). To test this hypothesis, we let the heat source decay from the starting value to a background value of 1W m^{-2} over a period of 25 years for the high-pressure simulation 6. Figure 8.17 shows that indeed a shift from hot, low-salinity, vapor-like fluids to cooler, high-salinity liquid-like fluids occurs. For a permeability of $10^{-15}m^2$ the transition from low-salinity fluids to seawater-like salinities occurs within 50 years, after which salinities keep

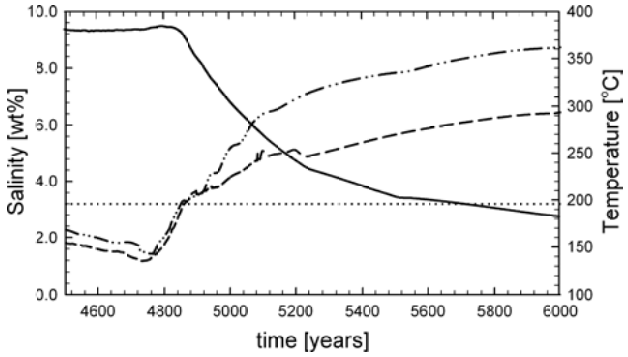

Fig. 8.17: Temperature (solid line), average (dashed line) and maximum (dashed-dotted line) bulk salinity moving through top boundary after shutting down the heat source of simulation 6 (see table 8.1).

increasing slowly to a maximum average salinity of 6wt%. Maximum salinities can become as high as 9wt%. In this transition period no simultaneous venting of high and low salinity fluids was observed.

8.5.5 Vent salinity

Except for the extremely low-salinity vapors generated at sub-critical conditions, as discussed in a previous section, the vent salinities in our simulations range from 0.5-9wt%, with short-lived peaks of 12wt%. This range is generally in good agreement with measurements at active systems (Von Damm, 1995). Since we used geometrically simple models, this shows that the thermodynamics of a H_2O-NaCl fluid can explain many of the observed spatial and transient variations in vent salinity. Phase-separation, and the depth at which this occurs, appear to be first-order controls on the salinity of vent-fluids and its variation in space and time. Both average temperature and bulk salinity of the venting fluids increase with increasing pressure (table 8.1). The upper limit of vent-salinity seems to be constrained by the pressure-gradient in the upflow zone as argued by Fontaine and Wilcock (2006).

In addition, our simulations emphasize the fundamental difference between phase-separation by boiling ("sub-critical") or brine condensation ("supercritical") and the effects they have on convection and vent fluid salinity. When phase-separation occurs at low-pressure conditions, a V+L boiling zone forms and simultaneous venting of brine and vapor is likely to occur periodically. At high pressures, phase separation occurs by brine condensation near the base of the hydrothermal system, resulting in low-salinity venting. Venting of high-salinity fluids could only be achieved by mining a previously formed brine-layer with a single-phase fluid following cessation of a magmatic heat source. The high-pressure simulations therefore never showed simultaneous venting of brine and vapor.

Black-smoker vent fluids have been observed to evolve from a low-salinity vapor directly following a magmatic event to high-salinity brines after several years (Von Damm et al., 1997, 2003). The generally accepted explanation for this observation is that phase-separation takes place only in the early stage, forming a brine layer at depth which is later mined by a single-phase convection cell. Like simulations from Schoofs and Hansen (2000), our simulations confirm that this mechanism is indeed possible. However, we propose an alternative expla-

nation in which continuous phase-separation creates brine regions in the upflow zone itself which, when the residual liquid saturation is exceeded, can rise and vent. These two hypothesis can, and are likely to, act simultaneously in natural systems. One way to distinguish between the two mechanisms is the occurrence of simultaneous brine and vapor venting by different smokers in the same field. If this is the case, then brine build up in the upflow zone is the likely mechanism. If not, then single-phase mining of a previously formed brine layer is likely.

In nature, simultaneous brine and vapor venting from different chimneys within one black-smoker field has been observed at several sites, all of them associated with phase-separation by boiling at sub- or near-critical conditions (Butterfield and Massoth, 1997; Massoth et al., 1989; Butterfield et al., 1990; Von Damm et al., 2003). In contrast, vent fields where phase-separation has been inferred to occur by condensation ("supercritical") consistently vent either low-salinity fluids or high-salinity fluids (Butterfield et al., 1994b; James et al., 1995; Charlou et al., 1996; Edmonds et al., 1996; Von Damm et al., 1998; Chiba et al., 2001; Seyfried et al., 2003; Gallant and Von Damm, 2006). Furthermore, vent-salinities of many of these high-pressure systems have been observed to remain constant for many years (Butterfield et al., 1994b; Chiba et al., 2001), in agreement with our simulation results. The consistency of these observation, as summarized in table 8.2, highlights the fundamental difference in convective behavior when phase-separation occurs either by boiling as opposed to brine condensation.

Deep hydrothermal systems are typically found on slow-spreading systems, like the Mid-Atlantic Ridge, whereas shallow systems are more common on fast-spreading ridges. The different tectonics and magmatic heat supply of slow- versus fast-spreading ridges certainly have an impact on the hydrothermal systems. In addition, magmatic events like dike injections are known to effect chemistry and temperature of vent fluids (Haymon, 1996; Von Damm, 2005). Nevertheless, our simulations show that the difference between phase-separation by boiling or condensation, and associated contrasting convective styles, can explain many of the observed spatial variations, rapid transient variations, or the absence of variation in vent-salinity in different black-smoker fields. The waterdepth of systems and the depth of phase-separation therefore appear to be first-order controls on black-smoker vent salinity.

8.6 Conclusions

We present the first multi-phase simulations of brine-vapor interactions at mid-ocean ridge hydrothermal systems. Although geometrically simple, our simulations accurately predict the range of salinities observed at natural systems. Shallow, boiling systems are characterized by rapid transient and sharp spatial variations in vent salinity. We show why, in such systems, brine and vapor can vent simultaneously from different chimneys in the same vent field. In simulations of deeper systems, phase separation occurs by brine condensation and simultaneous brine and vapor venting does not occur. The brine forms at depth and can only be mined by shutting down the heat source. Therefore, deep systems are characterized by vent salinities which remain constant over years. These results are in good agreement with long-term observations from shallow and deep natural systems. Our simulations show that whether phase-separation occurs by boiling or by condensation is a first-order control on vent-fluid salinity, and especially its variation in space and time.

Tab. 8.2:

Inferred "subcritical" phase-separation					
ridge	site	depth	venting		
			salinity	temperature	variation
JdF	CoAxial [a]	2000m	B+V	255-292°C	simultaneous B and V
JdF	Axial Volcano [b,c]	1542m	B+V	300-328°C	simultaneous B and V
JdF	North Cleft [d]	2270m	B+V	60-327°C	simultaneous B and V
JdF	South Cleft [e,f]	2300m	B	224-285°C	-
EPR	Brandon [g]	2850m	B+V	375-405°C	simultaneous B and V[r]
EPR	9°50'N [h]	2500m	B+V	350-388°C	From V to B in few years
MAR	Menez Gwen [i]	850m	V	275-284°C	-
Inferred "supercritical" phase-separation					
ridge	site	depth	venting		
			salinity	temperature	variation
JdF	Main Endeavour [j,k]	2200m	V	340-379°C	constant for 12 years
EPR	17°25'S [l]	2600m	V	300-340°C	-
EPR	18°15'S [l]	2600m	B	>300°C	-
EPR	18°25'S [l]	2600m	V	310°C	-
MAR	Lucky Strike [m,i]	1650m[s]	V	202-333°C	same salinity for one year
MAR	Broken Spur [n]	3100m	V	360-364°C	same salinity in all chimneys
MAR	TAG [o,p]	3700m	B	273-301°C	constant for 12 years
CIR	Kairei [q]	2450m	B	315-365°C	-
CIR	Edmond [q]	3300m	B	273-382°C	same salinity in all chimneys

Compilation of black-smoker fields where phase-separation was identified to be at either subcritical or supercritical conditions. Fields where this was undetermined, as well as sediment-covered fields, have been left out of this compilation. "B" and "V" refer to brine and vapor, i.e. higher and lower than sea-water salinity. JdF = Juan de Fuca ridge, EPR = East Pacific Rise, MAR = Mid-Atlantic Ridge and CIR = Central Indian Ridge. [a] Butterfield and Massoth (1997), [b] Massoth et al. (1989), [c] Butterfield et al. (1990), [d] Butterfield et al. (1994a), [e] Von Damm and Bischoff (1987), [f] Von Damm (1995), [g] Von Damm et al. (2003), [h] Von Damm et al. (1997), [i] Charlou et al. (2000), [j] Butterfield et al. (1994b), [k] Seyfried et al. (2003), [l] Charlou et al. (1996), [m] Von Damm et al. (1998), [n] James et al. (1995), [o] Edmonds et al. (1996), [p] Chiba et al. (2001), [q] Gallant and Von Damm (2006). [r] Phase-separation inferred to occur at the critical point in the chimney structure itself. [s] Phase-separation is inferred to occur very deep in the subseafloor (Von Damm et al., 1998)

9. CONCLUSIONS AND OUTLOOK

In this thesis a new computational tool is presented which enables realistic simulations of compressible, multi-phase fluid flow in hydrothermal systems. Such simulations are important since they can help to test the physical realism of scenarios derived from field observations but also guide field-based studies by predicting measurable phenomena. In the case of mid-ocean ridge hydrothermal systems, numerical modeling has an even more profound meaning since sub-seafloor observations are scarce and 3D data are essentially absent. An equally important benefit of modeling is that the physics itself can be elucidated by stepwise including or excluding certain component processes. This way, first-order effects can be separated from less important ones giving fundamental insights into the physics of the system.

The newly developed computational tool allows to realistically simulate fluid flow of boiling, salty fluids for the first time, and has been applied here to mid-ocean ridge hydrothermal systems. The results give new and some truly surprising insights in the nature of sub-seafloor convection at these largest magmatic-hydrothermal systems on Earth.

In 3D, flow not only organizes into pipe-like upflow zones, but these are surrounded by narrow downflow zones of relatively warm fluids - in sharp contrast to nearly all published cartoons showing broad across-axis fluid intake. Although contrary to the conceptual picture of most ocean-floor hydrologists, the concentric flow configuration is readily explained by the normally neglected non-linearities in fluid properties. The configuration ensures optimal heat transfer and has important consequences for the efficiency of metal leaching from the oceanic crust to form ore deposits.

Next to that, results show that sub-seafloor fluid-flow patterns are much more irregular and convection much more unstable than previously reported. This dynamic instability can directly explain variations in temperature and salinity as measured on the seafloor at natural systems. Multi-phase simulations reveal new mechanisms to either trap or mobilize the more heavy brine phase. In shallow-ocean systems, brine-transporting corridors form at the edges of two-phase boiling zones resulting in rapid changes in vent-fluid salinity. In contrast, deeper systems are characterized by single-phase upflow and relatively constant venting salinities. These predicted salinities and their relative stability or instability as a function of water depth are in excellent agreement with long-term observations of natural black-smoker systems. Also the fluctuation in vent temperature can be explained by the physics and dynamics of the convection cell alone, with the period of fluctuation depending on the permeability. These results therefore provide a simple explanation of how seismic events can trigger temperature fluctuations: The earthquake-induced permeability-increase shifts the hydrothermal system to the unsteady regime with accompanying fluctuating vent temperatures.

Although all presented models in this thesis are generic in nature, without the complexity of real mid-ocean ridge hydrothermal systems, the many key-characteristics of the latter are

accurately reproduced. Features like temperature and salinity changes of vent fluids, splitting of rising thermal plumes, regular spacing of black smoker fields and the location of recharge zones are all linked to the non-linearity in the fluid properties. Therefore, the non-linear thermodynamics of the fluid, irrespective of whether pure or salt water is used, are a first-order control on convection at mid-ocean ridge hydrothermal systems. This insight proved to be crucial in conceptualizing the results in all application-oriented chapters.

The most surprising result presented in this thesis is the focussed nature of recharge in regions directly surrounding active black smoker vent fields. Fluids entering the oceanic crust here flow all the way down to the base of the hydrothermal cell and have an expected residence time of as little as a few years. Therefore hydrologic tracer experiments seem possible in an acceptable time frame and the optimal location for tracer injection seems to be at a small radial distance outward from the edge of a black smoker field. Such tests could provide unique and critical data on permeability, porosity and flow paths which could be used again to fine-tune more detailed and sophisticated numerical models. The Main Endeavour Field on the Juan de Fuca ridge is arguably the best location to do such a challenging experiment.

This emerging, powerful, interaction between field-based observations and realistic numerical modeling should be applied to hydrothermal systems in other geologic settings in the near future. The newly developed computational tool can readily be applied to address open-questions in geothermal reservoir engineering and hydrothermal systems associated with porphyry-copper type environments. Next to those, the only recently discovered, and less well studied, active hydrothermal systems associated with submarine arc and back-arc volcanoes form an especially interesting target since these settings seem more favorable for high-grade ore deposit formation than mid-ocean ridge settings. For some of those systems - in particular for geothermal reservoirs - much more rigorous datasets are available or can more easily be acquired, compared to black smoker systems. This convenience is likely to lead to a more tighter and therefore more fruitful interaction between field-based and numerical studies. Such an approach could, for example, form a powerful exploration tool for finding new ore deposits, both on the continents and in the oceans.

The generic models presented in this thesis highlight the importance of numerical simulations to understand the physics of complex systems like sub-seafloor convection at mid-ocean ridges. They show that accurately accounting for non-linearities in the governing equations is key to understanding the physics and dynamics of convection and can explain many observations at natural systems. More generally, this study demonstrates that due to the complexity of these systems, a generic, step-wise approach is required to unravel cause and effect relationships and to separate first-order physical factors from less dominant ones. Only after these fundamentals have been understood then the role of geologic complexity and chemical interactions in modifying the first order picture can quantitatively be understood. While this thesis has provided a number of new, fundamental insights into the first order physics of mid-ocean ridge hydrothermal systems, more simulations are still required to fully understand the physics of three-phase thermohaline fluid flow and especially the dynamics of the brine phase. The major next step would be to understand three-dimensional fluid flow of multi-phase salt water. These challenging simulations will be CPU-intensive, but faster schemes as currently under development and in combination with parallel computing should make them possible within the next year.

BIBLIOGRAPHY

Alt, J., 1995. *Subseafloor processes in mid-ocean ridge hydrothermal systems* Seafloor Hydrothermal Systems. *(ed. S.E. Humphris, R.A. Zierenberg, L.S. Mullineaux and R.E. Thomson)*. Vol. 91 of Geophys. Monogr. pp. 85–114.

Anorsson, S., Stefansson, A., Bjarnason, J., 2007. *Fluid-fluid interactions in geothermal systems. In* Fluid-fluid interactions *(ed. A. Liebscher and C.A. Heinrich)*. Vol. 65. pp. 259–312.

Ashby, S., Bosl, W., Falgout, R., Smith, S., Tompson, A., 1999. A numerical simulation of groundwater flow and contaminant transport on the CRAY T3D and C90 supercomputers. Int. J. High Performance Comput. Appl. 13 (1), 80–93.

Aziz, K., Settari, A., 1979. Petroleum Reservoir Simulation. Applied Science Publisher, London, UK.

Babcock, J., Harding, A., Kent, G., J.A., O., 1998. An examination of along-axis variation of magma chamber width and crustal structure on the East Pacific Rise between 13 degrees 30'N and 12 degrees 20'N. J. Geophys. Res. 103 (B12), 30451–30467.

Bachler, D., Kohl, T., Rybach, L., 2003. Impact of graben-parallel faults on hydrothermal convection - Rhine graben case study. Phys. Chem. Earth 28, 431–441.

Bai, W., Xu, W., Lowell, R., 2003. The dynamics of submarine geothermal heat pipes. Geophys. Res. Lett. 30 (110).

Baker, E., Massoth, G., 1987. Characteristics of hydrothermal plumes from two vent fields on the Juan de Fuca Ridge, northeast Pacific Ocean. Earth Planet. Sci. Lett. 85, 59–73.

Baker, E., Urabe, T., 1996. Extensive distribution of hydrothermal plumes along the the superfast spreading East Pacific Rise, 13°30'-18°40'S. J. Geophys. Res. 101, 8685–8695.

Baliga, B., Patankar, S., 1980. A new finite-element formulation for convection diffusion problems. Num. heat trans. 3, 393–409.

Barnard, S., Simon, H., 1993. A fast multilevel implementation of recursive spectral bisection for partitioning unstructured problems. In: Proceedings of the sixth SIAM conference on Parallel Processing for Scientific Computing. SIAM, pp. 711–718.

Bear, J., 1972. Dynamics of Fluids in Porous Media. Dover, New York, USA.

Belayneh, M., 2003. Analysis of natural fracture networks in massive and well-bedded carbonates and the impact of these networks on fluid flow in dual porosity medium. Ph.D. thesis, Imperial College, London, United Kingdom.

Belayneh, M., Geiger, S., Matthai, S., 2006. Numerical simulation of water injection into layered fractured carbonate reservoir analogs. AAPG Bulletin 90 (10), 1473–1493.

Bhogeswara, R., Killough, J., 1982. Parallel linear solvers for reservoir simulation: Generic approach for existing and emerging computer architectures. In: Proceedings of 12th SPE Symposium on Reservoir Simulation, New Orleans, LA, Feb. 28 - Mar. 3. SPE, pp. 71–82.

Broad, W., 1997. First move made to mine mineral riches of seabed. New York Times 21 Dec., A1.

Brooks, R., Corey, A., 1964. Hydraulic properties of porous media. Hydrological Paper 3, 107–116.

Busse, F., Joseph, D., 1972. Bounds for heat transport in a porous layer. J. Fluid Mech. 54, 521–543.

Butterfield, D., Massoth, G., 1997. Seafloor eruptions and evolution of hydrothermal fluid chemistry. Phil. Trans. R. Soc. Lond. 355, 369–386.

Butterfield, D., Massoth, G., McDuff, R., Lupton, J., Lilley, M., 1990. Geochemistry of hydrothermal fluids from Axial Seamount hydrothermal emissions study vent field, Juan de Fuca Ridge: Subseafloor boiling and subsequent fluid-rock interaction. J. Geophys. Res. 95 (B8), 12895–12921.

Butterfield, D., McDuff, R., Mottl, M., Lilley, M., Lupton, J., Massoth, G., 1994a. Geochemistry of North Cleft segment vent fluids: Temporal changes in chlorinity and their possible relation to recent volcanism. J. Geophys. Res. 99 (B3), 4951–4968.

Butterfield, D., McDuff, R., Mottl, M., Lilley, M., Lupton, J., Massoth, G., 1994b. Gradients in the composition of hydrothermal fluids from the Endeavour segment vent field: phase separation and brine loss. J. Geophys. Res. 95 (B8), 9561–9583.

Calahan, D., 1982. Vectorized direct solvers for 2-D grids. In: Proceedings of Sixth SPE Symposium on Reservoir Simulation, New Orleans, LA, Feb. 1-3. SPE, pp. 489–497.

Campbell, C., Bowers, T., Measures, C., Falkner, K., Khadem, M., Edmond, J., 1988. A time series vent fluid composition from 21°N East Pacific Rise (1979,1981,1985) and the Guyamas Basin, Gulf of California (1982,1985). J. Geophys. Res. 93 (B5), 4537–4549.

Charlou, J., Donval, J., Douville, E., Jean-Baptiste, P., Radford-Knoery, J., Fouquet, Y., Dapoigny, A., Stievenard, M., 2000. Compared geochemical signatures and the evolution of Menez Gwen (37°50'N) and Lucky Strike (37°17'N) hydrothermal fluids, south of the Azores Triple Junction on the Mid-Atlantic Ridge. Chem. Geol. 171 (1-2), 49–75.

Charlou, J., Fouquet, Y., Donval, J., Auzende, J., Jean-Baptiste, P., Stievenard, M., Michel, S., 1996. Mineral and gas chemistry of hydrothermal fluids on an ultrafast spreading ridge: East Pacific Rise 17° to 19°S (Naudur cruise, 1993) phase separation processes controlled by volcanic and tectonic activity. J. Geophys. Res. 101 (B7), 15,899–15,919.

Cherkaoui, A., Wilcock, W., 1999. Characteristics of high Rayleigh number two-dimensional convection in an open-top porous layer heated from below. J. Fluid Mech. 394, 241–260.

Cherkaoui, A., Wilcock, W., 2001. Laboratory studies of high Rayleigh number circulation in an open-top Hele-Shaw cell: An analog to Mid-Ocean ridge hydrothermal systems. J. Geophys. Res. 106 (B6), 10983–11000.

Cherkaoui, A., Wilcock, W., Baker, E., 1997. Thermal fluxes associated with the 1993 diking event on the CoAxial segement, Juan de Fuca ridge: A model for the convective cooling of a dike. J. Geophys. Res. 102 (B11), 24887–24902.

Cherkaoui, A., Wilcock, W., Dunn, R., Toomey, D., 2003. A numerical model of hydrothermal cooling and crustal accretion at a fast spreading mid-ocean ridge. G-cubed 4 (9).

Chiba, H., Masuda, H., Lee, S., Fujioka, K., 2001. Chemistry of hydrothermal fluids at the TAG active mound, MAR 26°N, in 1998. Geophys. Res. Lett. 28 (15), 2919–2922.

Chouke, R., van Meurs, P., van der Poel, C., 1959. The instability of slow, immiscible, viscous liquid-liquid displacements in permeable media. Trans. AIME 216, 188–194.

Coogan, L., Howard, K., Gillis, K., Bickle, M., Chapman, H., Boyce, A., Jenkin, G., Wilson, R., 2006. Chemical and thermal constraints on focussed fluid flow in the lower oceanic crust. Am. J. Sci. 306, 389–427.

Corliss, J., Dymond, J., Gordon, L., Edmond, J., Herzen, R., Ballard, R., Green, K., Williams, D., Bainbridge, A., Crane, K., Vanandel, T., 1979. Submarine thermal springs on the Galapagos rift. Science 203, 1073–1083.

Coumou, D., Driesner, T., Geiger, S., Heinrich, C., Matthai, S., 2006. The dynamics of mid-ocean ridge hydrothermal systems: Splitting plumes and fluctuating vent temperatures. Earth Planet. Sci. Lett. 245, 218–231.

Coumou, D., Matthai, S., Geiger, S., Driesner, T., 2008. A parallel FE-FV scheme to solve fluid flow in complex geologic media. Comp. Geoscience, in press.

Cox, B., Pruess, K., 1990. Numerical experiments of convective heat transfer in water-saturated porous media at near-critical conditions. Transport Porous Med. 5, 299–323.

Dahlmann, A., Wallmann, K., Sahling, H., Sarthou, G., Bohrman, G., Petersen, S., Chin, C., Klinkhammer, G., 2001. Hot vents in an ice-cold ocean: Indications for phase separation at the southernmost area of hydrothermal activity, Bransfield Strait, Antarctica. Earth Planet. Sci. Lett. 193, 381–394.

Dewar, R., 2003. Information theory explanation of the fluctuation theorem, maximum entropy production and self-organized criticality in non-equilibrium stationary states. J. Phys. A. Math. Gen. 36.

Driesner, T., 2007. The system H_2O-NaCl. Part II: Correlations for molar volume, enthalpy, and isobaric heat capacity from 0 to 1000°C, 0 to 5000 bar, and 0 to $1X_{NaCl}$. Geochim. Cosmochim. Ac. 71, 4902–4919.

Driesner, T., Geiger, S., 2007. *Numerical simulation of multiphase fluid flow in hydrothermal systems. In* Fluid-fluid interactions *(ed. A. Liebscher and C.A. Heinrich)*. Vol. 65. pp. 187–212.

Driesner, T., Heinrich, C., 2003. Accurate P-T-X-V-H correlations for the system H_2O-NaCl from 0 to 800^{o}C, 0 to 500 MPa and 0 to 1 X_{NaCl}. Acta Mineral. Pet. Abstr. Ser. 2, 55–56.

Driesner, T., Heinrich, C., 2007. The system H_2O-NaCl. Part I: Correlation formulae for phase relations in temperature-pressure-composition space from 0 to 1000°C, 0 to 5000 bar, and 0 to 1X_{NaCl}. Geochim. Cosmochim. Ac. 71, 4880–4901.

Dunn, R., Toomey, D., Solomon, S., 2000. Three dimensional seismic structure and physical properties of the crust and shallow mantle beneath the at the East Pacific Rise at 9°30'N,. J. Geophys. Res. 105, 23537–23555.

Durlofsky, L., 1993. Accuracy of mixed and control volume finite element approximations to Darcy velocity and related quantities. Water Resour. Res. 30, 965–973.

Edmonds, H., German, C., Green, D., Huh, Y., Gamo, T., Edmond, J., 1996. Continuation of the hydrothermal fluid chemistry time series at TAG, and the effect of ODP drilling. Geophys. Res. Lett. 23 (23), 3487–3489.

Elkhoury, J., Brodsky, E., Agnew, D., 2005. Observed permeability increases generated by seismic waves. Eos Trans. AGU 86 (52), Fall Meet. Suppl., Abstract T42B–05.

Elmroth, E., Ding, C., Wu, Y., 2001. High performance computations for large scale simulations of subsurface multiphase fluid and heat flow. J. Supercomput. 18, 235–258.

Emmanuel, S., Berkowitz, B., 2007. Phase separation and convection in heterogenous porous media: Implications for seafloor hydrothermal systems. J. Geophys. Res. 112 (B05210).

Faust, C., Mercer, J., 1979. Geothermal reservoir simulation 2. Numerical solution techniques for liquid-dominated and vapor-dominated hydrothermal systems. Water Resour. Res. 15 (1), 31–46.

Fisher, A., 1998. Permeability within basaltic oceanic crust. Rev. Geophys. 36, 143–182.

Fisher, A., 2001. Energy and Mass Transfer in Marine Hydrothermal Systems. *(ed. P.E. Halbach, V. Tunnicliffe and J.R. Hein)*. Vol. 89 of Dahlem Workshop Report. pp. 29–52.

Fisher, A., 2005. Marine hydrogeology: Recent accomplishments and future opportunities. Hydrogeol J 13, 69–97.

Fisher, A., Davis, E. E., Hutnak, M., Spiess, V., Zuhlsdorff, L., Cherkaoui, A., Christiansen, L., Edwards, K., Macdonald, R., Villinger, H., Mottl, M., Wheat, C., Becker, K., 2003a. Hydrothermal recharge and discharge across 50 km guided by seamounts on a young ridge flank. Nature 421, 618–621.

Fisher, A., Stein, C., Harris, R., Wang, K., Silver, E., Pfender, M., Hutnak, M., Cherkaoui, A., Bodzin, R., Villinger, H., 2003b. Abrupt thermal transition reveals hydrothermal boundary and role of seamounts within Cocos Plate. Geoph. Res. Lett. 30 (11), 1550.

Fontaine, F., Wilcock, W., 2006. Dynamics and storage of brine in mid-ocean ridge hydrothermal systems . J. Geophys. Res. 111 (B6).

Fontaine, F., Wilcock, W., 2007. Two-dimensional numerical models of open-top hydrothermal convection at high Rayleigh and Nusselt numbers: Implications for mid-ocean ridge hydrothermal circulation. G-cubed 8 (7).

Fornari, D., Shank, T., Von Damm, K., Gregg, T., Lilley, M., Levai, G., Bray, A., Haymon, R., Perfit, M., Lutz, R., 1998. Time-series temperature measurements at high-temperature hydrothermal vents, East Pacific Rise 9°49'-51'N: Evidence for monitoring a crustal cracking event. Earth Planet. Sci. Lett. 160 (3-4), 491–431.

Forsyth, P., 1991. A control volume finite element approach to NAPL groundwater contamination. SIAM Journal of Scientific Computing 12, 1029–1057.

Foustoukos, D., Seyfried, W., 2007. *Fluid phase separation processes in submarine hydrothermal systems. In* Fluid-fluid interactions *(ed. A. Liebscher and C.A. Heinrich)*. Vol. 65. pp. 213–239.

Franklin, J., Gibson, H., Jonasson, I., Galley, A., 2005. *Volcanogenic Massive Sulfide Deposits. In* Economic Geology, 100th Anniversary Volume. *(ed. J.W. Hedenquist, J.F.H Thompson, R.J. Goldfarb and J.P. Richards)*. pp. 523–560.

Gallant, R., Von Damm, K., 2006. Geochemical controls on hydrothermal fluids from the Kairei and Edmond vent field, 23°-25°S, Central Indian Ridge. G-cubed 7 (6).

Geiger, S., 2004. Numerical simulation of the hydrodynamics and thermodynamics of NaCl-H_2O fluids. Ph.D. thesis, ETH Zurich, Switzerland.

Geiger, S., Driesner, T., Heinrich, C., Matthai, S., 2006a. Multiphase thermohaline convection in the Earth's crust: I. A novel finite element - finite volume solution technique combined with a new equation of state for NaCl-H_2O. Transport Porous Med. 63, 399–434.

Geiger, S., Driesner, T., Heinrich, C., Matthai, S., 2006b. Multiphase thermohaline convection in the Earth's crust: II. Benchmarking and application of a finite element - finite volume solution technique with a NaCl-H_2O equation of state. Transport Porous Med. 63, 435–461.

Geiger, S., Driesner, T., Matthai, S., Heinrich, C., 2005. On the dynamics of NaCl-H_2O fluid convection in the Earth's crust. J. Geophys. Res. 110 (B07101).

Geiger, S., Roberts, S., Matthai, S., Zoppou, C., Burri, A., 2004. Combining finite element and finite volume methods for efficient multiphase flow simulations in highly heterogeneous and structurally complex geologic media. Geofluids 4, 284–299.

German, C., Lin, J., 2005. *The thermal structure of the oceanic crust, ridge-spreading and hydrothermal circulation: How well do we understand their inter-connections? In* Mid-ocean ridges: Hydrothermal Interactions between the Lithosphere and Oceans. *(ed. C.R. German, J. Lin and L.M. Parson).* Vol. 148 of Geophys. Monogr. pp. 1–18.

Ginster, U., Mottl, M., Von Herzen, R., 1994. Heat flux from black smokers on the Endeavour and Cleft segments, Juan de Fuca Ridge. J. Geophys. Res. 99 (B3), 4937–4950.

Glickson, D., Kelley, D., Delaney, J., 2007. Geology and hydrothermal evolution of the Mothra hydrothermal field, Endeavour segment, Juan de Fuca Ridge. G-cubed 8 (Q06010).

Grant, M., Donaldson, I., Bixley, P., 1984. Geothermal reservoir engineering. Hemisphere Publishing Corporation.

Grant, M., Sorey, M., 1979. The compressibility and hydraulic diffusivity of a water-steam flow. Water Resour. Res. 15 (3), 684–686.

Gropp, W., Huss-Lederman, S., Lumsdaine, A., Lusk, E., Nitzberg, B., Saphir, W., Snir, M., 1996a. MPI - The complete reference, Volume 2, The MPI extensions. The MIT Press, Cambridge, Massachusetts (USA), London (UK).

Gropp, W., Lusk, E., Doss, N., Skjellum, A., 1996b. A high-performance, portable implementation of the MPI message passing interface standard. Parall. Comput. 6 (789–828).

Haar, Gallagher, Kell, 1984. NBS/NRC Steam Tables. Hemisphere Publishing Corporation.

Hannington, M., Jonasson, I., Herzig, P., Petersen, S., 1995. *Physical and Chemical Processes of seafloor mineralization at mid-ocean ridges. In* Seafloor Hydrothermal Systems: Physical, chemical biological and geological interactions. *(ed. E. Humphris, R. Zierenberg, L. Mullineaux and R. Thomson.)*. Vol. 91 of Geophys. Monogr. pp. 115–157.

Hayba, D. O., Ingebritsen, S., 1994a. The computer model HYDROTHERM, a three-dimensional finite-difference model to simulate ground-water flow and heat transport in the temperature range of 0 to 1200°C. U.S. Geological Survey Water-Resources Investigations Report 94-4045.

Hayba, D. O., Ingebritsen, S., 1994b. Multiphase groundwater flow near cooling plutons. J. Geophys. Res. 102 (B6), 12235–12252.

Haymon, R., 1996. *The response of ridge-crest hydrothermal systems to segmented episodic magma supply. In* Tectonic, Magmatic, Hydrothermal and Biological Segmentation of Mid-Ocean Ridges. *(ed. C.J. MacLeod, P.A. Taylor and C.L. Walker)*. pp. 157–168.

Haymon, R., Fornari, D., Von Damm, K., Lilley, M., Perfit, M., Edmond, J., Shanks, W., Lutz, R., Grebmeier, J., Carbotte, S., Wright, D., McLaughlin, E., Smith, M., Beedle, N., Olson, E., 1993. Volcanic eruption of the mid-ocean ridge along the East Pacific Rise crest at 9°45-52'N: Direct submersible observations of seafloor phenomena associated with an eruption event in April, 1991. Earth Planet. Sci. Lett. 119, 85–101.

Heinrich, C., 2007. *Fluid-fluid interactions in magmatic-hydrothermal ore formation. In* Fluid-fluid interactions *(ed. A. Liebscher and C.A. Heinrich)*. Vol. 65. pp. 363–387.

Hemley, J., Cygan, G., Fein, J., Robinson, G., Angelo, W., 1992. Hydrothermal ore-forming processes in light of studies in rock-buffered systems: I Iron-Copper-Zinc-Lead sulfide solubility relations. Econ. Geol. 87 (1), 1–22.

Herrington, R., Maslennikov, V., Zaykov, V., Seravkin, I., Kosarev, A., Buschmann, B., Orgeval, J., Holland, N., Tesalina, S., Nimis, P., R., A., 2005. Classification of VMS deposits: Lessons from the South Uralides. Ore Geol. Rev. 27 (1–4), 203–237.

Hofmeister, A., Criss, R., 2005. Earth's heat flux revised and linked to chemistry. Tectonophys. 395, 159–177.

Holland, M., Urai, J., Martel, S., 2006. The internal structure of fault zones in basaltic sequences. Earth Planet. Sci. Lett. 248 (1-2), 301–315.

Homsy, G., 1987. Viscous fingering in porous media. Ann. Rev. Fluid Mech. 19, 271–311.

Huber, R., Helmig, R., 1999. Multi-phase flow in heterogeneous porous media: A classical finite element method versus an implicit pressure-explicit saturation-based mixed finite element-finite volume approach. Int. J. Numer. Methods Fluids 29, 899–920.

Huyakorn, P., Pinder, G., 1983. Computational Methods in Subsurface Flow. Academic Press, New York, U.S.A.

Ingebritsen, S., Hayba, D. O., 1994. Fluid flow and heat transport near the critical point of H_2O. Geophys. Res. Lett. 21 (20), 2199–2202.

Ingebritsen, S., Sanford, W., Neuzil, C., 2006. Groundwater in geologic processes, 2nd Edition. Cambridge University Press, Cambridge, UK.

Istok, J., 1989. Groundwater modeling by the finite element method. Wat. Res. Monogr. 13.

James, R., Elderfield, H., Palmer, M., 1995. The high temperature reaction zone of the Oman ophiolite: New field data, microthermometry of fluid inclusions, PIXE analyses and oxygen isotopic ratios. Geochim. Cosmochim. Ac. 59, 651–659.

Johnson, H., Becker, K., Von Herzen, R., 1993. Near-axis heat flow measurements on the northern Juan de Fuca Ridge: Implications for fluid circulation in oceanic crust. Geophys. Res. Lett. 20 (17), 1875–1878.

Johnson, H., Hutnak, M., Dziak, R., Fox, C., Urcuyo, I., Cowen, J., Nabelekk, J., Fisher, C., 2000. Earthquake-induced changes in a hydrothermal system on the Juan de Fuca mid-ocean ridge. Nature 407, 174–177.

Jupp, T., Schultz, A., 2000. A thermodynamic explanation for black-smoker temperatures. Nature 403 (6772), 880–883.

Jupp, T., Schultz, A., 2004. Physical balances in subseafloor hydrothermal convection cells. J. Geophys. Res. 109 (B05101).

Juteau, T., Manac, G., Moreau, O., Lcuyer, C., Ramboz, C., 2002. The chemistry of hydrothermal fluids from the Broken Spur site, 29°N, Mid-Atlantic Ridge. Mar. Geoph. Res. 21 (3–4).

Kaarstad, T., Froyen, J., Bjorstad, P., Espedal, M., 1995. A massively parallel reservoir simulator. In: Proceedings of 13th SPE Symposium on Reservoir Simulation, San Antonio, TX, Feb. 12 - 15. SPE, pp. 467–478.

Kadko, D., Butterfield, D., 1998. The relationship of hydrothermal fluid composition and crustal residence time to maturity of vent fields on the Juan de Fuca Ridge. Geochim. Cosmochim. Ac. 62 (9), 1521–1533.

Kadko, D., K., G., Butterfield, D., 2007. Application of radium isotopes to determine crustal residence times of hydrothermal fluids from two sites on the reykjanes peninsula, iceland. Geochim. Cosmochim. Ac. 71, 6019–6029.

Karypsis, G., Kumar, V., 1998. METIS, A Software Package for Partitioning Unstructured Graphs, Partitioning Meshes, and Computing Fill-Reducing Orderings of Sparse Matrices. Version 4.0. University of Minnesota, Department of Computer Science / Army HPC Research Center, Minneapolis.

Kawada, Y. S., Yoshida, S., Watanabe, S., 2004. Numerical simulations of mid-ocean ridge hydrothermal circulation including the phase separation of seawater. Earth Planets Space 56, 193–215.

Kelley, S., Baross, J., Delaney, J., 2002. Volcanoes, fluids, and life at mid-ocean ridge spreading centers. Annu. Rev. Earth Planet. Sci. 30, 385–491.

Kelley, S., Gillis, K., Thompson, G., 1993. Fluid evolution in submarine magma-hydrothermal systems at the Mid-Atlantic Ridge. J. Geophys. Res. 98, 19579–19596.

Kent, G., Singh, S., Harding, A. J., Sinha, M. C., Orcutt, J., Barton, P. J., White, R. S., Bazin, S., Hobbs, R. W., Tong, C. H., Pye, J. W., 2000. Evidence from three-dimensional seismic reflectivity images for enhanced melt supply beneath Mid-Ocean-Ridge discontinuities. Nature 406, 614–618.

Kesler, S., 1994. Mineral Resources, economins and the environment. MacMillan College Publishing Company Inc, New York, USA.

Kessler, D., Levine, H., 1986. Theory of Saffman-Taylor finger. I & II. Phys. Rev. 33, 3625–3627.

Killough, J., Commander, D., 1999. Scalable parallel reservoir simulation on a Windows NT-based workstation cluster. In: Proceedings of 15th SPE Symposium on Reservoir Simulation, Houston, TX, Feb. 14 - 17. SPE, pp. 41–50.

Killough, J., Levesque, J., 1982. Reservoir simulation and the in-house vector processor experience for the first year. In: Proceedings of Sixth SPE Symposium on Reservoir Simulation, New Orleans, LA, Feb. 1-3. SPE, pp. 481–487.

Kissling, W., 2005a. Transport of three-phase hyper-saline brines in porous media: Examples. Transport Porous Med. 60, 141–157.

Kissling, W., 2005b. Transport of three-phase hyper-saline brines in porous media: Theory and code implementation. Transport Porous Med. 61, 25–44.

Koepke, J., Feig, S., Snow, J., 2005. Late stage magmatic evolution of oceanic gabbros as a result of hydrous partial melting: Evidence from the Ocean Drilling Program (ODP) leg 153 drilling at the Mid-Atlantic ridge. G-cubed 30, 385–491.

Krechel, A., Stuben, K., 2001. Parallel algebraic multigrid based on subdomain blocking. Parallel comput. 27, 1009–1031.

Krechel, A., Stuben, K., 2005. User's Manual SAMGp. Frauenhofer Institute SCAI, Schloss Birlinghoven, St. Augustin, Germany.

Laumbach, D., 1975. High-accuracy finite-difference technique for treating convection-diffusion equation . Soc. of Petr. Eng. Jour. 15 (6), 517–531.

Le Pichon, X., Langseth, M., 1969. Heat flow from mid-ocean ridges and sea-floor spreading. Tectonophys. 8, 319–344.

Lister, C., 1974. On the penetration of water into hot rock. Geophys. J. R. Astron. Soc. 39, 465–509.

Lorenz, R., 2003. Full steam ahead - probably. Science 299, 837–838.

Lowell, R., Germanovich, L., 1994. On the temporal evolution of high-temperature hydrothermal systems at ocean ridge crests. J. Geophys. Res. 99, 565–575.

Lowell, R., Germanovich, L., 2005. *Hydrothermal Processes at Mid-Ocean Ridges: Results From Scale Analysis and Single-Pass Models. In* Mid-ocean ridges: Hydrothermal Interactions between the Lithosphere and Oceans. *(ed. C.R. German, J. Lin and L.M. Parson).* Vol. 148 of Geophys. Monogr. pp. 219–244.

Lowell, R., Rona, A., Von Herzen, R., 1995. Seafloor hydrothermal systems. J. Geophys. Res. 10 (B1), 327–352.

Lowell, R., Vancappellen, P., Germanovich, L., 1993. Silica precipitation in fractures and the evolution of permeability in hydrothermal upflow zones. Science 260 (5105), 192–194.

Lowell, R., Yao, Y., Germanovich, L., 2003. Anhydrite precipitation and the relationship between focused and diffuse flow in seafloor hydrothermal systems. J. Geophys. Res. 108 (B9), 2424.

Ma, Y., Chen, Z., 2004. Parallel computation for reservoir thermal simulation of multicomponent and multiphase fluid flow. J. Comput. Phys. 201, 224–237.

Massoth, G., Butterfield, D., Lupton, J., McDuff, R., Lilley, M., Jonasson, I., 1989. Submarine venting of phase-separated hydrothermal fluids at Axial Volcano, Juan de Fuca ridge. Nature 340, 702–705.

Matthai, S., Geiger, S., Roberts, S., 2001. Complex Systems Platform: CSP3D3.0: user's guide. Eidgenossische Technische Hochschule Zurich, Switzerland.

Matthai, S., Geiger, S., Roberts, S., 2004. Complex Systems Platform: CSP5.0: user's guide. Eidgenossische Technische Hochschule Zurich, Switzerland / Imperial College London, UK.

Matthai, S., Geiger, S., Roberts, S., Paluszny, A., Belayneh, M., Burri, A., Mezentsev, A., Lu, H., Coumou, D., Driesner, T., Heinrich, C., 2007. Numerical simulation of multi-phase fluid flow in structurally complex reservoirs. Geol. Soc. London, Spec. Pub. 292, 405–429.

Matthai, S., Heinrich, C., Driesner, T., 2005. Is the Mount Isa copper deposit the product of forced brine convection in the footwall of a major reverse fault? Geology 32 (4), 357–360.

Mercer, J., Faust, C., 1979. Geothermal reservoir simulation.3. application of liquid-dominated and vapor-dominated hydrothermal modeling techniques of Wairakei, New-Zealand . Water Resour. Res. 15 (3), 653–671.

Narasimhan, T., Witherspoon, P., 1976. Integrated finite-difference method for analyzing fluid-flow in porous-media. Water Resour. Res. 21 (1), 57–64.

Nehlig, P., 1991. Salinity of oceanic hydrothermal fluids - a fluid inclusion study. Earth Planet. Sci. Lett. 102 (3-4), 310–325.

Nesbitt, B., Muehlenbachs, K., 1991. Stable isotope constrains on the nature of syntectonic fluid regime in the Canadian Cordillera. Geophys. Res. Lett. 18, 963–966.

Nicolas, A., Mainprice, D., 2005. Burst of high-temperature seawater injection. Terra Nova 17 (4), 326–330.

Oosting, S., Von Damm, K., 1996. Bromide/Chloride fractionation in seafloor hydrothermal fluids from 9-10°N East Pacific Rise. Earth Planet. Sci. Lett. 144, 133–145.

Palliser, C., McKibbin, R., 1998a. A model for deep geothermal brines I: State-space description. Transport Porous Med. 33, 65–80.

Palliser, C., McKibbin, R., 1998b. A model for deep geothermal brines II: Thermodynamic properties - Density. Transport Porous Med. 33, 129–154.

Palliser, C., McKibbin, R., 1998c. A model for deep geothermal brines III: Thermodynamic properties - Enthalpy and Viscosity. Transport Porous Med. 33, 155–171.

Paluszny, A., Matthai, S., Hohmeyer, M., 2007. Hybrid finite elementfinite volume discretization of complex geologic structures and a new simulation workflow demonstrated on fractured rocks. Geofluids 7, 1–23.

Peszynska, M. Wheeler, M., Yotov, I., 2001. Mortar upscaling for multiphase flow in porous media. Computat. Geosci 6, 73–100.

Pini, G., Putti, M., 1997. Parallel finite element Laplace transform method for the non-equilibrium groundwater transport equation. Int. J. Numer. Meth. Eng. 40, 2653–2664.

Pruess, K., 1987. TOUGH User's Guide. U.S. Nuclear Regulatory Commision, Report NUREG/CR-4645, Washington D.C., U.S.A.

Pruess, K., 2002. Numerical simulation of multiphase tracer transport in fractured geothermal reservoirs. Geothermics. 31 (4), 475–499.

Rabinowicz, M., Boulegue, J., Genthon, P., 1998. Two- and three-dimensional modeling of hydrothermal convection in the sedimented Middle Valley segment, Juan de Fuca Ridge. J. Geophys. Res. B10, 24045–24065.

Rabinowicz, M., Sempr, J., Genthon, P., 1999. Thermal convection in a vertical permeable slot: Implications for hydrothermal circulation along mid-ocean ridges. J. Geophys. Res. 104, 29275–29292.

Ramondenc, P., Germanovich, L., Von Damm, K., Lowell, R., 2006. The first measurements of hydrothermal heat output at 9°50'N, East Pacific Rise. Earth Planet. Sci. Lett. 245 (3-4), 487–497.

Rona, P., 2003. Resources of the seafloor. Science 299, 273–274.

Rosenberg, N., Spera, F., Haymon, R., 1993. The relationship between flow and permeability field in seafloor hydrothermal systems. Earth Planet. Sci. Lett. 116, 135–153.

Ruge, J., Stuben, K., 1987. Frontiers in Applied Mathematics, Multigrid Methods. Vol. 3. SIAM, Philadelphia, PA, Ch. Algebraic Multigrid (AMG), pp. 73–130.

Saccocia, P., Gillis, K., 1995. Hydrothermal upflow zones in the oceanic crust. Earth Planet. Sci. Lett. 136 (1-2), 1–16.

Saffman, P., Taylor, G., 1958. The penetration of a fluid into a porous medium or Hele-Shaw cell containing a more viscous liquid. P. Roy. Soc. Lond 245, 312–329.

Schamberger, S., Wierum, J., 2005. Partitioning finite element meshes using space-filling curves. Parallel comput. techn. 5, 759–766.

Schoofs, S., Hansen, U., 2000. Depletion of a brine layer at the base of the ridge-crest hydrothermal system. Earth Planet. Sci. Lett. 180 (3-4), 341–353.

Schoofs, S., Spera, F., Hansen, U., 1999. Chaotic thermohaline convection in low-porosity hydrothermal systems. Earth Planet. Sci. Lett. 174 (1-2), 213–229.

Scott, A., Sutton, B., Dunn, J., Minto, P., Thomas, C., 1982. An implementation of a fully implicit reservoir simulator on an icl distributed array processor. In: Proceedings of Sixth SPE Symposium on Reservoir Simulation, New Orleans, LA, Feb. 1-3. SPE, pp. 523–533.

Seyfried, W. J., Seewald, J., Berndt, M., Ding, K., Foustoukos, D., 2003. Chemistry of hydrothermal vent fluids from the Main Endeavour field, northern Juan de Fuca ridge: Geochemical controls in the aftermath of June 1999 seismic events. J. Geophys. Res. 108 (B9), 2429.

Singh, S., Kent, G., Collier, J., Harding, A. J., Orcutt, J., 1998. Melt to mush variations in crustal magma properties along the ridge crest at the southern East Pacific Rise. Nature 394, 874–878.

Sinton, J., Detrick, R., 1992. Mid-ocean ridge magma chamber. J. Geophys. Res. 168, 197–216.

Snir, M., Otto, S., Huss-Lederman, S., Walker, D., Dongarra, J., 1996. MPI - The complete reference, Volume 1, The MPI core. The MIT Press, Cambridge, Massachusetts (USA), London (UK).

Sohn, R., Fornari, D., Von Damm, K., Hildebrand, J., Webb, S., 1998. Seismic and hydrothermal evidence for a cracking event on the East Pacific Rise crest 9°50'N. Nature. 396, 159–161.

Stein, C., Stein, S., 1994. Constraints of hydrothermal heat flux through oceanic lithosphere from global heat flow. J. Geophys. Res. 99, 3081–3095.

Stein, J., Fisher, A., 2003. Observations and models of lateral hydrothermal circulation on a young ridge flank: Numerical evaluation of thermal and chemical constraints. G-Cubed. 4 (1026).

Straus, J., Schubert, G., 1977. Thermal convection of water in a porous medium: Effects of temperature and pressure-dependent thermodynamic and transport properties. J. Geophys. Res. 82 (2), 325–332.

Stuben, K., 2002. SAMG user's manual. Fraunhofer Institute SCAI, Schloss Birlinghoven, St. Augustin, Germany.

Tan, C., Homsy, G., 1986. Stability of miscible displacements in porous media: Rectilinear flow. Phys. Fluids 29 (11), 3549–3556.

Tan, C., Homsy, G., 1988. Simulation of non-linear viscous fingering in miscible displacement. Phys. Fluids 31 (6), 1330–1338.

Titley, S., Beane, R., 1981. Porphyry copper deposits. Econ. Geol. 75th Ann., 235–269.

Tivey, M., Johnson, H., 2002. Crustal magnetization reveals subsurface structure of Juan de Fuca Ridge hydrothermal vent fields. Geology. 30 (11), 979–982.

Tolstoy, M., Waldhause, F., Bohnenstiehl, D., Weekly, R., Kim, W., 2008. Seismic identification of along-axis hydrothermal flow on the East Pacific Rise. Nature 451, 181–185.

Travis, B., Janecky, D., Rosenberg, N., 1991. Three-dimensional simulation of hydrothermal circulation at mid-ocean ridges. Geophys. Res. Lett. 18 (8), 1441–1444.

Tsai, W., Shen, C., Fu, H., Kou, C., 1999. Study of parallel computation for groundwater solute transport. J. Hydrol. Eng. 4 (1), 49–56.

Van Ark, E. M., Detrick, R. S., Canales, J. P., Carbotte, S. M., Harding, A. J., Kent, G. M., Nedimovic, M. R., Wilcock, W. S. D., Diebold, J. B., Babcock, J. M., 2007. Seismic structure of the Endeavour segment, Juan de Fuca Ridge: Correlations with seismicity and hydrothermal activity. J. Geophys. Res. 112 (B02401).

Von Damm, K., 1990. Seafloor hydrothermal activity: Black smoker chemistry and chimneys. Annu. Rev. Earth Planet. Sci. 18, 173–204.

Von Damm, K., 1995. *Controls on chemistry and temporal variability of seafloor hydrothermal fluids. In* Seafloor hydrothermal systems. *(ed. S.E. Humphris, R.A. Zierenberg, L.S. Mullineaux and R.E. Thomson.)*. Vol. 91 of Geophys. Monogr. pp. 223–247.

Von Damm, K., 2001. Hydrothermal vent fluids, chemistry of. Encycl. of Ocean Sc., 1246–1253.

Von Damm, K., 2005. *Evolution of the Hydrothermal System at the* E*ast* P*acific* R*ise 9°50'*N*: Geochemical Evidence for changes in the upper oceanic crust. In* Mid-ocean ridges: Hydrothermal Interactions between the Lithosphere and Oceans. *(ed. C.R. German, J. Lin and L.M. Parson)*. Vol. 148 of Geophys. Monogr. pp. 285–304.

Von Damm, K., Bischoff, J., 1987. Chemistry of hydrothermal solutions from the southern Juan de Fuca Ridge. J. Geophys. Res. 92 (B11), 11334–11346.

Von Damm, K., Bray, A., Buttermore, L., Oosting, S., 1998. The geochemical controls on vent fluids from the Lucky Strike vent field, Mid-Atlantic Ridge. Earth Planet. Sci. Lett. 160, 521–536.

Von Damm, K., Buttermore, L., Oosting, S., Bray, A., Fornari, D., Lilley, M., Shanks, W., 1997. Direct observation of the evolution of a seafloor 'black smoker' from vapor to brine. Earth Planet. Sci. Lett. 149 (1-4), 101–111.

Von Damm, K., Lilley, M., Shanks, W., Brockington, M., Bray, A., O'Grady, K., Olson, E., Graham, A., Proskurowski, G., the SouEPR Science Party, 2003. Extraordinary phase separation and segregation in vent fluids from the southern East Pacific Rise. Earth Planet. Sci. Lett. 206, 365–378.

Von Damm, K., Oosting, S., Buttermore, L., Colodner, D., Edmonds, H., Edmond, J., Grebmeler, J., 1995. Evolution of East Pacific Rise hydrothermal vent fluids following a volcanic eruption. Nature. 375, 47–50.

Von Damm, K., Parker, C., Beers, K., Hyde, A., the PIRATES-1 Science Party, 2004. Continuing evolution of the hydrothermal system at the RIDGE2000 ISS, 9-10°N EPR: 1991-2004. Eos Trans. AGU 85 (47), Fall Meet. Suppl., Abstract B13A–0169.

Wang, P., Balay, S., Spernhoori, K., Wheeler, M., Abate, J., Smith, B., Pope, G., 1999. A fully implicit parallel EOS compositional simulator for large scale reservoir simulation. In: Proceedings of 15th SPE Symposium on Reservoir Simulation, Houston, TX, Feb. 14 - 17. SPE, pp. 63–71.

Wilcock, W. S. D., 1998. Cellular convection models of mid-ocean ridge hydrothermal circulation and the temperatures of black smoker fluids. J. Geophys. Res. 103 (B2), 2585–2596.

Wilcock, W. S. D., 2004. Physical response of mid-ocean ridge hydrothermal systems to local earthquakes. G-cubed 5 (Q11009).

Wilcock, W. S. D., McNabb, A., 1995. Estimates of crustal permeability on the Endeavour segment of the Juan de Fuca mid-ocean ridge. Earth Planet. Sci. Lett. 138, 83–91.

Wirsen, C., 2004. Is life thriving beneath the seafloor. Oceanus 42 (2).

Wolery, T., Sleep, N., 1976. Hydrothermal circulation and geochemical flux at mid-ocean ridges. J. Geology 84, 249–275.

Wu, Y., Zhang, K., Ding, C., Pruess, K., Elmroth, E., Bodvarsson, G., 2002. An efficient parallel-computing method for modeling isothermal multiphase flow and multicomponent transport in porous media. Adv. Wat. Res. 25, 243–261.

Yang, U., 2004. Parallel algebraic multigrid methods - High performance preconditioners. technical report UCRL-BOOK-208032, Lawrence Livermore National Laboratory.

Young, L., Hemanth-Kumar, K., 1991. High-performance block oil computations. In: Proceedings of 11th SPE Symposium on Reservoir Simulation, Arnaheim, CA, Feb. 17 - 20. SPE, pp. 135–144.

Zhang, K., Doughty, C., Wu, Y., Pruess, K., 2007. Efficient parallel simulation of CO_2 Geologic sequestration in saline acquifers. In: Proceedings of 2007 SPE Reservoir Simulation Symposium, Houston, USA, 26-28 Feb. SPE, p. 106026.

Zhang, K., Y.S., W., Ding, C., Pruess, K., 2001. Application of parallel computing techniques to large scale reservoir simulation. In: Proceedings of 26th Annual Workshop, Geothermal Reservoir Engineering, Stanford, CA, Jan. 29 - 31. Stanford University.

Zienkiewicz, O., Taylor, R., 2000. The finite element method. Volume 3: Fluid dynamics. Butterworth-Hienemann, Oxford, UK.

Zierenberg, R., Adams, M., Arp, A., 2000. Life in extreme environments: Hydrothermal vents. Proc. Nat. Acad. Sci. 97 (24), 12961–12962.

Curriculum Vitae

Personalia

Name Dingeman Coumou.

Citizenship Dutch. Born 5 April 1977, Eindhoven, The Netherlands.

Address Naunynstrasse 17
10997 Berlin, Germany

Tel. +49-331-288 2442

Email coumou@pik-potsdam.de

Education

2003–2008 PhD, Eidgenossische Technischer Hochschule (ETH), Zurich, Switzerland
Title: Numerical Modeling of Mid-Ocean Ridge Hydrothermal Systems
Supervisor: Dr. Thomas Driesner & Prof. Dr. Christoph A. Heinrich
Graduated: 28 March 2008 (provisional confirmation).

1995–2001 M.Sc. Geophysics, University of Utrecht, Utrecht, The Netherlands
Title: Modeling Hot Fractured Rock Systems. Case study of Soultz HFR reservoir
Supervisor: MA Dphil Christopher K. Harris
Graduated: 25 April 2001.

Work Experience

Research

2008–present Potsdam Institute for Climate Impact Research (PIK), Potsdam, Germany.
Post-doc position. Development of atmospheric module into Fortran based code Climber3 (Earth System Model of Intermediate Complexity)

2003–2008 Eidgenossische Technischer Hochschule (ETH), Zurich, Switzerland.
PhD-student position. Development of numerical solution techniques as well as parallel computing schemes (MPI) into the C++ based code CSMP++. I used the developed code to study multiphase fluid circulation of black smoker hydrothermal systems.

2000–2001 Shell International Exploration and Production B.V., Rijswijk, The Netherlands.
MSc trainee position in Shell's Geothermal Team. Numerical modeling and mathematical analytical analysis of thermal drawdown in geothermal heat-exchanger. Case study to European geothermal pilot project at Soultz-sous-Forets (Fr)

Exploration Geophysics

2001–2003 Dutch Onshore Offshore Recruitment BV (DOOR), Voorschoten, The Netherlands.
Marine Geophysicist. Assigned to several international companies active in the offshore industry (Van Oord-ACZ, Royal Boskalis-Westminster N.V., Gardline Surveys Ltd, Thales GeoSolutions Group). Responsible for mobilisation, data processing, quality control and interpretation during geophysical and hydrographical surveys. Final responsibility for geophysical data to be reported to client.

1995–2001 Geo-Resources BV, Rotterdam, The Netherlands.
Trainee Geophysicist (part-time). Geophysical data processing and interpretation, writing reports and involved in the development of new geophysical equipment (Sparker)

Publications

D. Coumou, T. Driesner, and C.A. Heinrich. The Structure and Dynamics of Mid-ocean Ridge Hydrothermal Systems. Science, accepted.

D. Coumou, T. Driesner, and C.A. Heinrich. Heat Transport at Boiling, Near-critical Conditions. Geofluids, in review.

D. Coumou, T. Driesner, C.A. Heinrich, and P. Weis. Phase-separation, Brine Formation and Salinity Variation at Black Smoker Hydrothermal Systems. Journal of Geophysical Research, in review.

D. Coumou. Numerical Simulation of Fluid Flow in Mid-ocean Ridge Hydrothermal Systems. PhD thesis, ETH-Zurich, 2008.

D. Coumou, S.K. Matthai, S. Geiger, and T. Driesner. A Parallel FE-FV Scheme to Solve Fluid Flow in Complex Geologic Media. Computers and Geosciences, in print.

S.K. Matthai, S. Geiger, S.G. Roberts, A. Paluszny, M. Belayneh, A. Mezentsev, H. Lu, D. Coumou, T. Driesner, and C.A. Heinrich. Numerical Simulation of Multiphase Fluid Flow in Structurally Complex Reservoirs. In Structurally Complex Reservoirs. (ed. S.J. Jolley, D. Bar, J.J. Walsh and R.J. Knipe). GSL Special Publications. 2007.

D. Coumou, S. Geiger, T. Driesner, C.A. Heinrich, and S.K. Matthai. The Dynamics of Mid-ocean Ridge Hydrothermal Systems: Splitting Plumes and Fluctuating Vent Temperatures. Earth and Planetary Science Letters, 245(1-2):218–231, 2006.

D. Coumou, C.K. Harris, and A.P. Berg vd. Application of Geocrack-2D and 3D to Model Thermal Drawdown in the Soultz Hot Dry Rock System. Transactions - Geothermal Resources Council, 25:167–172, 2001.

D. Coumou. Hot Fractured Rock systems. Case study of Soultz-sous-Forets HFR reservoir. Shell Technology Exploration and Production internal report EP 2001-5289, MSc thesis, University of Utrecht, 2001.

Selected Abstracts

D. Coumou, S. Geiger, T. Driesner and C.A. Heinrich. The influence of phase separation on the flow patterns of mid-ocean ridge hydrothermal systems, Geochim. Cosmochim. Acta, 72(12), p. A184-A184 Suppl.1, 2008.

D. Coumou, T. Driesner, C.A. Heinrich and S.K. Matthai. Can a sub-seafloor dike injection generate a mega-plume? Eos Trans. 87(52), Fall Meet. Suppl., Abstract B31B-1108, 2006.

D. Coumou, S. Geiger, T. Driesner and C.A. Heinrich. Timescales of Thermal Fluctuations and of Vent Location Changes in Mid-Ocean Ridge Hydrothermal Systems From Numerical Modelling, Eos Trans. 86(52), Fall Meet. Suppl., Abstract T31B-0498, 2005.

Computer skills

Geophysical Data Processing	ProMAX, Terramodel, QINSy, Delph Elics	Programming Languages	C++, FORTRAN77/90, MPI, MATLAB
Earth Scientific	Climber2/3, CSMP++, Geocrack2D/3D	Operating Systems	Windows, Linux, Unix

Languages

Dutch	Fluent	Mother tongue
English	Fluent	Reading, writing, conversation
German	Good	Reading, writing, conversation
French	Moderate	Reading, conversation
Spanish	Basics	Conversation

Selected Additional Courses

2006	Writing Research Papers for Publication at Sprachenzentrum ETH (Zurich, CH)
	Project Management at Business Tools AG (Zürich, CH)
2004-2005	Intensive German Course at Sprachenzentrum ETH and EBZ (Zurich, CH)
2002	Route Engineering Training at Global Marine Systems Ltd.(Chelmsford, UK)
	Underwater Acoustics at Skilltrade (Rotterdam, NL)
2001	QINSy Mapping and Route Design at QPS BV (Zeist, NL)
1998	Intensive Spanish course (San Pedro, Guatemala)
	PADI Open water & Advanced Open water dive courses (Utila, Honduras)

Selected Marine Geophysical Surveys

2003	Offshore rock dumping onboard flexible fallpipe vessels Tertnes and Rockness (Van Oord-ACZ), North Sea. Multibeam processing using TerraModel
	Port of Göteborg dredging and rock blasting project (Royal Boskalis Westminister NV), Sweden. Multibeam processing.
2002	Offshore Nigeria deep seismics oil exploration (Gardline Surveys Ltd.). Deep seismics, processing using ProMAX.
	Red Sea pipeline route survey offshore Ra's Ghärib (Thales GeoSolutions), Egypte. Side scan sonar, sub bottom profiler.
	Two pipeline route surveys in Gulf of Arabia (ADNOC). Side scan sonar, sub bottom profiler.
2001	Baltic pipeline route survey 2001 onboard M/V Geograph. Shallow seismics employing surface-tow sparker and Delph Elics processing software.

Selected Geologic Fieldworks

2005	Society of Economic Geologists (SEG) ore-deposit fieldwork to Peru
1998	Geology of the Pyrenees, organized by Geology department of University of Utrecht

Memberships

American Geophysical Union (AGU)

Society of Economic Geologists (SEG), Secretary from 2004 to 2006 of SEG-Zurich